

Scattering and Absorption of Light by Plasmonic Core-Shell Microgels: From Single Particle Response to Collective Resonances in Periodic Assemblies

Inaugural-Dissertation

zur Erlangung des Doktorgrades
der Mathematisch-Naturwissenschaftlichen Fakultät
der Heinrich-Heine-Universität Düsseldorf

vorgelegt von

Ekaterina Ponomareva
aus Moskau

DÜSSELDORF, APRIL 2022

aus dem Institut für Physikalische Chemie I
der Heinrich-Heine-Universität Düsseldorf

Gedruckt mit der Genehmigung der
Mathematisch-Naturwissenschaftlichen Fakultät der
Heinrich-Heine-Universität Düsseldorf

Berichterstatter:

1. Prof. Dr. Matthias Karg
2. Jun.-Prof. Dr. Markus Suta

Tag der mündlichen Prüfung: 07.06.2022

Eidesstattliche Erklärung

Ich, Ekaterina Ponomareva, versichere an Eides statt, dass die Dissertation von mir selbständig und ohne unzulässige fremde Hilfe unter Beachtung der „Grundsätze zur Sicherung guter wissenschaftlicher Praxis an der Heinrich-Heine-Universität Düsseldorf“ erstellt worden ist. Alle verwendeten Quellen und Hilfsmittel sind als solche gekennzeichnet und im Literaturverzeichnis aufgelistet.

Die vorliegende Dissertation wurde ausschließlich an der Mathematisch-Naturwissenschaftlichen Fakultät der Heinrich-Heine-Universität Düsseldorf vorgelegt. Es wurden keine früheren Promotionsversuche unternommen.

Ort, Datum

Unterschrift

Table of Contents

| | |
|--|--------------|
| List of Publications | VII |
| Presentations at Scientific Conferences | IX |
| List of Abbreviations and Symbols | XV |
| Danksagung | XVIII |
| Abstract | 1 |
| Zusammenfassung | 3 |
| 1 Introduction | 5 |
| 2 Theoretical Background | 9 |
| 2.1 Core-Shell Microgels | 9 |
| 2.1.1 Synthesis of the Metal Cores | 9 |
| 2.1.2 Synthesis of the Microgels | 11 |
| 2.1.3 Postmodification of the Cores | 12 |
| 2.1.4 Microgel Structure | 12 |
| 2.1.5 Volume Phase Transition Behaviour | 13 |
| 2.1.6 Collapse and Swelling Dynamics | 16 |
| 2.2 Scattering Techniques | 18 |
| 2.2.1 Dynamic Light Scattering | 19 |
| 2.2.2 Small Angle X-Ray and Neutron Scattering | 21 |
| 2.3 Colloidal Self-Assembly at Air/Liquid Interfaces | 25 |
| 2.3.1 Assembly Forces | 25 |
| 2.3.2 Two-Dimensional Colloidal Assembly Methods | 28 |
| 2.4 Plasmon Resonances of Noble Metal Nanoparticles | 31 |
| 2.4.1 Interaction of Light and Matter | 31 |
| 2.4.2 The Drude Theory of Metals | 33 |
| 2.4.3 Localized Surface Plasmon Resonances | 35 |
| 2.4.4 Coupling Phenomena | 38 |
| 2.4.5 Theoretical Calculations – Finite Difference Time Domain Simulations | 40 |
| 2.5 Image Analysis | 42 |
| 2.5.1 Fourier Analysis | 42 |
| 2.5.2 Pair Correlation Function | 43 |

| | | |
|----------|---|------------|
| 2.5.3 | Domain Size Analysis | 45 |
| 3 | Synopsis | 49 |
| 3.1 | Overview of the Thesis | 49 |
| 3.1.1 | The Fuzzy Sphere Morphology is Responsible for the Increase in Light Scattering During the Shrinkage of Thermoresponsive Microgels | 50 |
| 3.1.2 | Surface Lattice Resonances in Self-Assembled Gold Nanoparticle Arrays: Impact of Lattice Period, Structural Disorder, and Refractive Index on Resonance Quality | 50 |
| 3.1.3 | Temperature-Jump Spectroscopy of Gold-Poly(<i>N</i> -isopropylacrylamide) Core-Shell Microgels | 51 |
| 3.2 | Contributions to Joint Publications | 52 |
| 4 | The Fuzzy Sphere Morphology is Responsible for the Increase in Light Scattering During the Shrinkage of Thermoresponsive Microgels | 55 |
| 4.1 | Abstract | 56 |
| 4.2 | Introduction | 56 |
| 4.3 | Experimental Section | 59 |
| 4.3.1 | Chemicals | 59 |
| 4.3.2 | Synthesis | 59 |
| 4.3.3 | Methods | 61 |
| 4.4 | Theory | 63 |
| 4.4.1 | LCST and Cloud Point of PNIPAM | 63 |
| 4.4.2 | Light Scattering and Turbidity of PNIPAM Microgels | 64 |
| 4.4.3 | Absorbance Measurements and Scattering Cross-Section | 65 |
| 4.5 | Results and Discussion | 66 |
| 4.5.1 | General Characterization of CS Microgels | 66 |
| 4.5.2 | Temperature-Dependent Optical Properties | 69 |
| 4.5.3 | Volume Fraction of Polymer from Absolute Intensity Small-Angle Scattering Experiments | 72 |
| 4.5.4 | Light Scattering Properties Based on Effective, Average Volume Fractions | 79 |
| 4.5.5 | Light Scattering Properties Based on the Fuzzy Sphere Model | 81 |
| 4.6 | Conclusion | 85 |
| 4.7 | Supporting Information | 87 |
| 5 | Surface Lattice Resonances in Self-Assembled Gold Nanoparticle Arrays: Impact of Lattice Period, Structural Disorder, and Refractive Index on Resonance Quality | 109 |
| 5.1 | Abstract | 110 |
| 5.2 | Introduction | 110 |
| 5.3 | Experimental Section | 112 |
| 5.3.1 | Chemicals | 112 |

| | | |
|----------|---|------------|
| 5.3.2 | Synthesis | 112 |
| 5.3.3 | Fabrication of Periodic Particle Arrays | 113 |
| 5.3.4 | Methods | 113 |
| 5.4 | Results and Discussion | 115 |
| 5.4.1 | Au-PNIPAM Particle Characterization | 115 |
| 5.4.2 | Monolayers from Au-PNIPAM Particles | 115 |
| 5.4.3 | Optical Properties in an Asymmetric RI Environment | 120 |
| 5.4.4 | Optical Properties in Symmetric RI Environments | 121 |
| 5.4.5 | Direct Comparisons of Asymmetric and Symmetric RI Environments | 123 |
| 5.5 | Conclusions | 128 |
| 5.6 | Supporting Information | 130 |
| 6 | Temperature-Jump Spectroscopy of Gold-Poly(N-isopropylacrylamide) Core-Shell Microgels | 145 |
| 6.1 | Abstract | 146 |
| 6.2 | Introduction | 146 |
| 6.3 | Experimental Methods | 149 |
| 6.4 | Results | 152 |
| 6.4.1 | Steady-State Characterization | 152 |
| 6.4.2 | Temperature-Jump Spectroscopy | 156 |
| 6.5 | Discussion | 158 |
| 6.5.1 | Assigning T-Jump Spectra | 158 |
| 6.5.2 | Influence of Microgel Size and Cross-Linker Density | 159 |
| 6.5.3 | Collapse Mechanism | 163 |
| 6.6 | Conclusion | 168 |
| 6.7 | Supporting Information | 170 |
| 7 | Conclusion and Perspectives | 193 |
| | References | 197 |

List of Publications

1. **Ekaterina Ponomareva**, Kirsten Volk, Paul Mulvaney, and Matthias Karg
Surface Lattice Resonances in Self-Assembled Gold Nanoparticles Arrays: Impact of Lattice Period, Structural Disorder, and Refractive Index on Resonance Quality

Published in *Langmuir*, **2020**, *36*, (45), 13601-13612

2. **Ekaterina Ponomareva**, Ben Tadgell, Marco Hildebrandt, Marcel Krüsmann, Sylvain Prévost, Paul Mulvaney, and Matthias Karg
The Fuzzy Sphere Morphology is Responsible for the Increase in Light Scattering During the Shrinkage of Thermoresponsive Microgels

Published in *Soft Matter*, **2022**, *18*, 807-825

3. Ben Tadgell, **Ekaterina Ponomareva**, Matthias Karg, and Paul Mulvaney
Temperature-Jump Spectroscopy of Gold-Poly(*N*-isopropylacrylamide) Core-Shell Microgels

Published in *The Journal of Physical Chemistry C*, **2022**, *126*, (8), 4118-4131

4. Ben Tadgell, **Ekaterina Ponomareva**, Matthias Karg, and Paul Mulvaney
The Scattering of Visible Light by Au-PNIPAM Core-Shell Microgels

Manuscript in preparation for submission

5. Eric Sidney Aaron Görlitzer, Mario Zapata, **Ekaterina Ponomareva**, Aitzol Garcia-Etxarri, Ruben Esteban, Matthias Karg, Javier Aizpurua, and Nicolas Vogel
Induced Chirality in Structurally Achiral Surface Lattice Resonances

Manuscript in preparation for submission

Presentations at Scientific Conferences

1. **Ekaterina Ponomareva**, Kirsten Volk and Matthias Karg
Poster presentation: Angular-Dependent Optical Response of Self-Assembled Plasmonic Monolayers
Kolloid-Tagung "Multiresponsive Systems" (2017), Garching bei München, Germany
2. **Ekaterina Ponomareva** and Matthias Karg
Poster presentation: Spectroscopic Investigation of Periodic Plasmonic Superstructures
DPG-Frühjahrstagung (DPG Spring Meeting) (2018), Berlin, Germany
3. **Ekaterina Ponomareva** and Matthias Karg
Poster presentation: Spectroscopic Investigation of Periodic Plasmonic Superstructures
14th Zsigmondy Colloquium of the German Colloid Society (2018), Mainz, Germany
4. **Ekaterina Ponomareva**, Kirsten Volk and Matthias Karg
Oral presentation: Distance-Dependent Plasmon Resonance Coupling in Nanoparticle Superstructures
The 9th Australian Colloid and Interface Symposium (2019), Hobart, Tasmania
5. **Ekaterina Ponomareva**, Kirsten Volk and Matthias Karg
Oral presentation: Surface Lattice Resonances in Self-Assembled Plasmonic Gold Nanoparticle Arrays
15th Zsigmondy Colloquium of the German Colloid Society (2019), Dresden, Germany
6. **Ekaterina Ponomareva**, Kirsten Volk and Matthias Karg
Oral presentation: Surface Lattice Resonances in Self-Assembled Plasmonic Gold Nanoparticle Arrays
33rd Conference of The European Colloid and Interface Society (2019), KU Leuven, Belgium
7. **Ekaterina Ponomareva**, Kirsten Volk and Matthias Karg
Oral presentation: Tuning of Plasmon Coupling in Self-Assembled Plasmonic Monolayers
16th Zsigmondy Colloquium of the German Colloid Society (2020), Düsseldorf, Germany

List of Abbreviations and Symbols

| | |
|--------------------------|---|
| 2D | Two-dimensional |
| a | Lattice constant |
| A | Absorbance |
| AFM | Atomic force microscopy |
| α | Deswelling ratio, Complex polarizability |
| α_j | Angle between three particles |
| α_{mean} | Mean angle between three particles |
| a. u. | Arbitrary units |
| Au – NP | Gold nanoparticle |
| Au – PNIPAM | Gold Poly N -isopropylacrylamide microgel |
| \mathbf{B} | Magnetic induction |
| BA | Butenylamine hydrochloride |
| β | Wavelength exponent |
| β_{Siegert} | Coherence factor |
| BIS | N, N' -methylenebisacrylamide |
| c | Speed of light in vacuum (from Latin: celeritas) |
| c_0 | Bulk concentration of the salt |
| C_1, C_1 | Constants in Poisson-Boltzmann equation |
| C_{abs} | Absorption cross section |
| CDA, DDA | Coupled or discrete dipole approximation |
| C_{ext} | Extinction cross section |
| χ | Flory-Huggins-Stavermann interaction parameter, Dielectric susceptibility |
| CS | Core-shell |
| C_{sca} | Scattering cross section |
| CTAB | Cetyltrimethylammonium bromide |
| CTAC | Cetyltrimethylammonium chloride |
| cw | Continuous wave |
| d | Pathlength, interplanar spacing |
| D, D_T | Diffusion constant, translational diffusion constant |
| d_{c-c} | Nearest center-to-center interparticle distance |
| d_{core} | Core diameter |
| $\Delta\eta$ | Difference in scattering length density |
| ΔF | Change in free energy |
| ΔH | Change in enthalpy |

| | |
|--|--|
| $\Delta OD_{\text{fast}}, \Delta OD_{\text{slow}}, \Delta OD_{\text{total}}$ | Changes in fast, slow and total optical density |
| ΔS | Change in entropy |
| Dev_{α_j} | Standard deviation of the angle |
| Dev_{d_i} | Standard deviation of the distance |
| DFM | Dark-field microscopy |
| DFT | Discrete Fourier transformation |
| d_h | Hydrodynamic diameter |
| D | Dielectric displacement |
| DLS | Dynamic light scattering |
| d_{mean} | Mean interparticle distance |
| e | Electron charge |
| $E(t), \mathbf{E}$ | Electric field (vector) |
| e.g. | For example (from Latin: <i>exempli gratia</i>) |
| ε | Dielectric permittivity |
| ε_0 | Dielectric permittivity of vacuum |
| $\varepsilon_1, \varepsilon_2$ | Real and imaginagy componetns of complex dielectric function |
| ε_m | Dielectric permittivity of medium |
| ε_M | Dielectric permittivity of metal |
| ε_∞ | Dielectric constant |
| η | Viscosity |
| η_{FuzzySph} | Radial scattering length density for the fuzzy sphere |
| et al. | And others (from Latin: <i>et alii</i>) |
| η_{PNIPAM} | Radial scattering length of pure PNIPAM |
| $\eta_{\text{sol}}, \eta_{\text{solvent}}$ | Radial scattering length of solvent |
| η_{sph} | Radial scattering length of inner microgel region |
| FDTD | Finite difference time domain |
| FFT | Fast Fourier transformation |
| $F(k_x, k_y)$ | Fourier Trnasform of a function |
| FWHM | Full width at half-maximum |
| g^1 | First-order correlation function |
| g^2 | Autocorrelation function |
| $\Gamma, \bar{\Gamma}$ | Decay constant, mean decay constant |
| γ | Damping constant |
| $g(r)$ | Pair correlation function |
| H | Magnetic field |
| h | Planck's constant, sharpness of the transition |
| HAuCl_4 | Gold(III) chloride trihydrate |
| HeNe | Helium-Neon laser |
| h, k | Miller indices |
| $I_0, I(d)$ | Intensity of light |
| i | Imaginary unit |
| I_{dyn} | Dynamic scattering contribution (Ornstein-Zernicke) |

| | |
|--|---|
| i.e. | That is (from Latin: id est) |
| I_{FuzzySph} | Scattering intensity for the fuzzy sphere |
| I_{inc} | Intensity from incoherent background |
| $I_{\text{L}}(0)$ | Lorentzian intensity |
| ILT | Inverse Laplace transformation |
| I_{scat}, I | Scattering intensity |
| I_{stat} | Static scattering contribution |
| $\mathbf{J}_{\text{ext}}, \mathbf{J}, \mathbf{J}_{\text{tot}}$ | External, internal, and total current densities |
| K | Coefficient of the bulk modulus |
| κ | Inverse Debye length |
| k_{B} | Boltzmann constant |
| KCl | Potassium chloride |
| $\mathbf{k}_{\text{inc}}, \mathbf{k}_{\text{sca}}$ | Incident wave vector and scattering wave vector |
| \mathbf{k}, k_x, k_y | Wave vector |
| λ | Wavelength |
| $\lambda_{\text{Bragg}}, \lambda_{\text{hk}}$ | Wavelength of diffraction peak |
| λ_{LSPR} | Wavelength of localized surface plasmon resonance |
| λ_{max} | Wavelength of resonance position |
| λ_{RA} | Wavelength of Rayleigh Anomalie mode |
| LCST | Lower critical solution temperature |
| LSPR | Localized surface plasmon resonance |
| \mathbf{M} | Magnetization |
| m_0 | Effective electron mass |
| $M_{\text{Au-core}}$ | Average molecular weight of gold cores |
| m_e | Mass of an electron |
| MMP | Multiple Multipole Method |
| M | Molar mass |
| m_p | Mass of a photon |
| μ | Magnetic permeability, Coefficient of the shear modulus |
| μ_0 | Magnetic permeability of vacuum |
| n | Free electron density |
| N | Number density of particles |
| N_{A} | Avogadro's number |
| Na_3 citrate | Sodium citrate dihydrate |
| ∇ | Nabla operator |
| N_c | Number of chains in the polymer network |
| N_{gel} | Average number of monomers between the cross-links |
| NIPAM | <i>N</i> -isopropylacrylamide |
| N_{particle}, N | Number of particles |
| N_{tri} | Number of triangles |
| ν | Frequency |
| OD, OD' | Optical density, normalized optical density |

| | |
|--|--|
| OD_{\min}, OD_{\max} | Optical density of swollen and collapsed microgel state |
| ω | Angular frequency |
| ω_p | Plasma frequency |
| P | Polarization |
| PBC | Periodic boundary conditions |
| PDI | Polydispersity index |
| ϕ | Polymer volume fraction |
| ϕ_0 | Polymer volume fraction at the reference state |
| ϕ_{box} | Polymer volume fraction in the inner microgel region |
| ϕ_{eff} | Average polymer volume fraction |
| ϕ_{microgel} | Microgel volume fraction |
| ϕ_{shell} | Polymer volume fraction of the microgel shell |
| ϕ_{water} | Volume fraction of water |
| $P_{\text{inhom}}(q)$ | Form factor of an inhomogeneous sphere |
| $P_{\text{hom}}(q)$ | Form factor of a homogeneous sphere |
| Π | Osmotic pressure |
| $P(k_x, k_y)$ | Power spectrum |
| PML | Perfectly matched layer |
| PNIPAM | Poly- <i>N</i> -isopropylacrylamide |
| PPS | Potassium peroxodisulfate |
| $P(q)$ | Form factor |
| ψ | Electric potential |
| ψ_0 | Electric potential at the surface |
| Q | Quality factor |
| \mathbf{q} | Scattering vector |
| R, R_{final}, R' | Radius, final radius, normalized radius |
| RA | Rayleigh anomaly |
| R_{box} | Radius of the inner microgel region with homogeneous density |
| $R_{\text{core}}, R_{\text{Au}}$ | Radius of the gold core within microgel |
| R_{cut} | Cutoff radius |
| RDF | Radial distribution function |
| RDG | Rayleigh-Debye-Gans approximation |
| R_g | Radius of gyration |
| R_h | Hydrodynamic radius |
| ρ | Density |
| $\rho_{\text{ext}}, \rho, \rho_{\text{tot}}$ | External charge, internal and total charge |
| RI, n, n_p, n_s | Refractive index, refractive index of scattering objects and dispersing medium |
| n_{box} | Refractive index of the inner microgel region |
| $n_{\text{dispersion}}$ | Refractive index of the microgel dispersion |
| $n_{\text{microgel,eff}}$ | Averaged microgel refractive index |
| n_{shell} | Refractive index of the shell |

| | |
|--|--|
| R_{\max}, R_{\min} | Radius of fully swollen and collapsed microgel |
| R_{SANS} | Radius determined from SANS |
| R_t | Shell thickness |
| s | Standard deviation parameter |
| S | Array factor |
| SANS | Small angle neutron scattering |
| SAXS | Small angle X-ray scattering |
| SDS | Sodium dodecyl sulfate |
| SEM | Scanning Electron Microscopy |
| σ | Thickness of the fuzzy polymer shell, Conductivity |
| SLD | Scattering length densities |
| SLR | Surface lattice resonance |
| SLS | Static light scattering |
| SPP | Surface Plasmon Polariton |
| $S(q)$ | Structure factor |
| t | Time |
| T | Temperature |
| τ | Correlation time, lifetime |
| τ_c | Capacitor discharge time-constant |
| $\tau_{\text{fast}}, \tau_{\text{slow}}$ | Fast and slow lifetime |
| T_{cp} | Cloud point temperature |
| TEM | Transmission Electron Microscopy |
| TFSF | Total-field scattered-field |
| θ | Scattering angle |
| Tol_α | Tolerance parameter of the angle |
| Tol_d | Tolerance parameter of the distance |
| u | Displacement in the polymer network |
| v | Molar volume of solvent |
| UV – Vis | Ultraviolet-visible |
| V_0 | Volume at the reference state |
| vdW | Van der Waals force |
| V_h | Hydrodynamic volume |
| $V_{h,\text{swollen}}, V_{h,\text{collapsed}}$ | Hydrodynamic volume in the swollen and collapsed state |
| $V_{\text{microgel}}, \nu_0$ | Volume of microgel |
| V_{polymer} | Total volume of polymer |
| VPT | Volume phase transition |
| VPTT | Volume phase transition temperature |
| ξ | Correlation length |

Danksagung

Mit diesem Buch endet eine lange Reise, auf der mich viele Menschen begleitet und unterstützt haben. Ich möchte mir an dieser Stelle etwas Zeit nehmen und mich bei allen bedanken, ohne deren Beitrag diese Arbeit sicherlich nicht in dieser Form entstanden wäre.

Zuallererst gebührt mein Dank Prof. Dr. Matthias Karg, der mich in seinen Arbeitskreis aufgenommen hat und mir die Tür zu den spannenden Forschungsfeld der Mikrogele und Plasmonik öffnete. Mit seiner konstruktiven Kritik und seinen kreativen Ideen hat er stets meine Arbeit vorangetrieben. Er hat mich ermutigt meine Forschungsergebnisse auf zahlreichen Konferenzen vorzustellen und an der Bayreuth International Summer School teilzunehmen, wo ich vielen inspirierenden Menschen begegnet bin und teilweise sogar Freundschaften fürs Leben entstanden sind. Außerdem gab er mir die Chance einen Forschungsaufenthalt in Australien durchzuführen.

Prof. Paul Mulvaney (The University of Melbourne) danke ich für den sehr herzlichen Empfang in seinem Labor und für die wunderbare Kollaborationsarbeit, die in mehreren Publikationen gefruchtet ist. Die Arbeit in Exciton Science Labor wäre nicht halb so schön gewesen ohne der ganzen freundlichen und hilfsbereiten Menschen, die ich hier aufzählen möchte: Ben Tadgell, der mit mir zusammen an unseren großen Mikrogele Projekt gearbeitet hat und das Einleben in Melbourne erleichterte; Heyou Zhang, der mich bei TEM und DFM Messungen unterstützt hat und verdammt gute Cocktails mixt; Eser Akinoglu, der immer wieder neuen Input für meine Forschung gab; Hanbo Yang, mit der man einfach gute Zeit haben konnte; Yannic Brasse (Technische Universität Dresden), der gleichzeitig mit mir seinen Forschungsaufenthalt in Melbourne hatte und mit dem ich zusammen das neue Labor und die neue Stadt entdecken durfte; und zum Schluss Johanna Monk, die dafür sorgte, dass alles Organisatorische reibungslos verlief.

Weiterhin möchte ich mich bei Melanie Pöhlmann und Sylvia Sprödhuber bedanken, dafür dass sie mich herzlich in Melbourne-Bayreuth Polymer/Colloid Netzwerk aufgenommen und meine Reise nach Australien koordiniert haben. Natürlich danke ich auch dem Deutschen Akademischen Austauschdienst für die finanzielle Unterstützung der Reise.

Eric Görhlitzer und Prof. Dr. Nicolas Vogel (Friedrich-Alexander-Universität Erlangen-Nürnberg) danke ich für die schöne Kollaborationsarbeit.

Vielen Dank an Sylvain Prévost (Institut Laue-Langevin) für die SANS Messungen und sonstige Unterstützung bei den Analysen der Streudaten.

Meine Promotionszeit wurde stark durch das coole und lustige Team bereichert. Danke, Kristina, Kirsten, Arne, Julian, Marcel, Yichu, Marco, Marius, Tomo, Vahan, Kuk, Déborah und Caspar für zum einem das wunderbare Arbeitsklima, aber auch für die ganzen Freizeitaktivitäten wie Grillabende, Weihnachtsfeier und die unzähligen Kickerspiele, wo jeder von uns seine einzigartige Spieltechnik beherrschte. Ich bin sehr froh euch als Arbeitskollegen gehabt zu haben! Noch einen speziellen Dank an meine tollen Büronachbarinnen Kirsten Volk, Sophia Köhler und etwas später Keumkyung Kuk für Unterstützung in sämtlichen Fragestellungen. An dieser Stelle soll Andrea Lotzwick nicht unerwähnt bleiben, danke für deine freundliche Art und die herzlichen Gespräche.

Für das mühevollen Korrigieren, sowohl fachlich als auch sprachlich bedanke ich mich bei Nicholas, Julian, Déborah, Marco, Ben, Marius, Kuk, Dennis, Tobias und Michael.

Zum Schluss möchte ich mich noch bei meinem liebevollen Partner und Familie bedanken, die mich durch all die vielen Jahre stets auf jede erdenkliche Art unterstützt und immer an mich geglaubt haben.

Abstract

Hybrid core-shell microgels composed of metal nanoparticle cores and thermoresponsive polymer shells feature unique optical properties combining the absorption and the scattering of both components. Microgels are three-dimensional, cross-linked polymer networks that are often referred to as "smart" when they respond to external stimuli such as temperature. The most prominent examples are poly-(*N*-isopropylacrylamide) (PNIPAM) microgels cross-linked with *N,N'*-methylenebisacrylamide (BIS). PNIPAM microgels undergo a volume phase transition (VPT) at approximately 32 °C from a swollen to a collapsed state. In the swollen state, the microgel possesses a fuzzy-sphere morphology with a rather homogeneously cross-linked core and a fuzzy shell with gradually decreasing degree of cross-linking towards the surface. The microgel collapses above the volume phase transition temperature (VPTT), resulting in reduced size and a homogeneous sphere-like structure. The shrinkage of the microgel is accompanied by an increase in the polymer density and, therefore, the refractive index (RI). In the swollen state, the polymer density and the fuzziness strongly depend on the initial amount of cross-linker. In contrast, the polymer density differences are rather small in the collapsed state.

In this thesis, the microgel structure was obtained from scattering methods, *e.g.* small-angle X-ray and neutron scattering. The gold core within the shell allowed precise control over the shell's thickness and the high X-ray contrast of gold was used to determine particle number concentration in dispersion. Although the morphology of various microgel systems has been widely studied, the UV-visible spectroscopic properties of the PNIPAM microgels were surprisingly only rarely addressed in the literature. In the case of gold-PNIPAM microgels investigated in this work, the optical response consists of the strong scattering contribution of the shells and the localized surface plasmon resonance (LSPR) of the gold nanoparticles. During the VPT, the collapse of the microgel is accompanied by an increase in light scattering intensity. The capacitor-discharge temperature-jump spectroscopy can excellently monitor the collapse process via the changes in light scattering. Curiously, the dynamics of VPT from fuzzy microgels has been only scarcely investigated so far and the collapsing mechanism is not well understood. This thesis bridges the findings from microgel structure analysis with the temperature-dependent absorbance measurements and, based on these results, shows a two-step deswelling process for PNIPAM microgels.

The core-shell microgels were post-modified by overgrowing the gold cores to increase their size and absorbance. As a result, the absorbance contribution of the gold cores dominated over the scattering contribution of the shell, allowing the investigation of the optical behaviour of the metal cores. Gold particles with diameters of 100 nm or smaller primarily support dipolar LSPRs. These resonances can be excited with visible light

around the green wavelength, explaining the reddish appearance of gold nanoparticle dispersions. However, gold is a relatively poor plasmonic material with high absorption losses resulting in low qualities of the resonances. These losses can be significantly reduced by arranging gold particles into periodic arrays. In the case of gold-PNIPAM core-shell microgels, the polymer shell acts as a spacer between the gold cores and due to its ability to adsorb to liquid interfaces, makes those particles suitable for self-assembly. The thickness of the PNIPAM shell allows for tuning of the interparticle distances. The self-assembly approach allows the preparation of two-dimensional (2D) particle arrays with a broad range of interparticle spacings. Plasmonic arrays with wavelength-scale distances between the particles support plasmonic-diffractive coupling from single LSPRs to diffractive modes resulting in surface lattice resonances (SLRs). The appearance and quality of SLRs are strongly affected by the interparticle distance, the structural lattice disorder, and the RI environment surrounding the gold nanoparticles. The strongest plasmonic-diffractive coupling was achieved in a symmetric RI environment and interparticle distances on the visible wavelength-scale. Moreover, a spectral overlap between the single particle LSPR and diffractive mode of the lattice is crucial for high quality SLRs. This work identifies relevant criteria for the appearance of strong SLRs in self-assembled arrays and thereby contributes to the deeper understanding of coupling phenomena of plasmonic particles.

Zusammenfassung

Hybride Kern-Schale Mikrogele bestehend aus metallischen Nanopartikelkernen und thermoresponsiven Polymerschalen zeigen einzigartige optische Eigenschaften, indem sie die Absorption und die Streuung beider Komponenten vereinen. Mikrogele sind dreidimensionale, quervernetzte Polymernetzwerke, die häufig als „smart“ bezeichnet werden, wenn diese auf äußere Reize, wie zum Beispiel Temperatur reagieren. Das prominenteste Beispiel sind die Poly-(*N*-isopropylacrylamid) (PNIPAM) Mikrogele quervernetzt mit *N,N'*-Methylenbisacrylamid (BIS). PNIPAM Mikrogele durchlaufen einen Volumenphasenübergang (VPT) bei etwa 32 °C vom gequollenen zum kollabierten Zustand. Im gequollenen Zustand weist das Mikrogel die Morphologie einer unscharfen Kugel (eng.: fuzzy-sphere) mit einem homogenen quervernetzten Kern und einer Schale auf, deren Vernetzung graduell zur Oberfläche abnimmt. Das Mikrogel kollabiert oberhalb der Volumenphasenübergangstemperatur (VPTT), was zur Größenreduzierung und einer homogenen kugelartigen Struktur führt. Die Schrumpfung des Mikrogeles wird von einem Anstieg der Polymerdichte und des Brechungsindex begleitet. Während die Polymerdichte und die Schalendeformiertheit im gequollenen Zustand stark von der verwendeten Menge des Quervernetzers abhängen, sind die Polymerdichteunterschiede im kollabierten Zustand eher klein.

Die Mikrogelstruktur wurde mithilfe der Streumethoden wie Kleinwinkelröntgenstreuung und -neutronenstreuung erhalten. Der Goldkern innerhalb der Schale erlaubte eine präzise Kontrolle über die Schalendicke, während der hohe Gold-Röntgenkontrast für die Bestimmung der Anzahl der Partikel in der Dispersion verwendet wurde. Obwohl die Morphologie der verschiedenen Mikrogelesysteme ausgiebig studiert wurde, finden überraschenderweise UV-sichtbare spektroskopische Eigenschaften der PNIPAM Mikrogele kaum Erwähnung in der Fachliteratur. In dem Fall der in dieser Arbeit untersuchten Gold-PNIPAM Mikrogele besteht die optische Antwort aus dem starken Streubeitrag der Schale und der lokalisierten Oberflächenplasmonresonanz (LSPR) der Gold-Nanopartikel. Während der VPT wird der Mikrogelekollaps von einem Anstieg der Streuintensität begleitet. Die Kondensatorentladung Temperatursprung Spektroskopie (eng.: capacitor-discharge temperature-jump spectroscopy) kann den Prozess des Kollapses über die Änderung der Streuung hervorragend verfolgen. Seltsamerweise wurde die Dynamik der VPT der Mikrogele bisher wenig untersucht und der Kollapsmechanismus ist nicht gänzlich verstanden. Diese Arbeit verbindet die Erkenntnisse aus der Mikrogelstrukturanalyse mit den temperaturabhängigen Messungen der Absorbanz und zeigt darauf basierend einen Zwei-Stufen-Kollaps für die PNIPAM Mikrogele.

Die Kern-Schale Mikrogele wurden postmodifiziert, indem die Goldkerne vergrößert wurden, um deren Absorbanz zu erhöhen. Daraufhin dominierte der Absorbanzbeitrag des Goldkerns über die Streuung der Schale, was die Untersuchung des optischen Ver-

haltens der Metallkerne erlaubt. Goldpartikel mit einem Durchmesser von 100 nm oder kleiner unterstützen hauptsächlich die dipolaren LSPRs. Diese Resonanzen können mit sichtbarem Licht im grünen Bereich angeregt werden, wodurch Dispersionen von Gold-Nanopartikeln rötlich erscheinen. Jedoch gehört Gold aufgrund der hohen Absorptionsverlusten zu den schwachen plasmonischen Elementen, die zu einer niedrigeren Resonanzqualität führen. Die Verluste können signifikant reduziert werden, indem Goldpartikel periodisch in einem Gitter angeordnet werden. Im Fall der Gold-PNIPAM Kern-Schale Mikrogele dient die Polymerschale als Abstandshalter für die Goldkerne und die Mikrogele eignen sich für die Selbst-Assemblierung aufgrund ihrer Adsorptionsfähigkeiten zu den Flüssigkeitsgrenzflächen. Dabei wurde die Dicke der Schale dazu verwendet um die Partikelabstände anzupassen. Mittels der Selbst-Assemblierung wurden zweidimensionale (2D) Partikelanordnungen mit einem breiten Bereich von Interpartikelabständen hergestellt. In plasmonischen Gittern mit Abständen im Bereich von Wellenlängen zwischen den Partikeln können die LSPRs mit den Bragg-Moden koppeln, wodurch Oberflächengitterresonanzen (SLRs) entstehen. Das Auftreten und die Qualität der SLRs hängt stark von den Partikelabständen, den strukturellen Gitterunordnungen und dem Brechungsindex der Umgebung der Goldpartikel ab. Eine besonders starke plasmonisch-photonische Kopplung wurde in einer symmetrischen Brechungsindex Umgebung und Partikelabständen in Wellenlängengrößenordnung erreicht. Des Weiteren ist eine spektrale Überlappung zwischen der Einzelpartikel-LSPR-Mode und der Bragg-Mode des Gitters für hochqualitative SLRs nötig. Diese Arbeit identifiziert die relevanten Kriterien für das Auftreten starker SLRs in selbst-assemblierten Gittern und trägt zum tieferen Verständnis der Kopplungsphänomene der plasmonischen Partikeln bei.

1 Introduction

Microgels are three-dimensional, cross-linked polymer networks. They are sized between 100 nm and the micron range. Under good solvent conditions, microgels are swollen due to their ability to take up an enormous amount of solvent, usually water. Microgels are unique systems showing properties typical for colloids, macromolecules and surfactants, making them interesting for fundamental research and numerous potential applications^{1,2}. Like colloids, they can crystallize at high volume fractions, and like macromolecules, they are soft and deformable. The typical characteristic of surfactants is their ability to adsorb to liquid interfaces. The adsorption ability of microgels makes them suitable for interface-mediated self-assembly³. Responsive microgels are composed of polymers that can respond extremely fast to external stimuli such as temperature, pH and ionic strength. In comparison, macroscopic gels respond significantly slower due to their larger dimensions because the response speed correlates with the size of the gel^{4,5}. Because of this responsive behaviour, those gels are often referred to as "smart" systems. The most studied are poly-*N*-isopropylacrylamide (PNIPAM) microgels first introduced by Pelton and Chibante⁶. The PNIPAM gels are well-known for undergoing a volume phase transition (VPT) from a swollen hydrophilic state to a collapsed state where polymer-polymer interactions are favoured. The transition temperature is close to the human body temperature at approximately 32 °C⁷. While the structural transition of microgels from the swollen to the collapsed state has been widely investigated in the literature, surprisingly, less attention has been paid to the optical properties of PNIPAM microgels depending on the morphology and swelling state. During the VPT, the shrinkage of the microgel is accompanied by increasing scattering intensity (or absorbance) with increasing temperature^{8,9}. This observation seems to be counterintuitive since the scattering intensity strongly depends on the size of the object. In the case of particles smaller than the wavelength of the visible light, the relationship $I_{\text{sca}} \propto R^6$ is given according to the Rayleigh-Debye-Gans (RDG) approximation. The increase in absorbance is commonly attributed simply to the simultaneous increase of refractive index of the microgel^{9,10,11}. However, the origin of the scattering changes during the collapsing process has not been sufficiently addressed in the literature. Other open questions are how fast a microgel collapses when exposed to external stimuli and how its size and morphology affect the collapsing time. Knowledge of the microgel's structure is crucial to answering these questions. Scattering methods are commonly used to obtain the morphology of a microgel. The measured scattering intensity is proportional to the number of microgels in the dispersion. Therefore, a precise determination of the number of microgels per sample volume, *i.e.*, the particle number concentration, is necessary to obtain the microgel's structure. However, determining this number for dilute microgel dispersions can be challenging. An elegant solution is to incorporate

gold nanoparticle cores during the polymerization to obtain microgels containing exactly one core. Moreover, the gold seeds allow precise control over the microgel's size¹². Due to the high X-ray contrast of the gold particles, the absolute intensity of small-angle X-ray scattering can be used to determine particle number concentration. Generally, the merging of microgels and metal cores allows the fabrication of new nanocomposite materials with combined properties of inorganic and organic components. This offers countless possibilities for future devices.

Among all metals, gold nanoparticles are the most reported in the literature¹³ and have been used for longer than one would expect *a priori*. The earliest prominent example of nanotechnology is the Lycurgus Cup from the 4th century found in the Roman Empire¹⁴. The dichroic glass of the cup shows a unique colour phenomenon because of enclosed colloidal silver and gold in the glass. Metal nanostructures are known for their unique optical properties; their interactions with light differ strongly from bulk metal. Electromagnetic waves induce collective oscillations of the conduction electrons when irradiating a small metal particle. These oscillations are referred to as localized surface plasmon resonances (LSPRs)^{15,16}. In the case of gold, the excitation of LSPRs leads to absorption and scattering in the visible light range around green wavelengths. As a result, gold particles with nanometer dimensions appear in reddish colour¹⁷. The plasmon resonances are interesting for their sensitivity to the local dielectric environment and the concentrated, localized electromagnetic fields, making them suitable for many applications like ultrasensitive sensing¹⁸, lasing¹⁹ and photocatalysis²⁰. However, gold nanoparticles (Au-NPs) tend to aggregate. To prevent them from aggregation, they can be coated by polymers or small molecules¹³ or encapsulated into soft microgel shells⁸. The microgel shell provides high colloidal stability and allows post-modifications on the metal core due to its high porosity²¹.

From the optical point of view, gold is a relatively poor plasmonic material and suffers from strong damping effects and a short lifetime of the LSPR mode²². As a result, absorption losses and low quality factors limit Au-NPs for many nanophotonic applications. By arranging single Au-NPs into ordered lattices, the optical losses can be reduced and the quality factor significantly increased. For nanoparticles with wavelength-scale interparticle spacing, the plasmonic LSPR mode can couple with the photonic diffractive mode, resulting in surface lattice resonance (SLRs)^{23,24}. Such plasmonic lattices might be suitable for various applications such as lasing²⁵, light-emitting diodes²⁶, solar cells²⁷, photocatalysis²⁰, sensing²⁸ and colour printing²⁹. Looking at the current literature shows that engineering such arrays, tuning their optical properties, and understanding various optical phenomena is still of great interest to researchers.^{30,31,32,33} Various shapes of particles such as spheres³⁴, cuboctahedra³⁵ and even crescents³⁶ are studied. Therefore, a plethora of methods is available to achieve ordered lattices, including electron beam lithography³⁰, soft interference lithography³⁷, template-assisted self assembly^{33,35} and direct self-assembly of colloidal particles^{21,38}. Lithographic approaches were the preferred method to fabricate highly ordered particle arrays for a long time. However, colloidal self-assembly gained increasing interest over recent years because of the low cost and rapid production of cm² areas of particle lattices³⁹. Microgels are ideal building blocks for two-dimensional (2D) arrays via self-assembly. Self-assembled arrays support various

coupling phenomena, *e.g.*, SLRs, albeit their structural defects. Hence, it makes them interesting for investigation of the impact of the structural disorder on the coupling and resonance quality. A comparison between experimental and theoretical optical properties of imperfect particle lattices and the dependence of the properties on the interparticle distances is still missing. Consequently, an open question is: how competitive are self-assembled particle arrays to lithographically fabricated lattices that support plasmonic-diffractive coupling?

In this thesis, core-shell microgels (Au-PNIPAM) were synthesized using a plasmonic gold core and a soft PNIPAM polymer shell crosslinked with *N,N'*-methylenebisacrylamide (BIS). To investigate the scattering properties and temperature-induced collapse dynamics, the polymer shell was varied in thickness and density, while the gold core was kept at approximately 15 nm in diameter. Microgel structure at different swelling states was studied by small-angle neutron scattering and matched with findings from absorbance experiments. The correlation between structure and absorbance of the microgels was used to study the kinetics of the collapsing process. Thereby the kinetics during the VPT was monitored by capacitor-discharge temperature-jump spectroscopy.

In order to study the plasmonic properties, the gold cores were post-modified within the shell; the cores were overgrown with gold to increase their size (≈ 100 nm) and strengthen their optical response. Modified Au-PNIPAM microgels were then arranged into 2D lattices via interface-mediated self-assembly. During self-assembly the polymer shell acted as a spacer between the gold cores and allowed for lattices with a broad range of interparticle distances. The optical response of the particle arrays was investigated experimentally using UV-Vis spectroscopy and theoretically by finite difference time domain simulations. In particular, the work identified various coupling scenarios in particle arrays and discussed the effects of refractive index, structural disorders and lattice period.

The remainder of the thesis is organized as follows: the theoretical background (chapter 2) is divided into five major parts. The first part (section 2.1) presents core-shell Au-PNIPAM microgels, including the detailed synthesis path and the microgel morphology. The volume phase transition behaviour of the shell is described by Flory-Rehner theory, and swelling/collapse kinetics is discussed. Section 2.2 introduces the fundamental theory of dynamic and static light scattering methods; in particular, small-angle X-ray and neutron scattering (SAXS and SANS) are depicted. The third part (section 2.3) deals with colloidal self-assembly at air/liquid interfaces and highlights the forces that drive particles into ordered lattices. Furthermore, the section gives a presentation of selected colloidal assembly methods. The plasmonic properties of gold particles are introduced in section 2.4 starting with a general discussion about the interaction of light and matter by using the Maxwell equations. Furthermore, the section covers the Drude theory to describe metallic properties and presents different plasmonic coupling phenomena. The last section 2.5 closes with image analysis methods. The theoretical background is followed by a synopsis (chapter 3), which overviews the publications and outlines contributions to joint publications. In chapters 4 to 6, full publications are presented. Finally, the thesis ends with an overall conclusion and gives perspectives for future studies (chapter 7).

2 Theoretical Background

2.1 Core-Shell Microgels

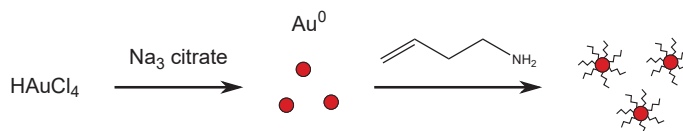
This section starts with an introduction of the synthesis of the Au-PNIPAM microgels, including a discussion about mechanisms of the gold core formation and the encapsulation into PNIPAM shells. It follows the presentation of the PNIPAM microgel structure by a radial polymer density profile introduced by Stieger *et al.*⁴⁰. The volume phase transition of the microgels in response to changes in temperature is described using Flory-Rehner theory^{41,42}. The section closes with a discussion on the collapse and swelling kinetics.

Core-shell microgels consisting of a gold core and a polymer shell are classified as hybrid systems. They combine the plasmonic properties of the inorganic metal core and the responsive behaviour to external stimuli such as the temperature of the organic polymer shell. In this work, the microgels were obtained by a classical wet-chemical synthesis that has two primary advantages i) narrow size distribution of the fabricated crystalline gold nanoparticles, and ii) precise control over polymer shell thickness and density. The synthesis path of the microgels can be divided into three major steps, which are schematically illustrated in figure 2.1. First, the synthesis of the metal nanoparticles with a diameter of approximately 15 nm and functionalization of their surface (figure 2.1 a)). Next, the synthesis of the microgel shell via the seeded precipitation polymerisation where the gold cores are encapsulated (figure 2.1 b)), and finally a postmodification of the metal cores. In this work, gold cores were overgrown with gold in order to increase their size (figure 2.1 c)). Each synthesis step will be discussed in more detail in the following subsections.

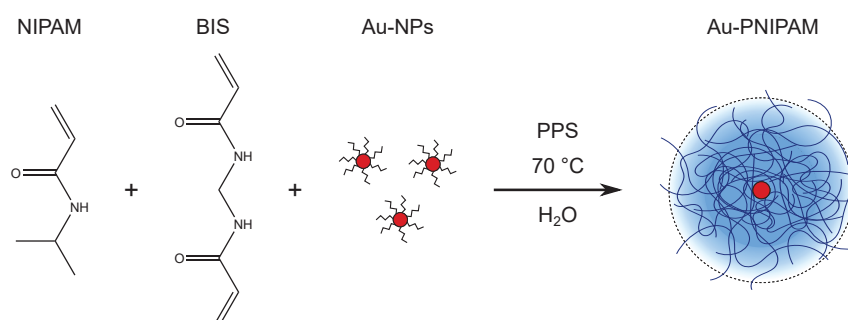
2.1.1 Synthesis of the Metal Cores

A common method to synthesize nanoparticles is the reduction of metal ions by using various reducing agents. Gold nanoparticles are widely studied in the literature and many different synthesis pathways are possible, including the Brust-Schiffrin method⁴³, the Seeded-Growth method⁴⁴, and reduction by ascorbic acid⁴⁵, to name a few. However, the most used methodology to generate spherical Au-NPs in the range of 10 nm is the Turkevich synthesis or its modified variation^{13,46}. As gold reagent for nanoparticles acts gold(III) chloride trihydrate (HAuCl_4). Trisodium citrate acts as a reducing agent and provides electrons to reduce the Au^{3+} ions to Au^0 atoms. The same molecule acts as a weak stabilizing agent and prevents aggregation of the particles. The formation of Au-NPs can be divided into the following steps¹³: first, clusters with 1-2 nm diameter are rapidly formed due to a high reduction rate. Next, the reduction rate decreases and the formed particles merge, leading to fewer particles. When the mean radius of 2.5 nm

a) Turkevich synthesis and functionalization of Au-NPs



b) Seeded precipitation polymerization of NIPAM and BIS



c) Overgrowth of Au cores with Au

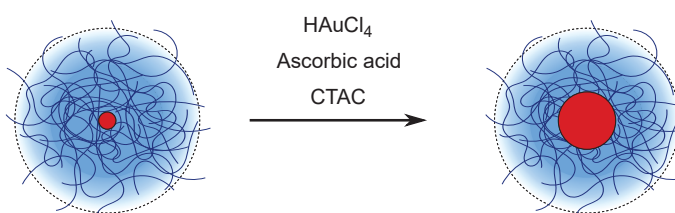


Figure 2.1: Schematic depiction of the core-shell microgel synthesis used in this thesis. a) Reduction of gold ions with sodium citrate dihydrate and formation of Au-NPs with diameter of approximately 15 nm using the Turkevich protocol. In the second step, the surface of the particles is functionalized with butenylamine. b) Encapsulation of functionalized Au-NPs into a microgel shell via the seeded precipitation polymerisation of PNIPAM and BIS. c) Overgrowth of the Au cores with further Au.

is reached, the number remains constant and the particles continue growing in size. In the third step, the size increases up to approximately 4-5 nm due to the diffusion of the gold atoms, which is reduced in the solution while the particles' polydispersity decreases. Finally, in the fourth and last step, the reduction rate of the gold ions increases drastically, followed by fast particle growth until the final size is reached. The small Au-NPs ($d \approx 15$ nm) used in this thesis were obtained from the Turkevich synthesis. Afterwards, the surface of the Au-NPs can be modified by replacing the weak-bonded citrate molecules with other stronger binding ligands in order to achieve greater colloidal stability or other functions⁴⁷.

2.1.2 Synthesis of the Microgels

The first synthesis of PNIPAM microgels was introduced by Pelton and Chibante⁶, who used the free radical polymerization. An overview of different synthesis methods to obtain microgels is given in the literature^{2,48,49}. The methodologies allow for fabrication of a variety of microgels, includes those with uniformly distributed nanoparticles, core-shell microgels consisting of either metal-polymer or polymer-polymer, and hollow microgels. The most commonly used method is free radical precipitation polymerization because of its adaptability and flexibility. The properties of the microgel can be tuned by applying different co-monomers into the polymer network, such as *N,N'*-methylenebisacrylamide (BIS) as a cross-linker or acrylic acid for the introduction of functional groups. In this work, Au-PNIPAM microgels were obtained via the seeded precipitation polymerization using the Au-NPs as seeded particles. Notably, the surface of Au-NPs was functionalized with butenylamine before the encapsulation into a PNIPAM polymer shell. Rauh *et al.*¹² investigated the role of the Au-NPs surface functionalization for the synthesis of gold-polymer core-shell microgels. They used Au-NPs functionalized either with citrate, 11-mercaptoundecanoic acid, butylamine or butenylamine molecules. In the next step, they carried out the seeded precipitation polymerizations of NIPAM and cross-linker BIS in the presence of the different functionalized seeds. The success of the gold core encapsulation strongly depended on the functionalization agent. Citrate-stabilized gold cores led to a mixture of pure gold and core-shell microgels. In the case of gold cores with 11-mercaptoundecanoic acid, mostly empty polymer microgels were obtained. In contrast, gold particles modified with butylamine or butenylamine molecules lead to core-shell microgels where almost every PNIPAM shell contained only one gold core. Thus, the hydrophobicity of the gold particle surface plays a crucial role for a successful encapsulation into a polymer shell. The encapsulation mechanism of gold cores into the polymer shell can be divided into four steps¹². First, in the heated (~ 70 °C) reaction mixture, the initiator potassium peroxydisulfate (PPS) decomposes into radicals due to the heat. Next, the initiator radicals attack the NIPAM and BIS monomers leading to the formation of oligomer radicals. The oligomer radicals grow further to polymer radicals. Due to the poor solvent conditions, the PNIPAM polymer starts to precipitate onto the gold particle's surface, which acts as a nucleation center. The polymerization continues until the monomers are consumed, resulting in a polymer shell surrounding

the cores. The shell provides colloidal stability of the metal nanoparticles due to steric repulsion and acts as a spacer between the gold cores in the two-dimensional arrays.

2.1.3 Postmodification of the Cores

The size of the gold cores within the polymer shell can be post modified via the overgrowth method. The gold seed growth process was presented by Rodríguez-Fernández *et al.*¹⁵, who synthesized gold particles from 12 nm up to 180 nm using cetyltrimethylammonium bromide (CTAB) as a surfactant stabilizer and ascorbic acid as a reducing agent. To obtain spherical particles with narrow size distribution, purification was crucial to eliminate nonspherical particles after the first growth step. Contreras-Cáceres *et al.*^{50,51} demonstrated an overgrowth of gold seeds within a PNIPAM shell with gold or silver. The porosity of the polymer shell allows for chemical reactions to occur directly on the metal cores. For the overgrowth with gold, they used CTAB and ascorbic acid. Moreover, they showed that the CTAB concentration is crucial for particle shape. While a high concentration (0.05 M) led to a spherical shape, the low concentration (0.015 M) led to the gold cores forming a flowerlike shape. A modified overgrowth synthesis was reported by Honold *et al.*²¹. Instead of CTAB, cetyltrimethylammonium chloride (CTAC) was chosen as a surfactant because it helps suppress the formation of nonspherical shapes. The redox potential of the gold salt changes through the complexation with CTAC molecules leading to complete reduction only at the gold core surface by using a mild reducing agent such as ascorbic acid⁵². Honold *et al.* achieved different gold core sizes between 30 and 92 nm by increasing the amount of the reducing agent and the feed solution. Au-PNIPAM microgels with a gold core diameter of approximately 100 nm used in this work were obtained using an adapted synthesis protocol from Honold *et al.*²¹.

2.1.4 Microgel Structure

Microgels are soft and deformable objects whose size is between 100 nm and the micron range^{1,2}. They feature a three-dimensional, crosslinked polymer network with gel-like structure. Under good solvent conditions, microgels are in their swollen state due to their ability to take up large amounts of solvent. In water, the volume of a microgel is characterized by water (ϕ_{water}) and polymer (ϕ) volume fractions. The structure of a microgel is commonly investigated by using scattering techniques, *e.g.* small-angle neutron scattering (SANS)^{53,54}. The referenced studies show that the microgel structure can be considered as a core-shell-like with a denser, higher cross-linked inner region and less high cross-linked outer shell with dangling ends at the microgel surface in their swollen state. In the PNIPAM microgels crosslinked with BIS, the inhomogeneities in the network occur due to the faster polymerization of the cross-linker BIS compared to NIPAM monomers⁵⁵. In comparison, in the collapsed state, *i.e.*, under poor solvent conditions, the PNIPAM microgels have a homogeneous hard sphere-like structure. Recently, super-resolution optical microscopy has confirmed the inhomogeneous network structure of microgels using real-space imaging^{56,57}.

Stieger *et al.*⁴⁰ introduced a well-accepted radial polymer density profile model that describes the form factor of microgels in their swollen and their collapsed state, including different crosslinking densities and microgel sizes. The form factors of various particles at different temperatures were obtained by analysing the SANS data. A detailed explanation of the technique and the form factor is given later in subsection 2.2.2. Figure 2.2 presents a schematic illustration of a microgel showing a fuzzy sphere morphology and the corresponding polymer volume fraction ϕ as a function of the microgel radius. It should be noted that the structure is only valid for the swollen state. The dimensions are drawn to scale for a representative Au-PNIPAM microgel with a crosslinking density of 15 mol% used in this work. The red circle in the centre is the small gold core with a diameter of 15 nm, while solid blue lines represent polymer chains. The inner region with homogeneous polymer density with radius R_{box} is highlighted by the red dashed line. A radial box profile characterises the polymer core. The thickness of the fuzzy polymer shell is given by the parameter σ . The overall radius of the particle determined from SANS is defined as $R_{\text{SANS}} = R_{\text{box}} + 4\sigma$ and highlighted by a green dashed line. The polymer volume fraction ϕ decreases gradually between both radii, starting at $\phi = 0.18$. The profile reaches the polymer fraction of half the inner polymer core at the radius $R = R_{\text{box}} + 2\sigma$ and zero at R_{SANS} . The loosely crosslinked polymer chains reaching beyond R_{SANS} contribute only to the hydrodynamic radius R_{h} (dashed blue line) commonly obtained from DLS. Thus the R_{SANS} is smaller compared to R_{h} . The fuzziness of the shell correlates strongly with the polymer crosslinking density. The increase of the cross-linker content leads to the reduction of the microgels fuzziness.

Stieger *et al.*⁴⁰ demonstrated that the microgels undergo a transition from the fuzzy sphere to homogeneous sphere-like particles when the temperature is increased from 25 to 39 °C. In the fully collapsed state the polymer density profile remains a simple box profile, *i.e.* $R_{\text{SANS}} = R_{\text{box}}$ and $\sigma = 0$. The transition process is accompanied by an increase in the polymer volume fraction ϕ . Lopez and Richtering⁵⁸ evaluated the polymer volume fraction of collapsed PNIPAM microgels determined from different methods. They found that the average ϕ value is 0.44 independent of the cross-linker content in the collapsed state.

2.1.5 Volume Phase Transition Behaviour

Responsive cross-linked microgels are often classified as "smart" due to their ability to respond to external stimuli, *e.g.* temperature, pH and ionic strength^{53,59,60,61,62,63}. The PNIPAM microgel undergoes a volume phase transition (VPT) at approximately 32 °C^{7,60} due to the lower critical solution temperature (LCST) behaviour of the polymer. Below the VPT temperature, the polymer network is swollen by solvent because of favourable interactions between the polymer chains and solvent molecules (here water). The microgel is soft and deformable at this stage. Above the VPTT, the microgel collapses, expelling the water and becoming a hard-sphere-like structure. The swelling capacity of a microgel can be expressed with the deswelling ratio α . The parameter gives the ratio between the volume of the microgel in its state at a certain temperature $V_{\text{h}}(T)$

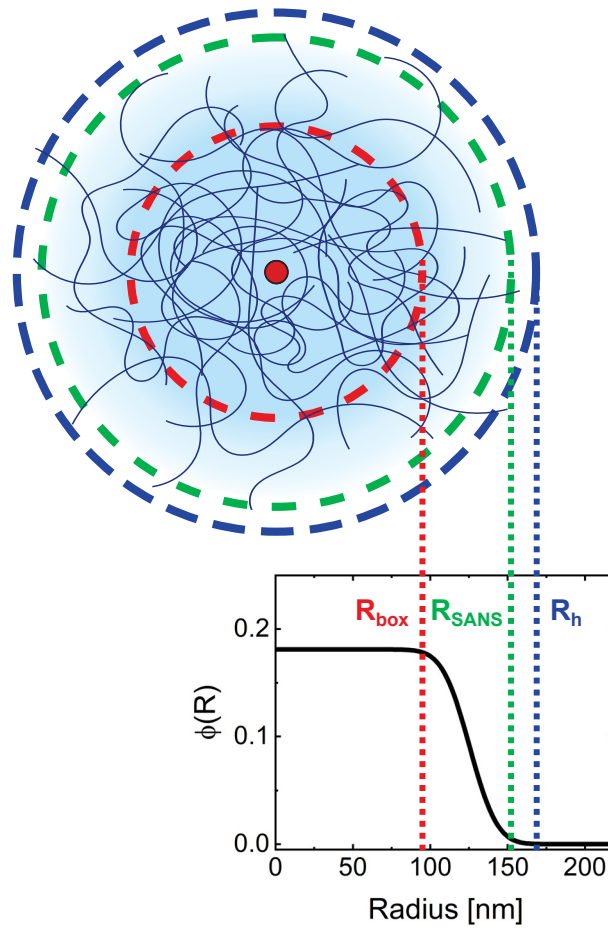


Figure 2.2: Schematic depiction of a Au-PNIPAM core-shell microgel. Dashed vertical lines highlight the radius of homogeneous polymer core R_{box} (red), the overall radius R_{SANS} from SANS (green) and the hydrodynamic radius R_h (blue). Bottom: corresponding radial density profiles presenting the polymer volume fraction ϕ versus the particle radius.

and the volume in the fully swollen state $V_{h,\text{swollen}}$. The required hydrodynamic radii for the calculations can be determined from the DLS measurements.

$$\alpha = \frac{V_h(T)}{V_{h,\text{swollen}}} \quad (2.1)$$

The Flory-Rehner theory^{41,42} is widely used to describe the swelling behaviour of thermoresponsive gels. In this theory, the macroscopic state of a polymer network is described in terms of the osmotic pressure Π . In case of neutral gels, Π consists of two contributions: i) the mixing term and ii) the elastic free energy term:

$$\Pi = \underbrace{-\frac{N_A k_B T}{v} [\phi + \ln(1 - \phi) + \chi \phi^2]}_{\text{mixing term}} + \underbrace{\frac{N_c k_B T}{V_0} \left[\left(\frac{\phi}{2\phi_0} \right) - \left(\frac{\phi}{\phi_0} \right)^{1/3} \right]}_{\text{elastic free energy term}}. \quad (2.2)$$

N_A is the Avogadro's number, k_B the Boltzmann constant, T the temperature, v the molar volume of solvent, N_c the number of chains in the polymer network, ϕ the polymer volume fraction, and V_0 and ϕ_0 are the respective volume and polymer volume fractions of the microgel at the reference state, commonly the fully collapsed state. χ is the Flory-Huggins-Stavermann interaction parameter⁶⁴ or the polymer-solvent interaction parameter, which is defined as

$$\chi = \frac{\Delta F}{k_B T} = \frac{\Delta H - T \Delta S}{k_B T} = \frac{1}{2} - A \left(1 - \frac{\theta}{T} \right) \quad \text{with} \quad (2.3)$$

$$A = \frac{2\Delta S + k_B}{2k_B} \quad \text{and} \quad \theta = \frac{2\Delta H}{2\Delta S + k_B}. \quad (2.4)$$

ΔF is the change in total free energy, ΔS and ΔH are the changes in entropy and enthalpy, respectively. The change in free energy occurs due to the mixing process of the solvent molecules and the polymer chains. For some mixtures, the correlation between the parameter χ and the polymer concentration is nonlinear, leading to the following expression⁶⁵:

$$\chi(T, \phi) = \chi_1(T) + \chi_2 \phi + \chi_3 \phi^2 + \dots \quad (2.5)$$

In the Flory-Rehner approach, the osmotic pressure Π is set to zero when the gel is in its equilibration state. Thereby isobar conditions are assumed for the temperature-dependent swelling of the gel. Thus, the expression for the temperature dependence of the polymer volume fraction ϕ can be written as⁶⁶:

$$T_{\Pi=0} = \frac{A \phi^2 \theta}{\frac{\phi_0}{N_{\text{gel}}} \left[\frac{1}{2} \left(\frac{\phi}{\phi_0} \right) - \left(\frac{\phi}{\phi_0} \right)^{1/3} \right] - \phi - \ln(1 - \phi) + (A - \frac{1}{2}) \phi^2 - \chi_2 \phi^3}. \quad (2.6)$$

Here, N_{gel} gives the average number of monomers between the cross-links. However, one should keep in mind that in the case of microgels, the cross-linker density decreases gradually from the centre to the surface⁴⁰. θ defines the temperature when the microgel hydrodynamic radius is minimized, while the parameter A describes roughly the entropy change. The polymer volume fraction ϕ of the microgels can be obtained from DLS measurements using the following relation when ϕ_0 is known:

$$\frac{\phi}{\phi_0} = \frac{V_{\text{h,collapsed}}}{V_{\text{h}}(T)}. \quad (2.7)$$

Although the classical Flory-Rehner approach provides a quantitative description of swelling behaviour of cross-linked polymer gels in general, the theory was successfully applied also to microgels^{58,67} which exhibit a different network structure compared to the macroscopic gels. However, using the Flory-Rehner theory is challenging because it requires the precise knowledge of the reference polymer volume fraction state ϕ_0 and other fitting parameters. ϕ_0 values vary significantly in the literature, leading as a consequence to different results^{40,54,58,67,68}.

2.1.6 Collapse and Swelling Dynamics

The collapse and swelling dynamics deal with the process of volume change of microgels induced by external triggers. Therefore, crucial questions are: i) what are the time scales for the collapse (or swelling)? And ii) what is the structural evolution of the gel during VPT? A prominent theory dealing with swelling kinetics of spherical gels was presented by Tanaka and Fillmore⁴. The theory correlates the time of swelling of gel particles and their size. The displacement of the polymer network during expansion by the solvent, *e.g.*, water, is given by the equation of motion, which is expressed as:

$$\frac{\partial u}{\partial t} = D \frac{\partial}{\partial R} \left[\frac{1}{R^2} \frac{\partial}{\partial R} (R^2 u) \right], \quad (2.8)$$

where $u = (R, t)$ is the displacement in the polymer network of a point from its final equilibrium location after the gel particle is fully swollen, t is the swelling time, and r is the radius of the gel. D denotes the collective diffusion constant, which is defined as

$$D = \frac{K + \frac{4\mu}{3}}{f}. \quad (2.9)$$

K and μ are the coefficients of the bulk and shear modulus, respectively. f is the friction coefficient between the polymer network and the solvent. Tanaka and Fillmore obtained the following solution of equation 2.8 for spherical gels:

$$u(R, t) = -6\Delta R_0 \sum_{n=1}^{\infty} \frac{(-1)^n}{n\pi} \left[\frac{X_n \cos X_n - \sin X_n}{X_n^2} \right] \times e^{-n^2 t / \tau}, \quad (2.10)$$

with $X_n \equiv n\pi \left(\frac{R}{R_{\text{final}}} \right)$ and $\tau \equiv \frac{R_{\text{final}}^2}{D}$, where ΔR_0 denotes the total increase in the radius of the sphere and R_{final} is the final radius of the sphere in equilibrium. To solve the

equation, Tanaka and Fillmore made the following assumptions: i) the shear modulus was $\mu = 0$, ii) the initial condition must be known, *i.e.* the gel particle was under uniform stress, and iii) the boundary condition that the surface stress becomes zero by transferring the gel into a solvent. They concluded that the swelling speed τ of any spherical gel is inversely proportional to the diffusion coefficient D and proportional to the square of R_{final} . This theory was later extended for nonspherical shapes, *i.e.* cylindrical and large disk gels by Li and Tanaka⁵. The relation $\tau \propto R_{\text{final}}^2$ was confirmed by several studies despite small exponent deviations^{4,69,70,71,72}.

Other approaches were introduced to describe the swelling kinetics of the gels including the linear and nonlinear poroelastic theories^{73,74,75,76,77,78,79}. However, a theory treating the swelling and collapse kinetics of fuzzy-sphere microgels as used in this work is still missing.

The volume change kinetic of the various microgels have been studied by temperature-jump^{80,81,82}, pH-jump⁷¹, pressure-jump⁸³ and cononsolvency (solvent-jump)^{84,85}. Thereby several studies^{83,84,85} (including this work) claimed a two-step collapse process of microgels induced by an external stimulus which is characterized by a fast and slow lifetime component, τ_{fast} and τ_{slow} . Keidel *et al.*⁸⁵ demonstrated for the first time the structural evolution of a microgel from swollen to collapsed states using time-resolved solvent-jump small angle X-ray scattering and computer simulations. They attributed the fast component τ_{fast} to the collapse of polymer chains forming clusters around the cross-linking areas, whereas τ_{slow} is correlated to slow rearrangements of polymer network resulting in a compact globular structure of the microgel. It should be noted that they used very loosely cross-linked microgels (0.25 mol% molar ratio of cross-linker). Wrede *et al.*⁸³ studied microgels with higher cross-linker density (4.11 mol%) by time-resolved pressure-jump small angle neutron scattering. They related the first step to the fast collapse of the loosely cross-linked fuzzy shell in the outer region and the slower second step to the polymer network rearrangement to the new equilibrium state. Furthermore, Wrede *et al.*⁸³ measured the swelling kinetics. The swelling process was significantly faster than the deswelling of microgels and contained only one time constant. Since the microgel systems and the experimental techniques varied considerably over the studies, the reported lifetimes are only comparable to a limited extent.

In this work, the collapse dynamics were measured by capacitor-discharge temperature-jump spectroscopy⁸⁶. In this technique, the solvent containing an electrolyte is heated via an induced electrical discharge and the changes of the absorbance or optical density (OD) due to microgels collapsing over time is monitored. As the microgel collapse is accompanied by an increase in absorbance (turbidity), UV-Vis spectroscopy can be used to characterize the structural changes during the VPT. Assuming the two-step transition, the experimental data can be fitted with a double exponential function to estimate both lifetimes. The correlation between the measured OD_{λ} at a certain wavelength and the lifetimes τ_{fast} and τ_{slow} is given by:

$$\Delta OD_{\lambda}(t) = \Delta OD_{\text{total}} - \Delta OD_{\text{fast}} e^{(-t/\tau_{\text{fast}})} - \Delta OD_{\text{slow}} e^{(-t/\tau_{\text{slow}})}. \quad (2.11)$$

Here ΔOD_{fast} and ΔOD_{slow} denote the changes in optical density due to fast and slow collapsing process respectively. ΔOD_{total} is the overall change and is defined as $\Delta OD_{\text{total}} = \Delta OD_{\text{fast}} + \Delta OD_{\text{slow}}$.

2.2 Scattering Techniques

Scattering techniques are a powerful tool to investigate the size, shape and internal network structure of microgels. In this thesis, various methods were used to characterize the Au-PNIPAM microgels. Figure 2.3 and table 2.1 give an overview of the used methods, the operating wavelengths, the corresponding \mathbf{q} ranges and scattering angles. Dynamic and static light scattering (DLS and SLS) are commonly used for the overall particle size in the submicron range, while small-angle X-ray and neutron scattering (SAXS and SANS) with much shorter wavelengths are used to investigate the area of interest in nm-range⁸⁷. The individual methods will be introduced in more detail in the next sections.

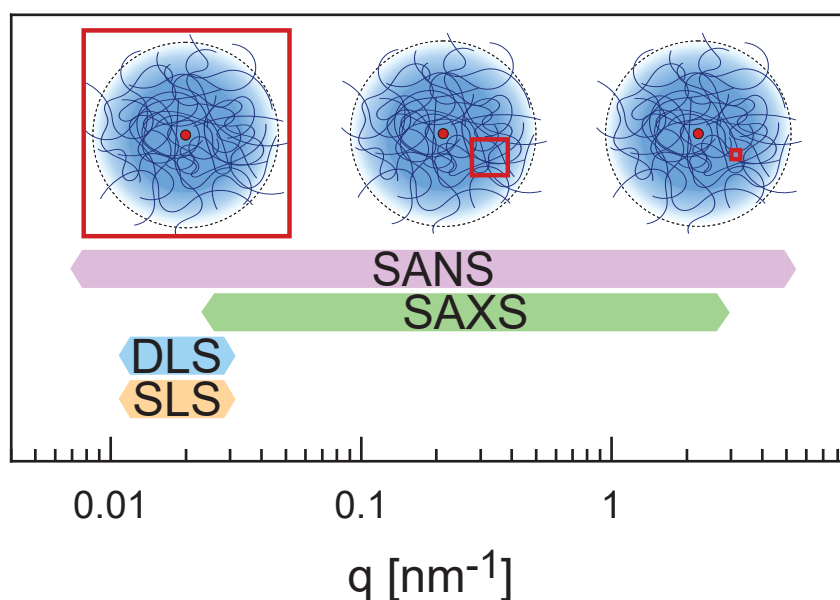


Figure 2.3: Overview of the scattering methods and corresponding scattering vector \mathbf{q} values respectively used in this thesis. DLS and SLS are suitable for determining the overall size of the microgel, while SAXS and SANS are used for the nm-range area of interest. Red squares highlight the magnitude of resolved length scales of a microgel.

Although the radiation types (light, X-rays and neutrons) of the scattering methods are different and thus the scattering mechanism is different depending on the radiation, the scattering vector \mathbf{q} is the most crucial quantity for all scattering experiments defined as⁸⁷:

Table 2.1: Radiation types, wavelengths, scattering vector values and scattering angles for the scattering methods used in this thesis.

| Scattering method | Radiation | Wavelength λ [nm] | Scattering vector \mathbf{q} [nm ⁻¹] | Scattering angle θ [°] |
|-------------------|-----------|------------------------------|---|----------------------------------|
| DLS | Light | 632.8 | 0.019 ¹ | 90 |
| SLS | Light | 632.8 | 0.019 ¹ | 90 |
| SAXS | X-rays | 0.154 | 0.023 – 2.947 | 0.02 – 3.10 |
| SANS | Neutrons | 0.46 | 0.007 – 5.751 | 0.02 – 18.19 |

¹ The value was calculated using the refractive index of water ($n = 1.332$) at 25 °C.

$$|\mathbf{q}| = q = \frac{4\pi n}{\lambda} \sin\left(\frac{\theta}{2}\right). \quad (2.12)$$

Here n is the refractive index of the dispersing medium, λ is the wavelength of the incident radiation, and θ gives the scattering angle between the incoming and scattered beam. Figure 2.4 depicts schematically a scattering process and the construction of the scattering vector \mathbf{q} . The blue circle represents a scattering centre. The incident radiation with wave vector \mathbf{k}_{inc} is scattered by the angle θ to the \mathbf{k}_{sca} . Hence the scattering vector \mathbf{q} is the difference between the two wave vectors.

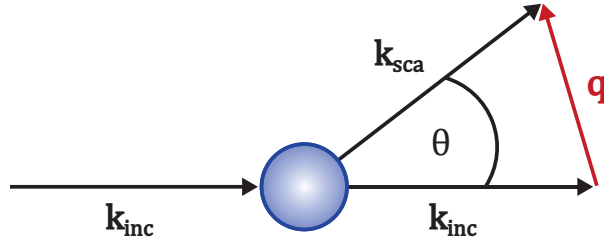


Figure 2.4: Schematic depiction of the scattering process. The incident beam with the wave vector \mathbf{k}_{inc} is scattered by the scattering center. The scattered wave has the vector \mathbf{k}_{sca} , and θ is the angle between both wave vectors. The scattering vector \mathbf{q} is given as $\mathbf{q} = \mathbf{k}_{\text{inc}} - \mathbf{k}_{\text{sca}}$.

2.2.1 Dynamic Light Scattering

Dynamic light scattering (DLS) is widely used for particle size analysis in the submicron and nanometre range. Figure 2.5 a) illustrates a simplified DLS setup. A continuous wave (cw) laser beam is focused on the cuvette containing the sample by using a lens. The particles scatter the incoming laser light and the scattered light is detected at a certain angle over time by a photomultiplier or an avalanche photodiode. Due to the

Brownian motion, the particles move randomly in the dispersion resulting in fluctuated scattering intensity. The particle motion strongly depends on the size, the temperature and the surrounding medium. The particle's velocity increases with their decreasing size resulting in faster scattering fluctuations. Schematic intensity fluctuations as a function of time are shown in figure 2.5 b). For the analysis of the data, the obtained scattering intensities $I(q, t)$ are transformed into the normalized autocorrelation function $g^2(\tau)$ with the correlation time τ ^{87,88,89}:

$$g^2(\tau) = \frac{\langle I(t)I(t + \tau) \rangle}{\langle I(t) \rangle^2}. \quad (2.13)$$

Here, $I(t)$ gives the scattering intensity at the time t and $I(t + \tau)$ defines the scattering intensity at a certain delay time $t + \tau$. The autocorrelation function describes, therefore, the similarity between both intensities. A DLS experiment cannot provide the knowledge of the exact movement of each particle in the dispersion; nevertheless, the relative motion of the particles to each other correlates with means of the scattered electric field correlation function. The normalized first-order correlation function is given by^{87,89}:

$$g^1(\tau) = \frac{\langle E(t)E(t + \tau) \rangle}{\langle E(t) \rangle^2}. \quad (2.14)$$

$E(t)$ and $E(t + \tau)$ define the scattered electric field at the time t and at $t + \tau$. Though these fields are experimentally not accessible, $g^2(\tau)$ and $g^1(\tau)$ can be coupled by the Siegert relation^{87,90} to analyse the obtained DLS data.

$$g^2(\tau) = B + \beta_{\text{Siegert}} [g^1(\tau)]^2 \quad (2.15)$$

Here B is the baseline usually approximately at 1 and β is a coherence factor that depends on the experimental geometry and the scattering properties of the particles. For monodisperse particles the autocorrelation function $g^1(\tau)$ is given as a simple exponential function with Γ as decay constant.

$$g^1(\tau) = e^{-\Gamma\tau} \quad (2.16)$$

Figure 2.5 c) demonstrates theoretical calculated functions $g^1(\tau)$ and $g^2(\tau)$ assuming $B = 1$ and $\beta = 1$ for monodisperse particles with hydrodynamic radius of 150 nm at 298 K. However, in the case of polydisperse particles, the various sizes and thus various decay constants have to be considered. Therefore equation 2.16 is modified by the distribution of decay rates expressed as follows:

$$g^1(\tau) = \int_0^{\infty} G(\Gamma) e^{-\Gamma\tau} d\Gamma. \quad (2.17)$$

The analysis of the autocorrelation function and the extraction of the mean decay constant $\bar{\Gamma}$ of the particles is commonly carried out by the Cumulant method⁹¹ or CONTIN algorithm based on Inverse Laplace Transformation (ILT)^{92,93}. The mean

decay constant $\bar{\Gamma}$ is directly related to the diffusion behaviour and can be used to determine the translational diffusion coefficient D_T at a given scattering vector q .

$$D_T = \frac{\bar{\Gamma}}{q^2} \quad (2.18)$$

The Stokes-Einstein equation (2.19) uses the determined D_T to obtain the hydrodynamic radius of the particles expressed as:

$$D_T = \frac{k_B T}{6\pi\eta R_h}. \quad (2.19)$$

k_B is the Boltzmann constant, T is the temperature and η is the viscosity of the medium surrounding the particles. The Stokes-Einstein equation can be used if Γ shows a linear relationship as a function of q^2 . The linear dependence indicates the absence of dynamic processes other than translational diffusion.

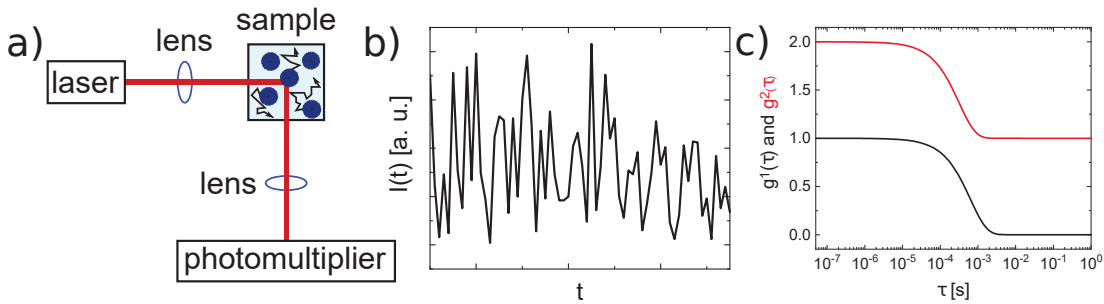


Figure 2.5: Dynamic light scattering experiment. a) Schematic depiction of the DLS setup. b) Example evolution of the scattering intensity as a function of time. c) Theoretical autocorrelation functions $g^1(\tau)$ (black line) and $g^2(\tau)$ (red line) using equations 2.12, 2.13, 2.14, 2.18 and 2.19 with following parameters: $n = 1.332$, $\lambda = 638.5$ nm, $\theta = 90^\circ$, $T = 298$ K, $\eta = 0.8904$ mPas and $R_h = 150$ nm.

2.2.2 Small Angle X-Ray and Neutron Scattering

In comparison to light scattering, SAXS and SANS instruments use significantly shorter wavelengths (table 2.1). Due to shorter wavelengths, smaller q vectors are achievable, which is crucial for investigating the structure of materials in the nm range⁸⁷. Typically, small angle scattering instruments need the following components: a beam source, a monochromator, a collimating system, and a detection system⁹⁴. Further specific components can be involved such as focusing mirrors, crystals and a beam stop. Figure 2.6 a) shows a scheme of a typical setup of a SAXS instrument. A monochromatic, collimated X-ray beam irradiates the sample (here microgel dispersion) in a transmission geometry. The collimation system keeps the divergence of the incoming beam small and consists basically of slits and pinholes. The scattered radiation is collected by a detector, while the direct beam is blocked by a beam stop to prevent the detector from damage⁹⁵.

The SANS measurements in this thesis were acquired using the D11 instrument at the ILL in Grenoble, France⁹⁶. The schematic setup is presented in figure 2.6 b). For steady-state instruments such as D11, the neutrons are generated by the fission process with the flux constant in time. The incident wavelength can vary in the range between 0.45 and 4.0 nm. The velocity selector acts as a monochromator and separates the slower from the faster neutrons. It consists of a certain number of neutron-absorbing blades that are arranged in a helix along the rotation axis. The set rotation speed of the selector allows only desired neutrons to pass through. Faster or slower neutrons will be absorbed on the blade surfaces. Using this selection process, a wavelength distribution of $\Delta\lambda/\lambda = 9\%$ can be achieved. Collimators are used to efficiently guide the neutrons coming from the selector to the sample. The inner surfaces of the collimators reflect the neutrons, thus providing the transport of maximum neutron flux. The diaphragms function as a pinhole and are used to give a shape to the beam. Depending on the hole or window size, a broader or sharper beam shape pass through. While a broader shape provides greater interactions between the neutrons and the sample, the sharper beam gives higher resolution due to smaller divergence. The detector (here, helium gas detector) operates inside the evacuated aluminium tube with a length of 40 m. The sample to detector distance can be varied between 1.2 and 39 m. The different distances allow the characterization of the sample at a broad q -range. The collected scattering data at different distances is merged afterwards for the data analysis.

Despite different radiation types in both methods, the same basic equations and laws can be used to analyse the scattering curves. This thesis considers only spherical particles such that only spherical shapes are discussed here. The scattering intensity $I(q)$ of spherically symmetric particles is given by⁹⁷:

$$I(q) = N\Delta\eta^2V^2P(q)S(q). \quad (2.20)$$

N denotes the number density of particles, $\Delta\eta$ is the difference in scattering length density between the particles and the solvent, V is the volume of the particles, $P(q)$ is the form factor and $S(q)$ defines the structure factor. The latter can be neglected for dispersions where the particles are dilute resulting in uncorrelated behaviour. In that case $S(q) = 1$ can be assumed⁹⁷. The difference in scattering length density, also called contrast, is crucial for the visibility of the particles embedded in a matrix material. If the contrast is too low, the objects cannot be distinguished from their environment. As mentioned earlier, the scattering mechanism depends on the radiation type and thus also the scattering length density. In the case of SAXS, samples with high electron density are suitable because X-rays are scattered by the electrons and the scattering intensity of an atom increases with the number of electrons⁸⁸. However, in SANS measurements, neutrons are scattered by nuclei in the sample. Moreover, the scattering intensity is not proportional to the atomic number and can vary for different isotopes. Thus the advantage of SANS method over SAXS is the possibility to increase the contrast of samples by using deuterium labelled components⁸⁸. Therefore, the choice of a SAXS or a SANS instrument depends strongly on the studied sample and the scattering contrast.

For chemically cross-linked gels, *e.g.* microgels, equation 2.20 is extended to

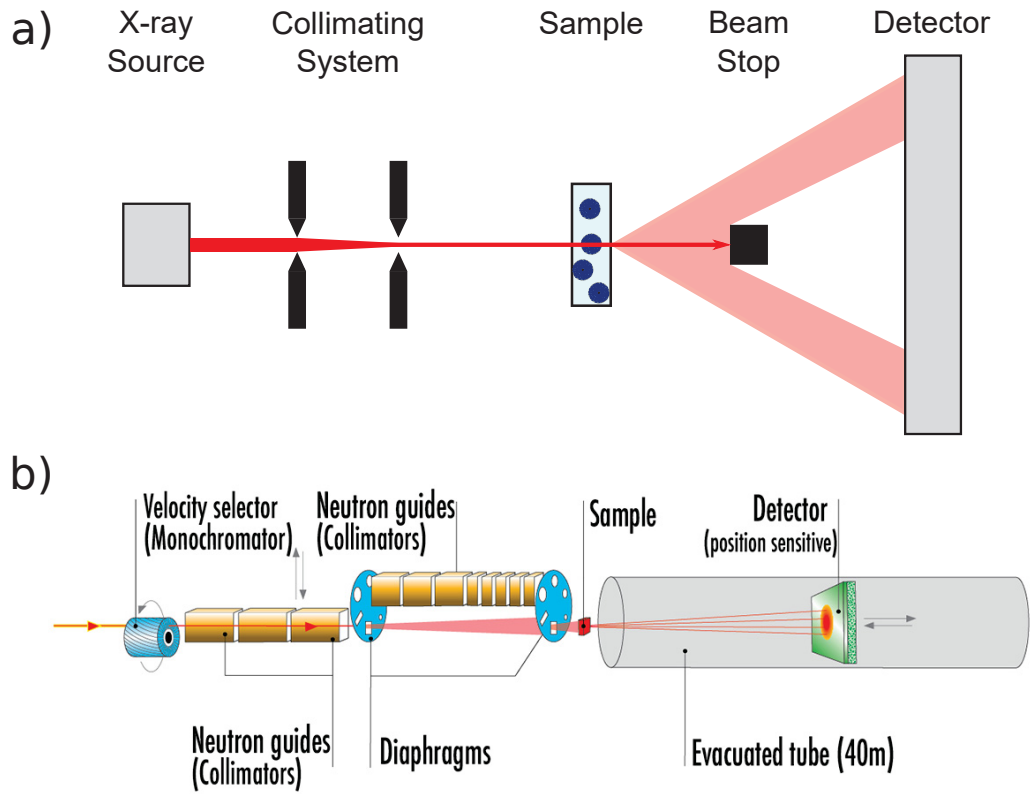


Figure 2.6: a) Scheme of the typical setup of a SAXS instrument. b) Schematic representation of the D11 Instrument from ILL using for SANS measurements. Reprinted from reference⁹⁶.

$$I(q) = N\Delta\eta^2V^2P(q)S(q) + I_{\text{dyn}}(q) + I_{\text{inc}}. \quad (2.21)$$

I_{inc} defines the incoherent background, which can be subtracted from the overall obtained intensity as an offset, since this contribution is mostly independent of q . $I_{\text{dyn}}(q)$ is the dynamic contribution also known as Ornstein-Zernicke contribution⁹⁸ occurring due to the liquid-like behaviour of the PNIPAM microgels. Microgels show local concentration fluctuations due to movements of the polymer chains in the microgels network, and these fluctuations can be observed for relatively large q vectors. The dynamic contribution is expressed by the Lorentzian function⁹⁹.

$$I_{\text{dyn}}(q) = \frac{I_{\text{L}}(0)}{1 + q^2\xi^2} \quad (2.22)$$

$I_{\text{L}}(0)$ denotes the Lorentzian intensity and ξ gives the correlation length⁹⁹. The correlation length depends on the cross-linker density and the swelling state⁹⁸.

As mentioned earlier, the form factor $P(q)$ is related to the size and shape of a particle. In the case of homogeneous spheres with radius R , $P(q)$ is defined as⁹⁷:

$$P_{\text{hom}}(q) = \left[3 \frac{\sin(qR) - qR\cos(qR)}{(qR)^3} \right]^2. \quad (2.23)$$

However, in the swollen state the microgels exhibit a pronounced cross-linker density gradient towards the surface leading to a fuzziness. This fuzziness is taken into account by convoluting P_{hom} with a Gaussian function giving the following form factor P_{inhom} for a fuzzy sphere⁴⁰:

$$P_{\text{inhom}}(q) = \left[3 \frac{\sin(qR) - qR\cos(qR)}{(qR)^3} \times \exp\left(-\frac{(\sigma q)^2}{2}\right) \right]^2. \quad (2.24)$$

Here, σ gives the width of the smeared particle surface and R defines the radius where the cross-linker density of the microgel decreases to half the density inside the particle. The microgel structure is introduced in section 2.1.4 and a detailed description of the fuzzy sphere model can be found in the literature⁴⁰. Figure 2.7 shows representative scattering curves of an Au-PNIPAM microgel dispersion. The curves were experimentally obtained from SAXS (2.7 a)) and SANS (2.7 b)) measurements. The scattering curves demonstrate that different types of radiation result in different scattering behaviour of the same sample. In the particular case of Au-PNIPAM microgels, the size and shape of the gold cores can be obtained from SAXS measurements due to the high X-ray contrast of the gold, while the polymer shell is barely visible. In comparison, SANS measurements give insights into the shell structure. The use of heavy water increases the contrast between the polymer and the surrounding medium, resulting in higher visibility of the PNIPAM shell.

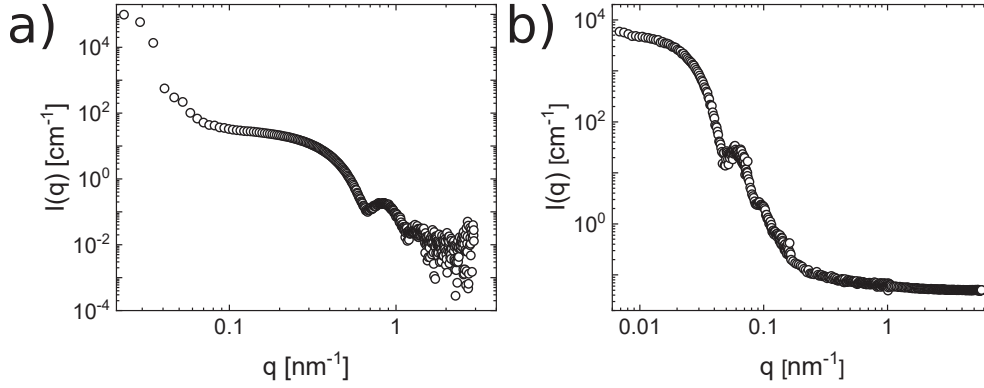


Figure 2.7: Representative scattering curves of Au-PNIPAM microgel dispersion obtained from SAXS (a) and SANS (b).

2.3 Colloidal Self-Assembly at Air/Liquid Interfaces

Colloidal particles and microgels are known for self-assembling into highly ordered lattices at the air/liquid interfaces. The particles are driven by various forces – spherical colloids with uniform size typically favour hexagonal crystal packing^{39,100,101}. Such periodic structures appear in iridescent colours due to the scattering and diffraction of light. The resulting structural colours are reminiscent of the visual appearance of periodic structures found in nature, *e.g.* opals, butterfly wings or feathers of birds^{39,101}. Although colloidal particle assemblies were initially used to understand the assembly process fundamentally, this research field gained interest for many applications, *e.g.* photonic crystals and sensing. In order to use particles as building blocks for arrays and control their interactions, the knowledge of various forces during the formation is necessary. In the following sections, the focus will be on the forces leading to self-organized particle arrays. Furthermore, selected two-dimensional colloidal assembly methods will be presented.

2.3.1 Assembly Forces

In dispersion, the colloidal particles are stabilized by Coulomb interactions (figure 2.9 b)) and steric repulsion (figure 2.9 c)). Coulomb interactions arise between charged particles and are a part of the DLVO theory named after its originators (Derjaguin B., Landau L., Verwey E. W. and Overbeek J. T. G.)^{102,103}. The Poisson-Boltzmann formalism describes the distribution of the electric potential ψ in solution towards the charged surface of the particles¹⁰⁴.

$$\nabla^2 \psi = \frac{c_0 e}{\varepsilon \varepsilon_0} \left(e^{\frac{e\psi}{k_B T}} - e^{-\frac{e\psi}{k_B T}} \right) \quad (2.25)$$

Here, c_0 is the bulk concentration of the salt, ε is the relative dielectric permittivity and ε_0 is the dielectric permittivity of vacuum. Equation 2.25 can be solved analytically for a planar surface. For low potentials ($e |\psi| \ll k_B T$) the Debye approximation provides the

linearized form of the Poisson-Boltzmann equation. The general solution of the linearized Poisson-Boltzmann equation is given by:

$$\psi(x) = C_1 \cdot e^{-\kappa x} + C_2 \cdot e^{\kappa x} \quad (2.26)$$

with κ as the inverse Debye length:

$$\kappa = \sqrt{\frac{2c_0 e^2}{\varepsilon \varepsilon_0 k_B T}}. \quad (2.27)$$

C_1 and C_2 are constants determined by the boundary conditions. The first boundary condition is the surface potential $\psi(x = 0) = \psi_0$, leading to $C_1 = \psi_0$. The second condition requires the potential to approach zero for large distances, leading to $C_2 = 0$. Considering both conditions, equation 2.26 can be rewritten as:

$$\psi(x) = \psi_0 \cdot e^{-\kappa x}. \quad (2.28)$$

The electrostatic repulsion exponentially decreases as a function of distance and decays to $1/e$ of the particle surface potential at the Debye length. This length – and thus the electrostatic repulsion – can be tuned by adding salt to the solution due to the ionic strength changes. The solvated polymer corona leads to the steric repulsion in the case of microgels. The osmotic pressure and the mechanical spring forces stabilize the particles in the dispersion³⁹.

The self-assembly process of colloids depends on various forces that the particles may be exposed to. Figure 2.9 gives an overview of possible forces for colloidal particles both within the dispersion and at the air/liquid interface. The involved forces can be divided generally into three groups: i) repulsive, which are responsible for colloidal dispersion stability and prevent the particles from aggregation, ii) attractive, which are crucial for the self-assembly process and finally iii) external^{39,105}.

Figure 2.9 a) shows dipolar interactions at the water/air or water/oil interface. The large differences between the dielectric constants between water and air or oil lead to the colloidal particle's asymmetric charge distribution. Water with relatively high dielectric permittivity $\varepsilon = 78.5$ at 20°C ¹⁰⁴ dissociates the ionic groups at the surface of colloids and stabilizes them. In contrast, these groups stay uncharged in air with low dielectric permittivity of approximately 1. The resulting dipoles align parallel to each other and perpendicular to the interface, leading to repulsion between particles^{106,107}.

Attractive forces counteract the repulsive interactions and support the particle agglomeration. At the interface, the lateral capillary forces (figure 2.9 h)) drive the particles together. The capillary interactions were described by Kralchevsky and Nagayama^{108,109}. They claimed that these interactions are often responsible for the two-dimensional ordering of the particles. When particles contact the liquid interface, they deform the liquid surface. As the surface deformation by the particles increases, the attractive capillary forces also increase. Furthermore, the authors distinguish between flotation and immersion lateral capillary forces (figure 2.8). In the former case (figure 2.8 a)), the forces appear between freely floating particles due to gravitational forces. However,

flotation forces disappear when the particles are too small ($R < 10 \mu\text{m}$) to deform the liquid surface. In the latter case (figure 2.8 b)), the particles are partially immersed in the liquid film. Instead of gravity, the wetting properties (position of the contact line and the contact angle between particle and liquid) of colloids cause the liquid surface deformation. These immersion forces occur even for 10 nm particles.

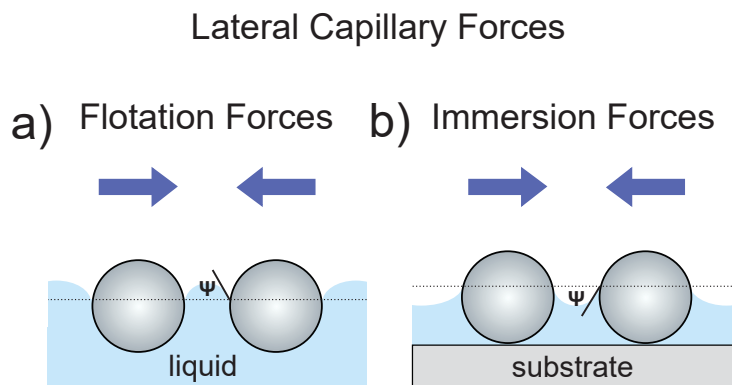


Figure 2.8: Schematic illustration of attractive lateral capillary forces: a) flotation and b) immersion forces.

Van der Waals (vdW) forces form the other part of the DLVO theory^{102,103} (figure 2.9 i)). The forces originate from charge fluctuations in molecules due to induced dipoles with attractive interactions. These forces are strongly distance-dependent; compared to the intermolecular vdW, the colloidal vdW forces act over larger distances³⁹. Other attractive interactions can occur such as bridging attraction due to single polymer chains between colloids (figure 2.9 g)) or depletion attraction due to presence of small objects (figure 2.9 k)).

By using a solid substrate, additional attractive interactions can occur, which are depicted in figure 2.9 d), e) and f). Scenario d) shows colloids trapped at the solid interface, which are driven together by the immersion capillary forces. In e) the hydrodynamic coupling is shown, while f) demonstrates the Coulomb attraction between charged particles and the oppositely charged solid substrate.

In addition to the repulsive and attractive interactions, external forces can also impact the particles. Mechanical barriers can be used to force floating particles at the liquid interface into ordered assemblies by decreasing the free space between particles (figure 2.9 l)). The most prominent method for barrier compression is the Langmuir trough technique, which has been used for various types of colloids^{110,111,112}. Figure 2.9 m) depicts schematically Brownian motion¹¹³, an omnipresent source of kinetic energy in which small particles or molecules move randomly in a liquid or gaseous medium. The last force that should be mentioned here is the gravitational force (figure 2.9 n)). This force depends on particle size and mass and the density difference between the colloid and the dispersing medium.

The self-assembly process is strongly affected by the choice of liquid medium and the particle properties including its structure, size, shape and material. In order to

achieve highly-ordered self-assembled particle arrays, a balance between the above-mentioned attractive and repulsive forces is necessary. The ordered particle arrays are stabilized when their state minimizes the thermodynamic energy. On one hand, the balance of attractive and repulsive forces must ensure the particles can overcome the energy barrier for self-assembly. On the other hand, the balance must also prevent particle agglomeration due to repulsive interactions^{39,105}.

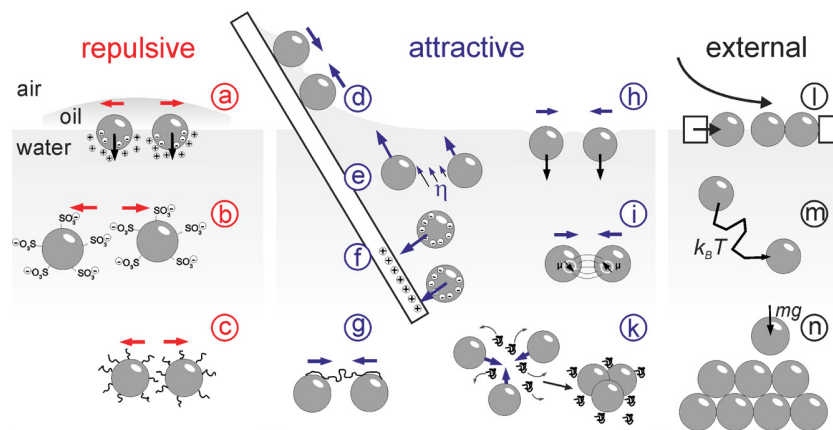


Figure 2.9: Schematic illustration of repulsive (red), attractive (blue) and external (black) forces for colloidal particles in bulk and interfaces: a) dipolar interactions, b) Coulomb interactions, c) steric repulsion, d) immersion capillary forces, e) hydrodynamic coupling forces, f) electrostatic attraction, g) bridging attraction, h) flotation capillary forces, i) van der Waals forces, k) depletion forces, l) barrier compression, m) Brownian motion and n) gravitational forces. Reprinted with permission from reference³⁹. Copyright 2015 American Chemical Society.

2.3.2 Two-Dimensional Colloidal Assembly Methods

To date, a plethora of methods has been developed to generate 2D ordered particle structures via self-assembly. Generally, these methods can be divided into two categories: i) direct assembly methods and ii) liquid interface-mediated methods³⁹. In the former case, particles are directly deposited and assembled on a solid substrate. Examples of direct assemble methods include controlled evaporation^{114,115}, vertical¹¹⁶ or horizontal deposition¹¹⁷, spin-coating¹¹⁸, and electrostatic deposition¹¹⁹, among others. In the liquid interface-mediated method, particles first self-assemble at the liquid interface, then the formed lattice is transferred on a solid substrate. This process allows the use of a broader range of substrates than in direct assembly methods³⁹. Thus, in this thesis, the periodic particle structures were fabricated via the liquid interface-mediated method. Further details on the method are given below.

The Langmuir trough is widely used for assemblies at air/water interface for hard incompressible particles such as silica or polystyrene¹²⁰ as well as for soft colloids^{112,121}.

After spreading the particles at the air/water interface, barriers are used to compress the particles together by reducing the free space between them. This way, densely packed particle lattices can be achieved. Afterwards, there are several possibilities to transfer the floating particles on a solid substrate. The monolayers can be transferred via several methods: by manual immersion of the substrate into bulk phase and withdrawal¹²², by reduction of the water level¹²³, by vertical Langmuir-Blodgett transfer^{124,125}, or by the Langmuir-Schaefer deposition^{126,127}.

However, recent years have seen the development of simplified methods that do not need sophisticated equipment, leading to lower costs and effortless performance. Retsch *et al.*¹²⁸ introduced the concept of "floating monolayers" in 2009. They used polystyrene particles with dimensions between 180 and 1150 nm in diameter. First, a dispersion drop was deposited on the glass slide and spin-coated. Next, the substrate with dried dispersion was gently immersed under a shallow angle into the water subphase. The particles detached and self-assembled into a close-packed ordered monolayer at the air/water interface at the substrate-water-air three contact line. The authors found that small amounts of surfactants like sodium dodecyl sulfate (SDS) in the water affected the floating monolayer. The surfactant acted as a soft barrier facilitating the packing process of the particles. Finally, the floating monolayer can then be transferred to another substrate.

Two years later, Vogel *et al.*¹²⁹ presented a direct assembly method for colloids at the air/water interface without the need of special equipment. They used polystyrene particles with diameters between 130 and 1000 nm diluted in ethanol with a weight concentration of 50 wt.-%. The dispersion was added via a glass slide tilted at an angle of 45° to the air/water interface. The spreading particles self-assemble into hexagonally ordered monolayer patches. By further addition of particles, patch sizes increase until the full interface was covered; only the accessible magnitude of the interface limits the monolayer size. The floating particle arrays are manually transferred on a wafer by immersion into the water subphase and then lifting at a shallow angle. Zhang *et al.*¹³⁰ showed a variation of the assembly method. Instead of using a glass slide to add the particles, they used the needle tip flow method to fabricate a 2D polystyrene particle lattice. A sharpened injection needle was placed in the middle of a glass dish at the water surface. The particle dispersion was then smoothly transferred to the air/water interface.

Based on the introduced assembly method by Vogel *et al.*^{121,129} Honold *et al.*²¹ fabricated highly ordered structures of colloidal particles with metal cores (gold or silver) and a polymer (PNIPAM) shell. Due to the polymer shell, the particles act like soft colloids rather than hard spheres. Compared to hard polystyrene particles, soft microgels favour the formation of non-close-packed monolayers if no compression is applied. Additionally, the softness leads to more complex interfacial behaviour and the particles can be significantly compressed¹²¹.

A variation of the method was used by Volk *et al.*¹³¹, which is shown in figure 2.10 a). Cm²-scale hexagonally ordered arrays of core-shell particles with an approximately 100 nm silver core and a hydrodynamic diameter of 326 nm were fabricated. Particles dispersed in a 1:1 mixture of water and ethanol were gently transferred to the air/water

interface using an Eppendorf pipette. At the interface, the particles spontaneously self-assemble into ordered lattices. In the second step, the free-floating monolayer was collected manually on a hydrophilic glass substrate by immersing the substrate into the water subphase and withdrawing the glass slide through the particle array. The obtained monolayer was dried using a heat-gun. Figure 2.10 b) shows the resulting particle structure recorded with Scanning Electron Microscopy (SEM). The fabrication of the Au-PNIPAM superstructures in this thesis was carried out by following the protocol of Volk *et al.*¹³¹ with one experimental change. The particles were dispersed in ethanol instead of an ethanol-water mixture.

Four forces play a significant role in the self-assembly of colloidal particles at the liquid interface: i) capillary forces for long-range attractions and ii) vdW interactions for short-range attractions. Additionally, iii) electrostatic and iv) dipole interactions act as contact barriers for particles³⁹. Particles used in this work are stabilised mainly by steric interactions resulting from relatively strong repulsion of the polymer dangling chains. The particle surface is only weakly negatively charged due to the anionic radical initiator used during the seeded precipitation polymerisation²¹. A balance of these forces is required for highly ordered monolayers.

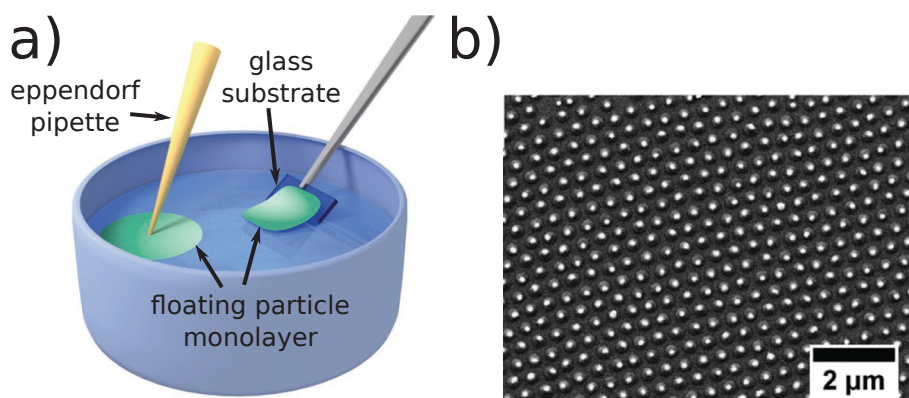


Figure 2.10: Schematic representation of the liquid interface mediated direct assembly method: a) transfer of the particles to the air/water interface with an Eppendorf pipette and collection of the floating monolayer onto a glass substrate. b) SEM image of the self-assembled core-shell (silver-PNIPAM) particles monolayer. Adapted from *Advanced Optical Materials*¹³¹, copyright 2017 WILEY-VCH Verlag GmbH & Co. KGaA, Weinheim.

The obtained particle monolayers on the glass substrates are suitable for various microscopic methods such as Atomic Force Microscopy (AFM) and Dark-Field Microscopy (DFM). AFM and DFM generate a digital image of the fabricated monolayer allowing the evaluation and quantitative analysis of the lattice order. The image analysis methods used in this work are presented in section 2.5 in detail.

2.4 Plasmon Resonances of Noble Metal Nanoparticles

This section starts with an introduction of Maxwell's equations which describe the interaction between light and matter, and is followed by Drude theory of metals. The properties of gold will be the focus of discussion because gold nanoparticles play a crucial role in this work. The physics of localized surface plasmon resonances (LSPR) will then be presented, followed by the discussion of various coupling phenomena, *i.e.* near-field and far-field coupling. Finally, the section closes with theoretical calculations focusing on the method of finite difference time domain (FDTD).

2.4.1 Interaction of Light and Matter

To understand how light and matter interact, the basic principles of light and matter must first be understood. Light is electromagnetic radiation whose speed is $c \approx 3 \times 10^8$ m s^{-1} in a vacuum, and is given by the wave equation:

$$\mathbf{E} = \mathbf{E}_0 e^{i(\omega t - \mathbf{k}\mathbf{x})}. \quad (2.29)$$

\mathbf{E} denotes the electric field vector, \mathbf{E}_0 is the amplitude, i is the imaginary unit, $\omega = 2\pi \frac{c}{\lambda}$ is angular frequency, t is time, $\mathbf{k} = \frac{\omega}{c}$ defines the wave vector and x the displacement. The wavelength range visible to the human eye is between 400 and 700 nm wavelength. However, the concept of light as a wave cannot describe all electromagnetic interactions with matter. Therefore, the theory of electromagnetic radiation as discrete bundles of energy was introduced. These bundles are known as photons which are treated as particles with a mass of $m = 0$ and speed of light. Planck's equation gives the relationship between the energy E and a single photon's frequency ν .

$$E = h\nu = \frac{hc}{\lambda} \quad (2.30)$$

Here, h denotes Planck's constant and λ is the wavelength.

Matter is made up of atoms with diameter in the range between 6×10^{-11} and 5×10^{-10} m. Each atom is composed of a positively charged nucleus (protons and neutrons) and a negatively charged electron shell. The electrons move freely within the shell and have a significantly smaller mass of $m_e \approx \frac{1}{1800} m_p$ compared to protons.

The interaction between light, *i.e.* electromagnetic waves, and matter can be understood as a change in the temporal and spatial propagation of electromagnetic waves in response to a new environment. Maxwell's theory is widely used to describe this response. In the most general form, the macroscopic electromagnetism equations are expressed as¹³²:

$$\nabla \cdot \mathbf{D} = \rho_{\text{ext}} \quad (2.31)$$

$$\nabla \cdot \mathbf{B} = 0 \quad (2.32)$$

$$\nabla \times \mathbf{E} = -\frac{\partial \mathbf{B}}{\partial t} \quad (2.33)$$

$$\nabla \times \mathbf{H} = \mathbf{J}_{\text{ext}} + \frac{\partial \mathbf{D}}{\partial t}. \quad (2.34)$$

\mathbf{D} is the dielectric displacement, \mathbf{B} the magnetic induction, \mathbf{E} the electric and \mathbf{H} the magnetic field. ρ_{ext} denotes the external charge, and \mathbf{J}_{ext} the external current densities. The charges and current densities are divided into external (free) and internal (bound) components. The total values are given by $\rho_{\text{tot}} = \rho_{\text{ext}} + \rho$ and $\mathbf{J}_{\text{tot}} = \mathbf{J}_{\text{ext}} + \mathbf{J}$. While ρ_{ext} and \mathbf{J}_{ext} drive the system, ρ and \mathbf{J} give a response to external stimuli. ∇ is the nabla operator defined as $\nabla = \left(\frac{\partial}{\partial x_1}, \dots, \frac{\partial}{\partial x_n} \right)$. The four fields are linked via the polarization \mathbf{P} and magnetization \mathbf{M} by

$$\mathbf{D} = \varepsilon_0 \mathbf{E} + \mathbf{P} \quad (2.35)$$

$$\mathbf{H} = \frac{1}{\mu_0} \mathbf{B} - \mathbf{M}. \quad (2.36)$$

ε_0 and μ_0 denotes the electric permittivity or the dielectric constant and magnetic permeability of vacuum. In SI-units, $\varepsilon_0 = 8.8542 \times 10^{-12} \text{ A s V}^{-1} \text{ m}^{-1}$ and $\mu_0 = 4\pi \times 10^{-7} \text{ V s A}^{-1} \text{ m}^{-1}$. However, in a nonmagnetic medium the magnetic response does not need to be considered.

Assuming a linear, isotropic and nonmagnetic medium the following constitutive relations can be expressed:

$$\mathbf{D} = \varepsilon_0 \varepsilon \mathbf{E} \quad (2.37)$$

$$\mathbf{B} = \mu_0 \mu \mathbf{H} \quad (2.38)$$

$$\mathbf{P} = \varepsilon_0 \chi \mathbf{E} \quad (2.39)$$

$$\mathbf{J} = \sigma \mathbf{E}. \quad (2.40)$$

ε and $\mu = 1$ (for nonmagnetic medium) are relative permittivity and permeability, respectively. The optical response of matter is characterized by ε and μ and it strongly depends on the electromagnetic field frequency. However, in the case of metals a complex dielectric function $\varepsilon(\omega)$ is used which will be introduced in the next section. χ gives the dielectric susceptibility and σ describes the conductivity. The introduced Maxwell's equations form the foundation of classical electromagnetism and solve the temporal and spatial evolution of the electromagnetic fields interacting with matter.

2.4.2 The Drude Theory of Metals

Metals are known for their high conductivity and reflectivity; the Drude theory proposed by Paul Drude in 1900¹³³ is widely used for the description of these properties despite some inaccuracies in the. Paul Drude applied the kinetic gas theory to understand the motion of electrons in metals. This theory introduces the electron gas plasma model and can be used for metals over a wide frequency range from alkali metals in the ultraviolet band to noble metals such as silver or gold at visible wavelengths where interband transitions occur¹³². In the Drude model, the metal is comprised of positively charged background cores, *i.e.* ions, and a gas of free, negatively charged electrons which are much smaller than the cores. Whereas fixed positions are assumed for the cores, the electrons are delocalized, allowing them to move freely through the bulk. The electron-electron interactions, as well as details of the lattice potential, are neglected in this theory. By applying an electromagnetic field \mathbf{E} , electrons start to oscillate following the field. However, due to collisions with cores, their motion is damped by frequency γ , whose value is characteristic for each metal.

$$\gamma = \frac{1}{\tau} \quad (2.41)$$

where τ denotes the relaxation time between two collisions. The dielectric function of the free electron gas also known as classical Drude model^{132,133} is given by

$$\varepsilon(\omega) = 1 - \frac{\omega_p^2}{\omega^2 + i\gamma\omega} = \varepsilon_1(\omega) + i\varepsilon_2(\omega) \quad (2.42)$$

with real $\varepsilon_1(\omega)$ and imaginary $i\varepsilon_2(\omega)$ components

$$\varepsilon_1(\omega) = 1 - \frac{\omega_p^2\tau^2}{1 + \omega^2\tau^2} \quad (2.43)$$

$$\varepsilon_2(\omega) = \frac{\omega_p^2\tau}{\omega(1 + \omega^2\tau^2)} \quad (2.44)$$

where ε denotes the relative permittivity that describes the general response of a medium to an electromagnetic field. ω_p^2 is the plasma frequency of the free electron gas given by

$$\omega_p^2 = \frac{ne^2}{\varepsilon_0 m_0}. \quad (2.45)$$

ε_0 defines the vacuum permittivity. n denotes the number density of charged carriers and e is the charge of the electron. m_0 defines the effective mass of the conduction electrons which differ from the free electron mass m_e . The plasma frequency is the eigenfrequency of the longitudinal electron oscillation in the bulk metal. Figure 2.11 shows calculated real and imaginary parts of the dielectric function of gold as a function of the wavelength. The real part has negative values over the visible wavelength range, while the imaginary part shows positive values. At low frequencies, more precisely for

$\omega < \omega_p$, the electromagnetic wave cannot propagate through the metal, resulting in reflection of the wave. This is the origin of the high reflectivity and the principle of a mirror. Moreover, at very low frequencies, metals tend to absorb rather than reflect incoming electromagnetic waves due to the oscillation of surface electrons in this case. At high frequencies with $\omega \geq \omega_p$, the electromagnetic wave propagates through the metal and the electron gas plasma supports the transverse propagating waves. The metal appears transparent and is only weakly absorbing. At $\omega = \omega_p$, damping is negligible for the free electron plasma.

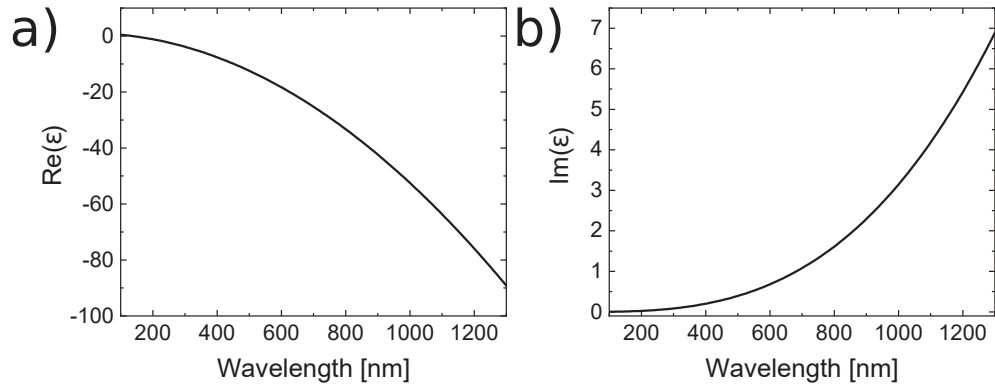


Figure 2.11: Calculated real part in a) and imaginary part in b) of the dielectric function of gold using equations 2.43 and 2.44 of the Drude model. The values of $\omega_p = 13.8 \times 10^{15} \text{ s}^{-1}$ and $\gamma = 1.075 \times 10^{14} \text{ s}^{-1}$ were taken from literature¹³⁴.

For noble metals such as silver or gold, equation 2.42 must be adjusted because noble metals are not ideal free-electron metals as assumed in the classical Drude model. For the case $\omega > \omega_p$, the optical response of noble metals is dominated by free electrons resulting in a highly polarized environment. To consider the effect of positive background cores, the dielectric constant ϵ_∞ is used, leading to the following modification of the free electron gas equation:

$$\epsilon(\omega) = \epsilon_\infty - \frac{\omega_p^2}{\omega^2 + i\gamma\omega}. \quad (2.46)$$

However, the Drude Model for gold and silver is limited to the near-infrared and visible wavelength range. The components $\epsilon_1(\omega)$ and $\epsilon_2(\omega)$ are not well described at high frequencies. Based on the Drude model, Johnson and Christy¹³⁴ determined the optical response of real metals. Their results are widely used as standard optical properties for gold in simulations software such as Lumerical Solutions, Inc. (FDTD Solutions) which was used for theoretical calculations in this thesis. The plasma frequency of gold is $\omega_p = 13.8 \times 10^{15} \text{ s}^{-1}$, while the damping constant is $\gamma = 1.075 \times 10^{14} \text{ s}^{-1}$ according to literature¹³⁴.

Table 2.2: Molar mass, density, free electron density, plasma frequency, damping constant and effective electron mass of gold.

| | Gold |
|--|------------------------|
| M [g mol ⁻¹] ¹³⁵ | 197.0 |
| ρ [g mL ⁻¹] ¹³⁵ | 19.3 |
| n [m ⁻³] ¹³⁵ | 5.90×10^{28} |
| ω_p [s ⁻¹] ¹³⁴ | 13.8×10^{15} |
| γ [s ⁻¹] ¹³⁴ | 1.075×10^{14} |
| m_0 ¹³⁴ | 0.99 |

2.4.3 Localized Surface Plasmon Resonances

The collective oscillations of free electrons in metals excited by electromagnetic fields are called plasmons. Depending on the metal size, three types of plasmons can be distinguished, which are illustrated in figure 2.12¹³²: first, Volume or Bulk plasmons, where the electrons oscillate longitudinally in the metal. Second, Surface Plasmon Polaritons (SPP) are two-dimensional, transverse oscillations of the electrons at the interface between a conductor such as metal and the dielectric medium. And finally, the localized surface plasmon resonances (LSPR) that belong to the non-propagating excitations. The latter occurs in nano-dimensional metal particles, as used in this work.

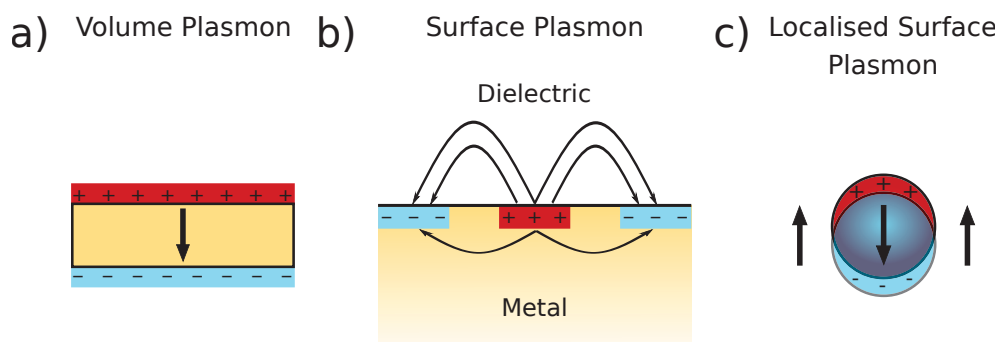


Figure 2.12: Schematic representation of plasmon types in metals. a) Volume plasmon: electrons oscillate longitudinal in the metal. b) Surface plasmon: electrons oscillate transverse at the metal/dielectric interface. c) Localized surface plasmon: electrons oscillate in-phase.

Silver and gold nanoparticles are known for supporting localized surface plasmon resonances^{16,132}. Due to the curved surface, an effective restoring force on the electrons is present, allowing their resonance. Moreover, these resonances can be excited by direct light illumination. The appearance and energy of the modes strongly depend on the metal type¹³⁶, the particle size and shape^{15,137,138,139}, and the surrounding environment^{137,140}. The properties of gold nanoparticles will be discussed here.

The LSPR of gold can be excited by light in the visible wavelength range, which explains the vivid colour of the gold nanoparticles^{17,132}. Figure 2.13 a) shows schematically a dipolar LSPR excited by the incoming electromagnetic wave, whereas 2.13 b) demonstrates an absorbance spectrum of gold nanoparticles in dilute, aqueous dispersion. The resonance manifests as a single absorbance peak at a wavelength of 518 nm. This is a characteristic wavelength for small gold particles with a diameter of approximately 15 nm. The inset photograph shows the corresponding particles, which have a in typical deep reddish colour.

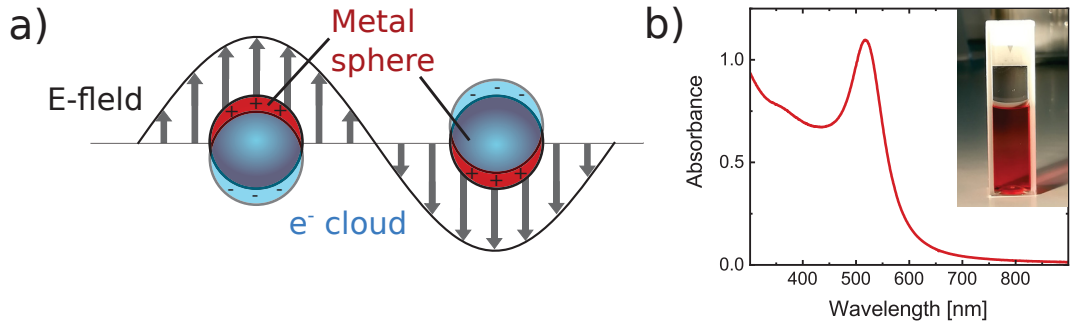


Figure 2.13: a) Schematic depiction of LSPR for a spherical particle excited by an incoming electromagnetic field. The conductive electrons oscillate due to the interaction with the field. b) Experimentally obtained absorbance spectrum of gold nanoparticles ($d \approx 15$ nm) in dilute, aqueous dispersion. The inset photograph shows the corresponding particle dispersion in a cuvette.

For analyzing the interaction of the light and the gold particles shown in figure 2.13, the quasi-static approximation can be used¹³². In the quasi-static regime, the particles are represented as ideal dipoles. This approach is valid for particles that are significantly smaller than the wavelength, *i.e.* $d \ll \lambda$. The quasi-static criterion is satisfied in this work, which uses 15-100 nm gold cores that are illuminated by visible wavelengths much larger than the cores. The dielectric response of the particles is given by the dielectric function $\epsilon(\omega)$ (eq. 2.42 and 2.46) while the surrounding medium is described by the dielectric constant ϵ_m assuming that it is isotropic and non-absorbing. To describe the scattering and absorption behaviours of metal nanoparticles, cross sections for scattering and absorption C_{sca} and C_{abs} are introduced^{132,141}:

$$C_{\text{sca}} = \frac{k^4}{6\pi} |\alpha|^2 = \frac{8\pi}{3} k^4 R^6 \left| \frac{\epsilon_M - \epsilon_m}{\epsilon_M + 2\epsilon_m} \right|^2 \quad (2.47)$$

$$C_{\text{abs}} = k \text{Im}[\alpha] = 4\pi k R^3 \text{Im} \left[\frac{\epsilon_M - \epsilon_m}{\epsilon_M + 2\epsilon_m} \right] \quad (2.48)$$

For simplicity, ϵ_M is used to represent the dielectric constant of metal instead of $\epsilon(\omega)$, but it is noted that permittivity still depends on frequency.

R denotes the radius and α defines the complex polarizability of the spherical particles expressed as:

$$\alpha = 4\pi R^3 \frac{\varepsilon_M - \varepsilon_m}{\varepsilon_M + 2\varepsilon_m}. \quad (2.49)$$

Large α values can be reached when $|\varepsilon_M + 2\varepsilon_m|$ is minimal. The polarizability is resonantly enhanced in this case, leading to the following resonance relationship (Fröhlich condition):

$$\text{Re}[\varepsilon(\omega)] = -2\varepsilon_m \quad (2.50)$$

This resonant mode is named the dipole surface plasmon and is only valid for small metal particles with dimensions $d \ll \lambda$. For gold spheres surrounded by air ($\varepsilon_m = 1$) treated with the Drude model, the Fröhlich criteria is fulfilled at the frequency $\omega_0 = \frac{\omega_p}{\sqrt{3}}$. The dielectric permittivity of the medium is linked to the refractive index via $n = \sqrt{\varepsilon_m}$. Increasing the refractive index of the medium surrounding the nanoparticles leads to the redshift of the LSPR^{132,137}. The enhanced polarizability α is interesting from the viewpoint of optics because of the coincidence of particle scattering and absorbing efficiency. The scattering efficiency scales with $C_{\text{sca}} \propto R^6$ but can be neglected for diameters below 100 nm. Therefore, for small particles, the absorption scaling with R^3 dominates over the scattering, resulting in a well-pronounced peak in an extinction spectrum as shown in figure 2.13 b). Finally, in the quasi-static limit for a spherical nanoparticle and the dielectric function (eq: 2.42), the sum of absorption and scattering contributions leads to the extinction cross section given by:

$$C_{\text{ext}} = C_{\text{abs}} + C_{\text{sca}} = 9 \frac{\omega}{c} \varepsilon_m^{3/2} V \frac{\varepsilon_2}{[\varepsilon_1 + 2\varepsilon_m]^2 + \varepsilon_2^2}. \quad (2.51)$$

V is the particle volume, ε_1 and ε_2 are the respective real and imaginary components of the dielectric function, as mentioned in the previous section. The particle size affects the intensity of the extinction, as seen in the equation above; the larger the particle, the higher the C_{ext} value. Moreover, the LSPR wavelength is strongly particle size-dependent. Increasing the particle size leads to a smaller restoring force between the charges at opposite interfaces; therefore, less energy is needed to oscillate the electrons resulting in a lower resonance frequency. In other words, due to the retardation effects, the spectral position shifts towards red with increasing particle size¹³².

In a standard absorbance spectroscopy experiment, the sample, *e.g.* a cuvette containing dispersed particles, is illuminated with light of intensity I_0 . The transmitted light loses the intensity due to absorption and scattering processes. The attenuation of the incoming light depends on the the extinction cross section C_{ext} of a single particle, the number of particles N and the pathlength d . The relation between the intensity loss and these parameters is given by the Beer-Lambert law.

$$I(d) = I_0 e^{-C_{\text{ext}} N d} \quad (2.52)$$

The measured light intensities can be converted into absorbance values. The Beer-Lambert law can be rewritten as:

$$A = \log_{10} \left(\frac{I_0}{I(d)} \right) = \frac{C_{\text{ext}} N d}{2.303}. \quad (2.53)$$

It has been experimentally shown that the introduced calculations of cross sections for scattering and absorption provide a good approximation for spherical particles with dimensions smaller than 100 nm, although the dipole plasmon theory is strictly valid only for much smaller particles¹³². However, when the particles become larger, the scattering and absorption can be well described by the Mie theory¹⁴². Since the approach is not required to treat the gold cores used in this work, it will not be introduced here.

2.4.4 Coupling Phenomena

Near-field plasmonic coupling

When noble metal nanoparticles are placed close to each other, their electric fields can overlap and interact, leading to near-field coupling. The coupling can be understood as the hybridization of plasmons similar to the molecular orbital theory^{143,144}. In the case of small particles, the fields (plasmons) are treated as dipoles¹³². These near-field interactions dominate with a distance dependence of d^{-3} and result in a spectral shift of the plasmonic resonance compared to the LSPR of an isolated particle. Depending on the polarization of the incident light and the particle separation, the plasmonic resonance position shifts to longer or shorter wavelengths. Polarization along the interparticle axis leads to a pronounced redshift with decreasing interparticle distance accompanied by a broadening of the peak^{145,146,147}. However, polarization orthogonal to the interparticle axis leads to a slight blueshift of the resonance with decreasing particle separation^{146,147}. In the case of gold nanoparticles, near-field coupling occurs for particle separation smaller than approximately 2.5 times the particle diameter¹⁴⁸.

Figure 2.14 shows experimentally obtained extinction spectra of gold nanodisc pairs with a diameter of 88 nm fabricated by electron beam lithography. In a) the incident light is polarized along the interparticle axis and in b) the polarization is orthogonal to the axis. The particle separation varies between 2 and 212 nm. In parallel polarization, the resonance position significantly redshifts by reducing the interparticle separation, while in the orthogonal case, the position shifts slightly blue, accompanied by decreasing intensity. Assuming a simple dipole-dipole coupling, the redshift of the plasmon resonance can be explained by the attractive interaction of the dipoles for parallel polarization. This results in the decrease of the plasmon frequency, *i.e.* red-shift. On the other hand, for the orthogonal polarization, the interactions are repulsive leading to higher plasmon frequency, *i.e.* blueshift¹⁴⁶.

Radiative plasmonic coupling

Particles arranged into a two-dimensional periodic array with lattice constant $a \approx \lambda$ possess a photonic diffractive mode, sometimes referred to as a Bragg mode. The position of the mode strongly depends on the lattice period and refractive index environment¹⁴⁹. For the in-plane diffraction modes, the spectral position where such mode occurs is

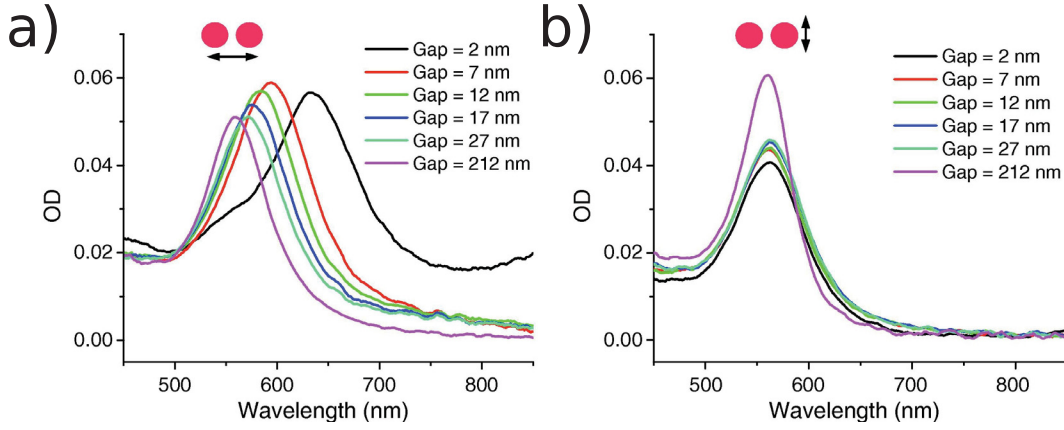


Figure 2.14: Extinction spectra of lithographically-fabricated arrays of gold nanodisc ($d = 88$ nm, $h = 25$ nm) pairs with various interparticle distances. a) Light polarization along the interparticle axis. b) Light polarization orthogonal to the interparticle axis. Adapted with permission from reference¹⁴⁶. Copyright 2007 American Chemical Society.

defined as a Rayleigh anomaly (RA)¹⁵⁰. Interparticle distances in the wavelength-scale of the single particle plasmon resonance support the collective radiative coupling between the plasmonic LSPR and the photonic diffractive mode known as surface lattice resonance (SLR)^{23,151}. SLRs are hybridized modes that exhibit both photonic and plasmonic properties. In the case of coupling to in-plane diffraction modes, a homogeneous refractive index environment is required for observing the SLRs²³.

As discussed in the previous section, α (eq. 2.49) expresses the polarizability of metal nanoparticles, which can be modelled as ideal dipoles for particles much smaller than the wavelength. In an array, each particle dipole contributes to the sum of the total field, modifying the polarizability α to α^* defined as¹⁵¹:

$$\alpha^* = \frac{1}{1/\alpha - S}, \quad (2.54)$$

where S denotes the array factor¹⁵¹, which depends on the interparticle distance and the particle arrangement. For normal incidence the array factor is given by

$$S = \sum_{dipoles} e^{i\mathbf{k}\mathbf{r}} \left[\frac{(1 - i\mathbf{k}\mathbf{r})(3\cos^2\theta - 1)}{\mathbf{r}^3} + \frac{\mathbf{k}^2\sin^2\theta}{\mathbf{r}} \right]. \quad (2.55)$$

\mathbf{k} is the wave vector, \mathbf{r} is the distance between the central particle to another particle, and θ defines the angle between \mathbf{r} and the dipole moment of a particle. The extinction spectrum of a particle array can be calculated using equation 2.51 and the modified polarizability. Figure 2.15 a) shows calculated extinction cross section per particle for a single silver particle and a particle placed in an array. The spectrum of a single particle exhibits only one relatively broad peak with a maximum at approximately 725 nm.

In contrast, the optical response of the array shows two maxima at ~ 645 and ~ 778 nm. Both peaks are attributed to the SLR; nevertheless, the second peak at longer wavelength appears much stronger than the first peak. Compared to the LSPR resonance, the SLR mode is redshifted and narrower. The smaller full width at half-maximum (FWHM) demonstrates the higher quality of the resonance resulting from longer lifetimes of the SLR in the picosecond range¹⁵² while the lifetime of LSPRs is in the order of femtoseconds¹³². Figure 2.15 b) shows calculated real and imaginary parts of the array factor S and additionally the $1/\alpha$ values. The dashed lines in a) and b) highlight the intersection points between the real parts of S and $1/\alpha$. At these points, both values are equal, leading to the large polarization of a particle in the lattice. This is the necessary condition for the occurrence of SLRs²³. The quality factor ($Q = \lambda/\Delta\lambda$) is often used to quantify the spectroscopic resonances. Strong damping of single gold nanoparticles leads to low Q values¹⁵³. However, arranging the particles into an ordered array reduces the losses and improves the Q-factor^{23,25}.

The SLR quality depends on several factors. Auguie and Barnes¹⁵¹ studied the effect of lattice period. Particle arrays with a diffractive mode position located towards slightly larger wavelengths than the LSPR position lead to a sharp and intense peak. Increasing the spectral separation of the LSPR and diffractive mode results in weaker coupling and thus broader resonances. Next, the number of particles within the lattice affects the SLR quality. Increasing the array size leads to a narrower resonance^{154,155} due to reduction of the scattering losses¹⁵⁶. Structural lattice disorder suppresses the SLR coupling while various sized particles broaden the resonance due to different LSPR contributions of each particle¹⁵⁷.

2.4.5 Theoretical Calculations – Finite Difference Time Domain Simulations

One of the widely used numerical methods for calculating extinction spectra and electromagnetic field maps of particle lattices is the finite difference time domain (FDTD) method¹⁵⁹. Other common numerical approaches include the Coupled or Discrete Dipole Approximation (CDA or DDA)^{160,161,162,163,164} and the Multiple Multipole (MMP) Method^{165,166}. However, the theory of CDA and MMP will be not discussed here. FDTD belongs to the space-grid time-domain procedures, which solves Maxwell's curl equations in two and three-dimensional geometries using finite-difference approximations. For the simulations, the continuous Maxwell equations are converted into discrete equations and the electromagnetic wave is calculated in a finite spatial region. Yee's algorithm presented in 1966 gives the basis for FDTD methods used today¹⁶⁷. The algorithm solves Maxwell's curl equations for the electric field \mathbf{E} as well as for the magnetic field \mathbf{H} . Figure 2.16 illustrates the Yee lattice cell showing the placement of \mathbf{E} and \mathbf{H} fields on a three-dimensional grid. Every electric field component is surrounded by four \mathbf{H} components and each magnetic field component surrounded as well by four \mathbf{E} components. Both field components are calculated in a leapfrog manner. The starting point is the calculation of the electric fields at the zero time point. The resulting data is used for magnetic field calculations at some later time point. The new \mathbf{H} field is used for the recalculation of

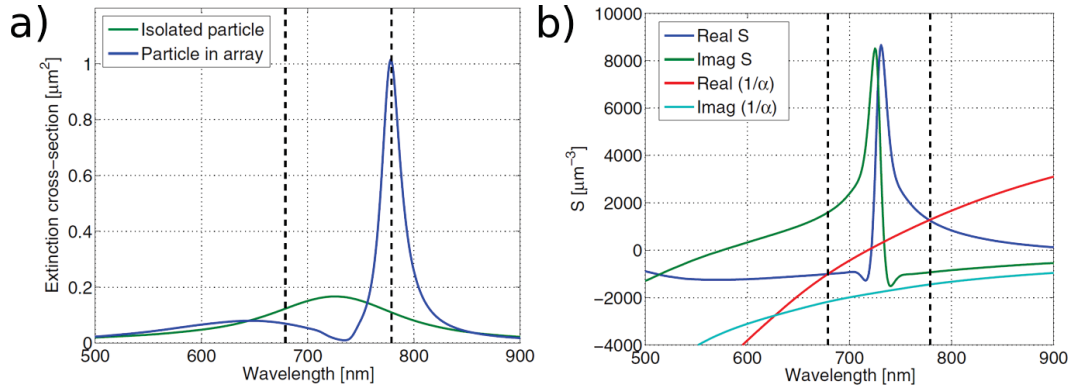


Figure 2.15: Comparison of LSPR with SLR of silver disks ($d = 120$ nm, $h = 30$ nm) in a homogeneous refractive index of $n = 1.515$; a) calculated extinction cross section per particle for an isolated particle (green) and a particle in an ordered lattice (blue). b) Array factor for a hexagonally ordered lattice with nearest neighbour center-to-center interparticle distance of 555 nm. The dashed lines highlights the intersection points between the real parts of S and of $1/\alpha$ in a) and b). A linearly polarized light at normal incidence was used with an electric field parallel to the y axis of the particle lattice. Reprinted and adapted with permission from reference¹⁵⁸. Copyright 2014 by the American Physical Society.

the \mathbf{E} fields, which is in turn used for recomputation of \mathbf{H} . The cycle continues until the time-stepping is concluded and the steady state is reached.

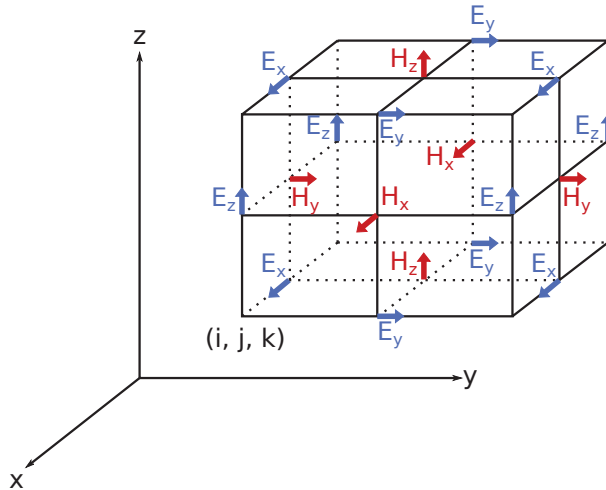


Figure 2.16: Yee lattice cell showing positions of the electric \mathbf{E} and magnetic \mathbf{H} field components. Adapted from literature¹⁶⁷.

Since each computer has limited memory space, boundary conditions are required for the simulation. One option is the perfectly matched layer (PML)¹⁶⁸. The PML mostly absorb the incident light and minimize the reflection. The ideal PML boundary conditions generate no reflection, but due to the discretization of the equations, reflection errors are produced in practice. Another option is the periodic boundary conditions (PBC)¹⁶⁹ especially suitable for periodic structures. PBCs copy the electromagnetic field from one side of the simulation and inject them at the other side, allowing for the calculation of a small unit cell instead of large (infinite) structures, which reduces the computation time.

In FDTD, each grid point is associated with a specific type of material containing information about its properties, *e.g.* permittivity and permeability. In the case of noble metal nanoparticles, parameters from the Drude model are often used, thus they can be easily inserted in the FDTD method^{132,170}. In this work, the commercial software from Lumerical Solutions, Inc. (FDTD Solutions, Version 8.18.1332) was used to obtain extinction spectra and E-field maps of single Au-PNIPAM particles and particle arrays in various refractive index environments.

However, although the FDTD simulations are very robust and produce accurate results for nanoscale structures, the method has also a disadvantage¹⁵⁹. The calculations require very fine meshes surrounding the metal sphere to reduce staircasing effects. Since applied meshes usually use a Cartesian grid with rectangular cells, curved surfaces of spherical particles can not be resolved entirely. Nevertheless, the effect can be neglected when the simulated structure is relatively large compared to the mesh size.

2.5 Image Analysis

This section presents methods for the evaluation and quantitative analysis of the lattice symmetry of periodic particle monolayers. Microscopic methods, *e.g.* atomic force microscopy (AFM) and dark-field microscopy (DFM), can be used for obtaining digital images of the particle lattices, whereas ImageJ¹⁷¹ software is a useful tool to process the images before analysis. Typically, the image noise is first reduced by adjusting the brightness and applying smoothing filters, *e.g.* Gaussian Blur (a standard feature of ImageJ). Next, the positions of particle centres are detected. Finally, the obtained particle centre position maps with x and y coordinates can be extracted either as an image or list. This data is used as an input for the Fast Fourier transformation (FFT), pair correlation and domain size analyses, which will be described in in the following sections.

2.5.1 Fourier Analysis

Fourier Transformations are a widely used method for image analysis and detection of image features such as periodic interferences. It transforms images of spatial domains, in this case AFM or DFM, from real space into power spectra in the reciprocal space, *i.e.* frequency domains. After the transformation, each pixel's location and distance relative to the image centre represent a periodic signal of a certain frequency in the original image. Regions near the transformed image center correspond to lower frequencies, while areas

located away from the centre point correspond to higher frequencies. The brightness of the pixel represents the intensity of the signal. Periodicities of structures in the original image manifest as bright peak. As a result, when analysing lattices, their number and orientation are characteristic of a particular lattice type. Such a power spectrum also resembles a diffraction pattern as it can be obtained by scattering methods.

To obtain the power spectrum $P(k_x, k_y)$ of an image, the image is considered to be a function $f : \mathbb{R}^2 \rightarrow \mathbb{R}$, mapping cartesian coordinates of the real space to the brightness at the corresponding image position. $P(k_x, k_y)$ of the image in the reciprocal space is obtained by¹⁷²

$$P(k_x, k_y) = |F(k_x, k_y)|^2. \quad (2.56)$$

where $F(k_x, k_y)$ is the Fourier Transform of the function $f(x, y)$ and is calculated by following equation¹⁷²:

$$F(k_x, k_y) = \int \int f(x, y) e^{2\pi i(k_x x + k_y y)} dx dy. \quad (2.57)$$

k_x and k_y define the wave vectors of the spatial frequency domains in the reciprocal space. However, equation 2.57 holds only if the $f(x, y)$ function is continuous. AFM or DFM images used in this work consist of discrete pixels. Therefore, the Discrete Fourier Transform (DFT) of the image must be used. For a square image of $N \times N$ pixels, it is defined as¹⁷²

$$F(k_x, k_y) = \frac{1}{N} \sum_{x=0}^{N-1} \sum_{y=0}^{N-1} f(x, y) e^{-i \frac{2\pi}{N} (k_x x + k_y y)}. \quad (2.58)$$

In this work, all DFT power spectra were obtained using ImageJ's¹⁷¹ implementation of the Fast Fourier Transform (FFT) algorithm.

Figure 2.17 a) shows an original real space AFM image of Au-PNIPAM particles, and b) shows a position map of the particle centers of the AFM image. The use of a position map instead directly using the AFM image reduces noise in the FFT power spectrum. Figure 2.17 c) demonstrates the corresponding calculated FFT. The image has been cropped to only show the most pronounced peaks (white) at low frequencies near the center. The power spectrum shows six clear peaks around the centre with more peaks spreading out in a hexagonal pattern. Towards the edges the peaks become less pronounced and at some point fade to gray. When analysing microscopic images of particle lattices there is a correlation between clarity of the outer peaks and long-range uniformity of the analysed lattice.

2.5.2 Pair Correlation Function

The pair correlation function $g(r)$, also known as radial distribution function (RDF), gives the average particle density in each direction around a reference particle relative to the overall particle density in the image. It thus describes the probability of finding

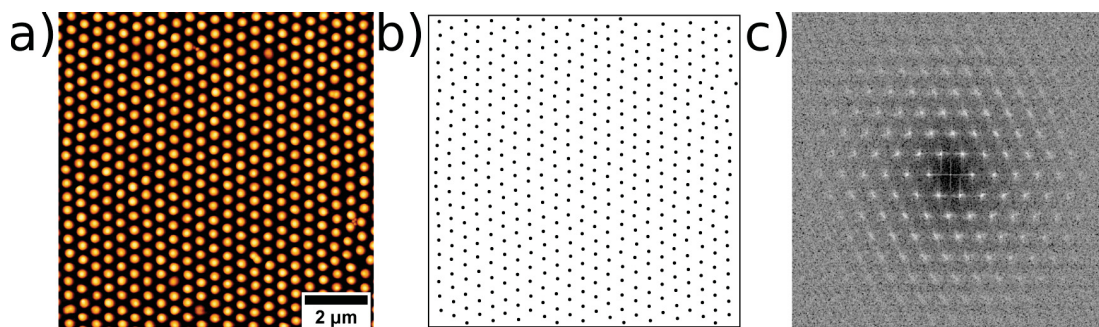


Figure 2.17: Fast Fourier transformation analysis of an Au-PNIPAM particle lattice. a) Real space $10 \times 10 \mu\text{m}^2$ AFM height profile image. b) Computed position map of the particle centres of mass from the AFM image. c) Corresponding calculated zoom-in cutout FFT.

a particle pair of a given distance compared to the average probability of all possible distances. For two-dimensional systems, $g(r)$ can be calculated as^{173,174}

$$g(r) = \frac{N(r)}{2\pi r \Delta r \rho}. \quad (2.59)$$

$N(r)$ denotes the number of particles between the distance r and $r + \Delta r$ from the reference particle, while ρ defines the overall particle density in the image¹⁷⁵. $g(r)$ is dimensionless.

Figure 2.18 schematically illustrates randomly ordered particles surrounding a green-coloured central particle. The corresponding pair correlation function shows distinct peaks at the approximate distance of the first and second-order neighbours (1st and 2nd coordination shell). The second peak is already significantly lower and wider than the first, which is related to the second ring's larger area and the particles not being distributed uniformly. Towards higher r a value of 1 indicates that the particle density at large distances approaches the average particle density.

For particle lattices, such as crystal structures, the function shows sharp peaks. An ideal lattice and a value of 0 for Δr would yield infinitely narrow peaks. Their positions and heights depend on the lattice structure, resulting in a characteristic pair distribution function for each lattice type. Lattice disorder strongly affects the peak shape by broadening and smearing them with increasing deviation from the ideal lattice. Therefore, $g(r)$ allows to determine the degree of order and the lattice type.

Figure 2.19 a) shows an AFM image of Au-PNIPAM particles self-assembled into a hexagonally ordered lattice. Coloured circles demonstrate the mean occurring interparticle distances of first-, second-, and third-order neighbours relative to a reference particle. Figure 2.19 b) demonstrates the corresponding $g(r)$, calculated using an in-house algorithm. Above the plot, coloured ticks correlate the peaks to corresponding interparticle distances highlighted in the AFM image. The first peak, corresponding to the red circle, refers to the nearest neighbour center-to-center interparticle distance (d_{c-c}). At shorter distances, a $g(r)$ value of zero indicates that the single particle centers

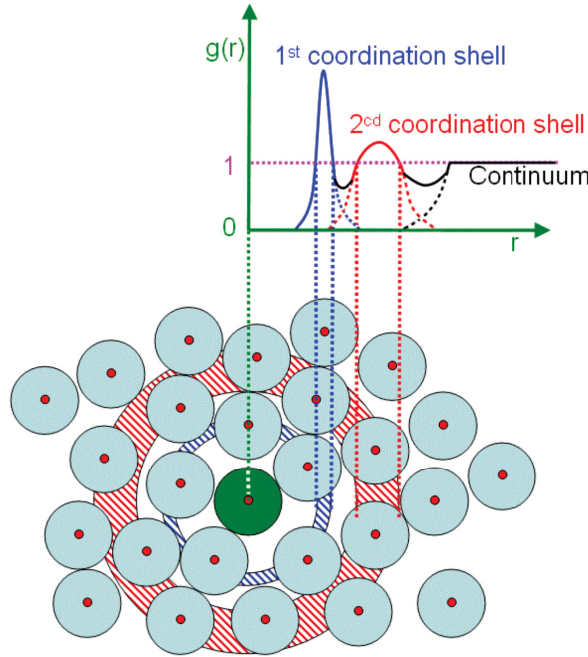


Figure 2.18: Schematic illustration of the pair correlation function $g(r)$. Reprinted from reference¹⁷⁶.

are not overlapping. For the second-order neighbours (blue and green), $g(r)$ shows a double peak. Finally, the third-order neighbours (purple and orange) also create a double peak with the first peak being significantly higher, reflecting the symmetry of the third-order neighbour shell. At larger distances the $g(r)$ function fluctuates around unity indicating a low degree of long-range order of the lattice.

2.5.3 Domain Size Analysis

As demonstrated by Hillebrand *et al.*, quantitative domain analysis of two-dimensional hexagonal lattices can be performed based on radial and angular distribution functions¹⁷⁷. Their methodology allows identification of domains and evaluation of their quality. Given an image of particles, the particles' x and y coordinates are first extracted. In a perfectly hexagonal ordered lattice, each particle can be connected with two neighbours to form an equilateral triangle with an angle of 60° . Neglecting the boundary effects, the number of triangles N_{tri} is given by:

$$N_{\text{tri}} = 2 \times N_{\text{particle}}. \quad (2.60)$$

N_{particle} is the number of particles of the two-dimensional lattice. However, experimentally obtained lattices, *e.g.* self-assembled colloidal monolayers as used in this work, contain structural disorders and lattice holes. Those defects cause boundaries between individual domains and reduce N_{tri} compared to an ideal lattice. Figure 2.20 a)

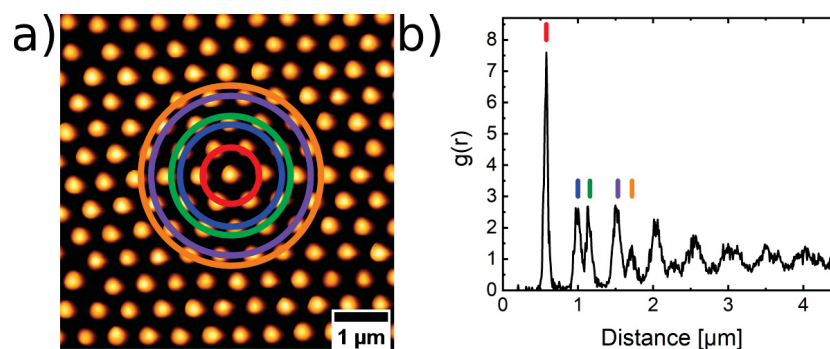


Figure 2.19: Pair correlation function $g(r)$ analysis of an Au-PNIPAM particle monolayer. a) AFM image of the monolayer. The coloured rings illustrate the nearest neighbours (red), second-order (blue and green) and third-order (purple and orange) particle neighbours with respect to the central particle. b) Computed function $g(r)$ of the monolayer. The ticks in the same colour code as in a) highlight corresponding neighbour distances.

shows a representative cutout of an AFM image of Au-PNIPAM particles containing a central particle with its six neighbours. d_i determines the centre-to-centre interparticle distance of two neighbours and α_j defines the angle of a triangle corner. R_{cut} is the radius surrounding the central particle, including nearest neighbours and is set to the minimum between the first and the second maximum of the radial distribution function. The parameter is needed as a termination criteria for the calculation of the triangles. The next step is calculating all distances and angles between the particles and, therefore, defining the set of triangles around each particle.

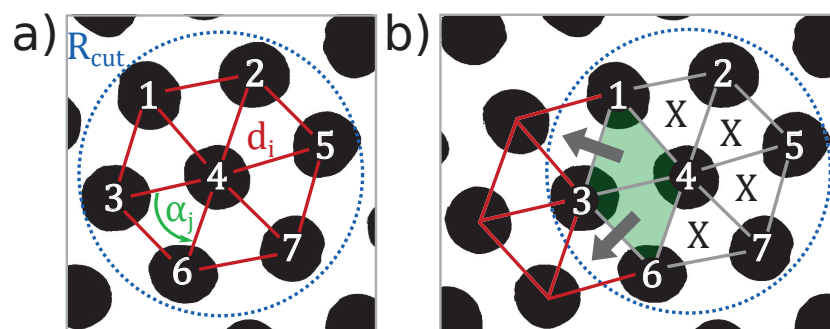


Figure 2.20: Schematic illustration of domain size analysis. a) AFM height profile image of nanoparticles with defined parameters interparticle distance d_i (red), interparticle angle α_j (green) and the cutoff radius R_{cut} (blue). b) Evolution of the spreading algorithm. Triangles highlighted in green fulfil the tolerance criteria, and triangles marked with 'X' are not accepted. The grey arrows show the spreading direction. Adapted from reference¹⁷⁷.

For evaluation of the lattice order degree, deviations from the perfectly ordered lattices must be calculated – more precisely, the standard deviations of the triangle lengths and angles as reported by Mátéfi-Tempfi *et al.*¹⁷⁸. The mean values of distances and angles are given by equations 2.61 and 2.62.

$$d_{\text{mean}} = \frac{d_{i1} + d_{i2} + d_{i3}}{3} \quad (2.61)$$

$$\alpha_{\text{mean}} = \frac{\alpha_{j1} + \alpha_{j2} + \alpha_{j3}}{3} \quad (2.62)$$

The standard deviation Dev_{d_i} of the mean distance and standard deviation Dev_{α_j} of the equilateral triangle angle in percent are quantified by equations 2.63 and 2.64.

$$Dev_{d_i}(\%) = 100 \times \frac{\sqrt{\frac{(d_{\text{mean}} - d_{i1})^2 + (d_{\text{mean}} - d_{i2})^2 + (d_{\text{mean}} - d_{i3})^2}{3}}}{d_{\text{mean}}} \quad (2.63)$$

$$Dev_{\alpha_j}(\%) = 100 \times \frac{\sqrt{\frac{(\alpha_{\text{mean}} - \alpha_{j1})^2 + (\alpha_{\text{mean}} - \alpha_{j2})^2 + (\alpha_{\text{mean}} - \alpha_{j3})^2}{3}}}{\alpha_{\text{mean}}} \quad (2.64)$$

Lower standard deviations for the triangle length and angle indicate a more precise hexagonal order of the particles. Tolerances Tol_d and Tol_α for the maximum allowable standard deviation can be used to control which triangles are considered to be "valid", *i.e.* part of an ordered lattice. Lower tolerances enforce strict ordering, whereas higher tolerances allow for more disorder. Given a fixed set of tolerances, Hillebrand *et al.* applied a flood-filling algorithm to find connected domains. The algorithm starts at a valid triangle and recursively adds all valid triangles to the domain, where each newly added triangle shared an edge with the existing domain (see Figure 2.20 b)). Moreover, these parameters help to identify boundaries between ordered areas, *i.e.* lattice domains.

The ordered areas are characterized by standard deviations Dev_{d_i} and Dev_{α_j} which are equal or smaller than set tolerance parameters. In other words, the considered triangles fulfil the quality criteria. It follows that triangles with larger deviations that do not fulfil the requirements are excluded from the domain.

$$Dev_{d_i} \leq Tol_d \quad \text{and} \quad Dev_{\alpha_j} \leq Tol_\alpha \quad (2.65)$$

$$Dev_{d_i} > Tol_d \quad \text{and} \quad Dev_{\alpha_j} > Tol_\alpha \quad (2.66)$$

Figure 2.20 b) shows schematically the evolution of the spreading algorithm used by Hillebrand *et al.*¹⁷⁷. The triangles of the central particle and its nearest neighbours are classified as those that fulfil the tolerance conditions (highlighted in green) and those that failed the criteria (marked with 'X'). The grey arrays illustrate the spreading direction of the algorithm. Triangles that will be evaluated next are coloured in red. Particles of accepted triangles are added to a valid domain.

The tolerance criteria have to be chosen reasonably and individually for each image. Choosing tolerances that are too low will yield many small domains, whereas tolerances that are too high simply return one large domain.

The number of particles N_{particle} belonging to accepted triangles defines the domain size and the smallest valid domain contains seven particles. The size, as well as the number of the domains, strongly depend on the analysed figure. For this approach to work using reasonable tolerances, the original image has to be of sufficient resolution and clarity. Otherwise, the particle centers cannot be determined precisely, thus requiring large tolerances for a usable result. Particle centers of highly resolved $10 \times 10 \mu\text{m}^2$ AFM images can be easily detected, but due to the small analysed lattice area incomplete domains may occur. In comparison, DFM images with lower resolution are challenging for the analysis and may result in a higher degree of disorder. In this work, an in-house algorithm adapted from Hillebrand *et al.*¹⁷⁷ was used for microstructure analysis from AFM and DFM images of Au-PNIPAM lattices.

3 Synopsis

3.1 Overview of the Thesis

This thesis deals with the optical properties and thermoresponsive behaviour of core-shell microgels. Chapter 4 introduces Au-PNIPAM microgels and their characterization using various methods, including the scattering approaches (DLS, SLS, SAXS and SANS), UV-Vis spectroscopy and theoretical calculations. The results linked the microgel morphology to the absorbance spectra during the volume phase transition. In chapter 5 the microgels were modified by increasing the size of the gold core within the polymer shell. The modified microgels were used as building blocks for 2D arrays by applying interface-mediated self-assembly. AFM and DFM characterized the order of the particle arrays and the optical properties were obtained from UV-Vis spectroscopy. The impact of several parameters, *i.e.* interparticle distances, structural disorder and refractive index, on the SLR, was studied. Chapter 6 addresses the collapse dynamics of the microgels presented in chapter 4. Here, the capacitor-discharge temperature-jump spectroscopy was used to monitor optical changes during the collapsing process of the microgels. This work contributes to a deeper understanding of the collapse mechanism.

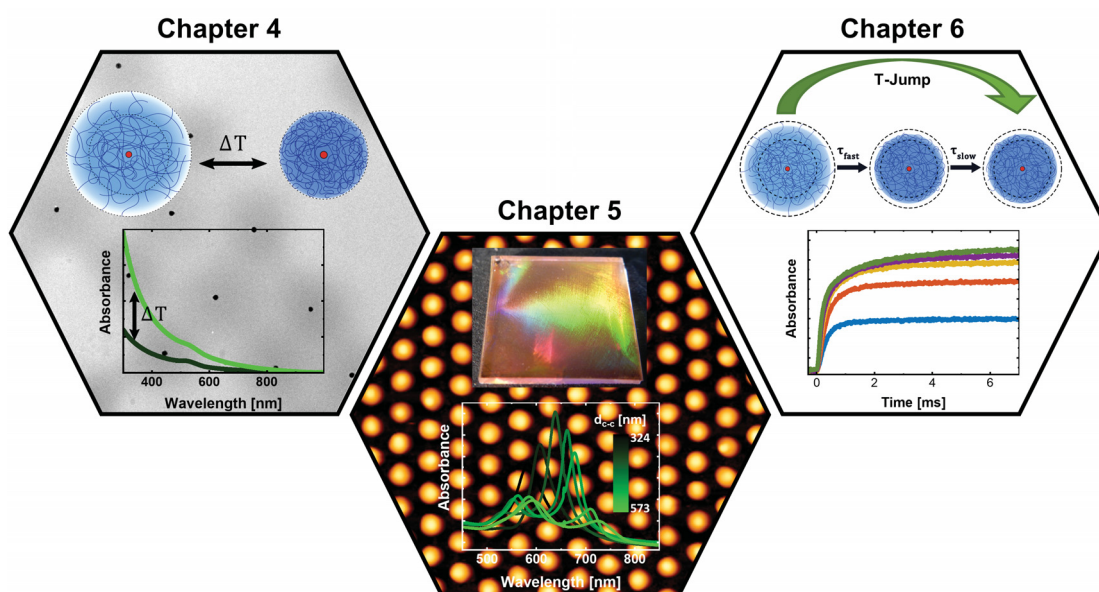


Figure 3.1: Graphical table of content of the publications.

3.1.1 The Fuzzy Sphere Morphology is Responsible for the Increase in Light Scattering During the Shrinkage of Thermoresponsive Microgels

The work introduces PNIPAM microgels carrying a small core with a diameter of approximately 15 nm with various polymer shell thicknesses and polymer densities. The key question was how the microgel morphology affects the scattering behaviour during the volume phase transition. Chapter 4 presents a combination of several methods to characterize the various core-shell microgels at different states of collapse. Furthermore, it shows that the Rayleigh-Debye-Gans (RDG) approximation cannot reproduce the experimental observations, although all used microgels fulfil the RDG criteria. This study is the first part of cooperation work with Paul Mulvaney and Ben Tadgell, which was made possible through the financial support from the German Academic Exchange Service (DAAD) through its thematic Network Melbourne-Bayreuth Polymer/Colloid Network.

The core-shell microgels were synthesized using seeded precipitation polymerization with PNIPAM as monomer and BIS as cross-linker comonomer. The incorporation of gold cores allowed precise control over the shell thickness and, due to its high X-ray contrast, acted as a marker for SAXS measurements to obtain the number density in the dispersions, which is crucial for the analysis of the small-angle neutron scattering (SANS) data. The scattering technique is a powerful tool to elucidate microgel structure down to the nanometer scale⁸⁷. In summary, the SANS data from four different states of the collapse of microgels revealed a fuzzy-sphere morphology in the fully swollen state for all investigated microgel types. Moreover, microgels with less cross-linking showed higher fuzziness and softness. The fuzzy shell collapsed on the inner homogeneous core with increasing temperature, resulting in higher polymer densities. In a fully collapsed state, all microgels had a hard sphere-like structure with an average of 60 % solvent inside. Furthermore, the study demonstrated that absorbance measurements are related to light scattering. Therefore, matching the findings of microgel structure from SANS and absorbance results open the opportunity to derive microgel size and its temperature-induced changes by simple UV-Vis spectroscopy.

The found microgel structure can be taken into account to calculate theoretical scattering behaviour by using FDTD simulations. However, although a fuzzy-sphere structure in the swollen state and a hard-sphere-like structure in the collapsed state were clearly obtained from SANS, the calculated spectra showed significantly lower scattering intensities. Thus, this study aims to stimulate further research on microgel optical properties.

3.1.2 Surface Lattice Resonances in Self-Assembled Gold Nanoparticle Arrays: Impact of Lattice Period, Structural Disorder, and Refractive Index on Resonance Quality

The focus of this study lies on the plasmonic properties of the gold cores inside the PNIPAM shell. Three batches of Au-PNIPAM particles were chosen for the investigations with similar polymer densities but different microgel sizes. Here, the role of the polymer shell is twofold: i) stabilization of the gold cores and ii) acting as a spacer in the 2D

particle arrays. Since the scattering contribution of the shell dominated the absorption of 15 nm gold cores, their size was increased to approximately 100 nm for the three batches. The Au-PNIPAM particles with significantly larger gold cores were then used as building blocks for ordered particle arrays. The central point of this study was the characterization of the fabricated particle arrays and the identification of various coupling phenomena.

The periodic particle arrays with a broad range of interparticle distances were obtained via interface-mediated self-assembly. The distance control was realized by i) using different polymer shell thicknesses and ii) using sequential transfer from floating particle lattices at the air/water interface. The distances between particles increased by every withdrawal of a sample. The microstructure of particle monolayers was quantitatively investigated by analyzing AFM and DFM images, including the pair correlation functions, fast Fourier transformations and triangulation analysis of the domain sizes¹⁷⁷. Overall, all fabricated particle monolayers showed high homogeneity and hexagonal symmetry on the mm^2 scale. However, structural disorders and multiple domains per sample were observed.

The optical properties of the hexagonal particle arrays in the symmetric and asymmetric environment were studied by UV-Vis spectroscopy and theoretical FDTD simulations. In an asymmetric environment, only weak coupling of long-range radiative of the dipoles was observed. However, by the homogenization of the environment, surface lattice resonances appeared. The strongest diffractive-plasmonic coupling was identified for monolayers where the diffractive modes were spectroscopically close to or slightly redshifted to the LSPR mode of a single gold particle. Moreover, it was found that the deviation of SLRs quality of the sample with the strongest coupling and respective theoretical infinite perfect lattice was relatively small.

3.1.3 Temperature-Jump Spectroscopy of Gold-Poly(N-isopropylacrylamide) Core-Shell Microgels

This study is also the result of the cooperation with Paul Mulvaney and Ben Tadgell at the University of Melbourne. Here we investigated the collapse dynamics of core-shell microgels presented in chapter 4. For the investigations, capacitor-discharge temperature-jump spectroscopy was used. In this technique, the microgel dispersion containing an electrolyte is heated up via induced electrical discharge and the VPT of the microgels is monitored via absorbance measurements over time. The interpretation of the kinetic data and proposed collapse mechanism was made in agreement with the findings from SANS experiments (chapter 4). The work is interesting twofold: i) the presented technique is barely used in colloid chemistry, ii) the volume change kinetics of microgels have been little studied and the collapse mechanism is not fully understood. Moreover, a theory treating swelling/deswelling of fuzzy-sphere microgels is still missing.

In summary, the work proposed a two-step collapse of the microgels where each step corresponded to a fast and slow lifetime, respectively. The first step corresponds to a fast collapse of the fuzzy shell followed by slow rearrangement and relaxation of the polymer chains. While the fast lifetime scaled linearly with radius changes, the slow lifetime was almost constant for all types of microgels.

3.2 Contributions to Joint Publications

The results presented in following chapters are from peer-reviewed joint publications. The contributions of all involved authors are listed below.

Chapter 4: The Fuzzy Sphere Morphology is Responsible for the Increase in Light Scattering During the Shrinkage of Thermoresponsive Microgels

The chapter is reprinted and adapted from *Soft Matter*, **2022**, *18*, 807-825

Ekaterina Ponomareva, Ben Tadgell, Marco Hildebrandt, Marcel Krüsmann, Sylvain Prévost, Paul Mulvaney, and Matthias Karg

I synthesized the Au-PNIPAM microgels with different sizes and cross-linker densities and evaluated the encapsulation success of gold cores into the shell from TEM images. The TEM measurements were performed by Heyou Zhang in the Melbourne Advanced Microscopy Facility. I carried out the temperature dependent absorbance measurements, refractive index measurements and finite difference time domain simulations. Ben Tadgell determined the hydrodynamic radii of all microgels. Marco Hildebrandt performed and analysed the SAXS measurements and Marcel Krüsmann carried out the SLS experiments. The SANS measurements were performed at the ILL using the D11 instrument by Sylvain Prévost and Matthias Karg. I analysed the obtained SANS data under the supervision of Matthias Karg and help of Sylvain Prévost and extracted the polymer volume fractions in dependence on the radius and the temperature. Moreover, I calculated the polymer volume densities from refractive index measurements and compared the results of both methods. I designed and prepared all figures and wrote the first version of the manuscript. Ben Tadgell, Paul Mulvaney and Sylvain Prévost contributed with helpful discussions. Matthias Karg coordinated the project and contributed to designing of the experiments and writing of the manuscript. All authors proofread the manuscript.

Chapter 5: Surface Lattice Resonances in Self-Assembled Gold Nanoparticle Arrays: Impact of Lattice Period, Structural Disorder, and Refractive Index on Resonance Quality

The chapter is reprinted and adapted from *Langmuir*, **2020**, *36*, 13601-1312

Ekaterina Ponomareva, Kirsten Volk, Paul Mulvaney, and Matthias Karg

I synthesized the Au-PNIPAM microgels and prepared the hexagonally ordered particle arrays via the self-assembly method. Moreover, I performed the absorbance, AFM, and DFM measurements. Kirsten Volk designed the FDTD simulation layout and supervised me with further simulations. I characterized the properties of single particles, the microstructure of prepared monolayers and analyzed the theoretically obtained data. Kirsten Volk and Paul Mulvaney contributed with helpful discussions. I designed and

prepared all figures and the animated movie of the self-assembly process, and wrote the first version of the manuscript. Matthias Karg coordinated the project and contributed to designing of the experiments and writing of the manuscript. All authors proofread the manuscript.

Chapter 6: Temperature-Jump Spectroscopy of Gold-Poly(*N*-isopropylacrylamide) Core-Shell Microgels

The chapter is reprinted and adapted from *The Journal of Physical Chemistry C*, **2022**, *126*, (8), 4118-4131

Ben Tadgell, Ekaterina Ponomareva, Matthias Karg, and Paul Mulvaney

Ben Tadgell built the capacitor-discharge temperature-jump spectroscopy set-up for microgels and performed all the T-jump measurements. Furthermore, he analyzed the data and extracted lifetimes for the collapse of the microgels depending on various parameters, *i.e.* microgel size and density, and magnitude of the temperature jump. I synthesized the Au-PNIPAM microgels and carried out the wavelength resolved absorbance spectra, while Ben Tadgell measured UV-Vis spectra at the selected wavelength of 450 nm. Moreover, Ben Tadgell performed the DLS and Zeta potential measurements. All authors had regular meetings with fruitful discussions about the data interpretation. Ben Tadgell wrote the first version of the manuscript and prepared the figures. Paul Mulvaney coordinated the project. All authors proofread the manuscript.

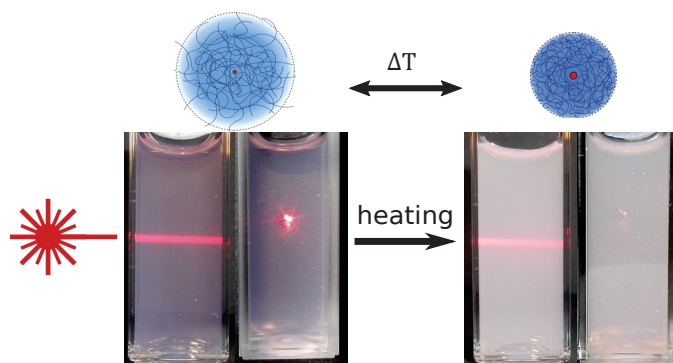
4 The Fuzzy Sphere Morphology is Responsible for the Increase in Light Scattering During the Shrinkage of Thermoresponsive Microgels

Ekaterina Ponomareva¹, Ben Tadgell², Marco Hildebrandt¹, Marcel Krüsmann¹, Sylvain Prévost³ Paul Mulvaney², and Matthias Karg^{1*}

¹Institut für Physikalische Chemie I: Kolloide und Nanooptik, Heinrich-Heine-Universität Düsseldorf, Universitätsstraße 1, D-40225 Düsseldorf, Germany

²ARC Centre of Excellence in Exciton Science, School of Chemistry, The University of Melbourne, Parkville, VIC 3010, Australia

³Large Scale Structures, Institut Laue-Langevin, 71 avenue des Martyrs, CS 20156, 38042 Grenoble Cedex 9, France



Reproduced from Ref. *Soft Matter* **2022**, *18*, 807-825 with permission from the Royal Society of Chemistry

4.1 Abstract

Thermoresponsive microgels undergo a volume phase transition from a swollen state under good solvent conditions to a collapsed state under poor solvent conditions. The most prominent examples of such responsive systems are based on poly-(*N*-isopropylacrylamide). When cross-linked with *N,N'*-methylenebisacrylamide, such microgels typically possess a fuzzy-spherelike morphology with a higher cross-linked core and a loosely cross-linked fuzzy shell. Despite the efforts devoted to understanding the internal structure of microgels and their kinetics during collapse/swelling, the origin of the accompanying changes in light scattering intensity have barely been addressed. In this work, we study core-shell microgels that contain small gold nanoparticle cores with microgel shells of different thicknesses and cross-linker densities. All microgels are small enough to fulfill the Rayleigh-Debye-Gans criterion at all stages of swelling. Due to the high X-ray contrast of the gold cores, we can use absolute intensity small-angle X-ray scattering to determine the number density in the dilute dispersions. This allows us to extract polymer volume fractions of the microgels at different stages of swelling from form factor analysis of small-angle neutron scattering data. We match our findings to results from temperature-dependent absorbance measurements. The increase in absorbance during the shrinkage of the microgels is related to the transition from fuzzy spheres to hard sphere-like scattering objects with a rather homogeneous density profile. We provide a first attempt to model experimental spectra using finite difference time domain simulations that take into account the structural changes during the volume phase transition. Our findings significantly contribute to the understanding of the optical properties of thermoresponsive microgels. Further, we provide polymer volume fractions and microgel refractive indices as a function of the swelling state.

4.2 Introduction

Microgels are soft polymeric objects with dimensions in the colloidal regime and an internal gel-like structure.² The properties of microgels lie between those of colloids, surfactants and macromolecules.¹⁷⁹ Under good solvent conditions, microgels can be swollen by enormous amounts of solvent rendering them soft and deformable.^{180,181,182,183,184,185} Responsive, or so-called ‘smart’, microgels are composed of polymers that respond to external stimuli such as temperature, pH, ionic strength and light. This response manifests itself as a significant reduction in the microgel volume in response to the stimulus, due to the release of solvent from the microgel interior. The most prominent examples are poly-(*N*-isopropylacrylamide) (PNIPAM) microgels. These gels feature a volume phase transition (VPT) in water with a transition temperature (VPTT) close to human body temperature. This VPT behavior is related to the lower critical solution temperature (LCST) behavior of linear PNIPAM homopolymers with a transition temperature, T_{LCST} , of approximately 32 °C.⁷ PNIPAM microgels were first introduced by Pelton and Chibante who used free radical polymerization for the microgel preparation.⁶ Due to faster consumption of the chemical cross-linker *N,N'*-methylenebisacrylamide (BIS)

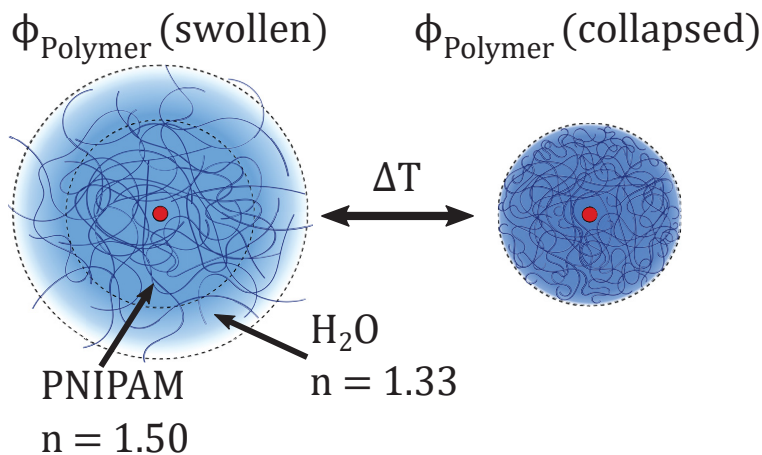
during the precipitation polymerization of NIPAM, PNIPAM microgels possess an inhomogeneous polymer density.⁵⁵ The swollen state microgel structure can be considered as core-shell-like with a denser, more highly cross-linked core and a less highly cross-linked outer shell.^{53,54} Above the VPTT, collapsed microgels can be considered as hard sphere-like with a homogeneous polymer density. This structural transition has been the topic of countless studies. Small-angle neutron scattering is one of the most frequently used methods for the investigation of the microgel form factor. Stieger *et al.* introduced a radial density profile model that describes the form factor of microgels in the swollen as well as in the collapsed state.⁴⁰ This fuzzy sphere model assumes an inner microgel core of homogeneous polymer content and an outer fuzzy shell with a continuously decaying polymer content. The model is well accepted and has been applied to many different microgel systems. Due to the fascinating development of superresolution optical microscopy techniques, the inhomogeneous network structure has also been confirmed by real-space imaging.^{56,186,187} Nowadays, computational numerical methods are powerful tools for describing microgels and their internal structure.^{188,189} While atomistic simulations are suitable for small systems, monomer-resolved models allow for simulations at longer times and larger length-scales.

The swelling behavior of thermoresponsive microgels is often described by the Flory-Rehner theory.^{42,190} While the evolution of the hydrodynamic particle size can be precisely measured by dynamic light scattering (DLS), the Flory-Rehner theory also requires the polymer volume fraction at a specified reference state. Several studies use volume fractions of collapsed microgels as the reference state where variations in cross-linking density appear rather negligible.^{40,58,68,191,192} Nevertheless, reference volume fractions used in literature vary significantly and are often estimated from different experiments.^{40,54,58,67,68,191,192,193,194}

Surprisingly, little attention has been paid to how the UV-visible spectroscopic properties of PNIPAM microgels depend on their state of swelling and thus polymer volume fraction. *A priori*, one would expect a decrease in light scattering intensity and thus absorbance when microgels collapse. The Rayleigh-Debye-Gans (RDG) approximation, which holds for particles that have a low refractive index contrast and dimensions smaller than the wavelength of visible light, would predict that the scattering intensity increases with the sixth power of the radius of scattering objects (R^6). However, absorbance is in fact observed to increase when microgels collapse in response to external stimuli as, for example, temperature. This is commonly attributed to the increase in microgel refractive index due to the release of water and the resulting increase in polymer volume fraction.^{10,11,195,196,197} Any increase in refractive index can be monitored optically by using gold nanoparticles as plasmonic probes. Since the localized surface plasmon resonance (LSPR) of gold nanoparticles is sensitive to the effective refractive index environment in the close vicinity of the nanoparticle surface, even small changes can be monitored as predicted theoretically¹⁹⁸ and demonstrated in experiments using gold-PNIPAM hybrid microgels.^{8,10,199,200,201} In order to use the LSPR to monitor structural transitions in thermoresponsive microgels one has to keep in mind that the intensity of light scattered by the microgels also changes during the VPT. Since this scattering is wavelength dependent, LSPR positions extracted directly from UV-Vis spectra are often

not correct due to the visible background scattering. As the wavelength scaling of the microgel scattering changes during microgel collapse, the LSPR is also affected. This can be accounted for by subtraction of the scattering contribution from measured spectra as described in detail in the Supporting Information of the paper by Rauh *et al.*²⁰² When scattering dominates the spectral response of gold-microgel hybrid particles, either due to small dimensions of the gold particles or very large microgel sizes, the extraction of LSPR positions from experimental spectra becomes highly defective or simply impossible.

In this work, we study the VPT behavior of core-shell (CS) microgels that feature small gold nanoparticle cores and thermoresponsive PNIPAM microgel shells. The general structure of these microgels is depicted in Scheme 4.1. Importantly the gold cores are too small to significantly influence the swelling behavior of the PNIPAM microgels. Thus, physically our CS microgels can be considered comparable to classical PNIPAM microgels that do not feature inorganic cores. We systematically study the influence of the microgel size and cross-linking density on the polymer volume fraction during different stages of swelling.



Schema 4.1: Schematic representation of an Au-PNIPAM CS microgel in the swollen (left) and collapsed state (right). The red circles represent the gold core. The solid blue lines represent the polymer chains. The volume fraction of PNIPAM polymer in the microgel shells increases as the microgels collapse leading to release of water from the PNIPAM network.

The CS microgels are colloidally stable in water below and above the VPTT. We used absolute intensity small-angle X-ray scattering (SAXS) to determine the particle number concentration using the large contrast in X-ray scattering of the otherwise negligible gold cores. Using form factor analysis of SANS data, we determined the polymer density profiles for different states of swelling from which we could derive refractive index profiles. Effective volume averaged refractive indices of the microgels were also determined by refractometry. Given the microgel size and the average refractive index, all studied microgels fulfill the RDG criterion, even in the collapsed state. This is different to other studies in literature where larger microgels were employed and a transition from RDG

scattering in the swollen state to Mie scattering in the collapsed state was observed.¹¹ We followed the VPT by simple absorbance measurements using temperature-dependent UV-Vis spectroscopy. The observed increase in absorbance, *i.e.* sample turbidity, as the microgels collapse could not be described by RDG theory using effective, averaged microgel refractive indices. A core-shell model was used to calculate theoretical scattering cross-sections on the basis of finite difference time domain (FDTD) simulations. With our work, we attempt to link the microgel morphology and structural transitions during the VPT to the visible wavelength absorbance of dilute microgel dispersions. A general light scattering theory that allows one to precisely account for the microgel structure is currently not available.

4.3 Experimental Section

4.3.1 Chemicals

Gold(III) chloride trihydrate (HAuCl_4 ; Sigma-Aldrich, $\geq 99.999\%$), sodium citrate dihydrate (Sigma-Aldrich, $\geq 99\%$), sodium dodecyl sulfate (SDS; Sigma-Aldrich, p.a.), butenylamine hydrochloride (BA; Sigma-Aldrich, 97%), *N*-isopropylacrylamide (NIPAM; TCI, $> 98.0\%$), *N,N'*-methylenebisacrylamide (BIS; Sigma-Aldrich, $\geq 99\%$), potassium peroxydisulfate (PPS; Sigma-Aldrich, $\geq 99\%$), heavy water (D_2O ; Deutero GmbH 99.9%) and 1,4-dioxane (p.a., Fisher Chemicals) were used as received. Water was purified with a MilliQ system (Millipore). The final resistivity of water was 18 $\text{M}\Omega\text{cm}$. MilliQ-water was used for all syntheses and purifications.

4.3.2 Synthesis

Au Nanoparticle Cores

Spherical gold nanoparticles were synthesized according to the reported protocol by Turkevich *et al.*⁴⁶ Briefly, 10 mL of a hot, aqueous sodium citrate dihydrate solution (1 wt %) were added to 200 mL of an aqueous gold(III)-chloride trihydrate solution ($c = 5 \times 10^{-4}$ M) under continuous stirring and boiling. Boiling was continued for approximately 20 minutes. Afterwards, the gold nanoparticle dispersion was allowed to cool down to room temperature. Then, 1.2 mL of 1 mM SDS aqueous solution were added to the dispersion to stabilize the particles. After another 20 minutes, the gold particles were functionalized by adding 0.652 mL butenylamine hydrochloride solution ($c = 1.4$ M).⁸ The functionalized particles were purified and concentrated by centrifugation for 14 hours at 1400g relative centrifugal force (rcf). In total, three batches of gold nanoparticles with mean diameters of 15.3 ± 1.3 nm, 15.3 ± 1.5 nm, and 15.3 ± 1.8 nm as obtained from TEM measurements were synthesized. Due to the similarity in size and polydispersity (on average 10 %), we will not distinguish between the different batches.

Au-PNIPAM Core-Shell Microgels

The functionalized gold nanoparticles were encapsulated by hydrogel shells using seeded precipitation polymerization with NIPAM as monomer and BIS as cross-linking comonomer. The general procedure was adapted from Rauh *et al.*¹² The AuNPs act as nucleation centers for the precipitating polymer during the polymerization. Therefore, changes in the monomer feed concentration can be used to tailor the microgel size within a certain range.⁸ We synthesized five core-shell microgels with different shell thicknesses and cross-linking densities by changing the respective monomer and comonomer feeds. The synthesis details for all samples are summarized in Table 1. Briefly, all polymerizations were carried out in 100 mL *MilliQ* water in three-neck round-bottom flasks. First, NIPAM and BIS were dissolved in water while stirring. Then the solution was heated up to 70 °C while degassing with nitrogen. Afterwards, 3.72 mL aqueous dispersion with functionalized gold nanoparticles were added dropwise to the colorless solution. The added volume of the AuNP stock dispersion corresponds to an elemental gold (Au⁰) concentration of 0.00622 mol L⁻¹ in all syntheses. After an equilibration time of 15 minutes, 2 mg of PPS dissolved in 1 mL of water were added to the mixture to initiate the polymerization. The polymerization was carried out for two hours. After cooling the obtained microgel dispersion to room temperature, purification was performed by centrifugation (90 minutes at 8400g rcf) and redispersion in water. Centrifugation/redispersion was repeated three times in total for each batch. The particles are labelled as CS1-5 in this work. CS1 to CS3 vary in shell thickness while having similar cross-linking densities. CS4 and CS5 possess similar collapsed state sizes to CS2 but have lower and higher cross-linker densities respectively.

Table 1: Masses of the monomer NIPAM and cross-linker BIS used for the synthesis of Au-PNIPAM particles, the nominal molar ratio of cross-linker and measured hydrodynamic radii (R_h) in the swollen (25 °C) and collapsed (50 °C) state, and corresponding polydispersity indices (PDI) in brackets.

| Sample | NIPAM m (g) | BIS m (g) | nominal molar ratio of cross-linker ¹ | R_h swollen (nm) | R_h collapsed (nm) |
|--------|----------------|--------------|---|-----------------------|-------------------------|
| CS1 | 0.228 | 0.048 | 15.3 mol% | 111 (0.03) | 78 (0.04) |
| CS2 | 0.587 | 0.134 | 16.7 mol% | 164 (0.02) | 118 (0.02) |
| CS3 | 0.946 | 0.194 | 14.8 mol% | 190 (0.03) | 139 (0.01) |
| CS4 | 0.587 | 0.040 | 5.0 mol% | 186 (0.04) | 104 (0.02) |
| CS5 | 0.587 | 0.200 | 24.9 mol% | 157 (0.03) | 124 (0.02) |

¹ The nominal molar cross-linker ratio values are the ones used in the synthesis and not the ratios in the final microgel polymer network.

4.3.3 Methods

Transmission Electron Microscopy (TEM)

A Tecnai F20 (FEI) TEM was used to determine the size and size dispersity of the metal core and to evaluate the encapsulation success. The measurements were performed at an acceleration voltage of 200 kV. For each sample 7 μL of the Au-PNIPAM particle dispersion was dried on carbon-coated, 300 mesh copper grids (Electron Microscopy Sciences). Various TEM images were used for the determination of the gold core size and 200 particles were measured by the ImageJ software¹⁷¹. Moreover, we used the TEM images to evaluate the encapsulation success of the cores in the PNIPAM shells.

UV-Vis Spectroscopy

Absorbance spectra were measured with a Specord S 600 spectrometer equipped with a temperature-controlled sample changer (Analytik Jena AG). Measurements were performed in the wavelength range of 300 – 1019 nm in transmission geometry over the temperature range between 10 and 60 °C. Afterwards, the detected light was converted into absorbance values. The dilute, aqueous particle dispersions (0.02 wt%) were measured in $1 \times 1 \text{ cm}^2$ PMMA cuvettes. A cuvette with water was used for the background correction for all extinction spectra.

Dynamic Light Scattering (DLS)

Hydrodynamic radii, R_h were determined by DLS using a Zetasizer NanoS90 (Malvern Panalytical). The device was equipped with a HeNe laser as the light source with a wavelength of 632.8 nm and a temperature-controlled jacket for the cuvette. The measurements were performed with a scattering angle of 90° in the temperature range between 25 and 50 °C in steps of 1 °C. Samples were allowed to equilibrate for 10 minutes at each temperature step before at least three measurements with an acquisition time of 60 s were performed. Swelling curves, *i.e.* the temperature evolution of the hydrodynamic radii (z-average), were fitted using sigmoidal functions (Boltzmann). Due to some scatter of the measured data, in particular in the swollen state, the hydrodynamic radii for the swollen and collapsed state at temperatures of 25 °C and 50 °C were obtained from the sigmoidal fits. Further details and measured swelling curves are provided in the Supporting Information. The obtained swollen and collapsed state radii are reported in Table 1.

Static Light Scattering (SLS)

SLS measurements were performed with a 3D LS spectrometer (LS Instruments) with a constant scattering angle of 90°. The measurements were repeated three times with an acquisition time of 15 s. The light source was a HeNe laser with a wavelength of 632.8 nm. Two avalanche photodiodes in pseudo-cross-correlation mode were used as detectors. The samples were measured in cylindrical quartz glass cuvettes with an outside diameter of 10 mm (Hellma Germany) in a heat-controlled decalin bath equipped with a

Julabo CF31 circulating water bath in the temperature range between 20 and 55 °C. The temperature was monitored by a Pt100 thermoelement. Before each measurement, the system was allowed to equilibrate for 900 s at each temperature step. SLS measurements were performed to confirm that the obtained absorbances from UV-Vis spectroscopy can be used as a direct measure for the light scattering intensity of the microgels.

Small-Angle X-Ray Scattering (SAXS)

The particle concentration of the Au-PNIPAM microgels was obtained by SAXS measurements using the Xeuss 2.0 device (Xenocs) at a sample to detector distance of 1.2 m. The beam wavelength was 0.154 nm (Cu K-Alpha). The scattering data was collected using a PILATUS3 300K detector (DECTRIS) with pixel size of $172 \times 172 \mu\text{m}^2$. Particle aqueous dispersions (1 – 5 wt%) were filled into 1 mm round capillaries delivered from WJM Glas, and the exposure time for each measurement was 3600 s. For all measurements, Milli-Q water was used for the background correction.

Small-Angle Neutron Scattering (SANS)

SANS measurements (DOI:10.5291/ILL-DATA.EASY-632) were performed at the Institut Laue-Langevin (ILL) in Grenoble (France) using the D11 instrument. The neutron wavelength was 0.46 nm for the sample-to-detector distances of 1.4, 8 and 39 m and 10 nm for 39 m. The signals were collected using the ^3He gas detector (CERCA) with an area of $96 \times 96 \text{ cm}^2$ and a pixel size of $3.75 \times 3.75 \text{ mm}^2$. To cover a broad q range, the data for the dilute samples in D_2O (0.5 wt%) were collected at sample-to-detector distances of 1.4, 8 and 39 m with acquisition times of 300, 600, and 1200 s, respectively. The SANS measurements of all CS microgels were performed at four different temperatures of 25, 35, 37 and 50 °C. However, due to limited beamtime, we could not record data at low q values at 37 °C. The dilute dispersions were measured in cylindrical quartz glass cells (Hellma Germany, light path 1 mm). The collected data was corrected for D_2O and empty cell scattering. Scattering data were radially averaged and normalized to absolute intensities using standard routines of the ILL (Lamp). The data reduction considered the sample transmission, sample thickness, detector noise (*via* a $^{10}\text{B}_4\text{C}$ absorber), flat field (from measurement of H_2O) and empty cell subtraction, providing data in absolute scale using water as a secondary standard. Instrument resolution accounts for the resolution in q based on the experimental direct beam width, wavelength spread ($\Delta\lambda/\lambda = 9\%$ (FWHM)) and detector pixel size. The recorded spectra at different sample-to-detector distances were merged and analyzed by SASfit software by Kohlbrecher²⁰³.

Refractive Index Measurements

Refractive indices of particle dispersions were recorded with an Abbemat-WR/MW refractometer (Anton Paar). The measurements were performed at the wavelength of 589.3 nm at 25 and 50 °C. The concentrations of the particles were kept the same as for the SAXS measurements. 500 μL of highly concentrated PNIPAM solution (1,4-dioxane)

were left to dry in the air in the measuring unit until a constant value was reached to obtain the pure linear PNIPAM film refractive index.

FDTD Simulations

Theoretical extinction spectra were calculated using finite difference time domain (FDTD) simulations employing commercial software from Lumerical Solutions, Inc. (FDTD Solutions, Version 8.18.1332). Absorption and scattering spectra were simulated in a box in x, y and z-direction with perfectly matched layer (PML) boundary conditions. We used a Total-Field Scattered-Field (TFSF) source and a box of power monitors consisting of the total field and scattered field monitors. The auto shut-off was set at 10^{-8} before reaching 1000 fs simulation time. Gold core sizes were simulated with a radius of 6 nm with a mesh of 0.25 nm. The radius is slightly smaller than obtained from TEM (7.7 nm) and SAXS (6.8 and 6.5 nm) measurements. The wavelength-dependent refractive index of the gold core was taken from literature¹³⁴. For the overall particle, we used mesh grading with a grading factor of 1.1. Water with $n = 1.332$ was used as the surrounding medium. Experimentally determined refractive indices and radii were used for the CS microgels.

4.4 Theory

4.4.1 LCST and Cloud Point of PNIPAM

In aqueous dispersion, PNIPAM features a miscibility gap above the LCST at T_{LCST} . When heated to $T > T_{LCST}$, the PNIPAM chains demix due to a drastically reduced solubility. For PNIPAM and LCST polymers in general, this demixing behavior is typically followed by turbidity measurements yielding the cloud point temperature T_{cp} . Below T_{cp} the polymer chains are in a soluble state. At T_{cp} the phase transition occurs and the polymer solution becomes turbid due to the formation of collapsed aggregates. This clouding of the solution is typically easy to monitor by a steep increase in turbidity. However, it is highly recommended to follow standard protocols for such measurements as reported values of T_{cp} can strongly differ due to differences in polymer concentration, wavelength, heating rate *etc.*²⁰⁴ Furthermore, it is important to note that T_{cp} and the LCST are typically not the same. The LCST corresponds to the temperature at the minimum of the binodal for which the concentration is equal to the lower critical solution concentration (LCSC).^{204,205} Thus, concentration dependent measurements are required if the LCST is to be determined. Often ignored is also that chain ends, *e.g.* from a chain transfer agent used in RAFT polymerization, can significantly alter the phase transition of a thermoresponsive polymer and affect T_{cp} , in particular for those with a low molecular weight. The molecular weight distribution is another factor crucial to the demixing as longer chains tend to precipitate first.²⁰⁵

The LCST behavior of PNIPAM in water is responsible for the volume phase transition observed for PNIPAM microgels.

4.4.2 Light Scattering and Turbidity of PNIPAM Microgels

In this work we study the optical response of dilute aqueous dispersions of thermoresponsive microgels composed of PNIPAM cross-linked with BIS. Thus, the system is significantly different to linear PNIPAM homopolymer chains in solution: 1) The cross-linker introduces chemical heterogeneities that are distributed inhomogeneously within the microgels. 2) As a consequence of 1), the number of monomer units between two cross-linking points has a large dispersity and increases towards the outer periphery of the microgels. 3) The outer fuzzy corona of the microgels contains uncross-linked dangling ends. 4) The anionic radical initiator used in the synthesis introduces sulfate groups that are deprotonated at neutral and basic pH. As a consequence the microgels are slightly ionic.

Despite these structural and chemical differences, the VPT of PNIPAM microgels is accompanied by similar turbidity changes to those observed for linear PNIPAM homopolymer chains. It is worth distinguishing between the two cases: 1) Non-ionic microgels or ionic microgels at sufficiently high ionic strength will aggregate at temperatures close to the phase transition temperature where steric stabilization is lost. Here, attractive forces dominate and the microgels lose their soft repulsive character.²⁰⁶ The formation of aggregates is accompanied by a steep increase in turbidity similar to the behavior of individual polymer chains discussed before. 2) With given high enough electrostatic stabilization, *i.e.* through charged groups from an ionic radical initiator or chargeable comonomers, repulsive interactions dominate even at temperatures well above the phase transition temperature. In this case, the dispersion remains colloidally stable and shows a continuous increase in turbidity during the VPT from the swollen to the collapsed state.

The second case will be the one relevant to this study. Due to the typical microgel size, aqueous microgel dispersions are turbid even at low concentrations and under good solvent conditions. This turbidity is caused by light scattering due to a refractive index mismatch between microgels and water as dispersing medium. Generally, the light scattering properties of a colloidal dispersion can be described by the RDG theory if the following criteria are fulfilled:²⁰⁷

1) The refractive index of the scattering objects, n_p , is close to the refractive index of the dispersing medium, n_s :

$$|1 - m| \ll 1 \quad (4.1)$$

with

$$m = \frac{n_p}{n_s} \quad (4.2)$$

2) The phase shift is small:

$$kn_s 2R |1 - m| \ll 1 \quad (4.3)$$

Here, $k = 2\pi/\lambda$ is the magnitude of the wave vector \vec{k} with the wavelength λ and R is the radius of the scattering object. Substitution gives:

$$\frac{4\pi n_s R}{\lambda} |1 - m| \ll 1 \quad (4.4)$$

As we will show later, both criteria are well fulfilled for our CS microgels in the swollen state and even in the collapsed state where the refractive index contrast is significantly higher.

The scattering cross-section of an RDG scatterer, C_{sca}^{RDG} is given by:^{207,208}

$$C_{sca}^{RDG} = \frac{24\pi^3 \left(\frac{4}{3}\pi R^3\right)^2}{\lambda^4} \left(\frac{m^2 - 1}{m^2 + 2}\right)^2 \quad (4.5)$$

Thus, at a given wavelength λ , the intensity of RDG scattering depends only on the particle radius and the refractive index contrast. In contrast to simple homogeneous spheres such as polystyrene or silica particles that possess a homogeneous refractive index, PNIPAM microgels are swollen by solvent with a solvent content that depends on the swelling state, *i.e.* the dispersion temperature. It is therefore necessary to consider the volume fractions of polymer (ϕ) and water ($\phi_{water} = 1 - \phi$) inside the microgels to estimate the value of n_p :

$$n_p = \phi \cdot n_{polymer} + (1 - \phi) \cdot n_{water} \quad (4.6)$$

The volume fraction of polymer is given by:

$$\phi = \frac{V_{polymer}}{V_{microgel}} = \frac{V_{polymer}}{\frac{4}{3}\pi R^3} \quad (4.7)$$

Here, $V_{polymer}$ is the total volume of polymer - in our case PNIPAM - inside one microgel and $V_{microgel}$ is the volume of the microgel with radius R . For thermoresponsive microgels, $V_{microgel}$ and thus ϕ depend on temperature. Assuming that $V_{polymer}$ does not change in the temperature window considered in this work, *i.e.* 25 to 50 °C, ϕ scales with R as:

$$\phi(T) \propto R^{-3}(T) \quad (4.8)$$

As ϕ increases when the microgels shrink, n_p also increases (see equation 4.6). This will in turn increase the light scattering. On the other hand, one has to keep in mind that the RDG scattering scales with the sixth power of R , leading to a reduction in scattering when the microgel shrinks, *i.e.* R decreases. We will later on address how each factor influences our CS microgels.

4.4.3 Absorbance Measurements and Scattering Cross-Section

The attenuation of incoming light of intensity I_0 due to scattering and/or absorption by a sample is given by the Beer-Lambert law:

$$I(d) = I_0 \exp(-C_{ext} N d) \quad (4.9)$$

Here, $I(d)$ is the intensity after the sample, C_{ext} is the extinction cross-section, N is the number density of the sample and d refers to the pathlength. In the case of a non-absorbing sample that contains objects that only scatter light, the extinction is directly related to the scattering cross-section C_{scat} , *i.e.* $C_{ext} = C_{scat}$. In a standard absorbance spectroscopy experiment, the measured absorbance A from a turbid, non-absorbing sample is given by:

$$A = \log_{10} \left(\frac{I_0}{I(d)} \right) = \frac{C_{scat}Nd}{2.303} \quad (4.10)$$

For more information regarding the conversion leading to equation 4.10 please see the Supporting Information. Depending on the size of the scattering objects and the refractive index difference between particles with n_p and dispersing medium with n_s , different theories can be applied to calculate and predict C_{scat} . In general, given a sample of low polydispersity scatterers, absorbance measurements can be applied to determine particle sizes.²⁰⁹ In this work, we will show that simple absorbance measurements are well-suited for following the scattering increase during microgel collapse.

4.5 Results and Discussion

We used seeded precipitation polymerizations to synthesize Au-PNIPAM CS microgels that differ in thickness and cross-linking of the shells. All syntheses were performed with polycrystalline, monodisperse AuNP cores. Three batches of cores were synthesized to yield the quantities needed for all CS systems. The average diameter of the cores from TEM is 15.3 nm for all batches. The standard deviation of the diameter shows small differences between the batches. On average the polydispersity is 10%. For the PNIPAM encapsulations, only the amounts of monomer and cross-linker were varied to yield the different CS particles (see Table 1). We want to highlight that the core volume is negligible with respect to the total microgel volume ($\ll 1\%$) for all samples. Consequently, we do not expect any significant influence of the cores on the swelling behavior of the PNIPAM shells. Physically the CS particles behave just like standard microgels without cores - apart from the absorption that is related to the LSPR of the AuNPs.²⁰² The role of the cores is twofold in our study: 1) The cores act as seeds for the precipitation of PNIPAM during the polymerization and thus allow for precise control of the microgel size.¹² 2) The cores serve as useful markers due to their LSPR properties and large scattering contrast in SAXS.

Before looking at the optical properties of the microgels in detail, we will discuss some of their general properties.

4.5.1 General Characterization of CS Microgels

The core size and shape as well as the morphology of the overall CS microgels were studied by TEM. Figure 1 a) shows representative TEM images of all five microgel batches. Due to the large difference in electron density, the cores and PNIPAM shells can be clearly distinguished. All samples have single AuNP cores homogeneously encapsulated

in the PNIPAM shells. A detailed analysis of several TEM images for each of the five CS microgels revealed that on average less than 5% of the microgels have no core. In the case of CS4, that is the sample with the lowest cross-linking density, the core positions seem to be mostly off-centre. This is something that we observed before for CS microgels with a cross-linker density of 10 mol-%.²⁰² The gold cores are not covalently bound to the PNIPAM network and thus are rather mobile in microgels with larger mesh sizes, *i.e.* lower cross-linking densities. Therefore, after the synthesis performed above the VPTT, we expect that the cores can change their position in the microgels when the samples are cooled down to room temperature leading to swelling of the PNIPAM network. For this work, the exact position of the cores in the CS particles is not important as long as each microgel contains a single NP core. Image analysis reveals an average core diameter of 15.3 nm. Due to the high vacuum conditions during the TEM investigation and due to the sample preparation (drying), the microgels are imaged in their collapsed state. Therefore, the overall CS diameter appears smaller than the respective hydrodynamic diameter in the swollen state at 25 °C. Nevertheless, the TEM images show clearly the increasing shell size for CS1 to CS2 to CS3.

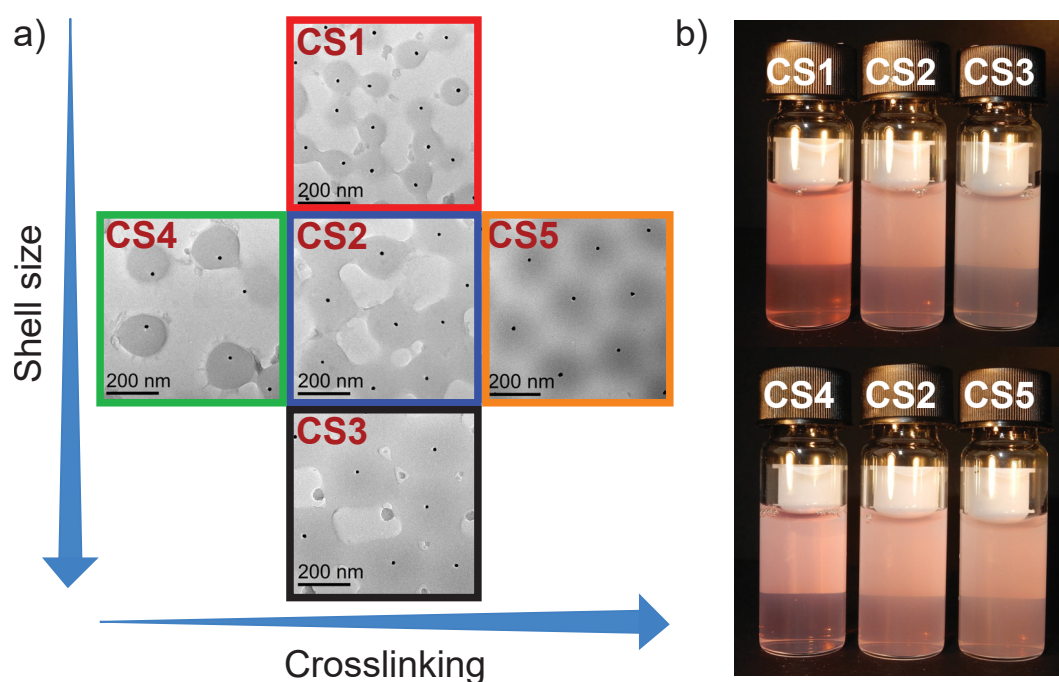


Figure 1: Results from TEM investigation and visual appearance. a) Representative TEM images of each microgel batch with increasing shell size and cross-linker density. b) Photographs of the microgels in dilute aqueous dispersion with the same weight concentrations.

Figure 1 b) shows photographs of dilute aqueous dispersions of the different microgels recorded at ambient conditions, *i.e.* with the microgels in their swollen states. The slightly red appearance of the samples is caused by the LSPR of the gold cores leading

to absorption of light in the green part of the visible spectrum. UV-Vis absorbance spectra of the AuNP cores from the different batches are shown in Figure S1 in the Supporting Information. As expected, because of their similar size and polydispersity, the spectra overlap perfectly. All batches reveal the typical dipolar LSPR at approximately $\lambda_{LSPR} = 518$ nm. The images of the CS microgels in the top row of Figure 1 b) show the increase in turbidity with increasing shell thickness from CS1 to CS3 caused by scattering from the microgels. The samples in the bottom row exhibit similar turbidity due to their similar size. At a closer look one can see a slight increase in turbidity from CS4 to CS2 to CS5, *i.e.* from left to right in the photograph. This increase is related to the increasing cross-linking density in agreement with our earlier findings.⁸ The differences in shell thickness and cross-linking are nicely revealed by results from DLS measurements. Figure S2 in the Supporting Information shows swelling curves obtained from temperature dependent measurements. All samples show the typical VPT behavior of PNIPAM microgels with continuously decreasing hydrodynamic radii, R_h , from the swollen state until plateaus are reached with nearly constant R_h at temperatures of 40 °C and higher. Aggregation of the microgels is not observed at any of the investigated temperatures. Even in the fully collapsed state where polymer-polymer interactions are favored, colloidal stability is high enough to prevent aggregation. The respective values of R_h in the swollen and collapsed state are summarized in Table 1. For a better comparison of the swelling characteristics of the microgels, we look at the deswelling ratios, α , in Figure 2. α is defined as the ratio of the hydrodynamic volume at any temperature T , $V_h(T)$, and the respective hydrodynamic volume in the swollen state $V_{h,swollen}$:

$$\alpha = \frac{V_h(T)}{V_{h,swollen}} \quad (4.11)$$

For our CS microgels, we consider only the volume of the swellable PNIPAM shell to calculate α :

$$V_h = \frac{4}{3}\pi(R_h^3 - R_{core}^3). \quad (4.12)$$

Here, R_{core} corresponds to the radius of the rigid AuNP cores, that do not change their volume in response to temperature in the relevant temperature window. We used data from the sigmoidal fits to the swelling curves at 25 °C to calculate $V_{h,swollen}$ (see Table 1).

In Figure 2 a) the deswelling behavior of the three microgels with different shell thicknesses but similar cross-linker contents are compared. The data of the different samples nearly collapse onto a common master curve with very similar VPTTs and only slight fluctuations - mostly at lower temperatures. Furthermore, very similar values of α of approximately 0.4 are reached at 50 °C. In other words, the shrunken state volume of the PNIPAM shells is only about 40% of the swollen state volume. The overlap of the data for the different CS batches indicates that indeed the degree of cross-linking is very similar for CS1-3.²¹⁰ In contrast, Figure 2 b) compares the deswelling behavior of the set of samples with different nominal cross-linker contents. The relative volume change between swollen and collapsed state is largest for CS4, which has the lowest

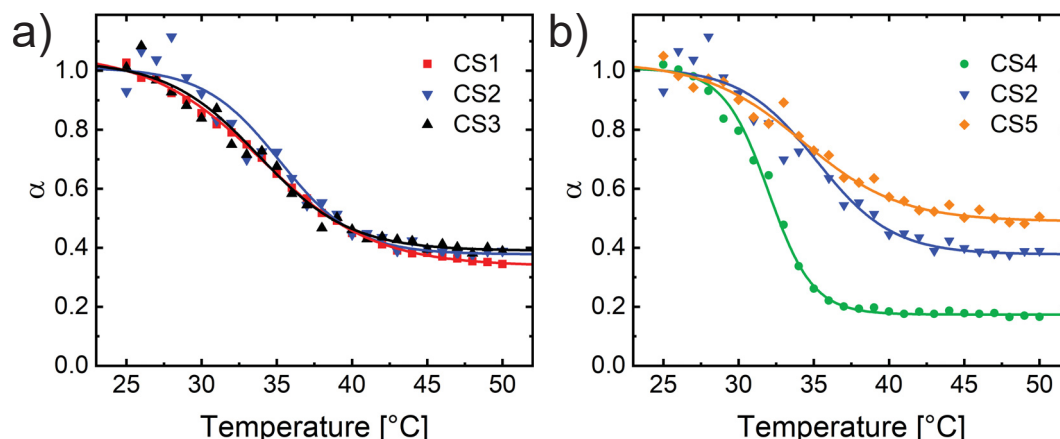


Figure 2: Deswelling ratios, α , as a function of temperature for all Au-PNIPAM microgels. a) Variation in microgel shell thickness (samples CS1, CS2 and CS3). b) Variation in cross-linker density (samples CS2, CS4 and CS5). Solid lines correspond to the sigmoidal fits used as guides to the eye.

nominal cross-linker content. In that case the values of α are smallest in the shrunken state (approximately 0.2). In contrast CS5 shows minimum values of α of approximately 0.5 at 50 °C. Thus, the DLS data confirm the increase in cross-linking density from CS4 to CS2 to CS5.^{8,202}

4.5.2 Temperature-Dependent Optical Properties

We now want to address the optical properties of the CS microgels and their dependence of the swelling state of the PNIPAM shells. Therefore, we measured absorbance spectra from dilute aqueous dispersions (0.02 wt%) using classical UV-Vis spectroscopy. Full spectra measured at different temperatures covering the VPT of the PNIPAM shells are shown in the Supporting Information (Figure S3). Generally, the spectra reveal two contributions: 1) The LSPR of the AuNP cores. Due to the small size of the cores, scattering is negligible and their interaction with light is dominated by absorption.²¹¹ 2) Light scattering from the PNIPAM shells that manifests itself as a continuous increase in absorbance with decreasing wavelength. Further details of the spectra are discussed in the Supporting Information. Here, we want to focus on the observed increase in absorbance with increasing temperature, *i.e.* when the shells collapse due to the VPT behavior. Figure 3 a) - e) show measured and normalized absorbances at selected wavelengths as a function of temperature for all CS microgels.

For a better direct comparison we normalized all data for each sample using the absorbances measured at $\lambda = 300$ nm in the fully collapsed state, *i.e.* at 60 °C. Due to the power law scaling of the wavelength in RDG scattering ($\propto \lambda^{-4}$, see equation 4.5), the absorbances at a given temperature decrease with increasing wavelength, *i.e.* from 300 to 400 to 523 nm, for each sample. We will come back to the experimentally observed power law scaling at a later stage in this work. At a given wavelength all

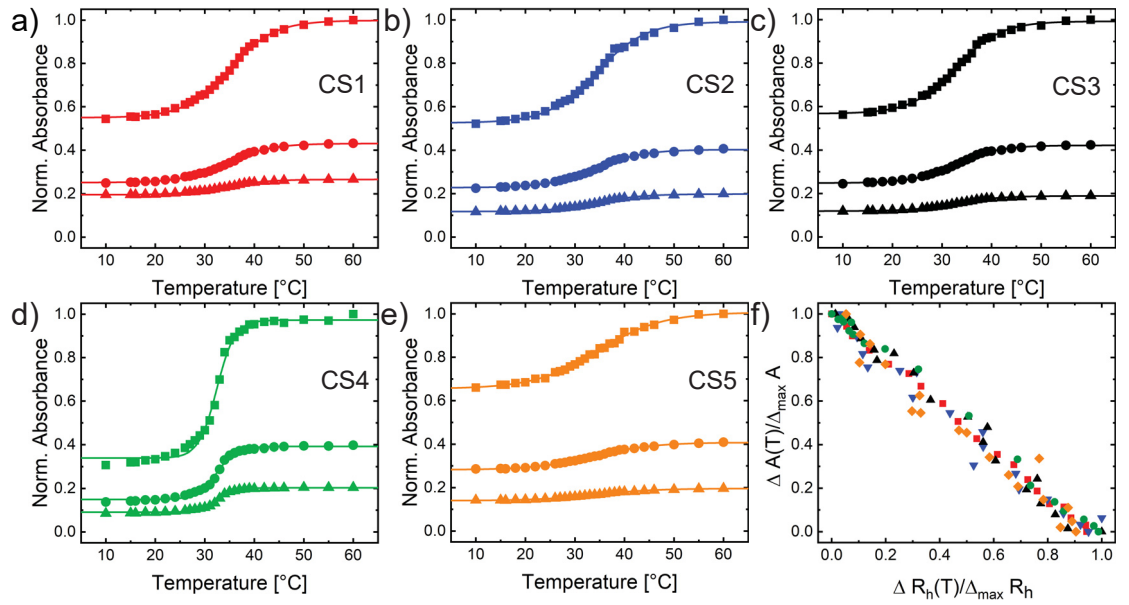


Figure 3: Optical properties of Au-PNIPAM microgels studied by UV-Vis spectroscopy. a)-e) Normalized absorbances at the wavelengths 300 (squares), 400 (circles) and 523 nm (triangles) as a function of temperature. The absorbance data from 300 nm are normalized to 1 at the collapsed state (60 °C). The corresponding data at 400 and 523 nm are divided by the same normalization factors as for 300 nm to keep the relative absorbance ratios between the different wavelengths the same. f) Normalized absorbances at 300 nm as a function of normalized hydrodynamic radius for all five samples. The color code is the same as in a)-e).

samples show a continuous increase in absorbance with increasing temperature in the region of the VPT, *i.e.* when the microgels collapse. The sigmoidal fits (solid lines) match the data very precisely. Comparing the different samples we find similar relative increases in absorbance for CS1-CS3, *i.e.* the samples with similar cross-linker densities but different shell thicknesses. In contrast, the relative change in absorbance significantly differs when comparing the samples with different cross-linker densities but similar shell thicknesses. CS5, the most cross-linked microgel, shows the smallest increase in absorbance with temperature. CS4, the sample with the lowest cross-linking, shows the largest increase in absorbance. These findings are in good agreement with the temperature-induced changes in R_h measured by DLS. To prove that we can use the absorbances as a measure for the light scattering properties of the microgels, we performed SLS measurements at $\lambda = 632.8$ nm as a function of temperature. Figure S4 in the Supporting Information compares normalized, relative scattering intensities from SLS to the corresponding normalized, relative absorbances measured at $\lambda = 632.5$ nm using UV-Vis spectroscopy. For each sample the data from both methods overlap perfectly. This demonstrates that the measured absorbances are indeed related to light scattering and that the relative changes as a function of temperature directly reflect its changes. This is not only the case for $\lambda \approx 633$ nm but also for other wavelengths as the perfect overlap between normalized absorbances at different wavelengths illustrates (see Figure S5 in the Supporting Information). VPTTs determined from the sigmoidal fits to the SLS and UV-Vis spectroscopy data are summarized in Table 2.

Table 2: VPTTs of the CS microgels obtained from UV-Vis spectroscopy and SLS applied to dilute, aqueous dispersions.

| Sample | VPTT (UV-Vis) [°C] | VPTT (SLS) [°C] |
|--------|--------------------|-----------------|
| CS1 | 33.5 ± 0.3 | 33.6 ± 0.3 |
| CS2 | 33.9 ± 0.2 | 34.1 ± 0.2 |
| CS3 | 33.0 ± 0.2 | 33.3 ± 0.2 |
| CS4 | 32.1 ± 0.2 | 32.8 ± 0.2 |
| CS5 | 34.1 ± 0.3 | 34.4 ± 0.3 |

The listed VPTTs range between 32.1 and 34.4 °C, while for each sample, both techniques reveal the same VPPTs within the experimental error. Samples CS1-3 possess very similar VPTTs. In contrast, the samples with different cross-linker contents show increasing VPTTs with increasing cross-linking, *i.e.* CS5 has the highest, CS4 the lowest VPTT. This dependence on the cross-linker content is in agreement with results from other studies on classical PNIPAM microgels (without cores).⁶⁷

Now, we want to derive the correlation between the swelling state of the microgels and the scattering intensity. Since we know the evolution of R_h as a function of temperature for all samples, we can derive the correlation between absorbances at given λ and the respective R_h . To be able to compare all samples, independent of their different swelling capacities, we calculate the difference in radius at each temperature with respect to the

collapsed state, $\Delta R_h(T)$, and normalize by the maximum difference in size between the fully swollen and collapsed state, $\Delta_{\max} R_h$:

$$\frac{R_h(T) - R_{h,\text{collapsed}}}{R_{h,\text{swollen}} - R_{h,\text{collapsed}}} = \frac{\Delta R_h(T)}{\Delta_{\max} R_h} \quad (4.13)$$

Similarly, we calculate the difference in absorbance at temperature T with respect to the minimum absorbance in the swollen state, $\Delta A(T)$, and normalize by the maximum difference in absorbance, $\Delta_{\max} A$:

$$\frac{A(T) - A_{\text{swollen}}}{A_{\text{collapsed}} - A_{\text{swollen}}} = \frac{\Delta A(T)}{\Delta_{\max} A} \quad (4.14)$$

Both quantities reflect the extent to which R_h and A respectively, have changed at a given temperature in relation to the maximum possible changes in R_h , respectively A . For R_h , we can treat $\frac{\Delta R_h(T)}{\Delta_{\max} R_h}$ as a measure for the degree of swelling, *i.e.* if the value is 0, the microgels are fully collapsed, if the value is 1, the microgels are fully swollen. Figure 3 f) compares the respective results for all samples based on measured absorbances at $\lambda = 300$ nm. The normalized change in absorbance scales linearly with the normalized change in R_h and the slope is -1. In other words, the absolute absorbance difference with respect to the swollen state, $\Delta A(T)$, is directly proportional to the absolute radius difference with respect to the collapsed state, $\Delta R_h(T)$. This implies that, for example, a temperature induced swelling by 10% results in a 10% decrease in normalised absorbance. This behavior is found for all five microgels. All data points collapse onto a master curve in Figure 3 f). We are not aware that such a relationship has been identified previously in literature dealing with PNIPAM microgels. Ultimately the observed relation is very convenient, because it allows the derivation of the microgel size and its temperature-induced changes using simple absorbance measurements. In the following section we want to address the internal structure of the microgels and the resulting volume fraction of polymer.

4.5.3 Volume Fraction of Polymer from Absolute Intensity Small-Angle Scattering Experiments

The measured absorbances, that result dominantly from light scattering of the microgels discussed in the previous section, depend on three sample parameters: 1) the number density N , that is the number of CS microgels per sample volume, *i.e.* per cm^3 ; 2) the refractive index contrast; and 3) the particle radius R .

The precise determination of N , in particular for dilute microgel dispersions as used in our case, is challenging. In principle, N can be derived from the microgel volume fraction ϕ_{microgel} , that is the volume occupied by the microgels in relation to the total volume of the dispersion, V . If the volume of a single microgel is ν_0 , the number density can be calculated:

$$N = \frac{\phi_{\text{microgel}}}{\nu_0} \quad (4.15)$$

Probably the most commonly applied method to measure $\phi_{microgel}$ in dilute dispersion where $\phi_{microgel}$ is equal to the generalized volume fraction ζ , is via measurements of the relative viscosity.^{180,185,212} To then calculate N requires knowledge of ν_0 that is particularly difficult to define for swollen microgels due to their fuzzy sphere morphology and the presence of dangling ends in the outer microgel periphery. Depending on which radius is used for the calculation of the microgel volume (*e.g.* hydrodynamic radius, Guinier radius, sphere radius from SLS), values of ν_0 differ strongly. Here, we choose a completely different approach to determine N and make use of the strong scattering contrast of our small AuNP cores: We use absolute intensity SAXS data and form factor analysis of the strong scattering signal from the AuNP cores to determine the number density of cores. Knowing that each microgel contains exactly one core, the number density of the cores is equal to N . The corresponding SAXS data including Guinier plots and detailed explanation of the calculations to determine N from samples of known weight concentration can be found in the Supporting Information (Figures S6 and S7). The determined values of N now also allow us to calculate extinction cross-sections from the measured absorbances (see equations 4.9 and 4.10). Figure S8 in the Supporting Information shows the respective results for the swollen and collapsed state of the CS microgels. As expected, for a given wavelength, the extinction cross-section increases with increasing microgel shell thickness, *i.e.* from CS1 to CS3, and for increasing cross-linking density, *i.e.* from CS4 to CS2 to CS5. This behavior is found for both states of swelling.

With the resulting correlation between N and the weight concentration of our samples, we can now address the refractive index contrast of the microgels. We do this in two different ways: using refractive index measurements and using absolute intensity SANS measurements. Measured refractive indices from the refractometer, $n_{dispersion}$, obtained from CS microgel dispersions of known weight concentration are listed in Table S3 and shown in Figure S9 in the Supporting Information. Since we know the relation between weight concentration and N from analysis of our absolute intensity SAXS data, we can estimate the volume fraction of microgels, $\phi_{microgel}$, using the hydrodynamic volumes V_h in equation 4.15. With $\phi_{microgel}$ we can then use the Maxwell-Garnett mixing rule^{213,214} to calculate the effective, volume averaged microgel refractive index, $n_{microgel,eff}$:

$$n_{microgel,eff} = \frac{n_{dispersion}(T) - n_{H_2O}(T) \cdot (1 - \phi_{microgel})}{\phi_{microgel}} \quad (4.16)$$

The determined values of $n_{microgel,eff}$ along with the resulting effective polymer volume fractions, ϕ_{eff} , are listed Table 3. Here, ϕ_{eff} was calculated using equation 4.6 with $n_{microgel,eff}$ as the input parameter for n_p .

In the swollen state, the determined effective, average refractive indices of the microgels lie between 1.342 and 1.371, with CS4 and CS5 having the lowest and highest refractive indices respectively. These values correspond to an averaged polymer content of 6 % (CS4) and 23 % (CS5) respectively. The CS1-3 microgels possess very similar polymer contents of 15 - 18 %. As expected these values lie between the determined polymer content of CS4 and CS5, which have lower and higher cross-linker contents respectively. In the collapsed state, the trend is not that clear. At 32 %, the CS4 microgels have

Table 3: Calculated effective, average refractive indices n_{eff} at 589.3 nm and polymer volume fractions of the CS microgels for the swollen (25 °C) and collapsed (50 °C) state.

| Sample | swollen state | | | collapsed state | | |
|--------|---------------------------|---------------------|--------------------------------------|---------------------------|---------------------|--------------------------------------|
| | $n_{\text{microgel,eff}}$ | ϕ_{eff} | $\frac{4\pi n_s R}{\lambda} 1 - m $ | $n_{\text{microgel,eff}}$ | ϕ_{eff} | $\frac{4\pi n_s R}{\lambda} 1 - m $ |
| CS1 | 1.363 | 0.18 | 0.08 | 1.427 | 0.57 | 0.16 |
| CS2 | 1.357 | 0.15 | 0.09 | 1.401 | 0.42 | 0.18 |
| CS3 | 1.357 | 0.15 | 0.11 | 1.394 | 0.38 | 0.19 |
| CS4 | 1.342 | 0.06 | 0.05 | 1.383 | 0.32 | 0.12 |
| CS5 | 1.371 | 0.23 | 0.14 | 1.405 | 0.45 | 0.20 |

the lowest effective polymer content, indicating that these lowest cross-linked microgels contain the largest amount of water in their collapsed state. Next, CS2, CS3 and CS5 have similar polymer contents in the range from 38 to 45 %. The CS1 microgels with the thinnest PNIPAM shell, but similar cross-linker content to CS2 and CS3, have the highest polymer content of 57 % in the collapsed state. These values serve as a first estimate from simple and quick refractive index measurements. However, we want to note that the determined values might be inaccurate despite the high precision of the refractive index values (see Table S3 in the Supporting Information). Potential sources of error are the precision of N from absolute intensity SAXS, the validity of the Maxwell-Garnett mixing rule for microgel dispersions and the use of the hydrodynamic radius to estimate ϕ_{microgel} . In the following we will show that only the latter factor, *i.e.* the use of the hydrodynamic microgel size, is relevant to the reliability of the determined values of $n_{\text{microgel,eff}}$ and consequently ϕ_{eff} . Already minor deviations in radius strongly affect the resulting refractive index of the polymer shell, where a reduction of the radius by a few nanometers leads to significantly increased values of ϕ_{eff} . Before we address this in more detail, it is useful to use the values from refractive index measurements to reconfirm that the microgels generally fulfill the RDG criterium (equation 4.4). Table 3 lists the resulting values of $\frac{4\pi n_s R}{\lambda} |1 - m|$ for the swollen and collapsed states. With values ranging between 0.05 and 0.14 the RDG criterium is well fulfilled in the swollen state. In the collapsed state the values are larger, by a factor of approximately 2, but still small enough that it is justified to treat the collapsed microgels formally as RDG scatterers.

We will now turn to the SANS measurements of the CS microgels and outline an alternative method to determine the polymer volume fraction. The scattering profiles measured at different states of swelling are shown in Figure 4.

All scattering profiles can be well described by a combination of a scattering contribution from the incoherent background, an Ornstein-Zernicke contribution to account for dynamic network fluctuations and the fuzzy sphere model to account for the microgel form factor. The latter model was first introduced for microgels by Stieger *et al.*⁴⁰ and comprises an inner microgel region with homogeneous density and a radius, R_{box} . The

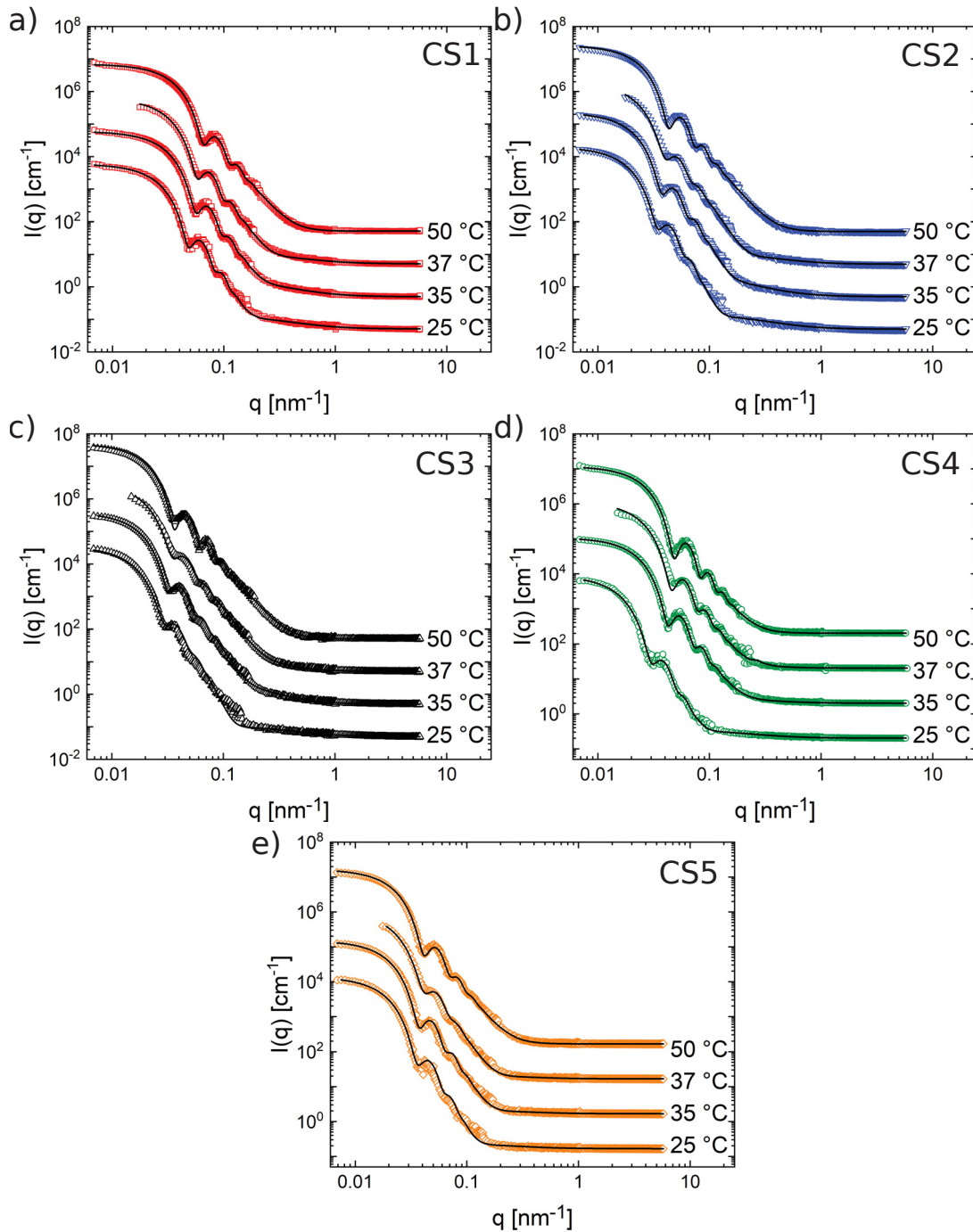


Figure 4: Results from SANS measurements of all samples. Measurements were performed at four different temperatures of 25, 35, 37 and 50 °C. a) – e) Symbols show experimental data of the samples CS1 – CS5. Black solid lines correspond to fits to the data using the fuzzy sphere model for the microgel form factor. The profiles were offset vertically by multiplication for the sake of clarity ($\times 1$, $\times 10$, $\times 100$ and $\times 1000$, from bottom to top).

thickness of the fuzzy shell is defined by the parameter σ . The total microgel radius, R_{SANS} is given by $R_{SANS} = R_{box} + 4\sigma$. The fits to the data shown as solid lines in Figure 4 describe the experimental data very well. Some small deviations in the mid q -range (at approximately 0.1 nm^{-1}) that are particularly visible for CS5 at $25 \text{ }^\circ\text{C}$ might be related to static internal inhomogeneities. Further details of the fuzzy sphere model and the fitting of our SANS data can be found in the Supporting Information. We want to highlight that recently more complex models have been derived for the description of the internal microgel morphology and the microgel form factors.^{189,215} These extended models might also be applicable to our samples and might provide more realistic density profiles. However, due to the limited resolution and the instrumental smearing in our SANS experiments, we want to stay with the well-established fuzzy sphere model and avoid increasing the number of fitting parameters because these will be used in the optical simulations presented later on in this work. We now want to focus on the fit results. For temperatures below ($25 \text{ }^\circ\text{C}$) and close to the VPTT (35 and $37 \text{ }^\circ\text{C}$), the best form factor fits with the fuzzy sphere model yield values of $\sigma > 0 \text{ nm}$. We want to highlight that a simple polydisperse sphere fit does not lead to a good description of the scattering data at these temperatures. Only in the fully collapsed state, at $50 \text{ }^\circ\text{C}$, the fuzzy sphere model yields $\sigma = 0 \text{ nm}$ and the model becomes equivalent to a polydisperse sphere form factor. In other words, the fully collapsed microgels resemble the scattering behavior of homogeneous, hard spheres in agreement with earlier findings for PNIPAM microgels, including those with ultra low cross-linker density.^{216,217,218} Figure 5 summarizes the results from our SANS measurements using CS2 as an example.

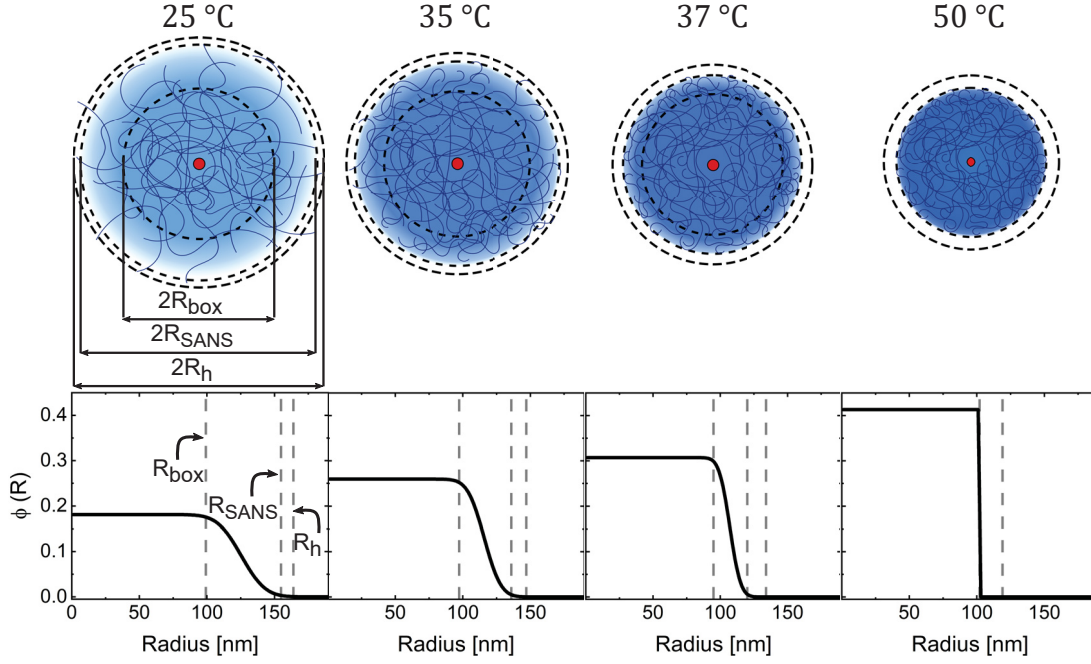


Figure 5: Microgel structure at different states of swelling. Top: Schematic depictions of the Au-PNIPAM microgel structure at different temperatures with shell dimensions drawn to scale for sample CS2. Small red circles in the centre of the particles represent the AuNP cores and solid blue lines represent the polymer chains. Black dashed lines indicate the determined radii from DLS (R_h) and SANS (R_{SANS} , R_{box}) Bottom: Corresponding radial density profiles as the result from form factor analysis of SANS data. Shown are the polymer volume fractions as a function of radius. Vertical grey dashed lines highlight the radii R_h , R_{SANS} and R_{box} .

At 50 °C, the polymer volume fraction profile $\phi(R)$ is consistent with a typical hard sphere-like profile with a constant value at $R \leq R_{SANS}$. Here $R_{SANS} = R_{box}$ and $\sigma = 0$ nm. The constant polymer volume fraction of the microgels is approximately 0.41. In other words, the collapsed microgel CS2 still contains almost 60% solvent by volume (here: D₂O). With decreasing temperature and consequently increasing swelling, the thickness of the fuzzy shell, σ , increases while R_{box} remains almost constant. From 37 down to 25 °C, the polymer volume fraction of the inner homogeneous microgel part ($R \leq R_{box}$) decreases from approximately 0.3 to approximately 0.18. The swollen CS2 microgel contains over 80% solvent by volume in the inner region of the microgel. The fact that R_{box} remains almost constant while $\phi(R \leq R_{box})$ continuously decreases with increasing degrees of swelling indicates rearrangement of the chains from the fuzzy corona during swelling/deswelling. The microgels undergo a transition from fuzzy spheres, with a gradually decreasing polymer density in the fuzzy corona, to homogeneous hard sphere-like particles with a simple box profile, as the temperature increases. During this transition the effective polymer volume fraction increases continuously with increasing temperature

until the microgels are fully collapsed. Due to limited beamtime, we could not perform measurements at temperatures higher than 50 °C. However, our absorbance data show only negligible changes in absorbance above 50 °C (see Figure S4 in the Supporting Information). Therefore, we conclude that the SANS profiles will also not show any significant changes for higher temperatures. As Figure 6 a) – e) shows, the SANS analysis yields very similar results for all CS microgels where the same temperature-dependent trend is observed for each system.

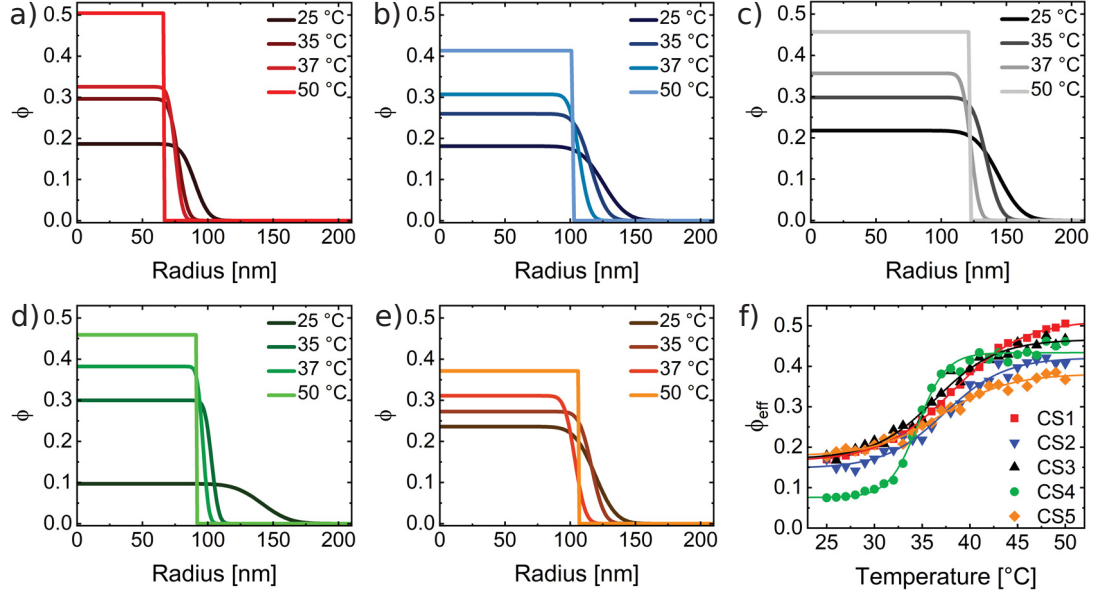


Figure 6: a) - e) Radial polymer volume fraction profiles at four different temperatures as obtained from analysis of the SANS data using the fuzzy sphere model. f) Calculated effective polymer volume fraction as a function of the temperature for all CS microgels. The effective volume fractions were calculated using the fully collapsed state as the reference state and the temperature-dependent hydrodynamic radii according to equation 4.17.

All fit parameters from the SANS analysis are listed in Tables S4-8 and the different radii from DLS and SANS are summarized in Figure S10 in the Supporting Information. The tables also list the radii of gyration R_g obtained from model-free Guinier analysis of the low q scattering regions. It is useful to compare the values of R_g with R_h . For homogeneous, hard spheres we expect to find $R_g/R_h = \sqrt{3/5} = 0.775$ ⁸⁸. In the swollen state (25 °C) the ratios R_g/R_h of our CS microgels are in the range of 0.56 – 0.71 and thus significantly smaller than the hard sphere value. This can be explained by the fuzzy corona and the dangling ends that contribute to R_h but less to R_g .^{68,219} When temperature is increased and the microgels collapse, the ratios increase to 0.68 – 0.74. Thus, the transition from fuzzy spheres to hard sphere-like particles is also reflected by R_g/R_h . Comparing the samples with the different cross-linker densities, we see the

strongest change in R_g/R_h for CS4 - the microgels with the lowest cross-linker density. CS4 exhibits the smallest R_g/R_h value of 0.56 in the swollen state and a significantly increased value of 0.72 in the collapsed state. This is in agreement with polymer volume fraction profiles shown in Figure 6 d) where the inner microgel volume contains 90% solvent by volume in the swollen state - significantly more than the other microgels. The CS4 microgels are the softest among the series of microgels studied. In contrast, the other microgels with higher cross-linking density and thus more rigid polymer networks, exhibit smaller changes in R_g/R_h with temperature. Surprisingly, the polymer volume fraction in the fully collapsed state is very similar for all microgels ranging between approximately 37.5% (CS5) and 45% (CS3 and CS4). Only CS1 shows a slightly higher polymer content of approximately 50% in the collapsed state. These are the smallest microgels and potentially possess more inhomogeneities in the polymer network. Thus, the CS1 microgels show a slightly different behavior than CS2 and CS3 with similar cross-linker contents. Generally the calculated polymer volume fractions in the collapsed state are in good agreement with values reported in literature,^{40,192} where, for example, Lopez and Richtering estimate a value of 0.44, independent of the cross-linking density and molar mass.⁵⁸ The collapsed state of microgels is often used as the reference state, for example, when the swelling behavior is described by the Flory-Rehner theory.^{54,58,191} In this case precise knowledge of the polymer volume fraction is crucial. While this value is often estimated rather than precisely measured,^{54,67} we provide an approach to determine the polymer volume fraction with great confidence. Furthermore, the values from our collapsed state SANS data are in good agreement with the results from refractive index measurements (Table 3) despite the slightly larger variation between samples for the latter dataset. This agreement supports our previous hypothesis that the dominant error in the evaluation of the refractive index measurements is related to the use of R_h in order to estimate the microgel volume fraction. The collapsed state is therefore the ideal reference state ($\phi = \phi_0$), because the microgels can be treated as homogeneous hard sphere-like particles with a homogeneous density profile and thus homogeneous refractive index. Similar polymer contents were determined independent of the shell thickness and the cross-linker content. We highly recommend the collapsed state to be used as the reference state in future studies on microgels.

4.5.4 Light Scattering Properties Based on Effective, Average Volume Fractions

With the results from collapsed state SANS, we now want to derive the effective, average polymer volume fractions ϕ_{eff} for different states of swelling using the hydrodynamic radii from DLS at different temperatures:

$$\phi_{\text{eff}} = \frac{R_h(50^\circ\text{C})^3 - R_{\text{core}}^3}{R_h(T)^3 - R_{\text{core}}^3} \cdot \phi_0 \quad (4.17)$$

We want to emphasize that this simple estimation does not take into account the transition from hard sphere-like behavior at the reference state (50 °C) to the fuzzy sphere morphology in the swollen state. Therefore, ϕ_{eff} rather corresponds to the volume

averaged polymer volume fraction with respect to the hydrodynamic microgel volume. Figure 6 f) compares the temperature evolution of ϕ_{eff} for all CS microgels. As expected the capacity for solvent uptake is the largest for the CS4 particles, which have the lowest cross-linking. In the fully swollen state, the CS4 microgels contain on average less than 10% polymer. For the other, higher cross-linked CS microgels, the average polymer content approaches values between 15 and 20% in the swollen state. Again we find good agreement with the values from refractive index measurements (Table 3) that also do not take into account internal density variations. In order to relate the polymer volume fractions to the light scattering properties of the microgels, we have to calculate the refractive index contrast using equation 4.6 with the values of ϕ_{eff} . Since we performed the absorbance measurements in H_2O , we use $n_{\text{H}_2\text{O}} = 1.33$ as the refractive index of the dispersing medium at $\lambda = 589.3 \text{ nm}$.²²⁰ To determine the refractive index of our PNIPAM microgel shells, n_{PNIPAM} , we measured the refractive index of dispersions of the CS3 microgels at $\lambda = 589.3 \text{ nm}$ and $25 \text{ }^\circ\text{C}$. The microgel dispersions were prepared from freeze-dried microgels and we took into account a residual water content of 5.7%.²⁰² In addition to the dispersion measurements, we measured a polymer film prepared from linear PNIPAM homopolymer. Figure S9 in the Supporting Information shows the measured refractive indices from dispersions of different weight concentrations and the PNIPAM homopolymer film. A linear scaling was observed and extrapolation to 100% polymer yielded $n_{\text{PNIPAM}} = 1.50$. Using this value, we calculated $n_{\text{eff}}(T)$ according to equation 4.6 which we then used to calculate $C_{\text{sca}}^{\text{RDG}}$ according to equation 4.5. Figure 7 shows the resulting scattering cross-sections as a function of temperature.

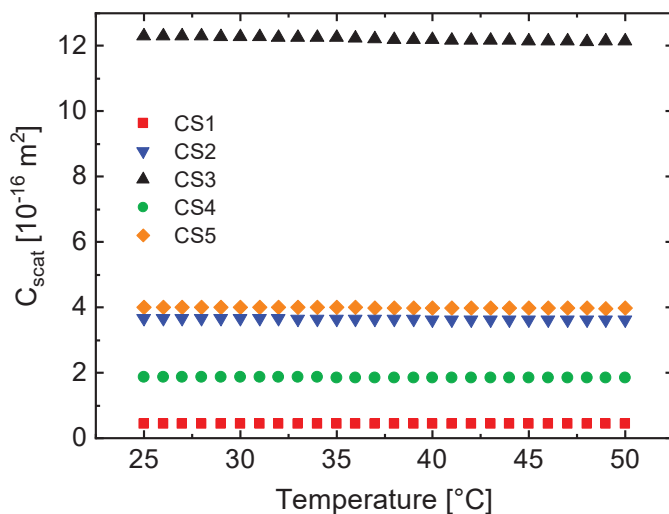


Figure 7: Calculated scattering cross-sections as a function of temperature according to equation 4.5.

For all CS microgels $C_{\text{sca}}^{\text{RDG}}$ remains nearly constant over the whole temperature range. On closer inspection, a slight decrease with increasing temperature is observed - opposite to the experimentally observed trend from absorbance measurements. However, the

decrease is only 1-2% and therefore negligible. Obviously the approach of using effective, average microgel volume fractions and measured hydrodynamic radii from DLS for RDG calculations does not describe the experimental results. Nevertheless, this finding is very important as it shows that for an optically homogeneous sphere composed of solvent and non-absorbing material (PNIPAM in our case) changes in size do not lead to noticeable changes in turbidity when the amount of material (PNIPAM) is conserved and only the solvent content is allowed to change. Although it is debatable whether R_h is the correct radius for this estimation, we claim that the main discrepancy arises due to the value used for the effective volume fraction, $\phi_{\text{eff}}(T)$, that ignores the fuzzy sphere character of the swollen microgels. This is supported by findings from Small *et al.* who investigated the scattering properties of core-shell particles with different refractive index contrasts.²²¹ They found that a different refractive index shell strongly influences the scattering intensity. For a shell refractive index close to that of the medium, the scattering is reduced. In order to account for our density profiles in the swollen state, we use FDTD simulations to calculate the scattering cross-sections in the following.

4.5.5 Light Scattering Properties Based on the Fuzzy Sphere Model

In order to account for the fuzzy sphere character of our swollen CS microgels, we used FDTD simulations to determine the theoretical scattering behavior. Table 4 lists the radii and refractive indices obtained from SANS that were used for the simulations.

Table 4: Radii of the homogeneous inner sphere (R_{box}), the shell thickness (R_t), the total radius (R_{total}) in the swollen state and radii (R) in the collapsed state of the particles with corresponding refractive indices n_{box} , n_{shell} and n used for the FDTD simulations.

| Sample | swollen state | | | | | collapsed state | |
|--------|-----------------------|------------|------------------------|------------------|--------------------|------------------------|-------|
| | R_{box} [nm] | R_t [nm] | R_{SANS} [nm] | n_{box} | n_{shell} | R_{SANS} [nm] | n |
| CS1 | 74.2 | 33.4 | 107.6 | 1.364 | 1.348 | 66.5 | 1.417 |
| CS2 | 99.2 | 55.6 | 154.8 | 1.363 | 1.347 | 102.0 | 1.401 |
| CS3 | 116.6 | 57.2 | 173.8 | 1.368 | 1.350 | 122.0 | 1.410 |
| CS4 | 110.5 | 66.2 | 176.7 | 1.348 | 1.340 | 91.6 | 1.410 |
| CS5 | 95.3 | 50.4 | 145.7 | 1.372 | 1.352 | 106.2 | 1.391 |

To simulate the scattering in the swollen state we used a simple core-shell model to describe the microgel shell. In this model the core corresponds to the inner microgel region with $R = R_{\text{box}}$ and a polymer volume fraction, ϕ_{box} , and a shell with thickness R_t that corresponds to the total thickness of the fuzzy shell. Thus, we use R_{SANS} as the total microgel radius. The refractive index of the shell, n_{shell} , corresponds to $\phi_{\text{shell}} = 0.5\phi_{\text{box}}$ as defined by the fuzzy sphere model. The collapsed state (50 °C) was simulated with a simple sphere of homogeneous refractive index and radius R_{SANS} . A gold sphere of 12 nm in diameter was included to account for the absorption contribution of the AuNP cores in our CS microgels. The diameter was chosen to be slightly smaller

than the experimental diameter from TEM since otherwise the absorption of the cores was strongly overestimated. Since the simulation uses monodisperse, perfectly spherical gold particles and also damping effects are less precisely considered - in particular for small AuNPs, as in our case - smaller gold dimensions are required to match better to the LSPR strength experimentally observed. In the experiment we deal with polydisperse (approximately 10%) and polycrystalline AuNPs that are only nearly spherical in shape. Figure 8 compares the results from FDTD simulations (dashed lines) to the measured absorbance spectra (solid lines). The experimental and simulated spectra were normalized at the wavelength of 400 nm allowing a direct qualitative comparison.

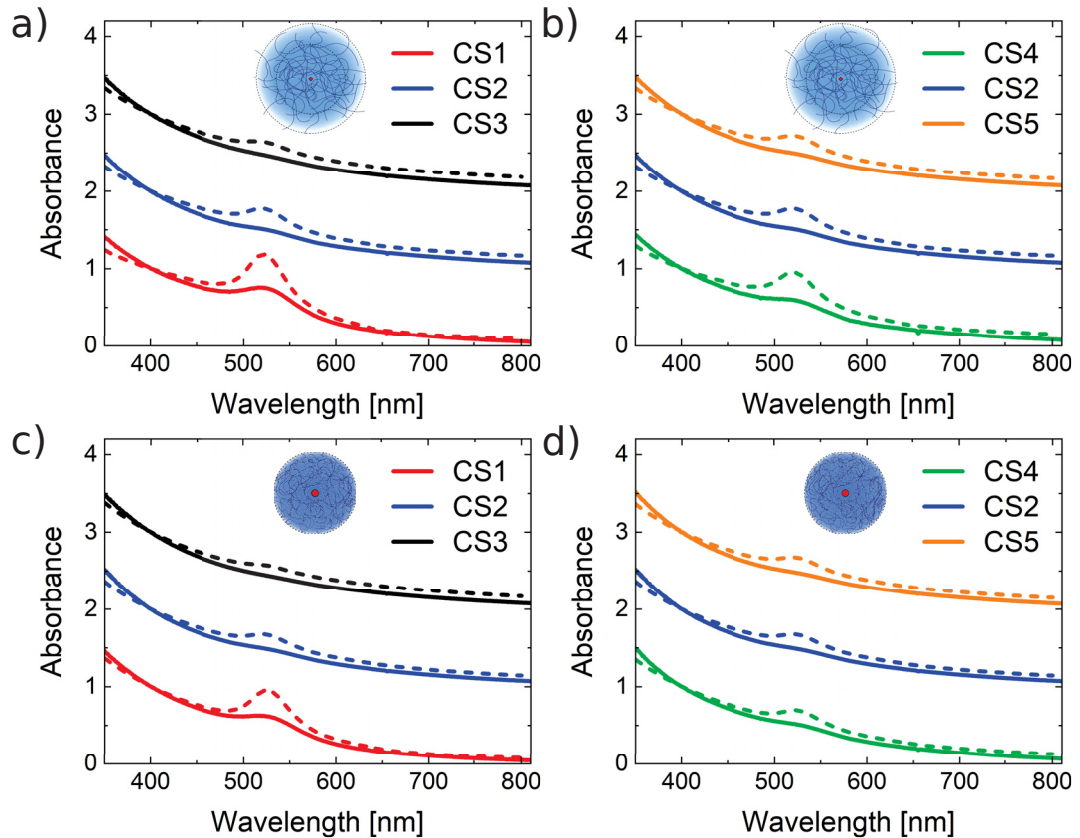


Figure 8: Comparison of simulated (dashed lines) and experimental absorbance spectra (solid lines). a) Shell size range (CS1, CS2, CS3) and b) Cross-linking density range (CS4, CS2, CS5) in the swollen state (25 °C). c) Shell size range and d) Cross-linking density range in the collapsed state (50 °C). All spectra are normalized at 400 nm, and for the sake of clarity, have offsets of 0, 1 and 2 from bottom to top in each subfigure. The insets show the corresponding schematic sketch of the microgels in the swollen and collapsed state.

At a first glance, the agreement between experimentally measured scattering and the numerical simulation is good for both states of swelling. In the collapsed state (c

and d), the scattering model, which treats the microgel as a sphere with homogeneous refractive index, matches well to the experimental result and supports the interpretation of the collapsed state as being hard-sphere-like. In the swollen state (a and b) our simple core-shell model with the shell accounting for the fuzzy microgel corona of lower polymer density yields satisfactory results for all samples. To provide a more quantitative comparison of the scattering, we look at the power law scaling (absorbance $\propto \lambda^{-\beta}$) with the wavelength exponent β .²²² For RDG scatterers we expect to find $\beta = 4$ according to equation 4.5. Indeed this is the case for the absorbance measured and simulated for spherical SiO₂ particles with $R_h = 14$ nm in water. Figure S11 in the Supporting information shows the perfect agreement between experimental data and simulated scattering cross-sections. The data perfectly follows the expected wavelength scaling of λ^{-4} for RDG scatterers. In the case of our CS microgels, we find significantly smaller values than $\beta = 4$. Table 5 compares the values of β determined from experimental and simulated spectra in the swollen and collapsed state.

Table 5: Scattering exponents β from experimental and simulated spectra in the swollen (25 °C) and collapsed state (50 °C).

| Sample | swollen state | | collapsed state | |
|--------|----------------------|----------------|----------------------|----------------|
| | β (experiment) | β (FDTD) | β (experiment) | β (FDTD) |
| CS1 | 2.36 | 1.46 | 2.73 | 2.28 |
| CS2 | 2.88 | 2.00 | 3.03 | 2.23 |
| CS3 | 2.86 | 2.14 | 3.05 | 2.41 |
| CS4 | 2.63 | 1.77 | 2.89 | 2.22 |
| CS5 | 2.93 | 2.11 | 3.05 | 2.24 |

In the swollen state, the simulated values of β range between 1.77 and 2.14 and between 2.36 and 2.93 in experiment. Nevertheless, there is a clear increase in β with increasing cross-linker density. The same trend is observed in the collapsed state where values are higher than in the swollen state and range between 2.22 and 2.41 for the simulations and between 2.73 and 3.05 in experiment. In all cases the values of β are smaller in the simulated spectra than in experiment. Comparing the samples with different shell thicknesses but similar cross-linker density, we find almost the same values of β for both states for CS2 and CS3. Only the CS1 microgels stand out with significantly smaller values. This deviation agrees with our previous discussion that the CS1 particles with the thinnest shell amongst the series might possess more inhomogeneities in the polymer network. Comparing the swollen and collapsed state, we find higher values of β , which indicates that the scattering becomes closer to the RDG prediction for homogeneous spheres. However, both particle size and refractive index influence the wavelength exponent.²²³ Heller *et al.* reported that for increasing sizes of scatterers, the wavelength exponent decreases until reaching 0.²²² This is the case for particles that do not fulfill the criterium of being "very small" compared to the wavelength. Our observed underestimation of β from FDTD simulations is more pronounced in the

swollen state where the microgels are significantly larger despite their refractive index being lower. In the collapsed state wavelength exponents from FDTD are closer to the experimental values indicating that optically our microgels can be considered as more homogeneous sphere-like. However, the scattering is obviously still far from matching the RDG prediction.

While the internal structure of PNIPAM microgels appears well understood and the fuzzy sphere model is well accepted, our data reveal the complexity when it comes to understanding simple absorbance properties: During the temperature induced collapse, PNIPAM microgels show an increase in scattering that cannot be explained by the RDG theory for homogeneous refractive index spheres. Even in the collapsed state, where SANS data clearly reveal the form factor of polydisperse hard spheres with a homogeneous polymer distribution, measured absorbances can neither be described with the RDG model nor by Mie theory calculations (see Figure S12 in the Supporting Information). This becomes particularly evident when comparing the power law scaling of the wavelength dependence. While refractive index measurements and form factor analysis yield very reasonable polymer volume fractions from which refractive index profiles can be derived, theoretical scattering cross-sections from FDTD simulation cannot reproduce the experimentally observed power law scaling of the wavelength-dependent absorbances.

Our study clearly shows that the fuzzy sphere structure of swollen microgels is responsible for the observed increase in absorbance during the VPT. In the swollen state, where the thickness of the fuzzy shell is largest and its effective, average refractive index is the lowest, the shell basically does not contribute to the visible wavelength scattering. Using the experimentally determined refractive indices of the inner microgel core (n_{box}) and of the fuzzy shell (n_{shell}) to calculate the refractive index contrast term in equation 4.5, we find a four times lower refractive index contrast of the fuzzy shell. As the fuzzy shell collapses during the VPT, polymer material from the fuzzy shell collapses on the inner microgel core that increases in polymer volume fraction. Consequently, the refractive index contrast of the inner, rather homogeneous core region increases leading to an increase in absorbance. This is supported by our finding of nearly constant radii, $R_{n_{\text{box}}}$, during the microgel collapse and the increase in polymer volume fraction in the core region as observed from the analysis of our SANS data.

With this work we want to stimulate further research in this direction - in particular in the development of theories that describe the optical scattering cross-sections of thermoresponsive microgels. To the best of our knowledge a model suitable for PNIPAM microgels does not exist so far. This knowledge gap hampers the quantitative analysis of microgels in general where it would be highly beneficial if, for example, number concentrations could be extracted from simple absorbance measurements. Furthermore, we believe that simple, fast and importantly, almost error-free absorbance measurements could be used to investigate the structural transitions of thermoresponsive microgels in great detail - given a precise theoretical model is available.

4.6 Conclusion

In a similar way to linear PNIPAM homopolymer chains, PNIPAM microgels show an increase in turbidity when undergoing a phase transition from good to poor solvent conditions. However, the origin of this turbidity increase is significantly different. We studied this behavior in detail using core-shell microgels with small gold nanoparticle cores and much larger PNIPAM shells of different thickness and cross-linking. Importantly, the measured absorbances in the visible wavelength range were strongly dominated by the light scattering from the PNIPAM shells while the absorption of the cores was almost negligible. Based on the microgel sizes and their effective, average refractive indices all samples studied fulfilled the RDG criterium in swollen and collapsed state. SANS measurements were used to determine the polymer density profiles and particle radii. Density profiles are very similar for similarly cross-linked microgels independent of their size. The cross-linker density largely determines the polymer volume fractions in the swollen state, while differences in the collapsed state are rather small. The relative change in absorbance during the volume phase transition is directly related to the determined changes in microgel size, polymer volume fraction and thus refractive index. Using the collapsed state as a reference state, we could derive the temperature-dependent profiles of the effective polymer volume fraction and refractive index. RDG calculations of the scattering cross-section using the latter data could not reproduce the increase in absorbance during shrinkage of the microgels. The fuzzy sphere character of the swollen microgels that was clearly identified by SANS measurements at temperatures close to and below the volume phase transition temperature was then taken into account in theoretical scattering calculations using FDTD simulations. The simulated spectra were found to match quite reasonably to the experimental absorbances despite significantly smaller power law exponents for the wavelength-dependence. We attribute the increase in absorbance (or turbidity) during the temperature induced microgel collapse to the transition from fuzzy spheres to hard sphere-like scatterers. In the swollen state where a significant fraction of the total microgel is forming the fuzzy shell with a continuously decreasing polymer density towards the surrounding medium, the fuzzy shell does not contribute significantly to the scattering. The scattering is dominated by the inner microgel region with a rather homogeneous polymer distribution and constant refractive index. As the microgels collapse due to an increase in temperature, the thickness of the fuzzy shell decreases, the polymer volume fraction in the inner microgel region rises and therefore the scattering increases until the microgels are fully collapsed. In the fully collapsed state, polymer material from the fuzzy shell has fully collapsed onto the inner homogeneous microgel core and chain rearrangements lead to a rather homogeneous polymer density profile. We therefore attribute the observed increase in microgel turbidity during the volume phase transition to changes related to the fuzzy shell.

A theory that precisely describes the light scattering properties of microgels is currently missing. With this work, we want to stimulate further research in this direction and provide a first general basis towards the understanding of simple absorbance spectra from thermoresponsive microgels. Such measurements are simple, quick and allow for great

resolution in time resolved studies of microgel swelling and deswelling phenomena. With a better understanding of the optical properties of microgels - ideally matching measured cross-sections to the respective state of swelling and the internal microgel structure - one could follow the volume phase transition with great time resolution while revealing internal structural transitions. A time-resolved deswelling study using temperature jump spectroscopy is currently in progress and will be presented elsewhere.

Conflict of Interest

There are no conflicts of interest to declare.

Acknowledgements

The authors acknowledge the Melbourne Advanced Microscopy Facility (Bio 21, The University of Melbourne) for access to electron microscopes and Heyou Zhang from the University of Melbourne with his support for the TEM measurements. The authors thank the Institut Laue-Langevin for allocation of SANS beamtime on D11 via EASY access; data are available on demand (DOI: 10.5291/ILL-DATA.EASY-632). The authors are also grateful for the financial support from the German Academic Exchange Service (DAAD) through its Thematic Network Melbourne-Bayreuth Polymer/Colloid Network, sponsored from funds of the Federal Ministry of Education and Research (BMBF). The authors thank the Center for Structural Studies (CSS) that is funded by the Deutsche Forschungsgemeinschaft (DFG Grant numbers 417919780 and INST 208/761-1 FUGG) for access to the SAXS instrument. P.M. thanks the ARC for support through Grant CE170100026. M.K. acknowledges the German Research Foundation (DFG) for funding under grant KA3880/6-1. The authors thank Gary Bryant (RMIT, Melbourne, Australia) for valuable discussions.

4.7 Supporting Information

Absorbance of the Gold Nanoparticle Cores

In total three batches of gold nanoparticles were synthesized according to the same protocol and then used as cores in the seeded precipitation polymerizations. **Figure S1** shows normalized absorbance spectra of the initial gold cores prior to the polymer encapsulation. All batches feature the typical localized surface plasmon resonance (LSPR) with its maximum at approximately 518 nm. Furthermore, all spectra overlap perfectly due to the similar size of the nanoparticles. Investigation by TEM revealed average diameter of 15.3 ± 1.3 nm, 15.3 ± 1.5 nm and 15.3 ± 1.8 nm. Due to the similarity in size and LSPR properties, we will not distinguish any further between the different batches of particles.

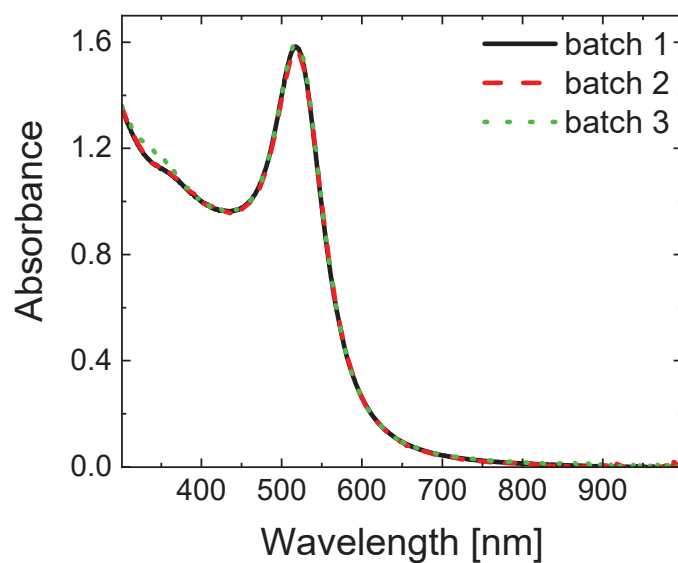


Figure S1: UV-Vis absorbance spectra of the different batches of gold nanoparticles. Measurements were performed in dilute aqueous dispersions and spectra were normalized at 400 nm.

Volume Phase Transition Monitored by DLS

We studied the temperature-dependent evolution of the hydrodynamic radius of the CS microgels by DLS. **Figure S2** a) and b) shows the resulting swelling curves. The samples CS1, CS2 and CS3, which have an increasing shell thickness and similar degrees of cross-linking (15 mol%) show a continuous decrease of R_h with rising temperature. At lower temperatures (25 °C), the particles are in a fully swollen state with hydrodynamic radii R_h of 111, 164 and 190 nm, respectively. With increasing temperature, the shell size decreases to 78 nm, 118 nm and 139 nm reaching the collapsed state (50 °C). The sample CS4 (5 mol% cross-linker) shows a sharper transition with a stronger decrease in size, *i.e.* from 186 to 104 nm. The highest cross-linked sample, CS5 (25 mol% cross-linking), shows a more continuous transition from 157 to 124 nm and with that the smallest total change in size. The hydrodynamic radii at temperatures of 25 °C and 50 °C were obtained from the sigmoidal fits to the measured data using:

$$R(T) = R_{\min} + \frac{R_{\max} - R_{\min}}{1 + \exp\left(\frac{T - VPTT}{h}\right)} \quad (4.1)$$

Here R_{\max} and R_{\min} denote the radii of fully swollen and collapsed microgel, respectively. VPTT gives the inflection point of the curve, and the parameter h describes the sharpness of the curve.

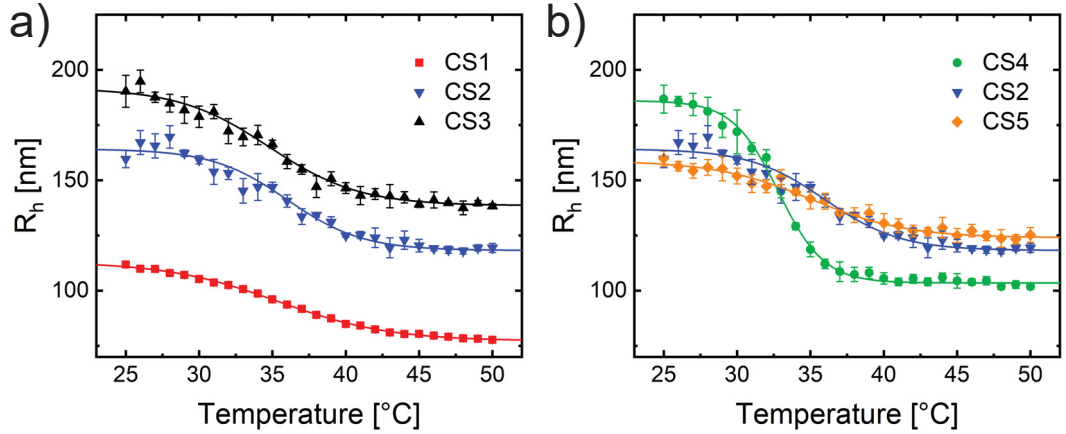


Figure S2: Results from temperature-dependent DLS measurements. a) Hydrodynamic radius versus temperature for samples CS1, CS2 and CS3, that have increasing microgel sizes. b) Hydrodynamic radius versus temperature for samples CS4, CS2 and CS5, that have increasing cross-linking density.

Absorbance of the CS Microgels

After encapsulation of the small gold cores with multiple times larger microgel shells, the absorbance spectra are dominated by the scattering of the PNIPAM shells while the LSPR is only barely visible. **Figure S3 a)** shows absorbance spectra of CS1 at 10, 30 and 60 °C, *i.e.* for the fully swollen state, a state close to the VPTT and for the collapsed state. The LSPR contribution of the gold core is visible but weaker compared to neat gold particles. Moreover, the LSPR position appears slightly red-shifted due to the higher refractive index environment.¹⁹⁸ With increasing temperature, the scattering of the shell increases, leading to higher absorbances. The temperature-dependent evolution of the absorbance spectra of all CS samples is shown in **Figure S3 b) – f)**. These spectra were recorded between 10 and 60 °C in 5 °C steps. For all samples increasing absorbances with increasing temperature are observed although the relative increase depends on the sample. For microgels with similar cross-linking density a similar increase in absorbance with increasing temperature is observed. In comparison, the CS4 sample with the lowest cross-linking density (5 mol%) reveals a significantly stronger and sharper increase in absorbance. In contrast, the CS5 sample has a more continuous absorbance increase and exhibits overall smaller changes compared to other samples. These findings are in agreement with the results from temperature-dependent DLS, *i.e.* the differences in the volume phase transition behavior are also reflected in the absorbance data.

Normalized absorbances from UV-Vis spectroscopy and scattering intensities obtained from SLS are shown in **Figure S4 a) – e)**. In each case the datasets were normalized to 1 at the collapsed state. For all samples the SLS data match perfectly to the absorbances. Therefore, it is well justified to use the measured absorbances as a direct measure for the light scattering.

Figure S5 a) – e) compares normalized absorbances for each CS microgel corresponding to wavelengths of 300, 400, 523 and 632.5 nm as a function of the temperature. The black lines correspond to the sigmoidal fits to the data. Overall the normalized absorbance is wavelength-independent and for each sample data collapse onto a single mastercurve.

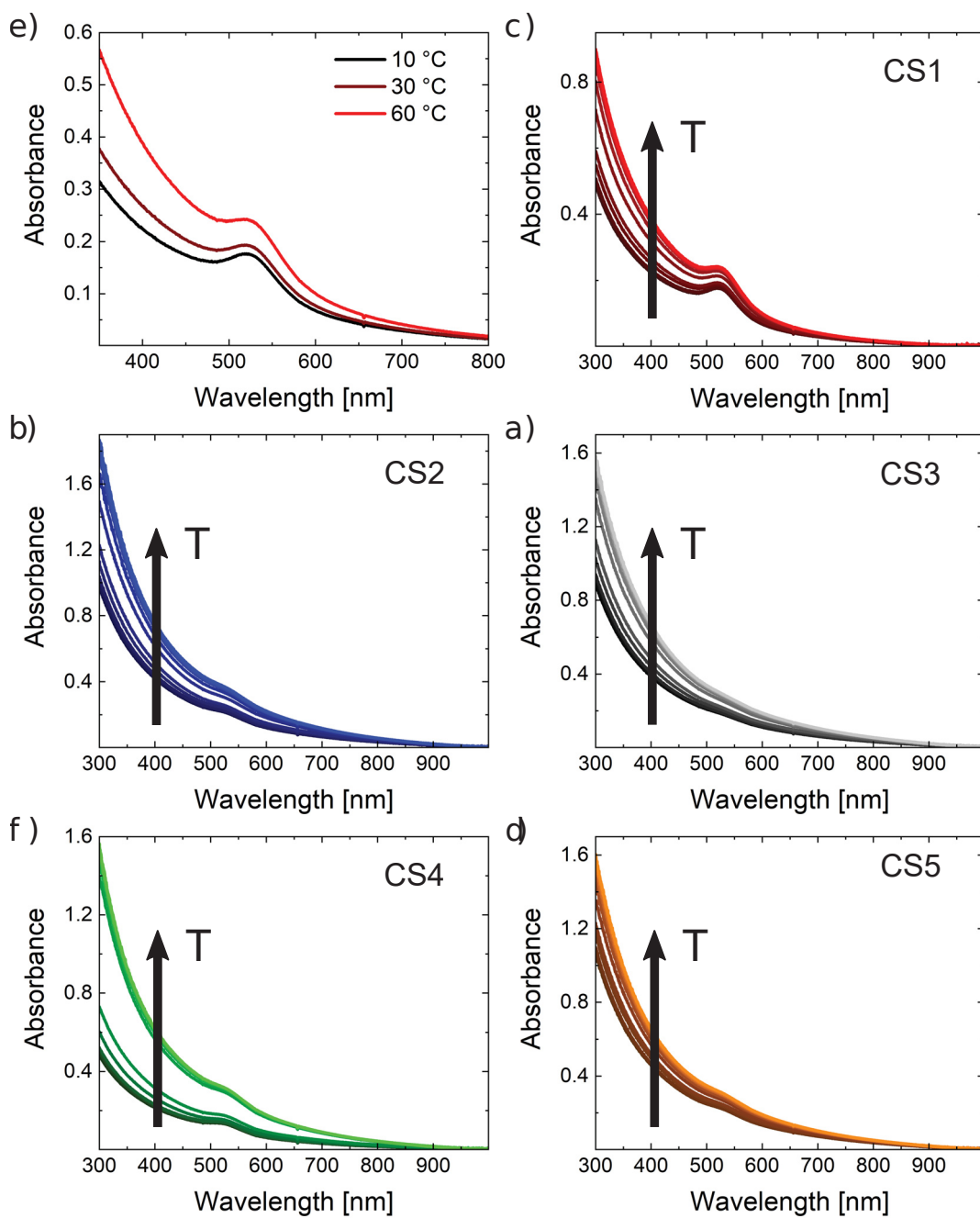


Figure S3: Evolution of the UV-Vis absorbance spectra of the CS microgels in dilute dispersion with increasing temperature. a) Sample CS1 at 10, 30 and 60 °C. b) - f) Spectra of CS1 - CS5 between 10 and 60 °C in 5 °C steps.

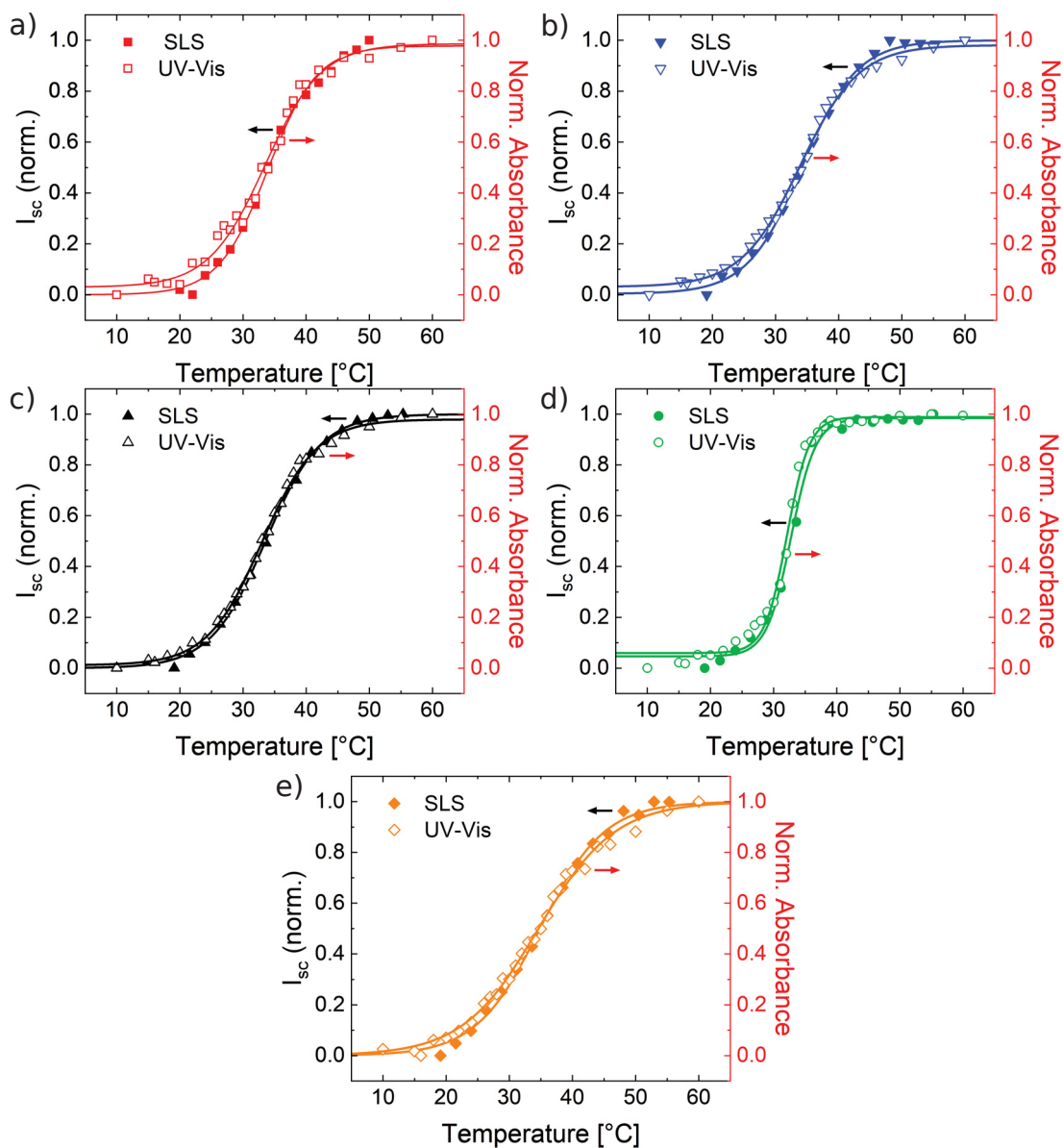


Figure S4: Comparison of the UV-Vis spectroscopy and SLS results. Absorbance data (filled symbols) correspond to a wavelength of 632.5 nm. Light scattering intensities from SLS (open symbols) were recorded at 632.8 nm. All datasets were normalized to 1 at the collapsed state. a) CS1, b) CS2, c) CS3, d) CS4, and e) CS5.

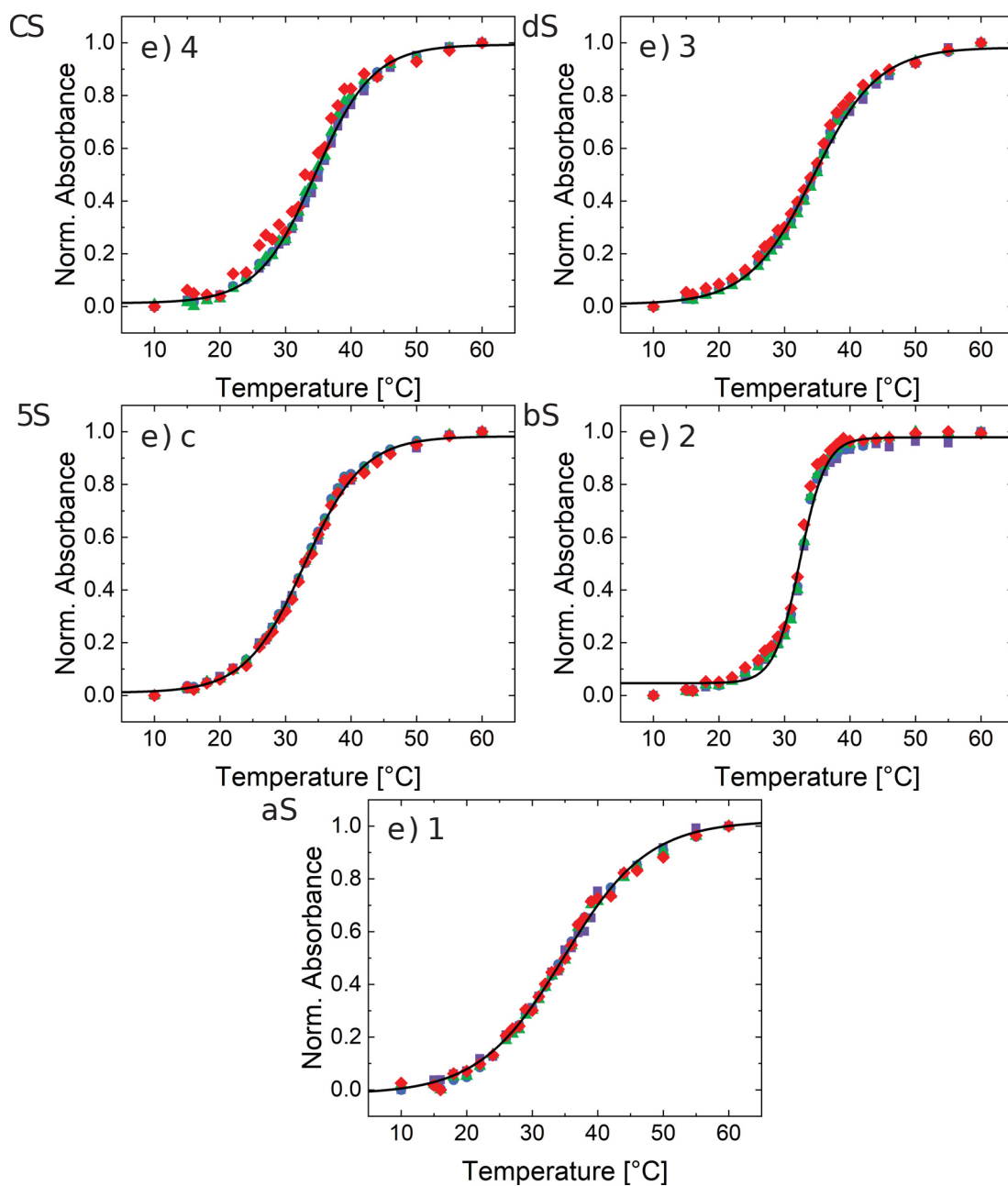


Figure S5: Normalized absorbances of the CS microgels at 300 nm (purple square), 400 nm (blue circles), 523 nm (green triangle) and 632.5 nm (red diamond) wavelengths as a function of temperature. Solid black lines correspond to the sigmoidal fits to the data. a) CS1, b) CS2, c) CS3, d) CS4, and e) CS5.

Scattering Contrasts for SAXS and SANS

Table S1 lists the scattering length densities (SLDs) of the used solvents (water and heavy water), gold, and PNIPAM for neutrons and X-rays as calculated using the SLD calculator provided by NIST.²²⁴ The SLD of PNIPAM was calculated assuming a density of 1.174 g cm^{-3} .²²⁵

Table S1: SLDs of water, heavy water, gold and PNIPAM for neutrons and X-rays. Also listed are scattering contrasts $|\Delta\text{SLD}|$ for gold and PNIPAM against the respective solvent.

| Source | SLD [\AA^{-2}] | | | | $ \Delta\text{SLD} $ [\AA^{-2}] | |
|----------|---------------------------|----------------------|----------------------|----------------------|--|----------------------|
| | H ₂ O | D ₂ O | Au | PNIPAM | Solvent-Au | Solvent-PNIPAM |
| neutrons | - | $6.34 \cdot 10^{-6}$ | $4.66 \cdot 10^{-6}$ | $8.69 \cdot 10^{-7}$ | $1.67 \cdot 10^{-6}$ | $5.47 \cdot 10^{-6}$ |
| X-rays | $9.50 \cdot 10^{-6}$ | - | $1.25 \cdot 10^{-4}$ | $1.10 \cdot 10^{-5}$ | $1.16 \cdot 10^{-4}$ | $1.50 \cdot 10^{-6}$ |

For our SANS experiments, the contrast ($|\Delta\text{SLD}|$) from the PNIPAM polymer in the CS microgel shell is more than three times higher than the contrast of gold against heavy water. The opposite is the case for SAXS. In SAXS, the contrast of the gold core is approximately two orders of magnitude higher than the contrast of PNIPAM against water.

Analysis of SAXS Data

Small-angle X-ray scattering (SAXS) measurements were performed to obtain the size, shape and dispersity of the AuNP cores as well as their number concentration. **Figure S6** shows the obtained scattering curves for the CS1 – CS5 samples.

As can be seen the form factors of the AuNP cores are nicely resolved with 1-2 form factor oscillations in the high q region and the Guinier plateau approaching in the mid to low q range (at approximately 0.1 nm^{-1}). In the low q region we observe a pronounced increase in scattering intensity for CS1, CS2, CS4 and CS5. This additional contribution is related to scattering from the PNIPAM microgel shells. Only for the largest microgels, CS3, this increase is not observed in the available q range. Due to the limited q range and the poor statistics at lowest q the form factors of the shells are not well resolved and we did not attempt to fit the microgel contribution. In contrast, the form factor contribution of the AuNP cores could be nicely described by a simple polydisperse sphere model. The black solid lines in each plot correspond to the respective form factor fits. The fits match the data nicely in the mid to high q range. The fits revealed average core radii of 6.5 nm for samples CS1 to CS3 and 6.8 nm for samples CS4 and CS5.

To access the particle number densities, N , we determined the forward scattering intensities, I_0 , from Guinier plots of each sample. **Figure S7** shows the respective Guinier plots with linear fits to the data (black, solid lines). I_0 was extracted from the intercepts of the linear fits.

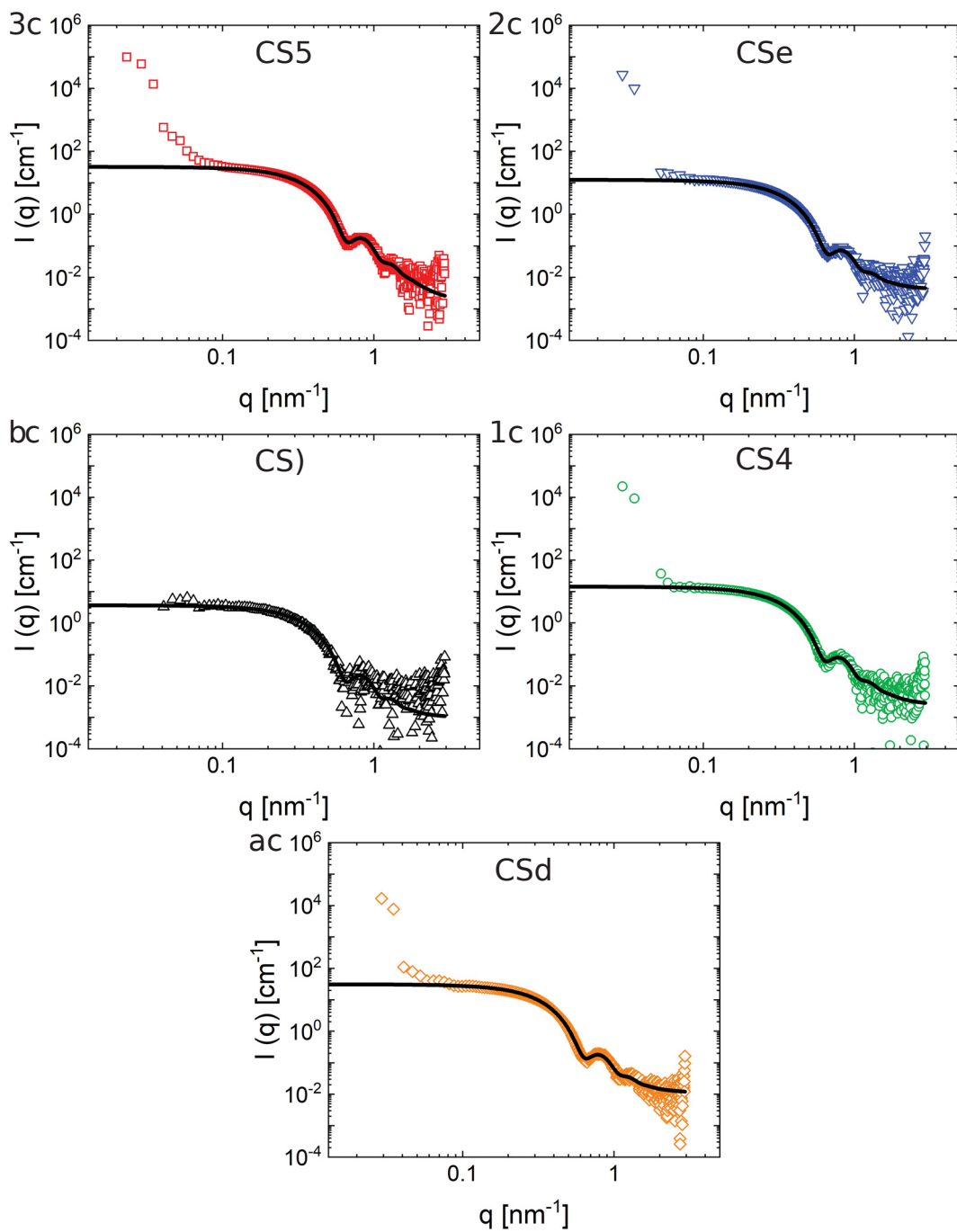


Figure S6: Results from SAXS measurements of the CS microgels. Symbols correspond to the measured data and black lines to the form factor fits (AuNP cores only). a) CS1, b) CS2, c) CS3, d) CS4, and e) CS5.

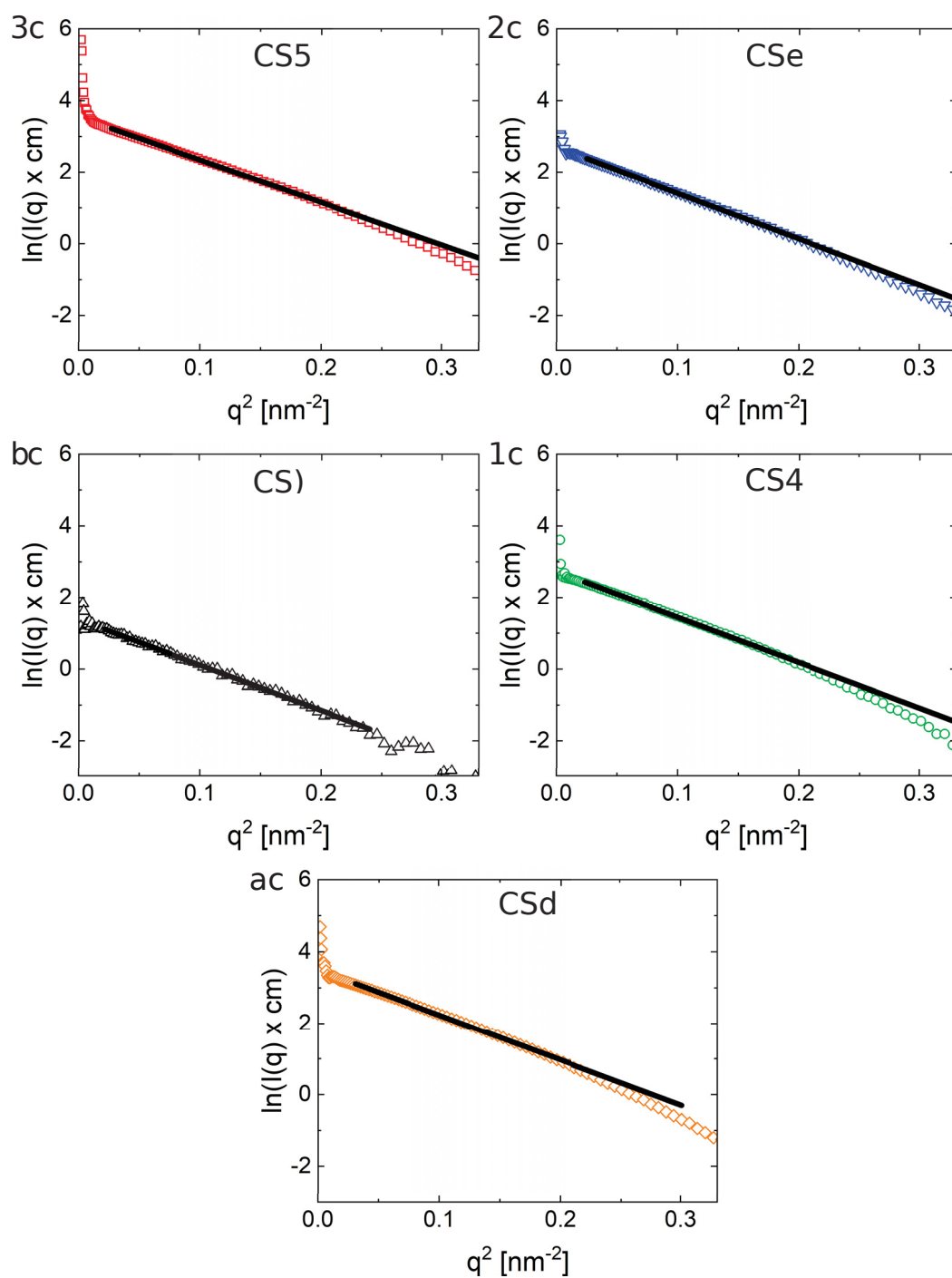


Figure S7: Guinier plots of the SAXS data for a) CS1, b) CS2, c) CS3, d) CS4, and e) CS5 respectively. The solid black lines correspond to linear fits to the data.

Using the obtained values of I_0 , we can calculate the AuNP mass concentration, c , as follows:

$$c = \frac{I_0 \cdot N_A \cdot \rho^2}{M_{\text{Au-core}} \cdot \Delta\eta^2} \quad (4.2)$$

Here, N_A is the Avogadro constant, ρ the density of gold (19.32 g mL^{-1}), $M_{\text{Au-core}}$ is the average molecular weight of the gold cores, and $\Delta\eta$ is the scattering length density difference between gold and water (see table S1). The molecular weight of the AuNP cores was calculated using the density of gold and the core volume calculated using the radii from the form factor analysis of the SAXS data, *i.e.* 6.5 and 6.8 nm. With the values of c we could then calculate N taking into account the average mass, m , of the gold cores:

$$N = \frac{c}{m} = \frac{c \cdot N_A}{M_{\text{Au-core}}} \quad (4.3)$$

From TEM image analysis we know already that on average each CS microgel contains only a single AuNP core. This is the case for all batches of CS microgels. Therefore, values of N correspond to the number densities of CS microgels since the number of microgels is on average the same as the number of cores. The resulting number densities of the microgels are summarized in **Table S2**.

Table S2: Calculated microgel number densities, N , from absolute intensity SAXS measurements performed on samples with different weight concentrations (wt %).

| Sample | wt % | $N [\text{cm}^{-3}]$ |
|--------|------|----------------------|
| CS1 | 1.9 | $1.97 \cdot 10^{13}$ |
| CS2 | 1.9 | $8.46 \cdot 10^{12}$ |
| CS3 | 0.9 | $2.28 \cdot 10^{12}$ |
| | 2.4 | $5.74 \cdot 10^{12}$ |
| | 4.7 | $1.21 \cdot 10^{13}$ |
| CS4 | 1.9 | $6.66 \cdot 10^{12}$ |
| CS5 | 0.9 | $2.57 \cdot 10^{12}$ |

Extinction Cross-Sections

Measured absorbances for the CS microgels were transformed into extinction cross-sections, C_{ext} , using the number densities, N , from SAXS measurements using the Lambert-Beer law:

$$\begin{aligned}
 I(d) &= I_0 \exp(-C_{\text{ext}} N d) \\
 \Leftrightarrow \ln\left(\frac{I_0}{I(d)}\right) &= C_{\text{ext}} N d \\
 \Leftrightarrow \log_{10}\left(\frac{I_0}{I(d)}\right) &= A = \frac{C_{\text{ext}} N d}{2.303}
 \end{aligned} \tag{4.4}$$

Here, I_0 corresponds to the incident light intensity before the sample and $I(d)$ to the attenuated intensity after the sample of thickness d . An example of the cross-section calculation using the absorbance A at 350 nm for CS1 is demonstrated in following:

$$C_{\text{ext}} = \frac{2.303A}{Nd} = \frac{2.303 \cdot 0.339}{1.832 \cdot 10^{17} \text{m}^{-3} \cdot 0.01 \text{m}} = 4.262^{-16} \text{m}^2 \tag{4.5}$$

Figure S8 shows wavelength-dependent extinction cross-sections for all CS microgels at selected temperatures of 25 °C and 50 °C. **Figure S8** a) and b) illustrate spectra in the swollen state at 25 °C. It can be seen that the extinction cross-section at a given wavelength increases with increasing particle size (CS1 – CS3) and with increasing cross-linking density (CS4, CS2 and CS5). **Figure S8** c) and d) show the corresponding spectra in the collapsed state. Compared to the swollen state, the values of C_{ext} are significantly higher. Still the same trends are observed in the swollen state apart from the very similar extinctions for CS4 and CS2.

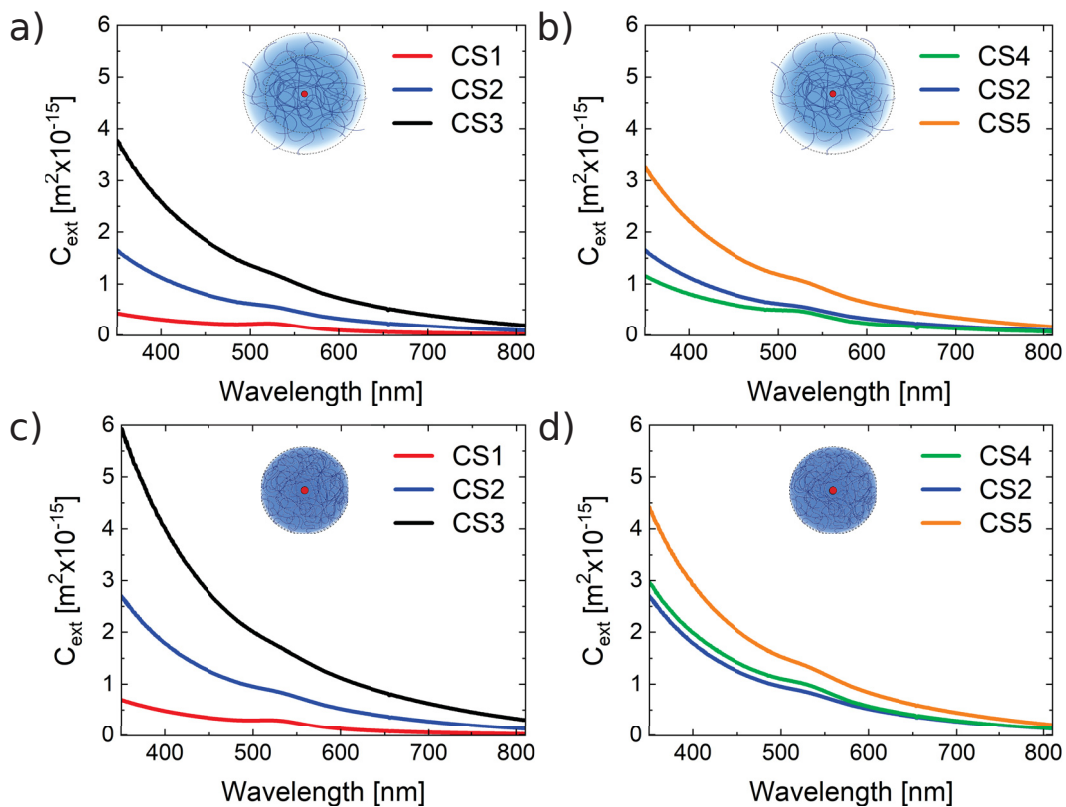


Figure S8: Extinction cross-sections for the CS microgels in the swollen state at 25 °C (a and b) and in the collapsed state at 50 °C (c and d).

Refractive Index Measurements

Table S3 lists refractive indices at $\lambda = 589.3$ nm measured from dilute, aqueous dispersions of the CS microgels, a dried film prepared from linear PNIPAM homopolymer and water. Measurements were performed at 25 °C and 50 °C, *i.e.* in the swollen and collapsed state of the microgels.

Table S3: Measured refractive indices $n_{\text{dispersion}}$ at $\lambda = 589.3$ nm of dispersions of the CS microgels with various weight concentrations (wt %), of a PNIPAM homopolymer film and water at 25 °C and 50 °C.

| Sample | wt % (polymer) | $n_{\text{dispersion}}$ (25 °C) | $n_{\text{dispersion}}$ (50 °C) |
|-------------|----------------|---------------------------------|---------------------------------|
| CS1 | 1.9 | 1.3359(5) | 1.3329(4) |
| CS2 | 1.9 | 1.3363(2) | 1.3332(8) |
| CS3 | 0.9 | 1.3342(4) | 1.3310(5) |
| | 2.4 | 1.3367(3) | 1.3364(8) |
| | 4.7 | 1.3411(8) | 1.3379(6) |
| | 9.4 | 1.3488(2) | 1.3451(7) |
| CS4 | 1.9 | 1.3342(0) | 1.3308(1) |
| CS5 | 0.9 | 1.3340(9) | 1.3306(7) |
| PNIPAM film | 94.3 | 1.4875(3) | - |
| Water | 0 | 1.3324(9) | 1.3291(1) |

Figure S9 shows measured refractive indices obtained from different concentrations of aqueous dispersions of the CS3 microgels and additionally a PNIPAM homopolymer film recorded at 589.3 nm. Freeze-dried particles were used to obtain dispersions with 0.9, 2.4, 4.7 and 9.4 weight concentration (wt %). The values were corrected for the 5.7 % residual water.²⁰² For the PNIPAM homopolymer film we used linear PNIPAM (65,000 g mol⁻¹) synthesized by RAFT according to Ebeling and Vana.²²⁶ The perfect linear scaling (red line) of the data allowed to extrapolate to 100% PNIPAM yielding a refractive index of 1.50.

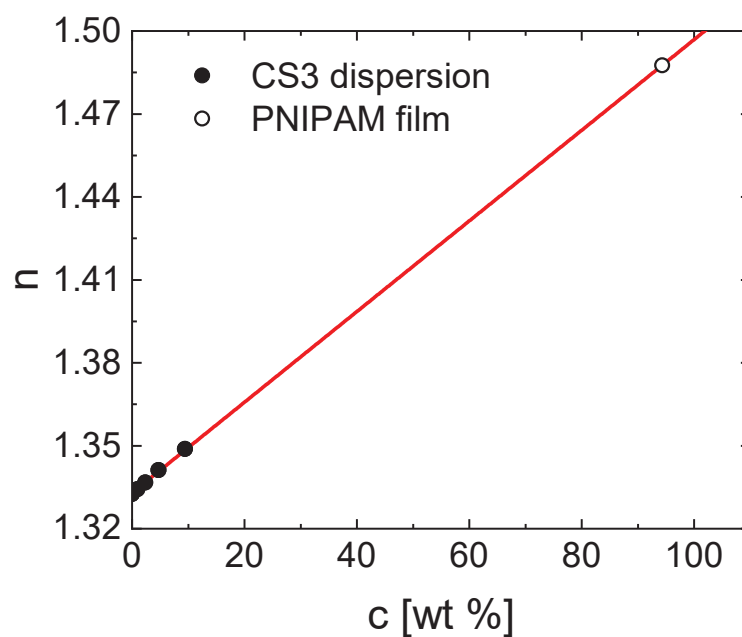


Figure S9: Results from refractive index measurements at 589.3 nm (25 °C) of the sample CS3 of differently concentrated dispersions and a PNIPAM homopolymer film (empty circle). The red line corresponds to a linear fit to the measured data.

Analysis of SANS Data

We performed SANS measurements with all CS microgels at four different temperatures of 25, 35, 37 and 50 °C to cover the most critical stages during the VPT. For each sample and temperature, the recorded data at different sample-to-detector distances were radially averaged, normalized to absolute scale and merged to yield single scattering profiles covering a broad q range. Analysis of the scattering profiles was done using the SASfit software.²⁰³

The instrument resolution was taken into account as described in the experimental section of the main manuscript.

Before we discuss the data analysis, we want to note that we neglect the presence of the gold cores in our CS microgels because of two reasons: 1) The scattering contrast of gold in heavy water is relatively low. 2) The gold cores are very small as compared to the overall microgel volume.

The scattering intensity, $I(q)$, of chemically cross-linked gels is usually the result of static and dynamic contributions.⁹⁸ Thus, in a typical SANS experiment $I(q)$ is given by:

$$I(q) = I_{stat}(q) + I_{dyn}(q) + I_{inc} \quad (4.6)$$

Here, I_{inc} denotes the incoherent background, which is most often a simple, q -independent offset. The static contribution $I_{stat}(q)$ is caused by the static network heterogeneities due to the cross-linking points. The dynamic contribution I_{dyn} is related to local concentration fluctuations.²²⁷ The latter contribution is typically taken into account by a Lorentzian function (Ornstein-Zernicke contribution):⁹⁹

$$I_{dyn}(q) = \frac{I_L(0)}{1 + q^2\xi^2} \quad (4.7)$$

$I_L(0)$ defines the Lorentzian intensity and ξ is the correlation length, which is related to the blob, respectively, mesh size of the network in the swollen state. The latter parameter depends on the cross-linking and swelling state of the polymer microgel.⁹⁸

For spherical microgels - depending on their size and the studied q range - the static scattering contribution is typically dominated by the form factor, $P(q)$ of the microgels. In the collapsed state this form factor is typically well described by a simple polydisperse sphere model. For a homogeneous, spherical object with radius R , the form factor, P_{hom} , is given by:

$$P_{hom}(q) = \left[3 \frac{\sin(qR) - qR\cos(qR)}{(qR)^3} \right]^2 \quad (4.8)$$

In the swollen state, PNIPAM microgels cross-linked with BIS show a pronounced gradient in cross-linking. This core-shell structure, where the inner polymer network is higher cross-linked than the outer region, can be described by the fuzzy sphere model, first introduced for microgels by Stieger *et al.*⁴⁰ This form factor is obtained by convoluting equation 4.8 with a Gaussian:

$$P_{inhom}(q) = \left[3 \frac{\sin(qR) - qR \cos(qR)}{(qR)^3} \times \exp\left(-\frac{(\sigma q)^2}{2}\right) \right]^2 \quad (4.9)$$

Here, σ defines the thickness of the fuzzy shell. More precisely, the total radius from SANS is given by $R_{\text{SANS}} = R + 2\sigma$, while the radius of the inner homogenous density microgel region is given by $R_{\text{box}} = R - 2\sigma$. In the limiting case where $\sigma = 0$, equation 4.9 becomes equal to the form factor of homogeneous spheres, P_{hom} . The radial scattering length density profile for the fuzzy sphere model, η_{FuzzySph} , is given by:

$$\eta_{\text{FuzzySph}}(r) = (\eta_{sph} - \eta_{sol}) \left(\frac{\left(\exp\left[-\frac{(r+R)^2}{2\sigma^2}\right] - \exp\left[-\frac{(r-R)^2}{2\sigma^2}\right] \right) \sigma}{\sqrt{2\pi}r} + \frac{1}{2} \operatorname{erf}\left[\frac{r+R}{\sqrt{2}|\sigma|}\right] - \frac{1}{2} \operatorname{erf}\left[\frac{r-R}{\sqrt{2}|\sigma|}\right] \right) \quad (4.10)$$

Here, η_{sph} corresponds to the scattering length density of the inner homogeneous microgel region and η_{sol} refers to the scattering length density of the dispersion medium. In our case heavy water was used as dispersion medium in the SANS experiments. With the scattering length densities from **Table S1** one can extract the radial profiles of the polymer volume fractions ϕ :

$$\eta_{\text{FuzzySph}}(r) = \eta_{sol}(1 - \phi(r)) + \eta_{\text{PNIPAM}}\phi(r) \quad (4.11)$$

The scattering intensity for a fuzzy sphere, I_{FuzzySph} , is given by:

$$I_{\text{FuzzySph}}(q) = \left[(\eta_{sph} - \eta_{sol}) 4\pi R^3 \frac{\sin(qR) - qR \cos(qR)}{(qR)^3} \exp\left[-\frac{1}{2}\sigma^2 q^2\right] \right]^2 \quad (4.12)$$

All our SANS profiles were successfully fitted using:

$$I(q) = I_{\text{FuzzySph}}(q) + \frac{I_L(0)}{1 + q^2\xi^2} + I_{inc} \quad (4.13)$$

The respective SANS profiles and fits to the data can be found in the main manuscript.

Figure S10 summarizes the experimentally determined radii of the CS microgels from DLS and SANS at different temperatures. Generally, all samples reveal the same trends. The hydrodynamic radii are always the largest independent of the swelling state of the microgels. The radii of the inner, more homogeneous microgel regions, R_{box} remain almost constant for each CS microgel while the thickness of the fuzzy shell constantly decreases with increasing temperature leading to the reduction in R_{SANS} .

Tables S4 – S8 give an overview of the obtained fitting parameters from SANS data analysis. The particle number densities, N , were obtained from SAXS measurements. I_{inc} corresponds to the constant background intensity, values R and σ are the radius of the fuzzy sphere and the thickness of the fuzzy shell, respectively. The radius of the

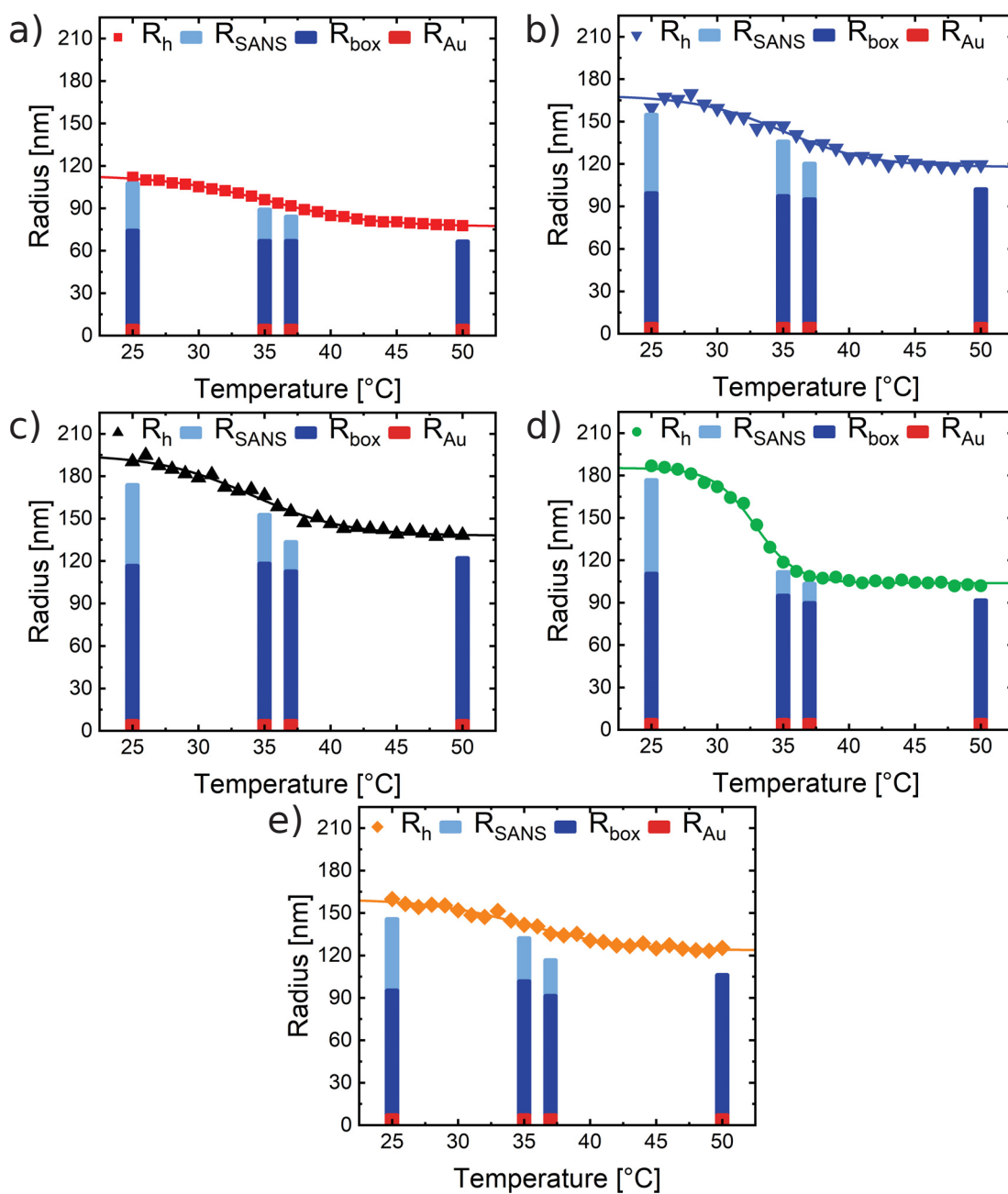


Figure S10: Experimentally determined radii from DLS and SANS as a function of temperature. a) CS1, b) CS2, c) CS3, d) CS4, and e) CS5. Filled symbols correspond to the hydrodynamic radii. The red bars highlight the gold core radii, light blue bars the radii of the microgels according to SANS analysis, and the dark blue bars correspond to R_{box} .

homogeneous inner region R_{box} and the overall particle radius R_{SANS} are given by: $R_{box} = R - 2\sigma$ and $R_{SANS} = R + 2\sigma$. The polydispersity was taken into account by a Gaussian distribution function with the standard deviation parameter s . The radius of gyration R_g was obtained by a Guinier approximation. The hydrodynamic radii R_h were obtained by DLS. $\eta_{solvent}$ is the scattering length density of the solvent, here heavy water and η_{box} is the scattering length density of the inner homogeneous polymer region with R_{box} . We used equations 4.11 and 6 (main manuscript) for the calculation of the polymer volume fraction ϕ_{box} and n_{box} . For the fuzzy shell, we define ϕ_{shell} , to be to half the value of ϕ_{box} .

Table S4: Overview of parameters obtained from fitting of the SANS data of sample CS1.

| | 25 °C | 35 °C | 37 °C | 50 °C |
|--|------------------------|------------------------|------------------------|------------------------|
| N [cm^{-3}] | 4.924×10^{12} | 4.924×10^{12} | 4.924×10^{12} | 4.924×10^{12} |
| I_{inc} [cm^{-1}] | 0.051 | 0.050 | 0.051 | 0.052 |
| R [nm] | 90.9 | 78.0 | 75.5 | 66.5 |
| σ [nm] | 8.37 | 5.58 | 4.3 | 0 |
| R_{box} [nm] | 74.2 | 66.8 | 66.9 | 66.5 |
| R_{SANS} [nm] | 107.6 | 89.2 | 84.1 | 66.5 |
| R_h [nm] | 111 | 96 | 91 | 78 |
| R_g [nm] | 78.5 | 68.4 | 63.3 | 58.0 |
| R_g/R_h | 0.71 | 0.71 | 0.70 | 0.74 |
| s [nm] | 9.1 | 8.0 | 7.9 | 6.8 |
| $\eta_{solvent}$ (D_2O) [nm^{-2}] | 0.000634 | 0.000634 | 0.000634 | 0.000634 |
| η_{box} [nm^{-2}] | 0.000532 | 0.000472 | 0.000456 | 0.000358 |
| ϕ_{box} | 0.19 | 0.30 | 0.33 | 0.50 |
| n_{box} | 1.364 | 1.382 | 1.387 | 1.417 |
| ϕ_{shell} | 0.09 | 0.15 | 0.016 | - |
| n_{shell} | 1.348 | 1.357 | 1.359 | - |

Table S5: Overview of parameters obtained from fitting of the SANS data of sample CS2.

| | 25 °C | 35 °C | 37 °C | 50 °C |
|--|------------------------|------------------------|------------------------|------------------------|
| N [cm^{-3}] | 2.115×10^{12} | 2.115×10^{12} | 2.115×10^{12} | 2.115×10^{12} |
| I_{inc} [cm^{-1}] | 0.050 | 0.050 | 0.050 | 0.051 |
| R [nm] | 127.0 | 116.6 | 107.5 | 102 |
| σ [nm] | 13.9 | 9.7 | 6.3 | 0 |
| R_{box} [nm] | 99.2 | 97.3 | 94.9 | 102 |
| R_{SANS} [nm] | 154.8 | 135.9 | 120.1 | 102 |
| R_h [nm] | 164 | 147 | 134 | 118 |
| R_g [nm] | 109.5 | 95.8 | 94.6 | 85.3 |
| R_g/R_h | 0.67 | 0.65 | 0.71 | 0.72 |
| s [nm] | 15.5 | 14.3 | 12.3 | 13.5 |
| $\eta_{solvent}$ (D_2O) [nm^{-2}] | 0.000634 | 0.000634 | 0.000634 | 0.000634 |
| η_{box} [nm^{-2}] | 0.000535 | 0.000492 | 0.000466 | 0.000408 |
| ϕ_{box} | 0.18 | 0.26 | 0.31 | 0.41 |
| n_{box} | 1.363 | 1.376 | 1.384 | 1.401 |
| ϕ_{shell} | 0.09 | 0.13 | 0.15 | - |
| n_{shell} | 1.347 | 1.354 | 1.354 | - |

Table S6: Overview of parameters obtained from fitting of the SANS data of sample CS3.

| | 25 °C | 35 °C | 37 °C | 50 °C |
|--|------------------------|------------------------|------------------------|------------------------|
| N [cm^{-3}] | 1.140×10^{12} | 1.140×10^{12} | 1.140×10^{12} | 1.140×10^{12} |
| I_{inc} [cm^{-1}] | 0.050 | 0.049 | 0.050 | 0.050 |
| R [nm] | 145.5 | 135.3 | 123.0 | 122 |
| σ [nm] | 14.3 | 8.6 | 5.2 | 0 |
| R_{box} [nm] | 116.6 | 118.0 | 112.6 | 122 |
| R_{SANS} [nm] | 173.8 | 152.6 | 133.3 | 122 |
| R_h [nm] | 190 | 166 | 155 | 139 |
| R_g [nm] | 123.0 | 111.0 | 107.2 | 99.0 |
| R_g/R_h | 0.65 | 0.67 | 0.69 | 0.71 |
| s [nm] | 19.5 | 14.5 | 16 | 9.7 |
| $\eta_{solvent}$ (D_2O) [nm^{-2}] | 0.000634 | 0.000634 | 0.000634 | 0.000634 |
| η_{box} [nm^{-2}] | 0.000515 | 0.000471 | 0.000439 | 0.0003837 |
| ϕ_{box} | 0.22 | 0.30 | 0.37 | 0.46 |
| n_{box} | 1.368 | 1.382 | 1.392 | 1.410 |
| ϕ_{shell} | 0.11 | 0.15 | 0.18 | - |
| n_{shell} | 1.350 | 1.357 | 1.362 | - |

Table S7: Overview of parameters obtained from fitting of the SANS data of sample CS4.

| | 25 °C | 35 °C | 37 °C | 50 °C |
|---|------------------------|------------------------|------------------------|------------------------|
| N [cm ⁻³] | 1.666×10^{12} | 1.666×10^{12} | 1.666×10^{12} | 1.666×10^{12} |
| I_{inc} [cm ⁻¹] | 0.202 | 0.202 | 0.202 | 0.203 |
| R [nm] | 143.6 | 103.2 | 96.5 | 91.6 |
| σ [nm] | 16.6 | 4.2 | 3.4 | 0 |
| R_{box} [nm] | 110.5 | 94.9 | 89.7 | 91.6 |
| R_{SANS} [nm] | 176.7 | 111.6 | 103.3 | 91.6 |
| R_h [nm] | 186 | 119 | 109 | 104 |
| R_g [nm] | 104.5 | 82.9 | 78.8 | 75.2 |
| R_g/R_h | 0.56 | 0.70 | 0.72 | 0.72 |
| s [nm] | 16.7 | 9.9 | 9.0 | 7.2 |
| $\eta_{solvent}$ (D ₂ O) [nm ⁻²] | 0.000634 | 0.000634 | 0.000634 | 0.000634 |
| η_{box} [nm ⁻²] | 0.000581 | 0.000470 | 0.000425 | 0.000383 |
| ϕ_{box} | 0.10 | 0.30 | 0.38 | 0.46 |
| n_{box} | 1.348 | 1.382 | 1.396 | 1.410 |
| ϕ_{shell} | 0.05 | 0.15 | 0.19 | - |
| n_{shell} | 1.340 | 1.357 | 1.364 | - |

Table S8: Overview of parameters obtained from fitting of the SANS data of sample CS5.

| | 25 °C | 35 °C | 37 °C | 50 °C |
|---|------------------------|------------------------|------------------------|------------------------|
| N [cm ⁻³] | 1.286×10^{12} | 1.286×10^{12} | 1.286×10^{12} | 1.286×10^{12} |
| I_{inc} [cm ⁻¹] | 0.166 | 0.166 | 0.167 | 0.168 |
| R [nm] | 120.5 | 117.0 | 104.0 | 106.2 |
| σ [nm] | 12.6 | 7.6 | 6.3 | 0 |
| R_{box} [nm] | 95.3 | 101.8 | 91.4 | 106.2 |
| R_{SANS} [nm] | 145.7 | 132.2 | 116.6 | 106.2 |
| R_h [nm] | 157 | 142 | 135 | 124 |
| R_g [nm] | 95.5 | 93.9 | 93.2 | 84.9 |
| R_g/R_h | 0.61 | 0.66 | 0.69 | 0.68 |
| s [nm] | 13.5 | 12.0 | 14.0 | 11.0 |
| $\eta_{solvent}$ (D ₂ O) [nm ⁻²] | 0.000634 | 0.000634 | 0.000634 | 0.000634 |
| η_{box} [nm ⁻²] | 0.000505 | 0.000485 | 0.000464 | 0.000431 |
| ϕ_{box} | 0.24 | 0.27 | 0.31 | 0.37 |
| n_{box} | 1.372 | 1.378 | 1.384 | 1.394 |
| ϕ_{shell} | 0.12 | 0.14 | 0.16 | - |
| n_{shell} | 1.352 | 1.355 | 1.358 | - |

Extinction of Small Silica Nanoparticles

Figure S11 a) shows an absorbance - actually the extinction or scattering - spectrum (black, solid line) recorded from a dilute, aqueous dispersion of silica nanoparticles as non-absorbing reference particles. DLS provided a hydrodynamic radius of 14 nm. The dashed line corresponds to the results from FDTD simulations. Both datasets were normalized at 400 nm. The simulated spectrum matches nicely the experimental data. **Figure S11 b)** shows the same data plotted against λ^{-4} corresponding to the power law scaling for Rayleigh scattering. Both the experimental and theoretical data show linear scaling with λ^{-4} with only small deviations.

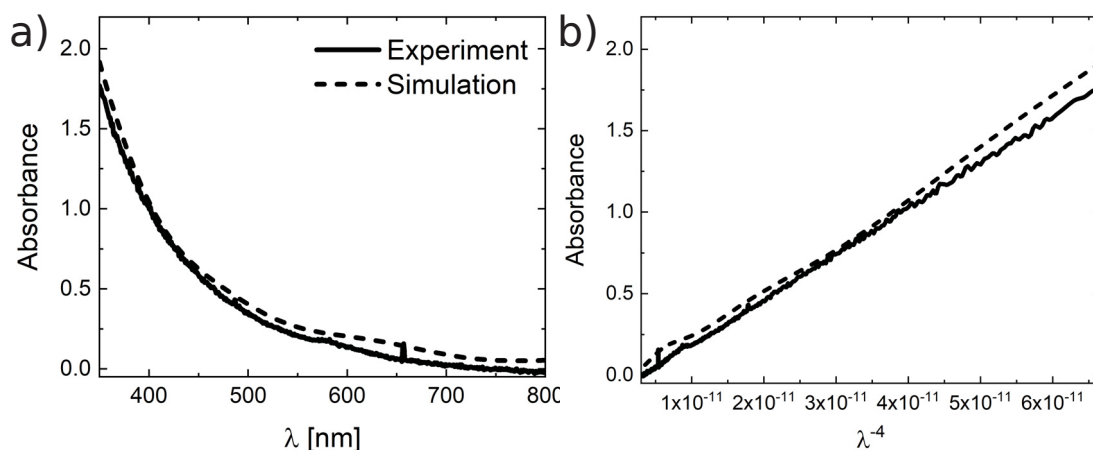


Figure S11: Absorbance spectra of SiO_2 nanoparticles ($R_h = 14$ nm) in dilute dispersion. Black solid lines correspond to the experimental spectra and the dashed lines to the FDTD simulation results. The curves were normalized at 400 nm. a) Absorbance versus wavelength. b) Absorbance versus λ^{-4} .

Mie Theory Calculation

Figure S12 compares experimental and calculated spectra (Mie theory) for CS2 particles in the swollen (a) and collapsed state (b). The calculations were done using the MieLab²²⁸ software using the same radii and refractive indices as for our FDTD simulations (**Table 4** main manuscript). The spectra were normalized at 400 nm to allow for better direct comparison. For the swollen state, shown in a), we used a simple core-shell model and for the collapsed state, in b), we assume a homogeneous sphere for the simulations. Qualitatively the calculated spectra are in agreement with the measured data although the power law scaling is significantly different. The experimental data show much steeper increases in absorbances with decreasing wavelength for both states of swelling.

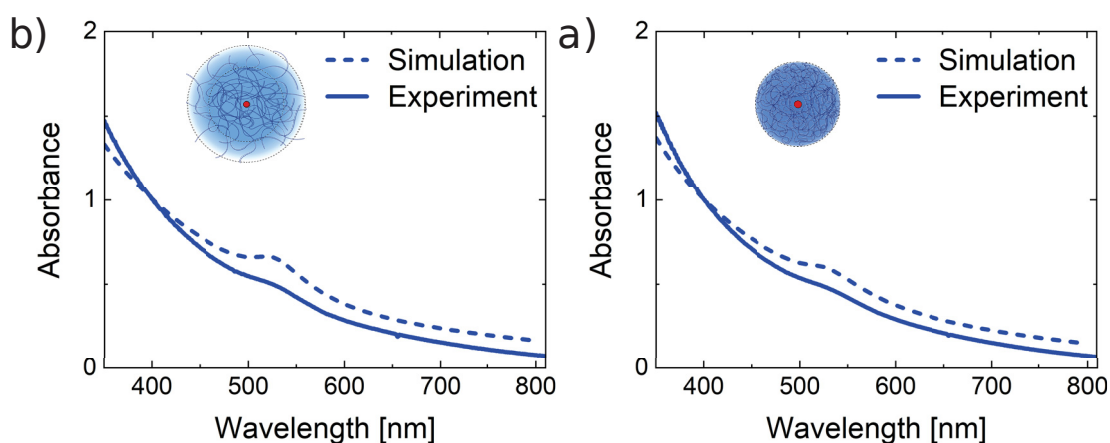


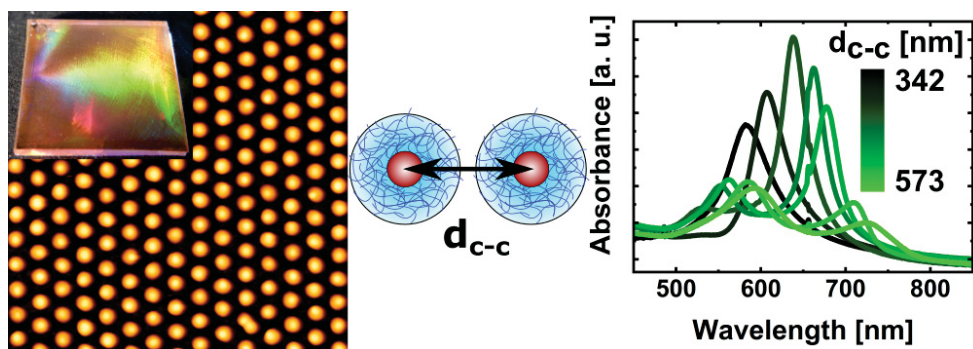
Figure S12: Comparison of calculated (dashed lines) and experimental absorbance spectra (solid lines) of the CS2 sample. a) Swollen state (25 °C). b) Collapsed state (50 °C). All spectra were normalized at 400 nm.

5 Surface Lattice Resonances in Self-Assembled Gold Nanoparticle Arrays: Impact of Lattice Period, Structural Disorder, and Refractive Index on Resonance Quality

Ekaterina Ponomareva¹, Kirsten Volk¹, Paul Mulvaney²,
and Matthias Karg^{1*}

¹Institut für Physikalische Chemie I: Kolloide und Nanooptik,
Heinrich-Heine-Universität Düsseldorf, Universitätsstraße 1, D-40225 Düsseldorf,
Germany

²ARC Centre of Excellence in Exciton Science, School of Chemistry, The
University of Melbourne, Parkville, VIC 3010, Australia



Reprinted with permission from *Langmuir* 2020, 36, 13601-1312
Copyright 2020 American Chemical Society

5.1 Abstract

Surface lattice resonances are optical resonances composed of hybridized plasmonic and diffractive modes. These collective resonances occur in periodic arrays of plasmonic nanoparticles with wavelength-scale interparticle distances. The appearance and strength of surface lattice resonances strongly depend on the single particle localized surface plasmon resonance and its spectral overlap with the diffractive modes of the array. Coupling to in-plane orders of diffraction is also strongly affected by the refractive index environment and its symmetry.

In this work, we address the impact of the interparticle distance, the symmetry of the refractive index environment, and structural imperfections in self-assembled colloidal monolayers on the plasmonic-diffractive coupling. For this purpose, we prepared hexagonally ordered, non-close packed monolayers of gold nanoparticles using a fast and efficient, interface-mediated, colloidal self-assembly approach. By tuning the thickness and deformability of the polymer shells, we were able to prepare monolayers with a broad range of interparticle distances. The optical properties of the samples were studied experimentally by UV-Vis spectroscopy and theoretically by finite difference time domain simulations. The measured and simulated spectra allow a comprehensive analysis of the details of electromagnetic coupling in periodic plasmonic arrays. In particular we identify relevant criteria required for surface lattice resonances in the visible wavelength range with optimized quality factors in self-assembled monolayers.

5.2 Introduction

Metal nanostructures are known to interact with external electromagnetic fields due to the excitation of surface plasmon modes—collective oscillations of the conduction electrons¹⁶. The strength and energy as well as the number of these modes depend critically on the type of metal¹³⁶, the nanostructure size^{15,137} and shape^{137,138,139}, the dielectric properties of the surrounding environment^{137,140}, and the nanostructure arrangement^{229,230,231,232,233,234}. Individual nanoparticles composed of gold or silver with diameters smaller than approximately 100 nm primarily support single localized surface plasmon resonances (LSPRs) that are due to dipolar excitations of the conduction electrons.^{15,235} These dipolar LSPRs can be excited with light in the visible wavelength range and this phenomenon explains the vivid colors of dilute dispersions of gold and silver nanoparticles.^{17,236} Meanwhile, for the smallest sizes, up to a few tens of nanometers in diameter, the interaction with light is dominated by absorption, and scattering becomes dominant for larger sizes because (Rayleigh) scattering intensity scales with the sixth power of the particle diameter ($I_{sc} \propto D^6$). LSPRs concentrate electromagnetic fields into nanoscale volumes and exhibit extinction cross sections exceeding those of molecular absorbers such as organic dyes by several orders of magnitude and consequently, they may have applications in solar energy harvesting^{27,237}, ultrasensitive sensing¹⁸, lasing¹⁹ and photocatalysis²⁰. Nevertheless, gold, in particular, is a relatively poor plasmonic material and suffers high intrinsic absorption losses in the visible region, in particular,

at shorter wavelengths.^{22,153} The full width at half maximum (FWHM) of the LSPR is approximately 80-100 nm for gold nanoparticles in a size range of ~ 8 -100 nm^{23,238}. The strong damping and the resulting low quality factors ($Q = \lambda/\Delta\lambda$) limit the potential of gold nanoparticles for many nanophotonic applications. Consequently, strategies are needed to enhance the Q-factor; ideally these strategies should employ both simple building blocks and scalable fabrication procedures. A powerful strategy for reducing losses in noble metal nanostructures is to arrange the nanoparticles into periodic arrays with wavelength-scale periodicities. Short- and long-range interactions in such arrays can result in higher field enhancements and resonances with significantly improved Q-factors^{25,154}. For large enough periodicities, spectrally narrow surface lattice resonances (SLRs) result from the collective radiative coupling between the single particle LSPRs and diffractive modes. In the case of coupling to in-plane modes of diffraction, *i.e.* the grating Rayleigh anomaly (RA)¹⁵⁰, a uniform dielectric environment surrounding the plasmonic particle array is required^{23,239}. It has been shown that an asymmetric environment suppresses long-range interactions between the nanoparticles due to scattering losses²⁴⁰. For an in-plane homogeneous environment, the RAs lead to the formation of propagating grazing waves in the plane of the array³⁰. SLRs were first observed and described in 2008 by Kravets *et al.*²⁴¹ and by Augu e and Barnes.¹⁵¹ Since then, fundamental spectroscopy of SLRs and the experimental realization of periodic plasmonic arrays that can support high Q-factor SLRs have both become topics of intense studies, as reflected by the appearance of several recent reviews.^{23,230,242}

Until now, electron-beam lithography has been the method of choice for producing periodic particle arrays with nearly perfect structural control. Using this method arrays with different lattice symmetries¹⁵⁸ and even arrays comprising asymmetric particle dimers²⁴³ have been prepared. However, more recently methods suitable for large area fabrication such as soft interference lithography have gained increasing interest²⁴⁴. As an alternative, our group has demonstrated that colloidal self-assembly of core-shell building blocks is well suited to the production of periodic plasmonic particles arrays that can extend over cm² areas^{21,38,245}. We have also shown that such arrays can support the formation of SLRs, albeit possessing relatively low Q-factors^{34,131}. Although self-assembly offers rapid, low-cost and low-tech production of large area arrays from relatively simple building blocks²³¹, the method typically results in significantly more defects and smaller domain sizes. Hence, it is important to identify experimental parameters that can yield high quality resonances. For domain sizes much larger than the exciting wavelength, a larger lattice period will result in a higher quality mode^{151,246}; however, different rules may apply to self-assembled lattices with limited domain size and multidomain character. A direct comparison between experimental and theoretical extinction properties of imperfect periodic particle arrays as a function of lattice period is currently not available. Consequently, it remains unclear how competitive self-assembly strategies are compared to other techniques used for the fabrication of particle arrays that support SLRs.

In this work, we investigate the optical properties of periodic plasmonic monolayers in both symmetric and asymmetric refractive index environments. We prepare these monolayers by a readily available, robust, and efficient interface-mediated self-assembly

procedure that yields hexagonally ordered particle arrangements on cm^2 substrates. By using colloidal building blocks with plasmonic gold nanoparticle cores and soft, deformable polymer shells of different thicknesses, we obtain lattices with a broad range of interparticle distances. This allows us to study the optical response of the periodic structures and the effects of spectral overlap between the single particle LSPRs and the in-plane modes of diffraction. Different electromagnetic coupling scenarios are identified including long-range (radiative) coupling to grating RAs. We study the effects of limited domain size, scattering losses at domain boundaries and other structural imperfections. Our findings enable the Q-factor of surface lattice resonances in self-assembled periodic plasmonic monolayers to be optimized.

5.3 Experimental Section

5.3.1 Chemicals

Gold(III)chloride trihydrate (HAuCl_4 ; Sigma-Aldrich, $\geq 99.999\%$), sodium citrate dihydrate (Sigma-Aldrich, $\geq 99\%$), sodium dodecyl sulfate (SDS; Sigma-Aldrich, p.a.), butenylamine hydrochloride (BA; Sigma-Aldrich, 97%), *N*-isopropylacrylamide (NIPAM; TCI, $> 98.0\%$), *N,N'*-methylenebisacrylamide (BIS; Sigma-Aldrich, $\geq 99\%$), potassium peroxydisulfate (PPS; Sigma-Aldrich, $\geq 99\%$), cetyltrimethylammonium chloride (CTAC; Sigma-Aldrich, 25 wt%, H_2O), ascorbic acid (Roth, p.a.), ethanol (Honeywell, p. a.) and 1,4-dioxane (p.a., Fisher Chemicals) were used as received. Milli-Q water (Millipore, $R > 18 \text{ M}\Omega \text{ cm}$) was used for all syntheses, purifications and self-assembly steps.

5.3.2 Synthesis

Core-shell particles with polycrystalline gold cores and soft hydrogel shells (Au-PNIPAM) were synthesized in different steps. First, spherical, citrate-stabilized gold nanoparticles (Au-NPs) of approximately 15 nm in diameter were synthesized according to the Turkevich protocol⁴⁶. Afterward, seeded precipitation polymerization of NIPAM and the cross-linker BIS using the Au-NPs as seed particles was performed following the protocol by Rauh *et al.*¹². Using three different NIPAM feed concentrations and fixed cross-linker contents (15 mol% referred to NIPAM) we prepared core-shell particles with different shell sizes (see Table 1). Finally the gold cores of all Au-PNIPAM batches were stepwise overgrown with gold to reach approximately 100 nm in diameter. The overgrowth protocol was adapted from Honold *et al.*²¹. For the sake of clarity, the different core-shell samples are labeled Au-PNIPAM₃₃₆, Au-PNIPAM₃₅₄ and Au-PNIPAM₃₆₇ with the numbers in subscripts corresponding to the hydrodynamic radius of the core-shell particles measured at 25 °C. The final particles were purified by centrifugation and redispersion of the residues in water. Centrifugation and redispersion were repeated three times at 5200 rcf (relative centrifugal force) for 30 min each. After the last centrifugation, the entire batch particles was redispersed in 150 μL of ethanol. A detailed description of the synthesis steps, as well as exemplary TEM images and UV-Vis absorbance spectra from each synthesis step (Figure S1) can be found in the Supporting Information.

Table 1: Concentration (c) and Masses (m) of the Monomer (NIPAM) and Cross-Linker (BIS) Used for the Seeded Precipitation Polymerization. The reaction volumes were 100 ml for each synthesis. Hydrodynamic diameter (d_h) of the core-shell particles from dynamic light scattering measured in dilute aqueous dispersion in the swollen state of the shell (25 °C).

| sample | $c(\text{NIPAM})$ [M] | $m(\text{NIPAM})$ [g] | $m(\text{BIS})$ [g] | d_h [nm] |
|--------------------------|-----------------------|-----------------------|---------------------|------------|
| Au-PNIPAM ₃₃₆ | 0.052 | 0.587 | 0.134 | 336 |
| Au-PNIPAM ₃₅₄ | 0.058 | 0.656 | 0.134 | 354 |
| Au-PNIPAM ₃₆₇ | 0.084 | 0.946 | 0.194 | 367 |

5.3.3 Fabrication of Periodic Particle Arrays

The fabrication of hexagonally ordered Au-PNIPAM particle arrays on glass substrates was carried out by following the protocol of Volk *et al.*¹³¹. Briefly, a small crystallization dish was filled with Milli-Q water and 7 μL of the particle dispersion (purified, in ethanol) was gently transferred to the air/water interface. At the interface the particles spontaneously self-assembled into a freely floating monolayer. Floating monolayers were transferred onto glass substrates by immersing the substrate fully in the bulk water phase below the monolayer and then withdrawing the substrate slowly through the monolayer. Therefore, the monolayer was collected onto the glass. Immediately after withdrawal of the substrates, the samples were dried using a heat-gun to blow warm air onto the back of the glass. A video demonstrating the self-assembly process can be found in the Supporting Information. To achieve the homogeneous refractive index environment required for radiative coupling to in-plane modes of diffraction, the monolayer samples were coated in a PNIPAM layer by spin-coating linear PNIPAM (65,000 g/mol, synthesized according to Ebeling and Vana²²⁶). Spin-coating was performed by applying 60 μL of a 1,4-dioxane solution containing the polymer (100 mg of PNIPAM in 2 mL of dioxane) and then applying 2000 rpm for 90 s. Under these conditions the resulting PNIPAM films had thicknesses of approximately 300 nm.

5.3.4 Methods

Transmission Electron Microscopy

A Zeiss CEM902 transmission electron microscope (TEM) was used for the determination of particle size, size dispersity, and structure. TEM measurements were performed at an acceleration voltage of 80 kV in bright-field mode. For each sample, a drop of a dilute aqueous particle dispersion was placed on carbon-coated copper grids and left to dry in air. Statistical analysis of the core sizes was carried out by measuring 200 particles from various TEM images using the ImageJ software¹⁷¹.

Atomic Force Microscopy

Atomic force microscopy (AFM) topographic images ($10 \times 10 \mu\text{m}^2$) were recorded with a Nanowizard 4 (JPK Instruments) in intermittent contact mode against air. OTESPA-R3 AFM probes (Bruker) were employed for image recording. The cantilevers possess a resonance frequency of approximately 300 kHz and a spring constant of approximately 26 N/m. The tip geometry was a visible apex with a nominal tip radius of 7 nm.

UV-Vis Spectroscopy

The extinction spectra were recorded with a Specord S 600 UV-vis spectrophotometer (Analytik Jena AG) in transmission geometry. The spectra of the particle dispersions were measured in $1 \times 1 \text{ cm}^2$ PMMA cuvettes. Particle monolayers on glass substrates were positioned upright in the light path using a solid sample holder. Thus, the illumination is normal to the monolayer plane. The transmitted light is detected and converted into absorbance values. The measurement geometry is also depicted in a sketch in the Supporting Information (Figure S8). All extinction spectra were corrected for background using either a cuvette with water or a clean glass substrate.

Dark-Field Microscopy

The optical microscopy images were captured in dark-field mode with reflection configuration using a Nikon ECLIPSE LV100D-U microscope equipped with a halogen lamp (12 V, 50 W), a dark-field condenser and a CMOS camera (Thorlabs, DCC1645c-HQ). The microscope was equipped with three lenses, Nikon LU Plan Fluor 20x/0.45, Nikon LU Plan ELWD 50x/0.55, and Nikon Lu Plan Fluor 100xA/0.9. The local transmission spectra were recorded with a CCD camera (Princeton Instruments, Pixis 1024F) and an imaging spectrograph (Princeton Instruments, Acton MicroSpec 2150i).

FDTD Simulations

The extinction spectra and E-field maps were calculated using the FDTD (finite difference time domain) method with commercial software from Lumerical Solutions, Inc. (FDTD Solutions, Version 8.18.1332). For the finite size lattices, the absorption and scattering spectra were simulated in a box with perfectly matched layer boundary conditions in the x- and y-directions (layer direction) and the z-direction. Unless otherwise specified the finite size lattices consisted of 61 particles which corresponded to a domain size of four. We utilized a total-field scattered-field source and a box of power monitors consisting of the total field and scattered field monitors. For the infinite lattices and electromagnetic field simulations periodic boundary conditions in both the x- and y-directions (layer direction) and a perfectly matched layer in the z-direction (beam direction) were used. A linear polarized plane wave source with excitation along the z-axis was injected. A transmission monitor was located at both ends of the FDTD simulation box in the beam direction. The following settings were kept the same for all simulations. Particle sizes and distances were used as obtained from the experiments. The

wavelength dependent RI (refractive index) of the gold core was taken from literature¹³⁴. For the glass substrates a constant RI of 1.52 was used and for the air background 1. The PNIPAM film was simulated with 300 nm thickness and a constant RI of 1.49²⁴⁷ slightly smaller than 1.50 (at $\lambda = 600$ nm)²⁴⁸ to account for a small amount of residual water. The auto shut-off was set at 10^{-5} . A schematic depiction of the simulation geometry is shown in the Supporting Information (Figure S8).

5.4 Results and Discussion

5.4.1 Au-PNIPAM Particle Characterization

Core-shell colloids with polycrystalline plasmonic gold cores and three thicknesses of soft PNIPAM hydrogel shells were synthesized. A schematic representation of the particles is shown in Figure 1 a. We aimed at synthesizing particles that feature nearly the same core diameter (d_{core}) so that the plasmonic properties, *i.e.* the position and intensity of the LSPR, are comparable despite the different thicknesses of the dielectric PNIPAM shells. Figure 1 b shows normalized the absorbance spectra recorded from dilute aqueous dispersions of the Au-PNIPAM particles. All samples feature a single LSPR peak attributed to a dipolar mode. The LSPR positions are $\lambda_{LSPR} = 577$ nm for Au-PNIPAM₃₃₆, $\lambda_{LSPR} = 582$ nm for Au-PNIPAM₃₅₄ and $\lambda_{LSPR} = 583$ nm for Au-PNIPAM₃₆₇, thus matching closely. Due to the relatively large linewidths (FWHM ≈ 137 nm) all particles possess low Q-factors of $Q \approx 4$. Figure 1 c-e shows TEM images of the different particles. In all the three images, the core-shell structure is clearly visible due to the pronounced contrast difference between the high electron density gold cores and the low electron density PNIPAM shells. The shells were imaged in their dried and collapsed state because of the measuring conditions during TEM imaging. Thus the shells appear thinner than in their swollen state in aqueous dispersion. Dynamic light scattering from dilute dispersions measured at 25 °C (swollen state) revealed hydrodynamic diameters of $d_h = 336$ nm, $d_h = 354$ nm, and $d_h = 367$ nm. The average core sizes (d_{core}) were determined directly from TEM images. The cores of the three core-shell systems have nearly the same size ($d_{core} = 99 \pm 8$ nm (Au-PNIPAM₃₃₆), $d_{core} = 102 \pm 8$ nm (Au-PNIPAM₃₅₄) and $d_{core} = 96 \pm 9$ nm (Au-PNIPAM₃₆₇)). The corresponding size distributions are shown in Figure 1 f-h. The standard deviations of the average diameter are 8-9 %, emphasizing the good control of our overgrowth procedure (see the Experimental Section and Supporting Information for more details). A further reduction in the polydispersity of the core sizes might be achievable by further optimization of the synthesis protocol but this is not expected to cause any significant increase in the Q-factor of the LSPR. Indeed, a further increase in core diameter will eventually lead to broader linewidths and thus reduced Q values due to the appearance of quadrupolar modes and retardation of the dipolar mode²³⁸.

5.4.2 Monolayers from Au-PNIPAM Particles

We used the different Au-PNIPAM core-shell particles to prepare hexagonally ordered monolayers with a broad range of nearest-neighbor center-to-center interparticle

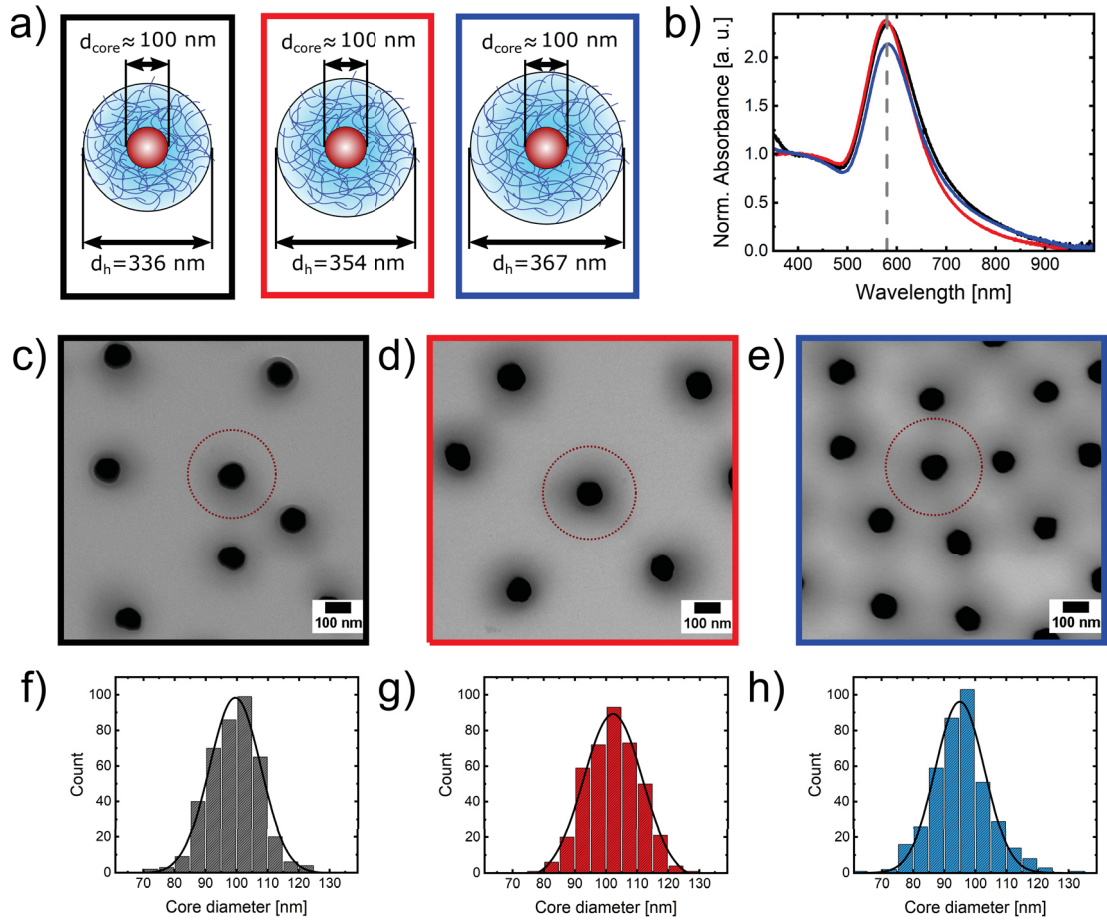


Figure 1: Au-PNIPAM building blocks for monolayer preparation: Au-PNIPAM₃₃₆ in black, Au-PNIPAM₃₅₄ in red and Au-PNIPAM₃₆₇ in blue. (a) Schematic representation of the core-shell structure of the Au-PNIPAM particles with d_{core} indicating the core diameter and d_h corresponding to the hydrodynamic diameter. (b) Absorbance spectra normalized to the absorbance at 400 nm. The dashed gray line highlights the LSPR position, λ_{LSPR} . (c - e) Representative TEM images for each batch of particles. The red dotted circles indicate the corresponding hydrodynamic size determined from DLS. (f - h) Histograms for the core diameters determined from TEM images.

distances (d_{c-c}) by an interface-mediated self-assembly approach¹³¹. Control of d_{c-c} was realized (1) by using different shell thicknesses and (2) by using sequential transfer from floating monolayers at the air/water interface where the packing fraction is reduced after every withdrawal of a monolayer sample. A densely packed monolayer is first prepared at the interface. In this case, the value of d_{c-c} is close to the bulk hydrodynamic diameter of the particles³⁸. Then, a fraction of the monolayer is removed from the interface by transferring onto the first substrate, resulting in an expansion of the remaining monolayer driven by interfacial tension and the deformability of the PNIPAM shells. Now, withdrawal of some of this monolayer onto another substrate yields a sample with a slightly reduced particle density, and d_{c-c} is increased by about 1.02 up to 1.1. Using this multistep transfer process in combination with particles having a range of different shell thicknesses, allows the fabrication of monolayers with various values of d_{c-c} . In this work d_{c-c} was varied between 342 and 448 nm using the Au-PNIPAM₃₃₆ particles, between 448 and 500 nm using the Au-PNIPAM₃₅₄ particles and between 500 and 573 nm with the Au-PNIPAM₃₆₇ particles. A video of the assembly approach is provided in the Supporting Information where changes in the monolayer density become clearly visible because the reflected color changes due to the changing particle spacing. Since the spacing in the monolayers is only determined by the dielectric PNIPAM shells and because the sizes and thus LSPR properties of the cores are nearly identical, the only optically relevant parameter that is altered between the samples is the lattice spacing.

Figure 2 a,d shows the photographs of the light reflection from particle arrays with different lattice spacings on glass substrates illuminated by a white light source from the side. In both cases the monolayers cover the full, macroscopic substrates as evident from the opalescent colors. Additionally, images of the same samples were taken using a dark-field microscope (DFM) at different magnifications to look at the largest possible area of the monolayers. At 20 \times magnification (Figure 2 b,e), the two samples show clear differences in color. The sample with $d_{c-c} = 458 \pm 29$ nm in Figure b appears orange, while the sample with the larger lattice spacing ($d_{c-c} = 567 \pm 32$ nm) appears green. The observed colors are a combination of the scattering from the individual particles and the Bragg diffraction. The latter depends strongly on the distance between the particles, the light incident and the detection angle. At 100 \times magnification, both samples appear similar in color, yellowish-orange caused by the scattering of individual gold particles. Due to the larger aperture of the objective, diffraction of light by the lattices cannot be observed. The DFM images confirm the homogeneity of the samples on different length scales. Furthermore the images taken at the highest magnification allow for identification of particle positions at the single particle level. The DFM images recorded at 100 \times magnifications are also shown in the Supporting Information with larger image sizes (see Figure S2). Using the particle positions, we calculated the fast fourier transformations (FFTs) that are shown as insets in Figure 2 c,f to evaluate the lattice order on statistically relevant areas with nearly mm² size. Both FFTs show Bragg peaks with hexagonal symmetry and at least four to five diffraction orders, reflecting the high degree of hexagonal ordering. Thus, on average our samples feature domain sizes of at least three (37 particles) to four (61 particles). We will later show that indeed we

get very good agreement between experimental extinction spectra and FDTD simulation results based on a domain size of four.

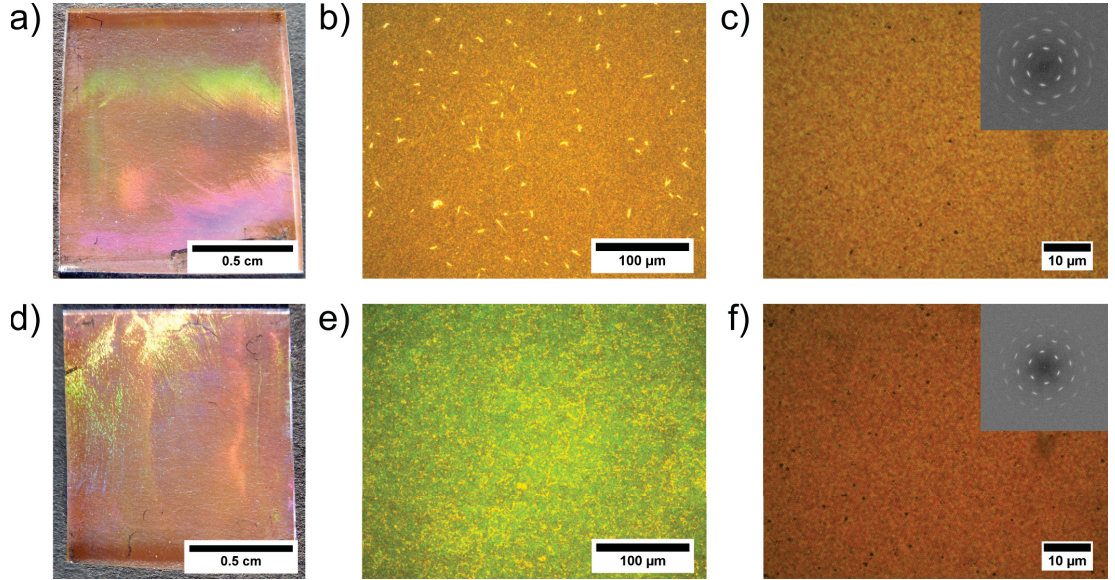


Figure 2: Monolayer characterization at different magnifications. Top row: Monolayer with $d_{c-c} = 458 \pm 29$ nm. Bottom row: $d_{c-c} = 567 \pm 32$ nm. (a, d) Digital photographs of the samples. (b, e) DFM images with $20\times$ magnification. (c, f) DFM images with $100\times$ magnification. The insets show FFTs calculated from the DFM images.

Since the resolution of the DFM image in Figure 2 f is sufficient to track the positions of the large majority of the particles at the single particle level, we can use this image to analyze the crystalline domains. Therefore, we have used triangulation analysis introduced by Hillebrand *et al.*¹⁷⁷. Figure 3 shows the DFM image with the detected single crystalline domains (hexagonal order) highlighted in different colors. Particles without hexagonal coordination are highlighted in white. At first glance, we see that the majority of the particles have hexagonal coordination and thus are assigned to crystalline domains which is in good agreement with the FFT results. The image contains a rather large number of domains of various sizes. The largest domain contains more than 5000 particles. Furthermore, we are able to identify 16 domains that contain 100 or more particles.

In order to look more closely at the microstructures and the crystalline domains, we employed AFM to study monolayers with different values of d_{c-c} . Since here we look at smaller sample areas, structural deviations between different sample locations are expected. Overall the AFM results will be less statistically relevant but still provide important insights into the lattice structure. Representative images are shown in Figure S3 (Supporting Information). The images and the respective FFTs of the particle positions confirm the hexagonal ordering of the samples. Furthermore, pair correlation functions

$g(r)$ were calculated allowing quantitative analysis of the degree of lattice order on smaller lengthscales than the DFM data allow. For all selected samples, $g(r)$ shows at least six to seven clearly distinguishable peaks indicating large crystalline domain sizes. Throughout this manuscript, the values of d_{c-c} have been calculated from the first maximum of $g(r)$, which has in turn been determined from a Lorentz fit to the function. Since the AFM images still capture several hundreds to thousands of particles, the values of d_{c-c} are representative of the whole monolayer and the error is expected to be small. In order to analyze the domain sizes of monolayers with smaller lattice constants where DFM cannot resolve individual particles, we have recorded height profiles by AFM. Figure S4a in the Supporting Information shows the $40 \times 40 \mu\text{m}^2$ scans of monolayer samples with values of d_{c-c} of 375, 458 and 567 nm. From the domain analysis in Figure S4b,c, we find (1) that much larger, single crystalline domains are detected as compared to the previously discussed DFM image and (2) that the domain size seems to increase with increasing d_{c-c} . We can certainly conclude that the degree of order does not decrease with increasing d_{c-c} . This will become relevant when discussing diffractive-plasmonic coupling later on. The fact that larger domains are found from analysis of the AFM images is simply related to the better spatial resolution in AFM. Thus AFM allows a much more precise determination of the central x- and y-positions of individual particles.

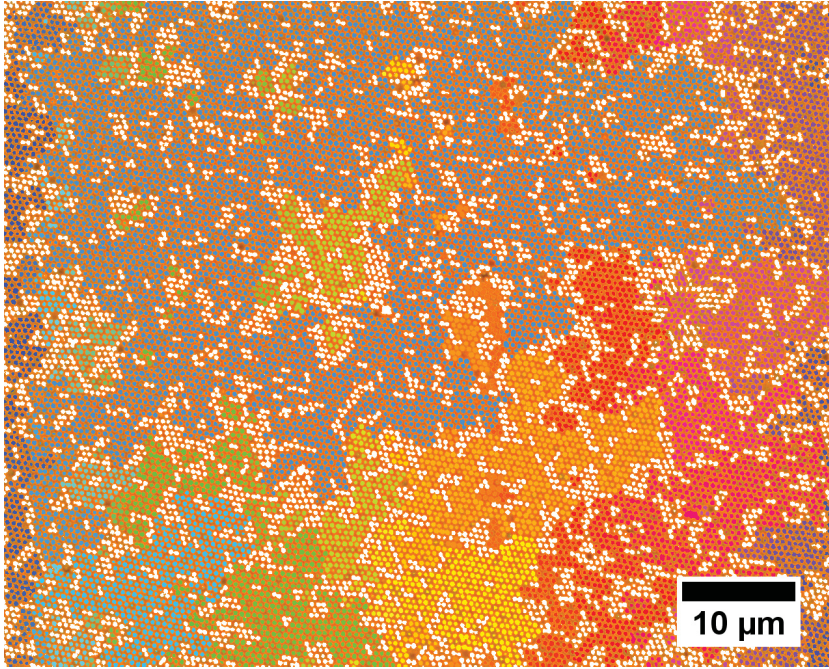


Figure 3: Analysis of crystalline domains. DFM image with $d_{c-c} = 567 \pm 32$ nm. Different crystalline domains are highlighted in different colors. Particles without hexagonal coordination are colored in white.

5.4.3 Optical Properties in an Asymmetric RI Environment

In the following we will address the dependence of the optical properties of our periodic particle arrays on the interparticle spacing (d_{c-c}). We start by considering arrays where there is a glass substrate (RI = 1.52) and air (RI = 1.00) is the superstrate. A schematic depiction of the sample geometry is shown in Figure 4 a. Figure 4 b summarizes the absorbance spectra of selected samples measured in normal transmission. The spectra from a larger set of monolayers can be found in the Supporting Information (Figure S5a). All of these arrays exhibit a single resonance peak whose resonance position, width, and intensity depend on the lattice spacing. With decreasing d_{c-c} , the resonance shifts to smaller wavelengths, becoming more intense and the FWHM decreases. The increase in resonance intensity is primarily attributed to the increasing particle density (Beer-Lambert law) as the lattice spacing is reduced. For the largest spacing, where $d_{c-c} = 573$ nm, we find a resonance position $\lambda_{max} = 595$ nm and a FWHM of 145 nm. Both values are close to the ones obtained from measurements in dilute aqueous dispersions (RI = 1.33) with $\lambda_{max} \approx 580$ nm and a FWHM of 137 nm. The slight redshift of the monolayer sample is related to the small increase in the effective RI for the combination of the glass substrate with the air superstrate. There is also a small increase in the effective RI due to the collapsed PNIPAM shell surrounding each gold core. We have also measured the spectrum of a monolayer sample on glass with a random particle distribution and a very small packing fraction (see Figure S6). This yields a resonance at $\lambda_{max} = 595$ nm perfectly matching the resonance of the ordered monolayer sample with $d_{c-c} = 573$ nm. This confirms that electromagnetic coupling is absent for large lattice spacings and the observed resonance shifts compared to particles in solution are due to changes in RI environment. If we now look at the monolayer sample with the smallest lattice spacing ($d_{c-c} = 342$ nm), the resonance peak appears at $\lambda_{max} = 561$ nm, *i.e.*, it is significantly blueshifted compared to the LSPR observed in dilute particle dispersions. Furthermore, the FWHM is reduced to 78 nm. Both the blueshift and the reduction in linewidth are attributed to long-range radiative interactions between the gold nanoparticle dipoles^{249,250}. At these still relatively large interparticle distances, we can exclude near-field electromagnetic coupling. Near-field coupling becomes significant for interparticle spacings smaller than 2.5 times the particle diameter in the case of gold¹⁴⁸. Furthermore, coupling via the near-fields is expected to result in a redshift and resonance broadening in stark contrast to our observation. Thus, our resonance effect is clearly radiative (far-field). In our case, the interparticle distances are on the order of half the LSPR wavelength. Such blue shifts have been observed in similar periodic arrays and attributed to radiative dipole interactions and retardation effects²⁴⁹. The blueshift and narrowing with decreasing distance have also been observed in random particle monolayers²⁵⁰. This suggests that the long-range radiative coupling is mostly determined by the average interparticle distance rather than the arrangement of the plasmonic building blocks. Unfortunately a detailed description of the physical origin of the blueshift, for example whether this is an effect related to changes in the scattering or absorption properties of the particle ensemble, is still missing until now.

In order to support our experimental findings, we have also performed FDTD simulations. The calculated spectra are shown in Figure 4 c. The observed peak positions, widths and intensities nicely match our experimental results, as is seen from a direct comparison of the corresponding values summarized in Table 2.

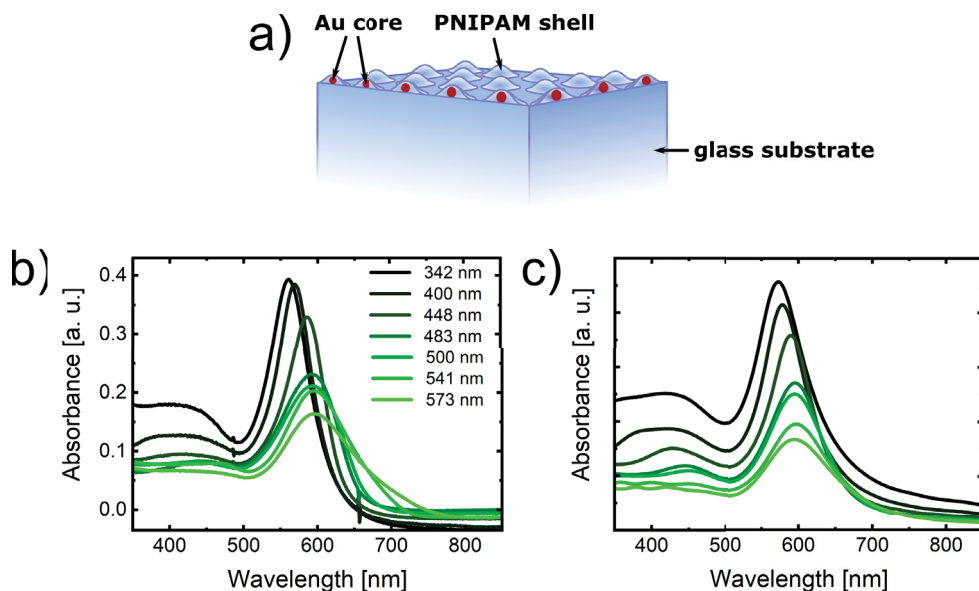


Figure 4: Optical properties of particle arrays in an asymmetric RI environment. (a) Schematic depiction of the periodic particle array on a glass substrate with air as a superstrate. (b) Experimental absorbance spectra measured from samples with values of d_{c-c} ranging from 342 to 573 nm. (c) Corresponding theoretical spectra from FDTD simulations of finite lattices (domain size four) using the experimental values of d_{c-c} from (b). The same color code was used as in (b).

5.4.4 Optical Properties in Symmetric RI Environments

In order to enhance radiative electromagnetic coupling, we need a higher RI superstrate that closely matches the RI of the glass substrate. To achieve this, we have deposited 300 nm thick polymer coatings on top of the particle arrays. This thickness is sufficient to enable observation of diffractive-plasmonic coupling³⁴. In contrast to other existing strategies for refractive index matching using immersion oils or photoresists, our superstrate is swellable by solvents¹³¹ and will in principle enable the diffusion of small analytes into the film as desired for example in sensing applications²⁵¹. A schematic depiction of the sample geometry is shown in Figure 5 a. Note that, first of all, we need to determine the uncoupled single particle resonance as a reference. Figure 5 b shows the simulated, single particle spectrum for a Au-PNIPAM particle on a glass substrate with a 300 nm thick topcoating of PNIPAM (RI = 1.49). We predict an LSPR at $\lambda_{LSPR} = 604$ nm, highlighted by the vertical gray dashed line. As a consequence of

the higher RI superstrate, the LSPR position is redshifted (by approximately 9 nm). The colored vertical lines in Figure 5 b correspond to the calculated spectral positions of the $\{1, 0\}$ diffraction modes for the hexagonally ordered monolayers with varying d_{c-c} . The theoretical wavelengths of the Bragg modes were calculated using eq 5.1 and 5.2³⁴

$$\frac{1}{d^2} = \frac{4}{3} \left(\frac{h^2 + hk + k^2}{a^2} \right) \quad (5.1)$$

Here, d is the interplanar spacing, h and k are the Miller indices (in our case 1 and 0, respectively) and a is the lattice constant. For our hexagonally ordered monolayers, a corresponds to the nearest-neighbor interparticle distance d_{c-c} . Multiplication of the interplanar spacing d with the refractive index yields the Bragg wavelengths

$$\lambda_{hk} = RI \times d \quad (5.2)$$

Figure 5 c shows the experimental absorbance spectra for selected monolayer samples immersed in symmetric RI environments. The spectra from a larger set of monolayers can be found in the Supporting Information (Figure S5b). To allow for a better comparison of the resonance intensities, the spectra in Figure 5 c have been normalized to the same particle density (10 particles per μm^2). Looking at the smallest values of d_{c-c} (342 and 400 nm) where the diffractive modes are significantly blueshifted compared to the single particle LSPR (Figure 5 b), we observe single resonance peaks. Here the sample with $d_{c-c} = 400$ nm features a resonance that is more intense, redshifted and with a reduced linewidth compared to $d_{c-c} = 342$ nm. As in the case of asymmetric RI environments, we attribute these spectral differences to long-range radiative interactions between the dipoles. At $d_{c-c} = 448$ nm the strongest resonance appears at 638 nm with an even higher intensity and reduced linewidth. For this sample the $\{1, 0\}$ diffraction modes and the single particle LSPR overlap strongly and diffractive-plasmonic coupling is enabled, resulting in a true SLR. Although the RI values of the PNIPAM superstrate (RI = 1.49) and the glass substrate (RI = 1.52) are not perfectly matched, an SLR is supported. This finding is in agreement with the work of Yang *et al.* who showed that SLRs are tolerant of RI mismatches up to $\Delta RI \approx 0.05$ ²⁵². In addition, the spectrum features a weak shoulder at approximately 530 nm. This mode is attributed to a weak plasmonic contribution²⁵³. With further increases in d_{c-c} , the SLRs redshift and become broader and weaker. At the same time, the plasmonic contribution at shorter wavelengths becomes more pronounced. For the sample with the largest spacing ($d_{c-c} = 573$ nm), where the $\{1, 0\}$ diffraction modes appear in the long wavelength tail of the single particle LSPR, the plasmonic contribution almost resembles the uncoupled LSPR response of the component building blocks and only a weak and broad SLR at 726 nm is observed. The increase in linewidth of the SLR with increasing d_{c-c} indicates a decrease in the coupling strength. Although for a perfect particle lattice with an effectively infinite particle number, a reduction of the SLR linewidth is expected for increasing lattice constants, we clearly observe the opposite effect.

We explain this in terms of the finite size of the single crystalline domains in our monolayers as discussed in the previous section. Our explanation is supported by the

work of Zou *et al.*¹⁵⁵ Those authors studied the optical response of a two-dimensional array of 400 nanoparticles in a hexagonal arrangement and found an increase in resonance linewidth with increasing spacing. Apart from the influence of the domain size we also expect the multidomain character of the samples to contribute to the resonance broadening at large lattice constants. The multidomain character and the resulting large number of grain boundaries dampen the diffractive modes. In addition, there will be significant scattering losses at the domain boundaries as observed for guided resonances in 2D photonic crystals¹⁵⁶.

To further support our experimental findings we performed FDTD simulations of lattices with finite sizes. Figure 5 d shows the calculated spectra using the same lattice parameters as in the experiment and a domain size of four corresponding to 61 particles. Again, the simulated spectra have been normalized to 10 particles per μm^2 . All peak positions as well as the experimental and simulated values of the resonance FWHM are presented in Table 2. We find a very good match between experiments and simulation for all the different monolayers investigated, despite a small deviation in the SLR position that can be explained in terms of a small amount of positional disorder in the self-assembled lattices. This disorder weakens the dipolar coupling in our lattices, resulting in slightly blueshifted SLRs as compared to perfectly ordered lattices used in simulation. SLRs are coherent modes that result from the collective radiative coupling between individual plasmonic nanoparticles in the periodic lattices. The stronger the coupling and consequently the larger the coherence, the stronger is the redshift of the SLR with respect to the diffraction edge¹⁵⁷. In contrast, for randomly arranged plasmonic particles in a monolayer, the SLR is expected to disappear, while the purely plasmonic contribution at lower wavelength completely reappears. This is in agreement with the study of Augu e and Barnes¹⁵⁷. Those authors found a blueshift and broadening of SLRs for increasing disorder.

In addition to the far-field extinction spectra, we have also recorded the local transmission spectra using a light microscope. The resulting spectra for the monolayer samples with $d_{c-c} = 449$ nm and $d_{c-c} = 573$ nm in asymmetric and symmetric RI environments are shown in the Supporting Information (Figure S7). The local spectra resemble the spectra collected by standard extinction spectroscopy. For the symmetric RI environment we observe SLRs for both lattice constants, while the $d_{c-c} = 573$ nm sample exhibited a pronounced plasmonic contribution that almost matches the expected single particle LSPR as well as the non-coupling case in an asymmetric RI environment.

5.4.5 Direct Comparisons of Asymmetric and Symmetric RI Environments

We now want to directly compare and discuss the differences in optical response in asymmetric and symmetric RI environments. In order to be comparable to other studies in the literature and to other lattice symmetries, we will use the lattice period instead of d_{c-c} in the following discussions. Figure 6 a shows the extinction cross-sections obtained from FDTD simulations for hexagonal infinite lattices of spherical AuNPs (100 nm in diameter) for various lattice periods in 10 nm steps. A constant RI = 1.49 for the PNIPAM topcoating as a superstrate and RI = 1.52 for the glass substrate were

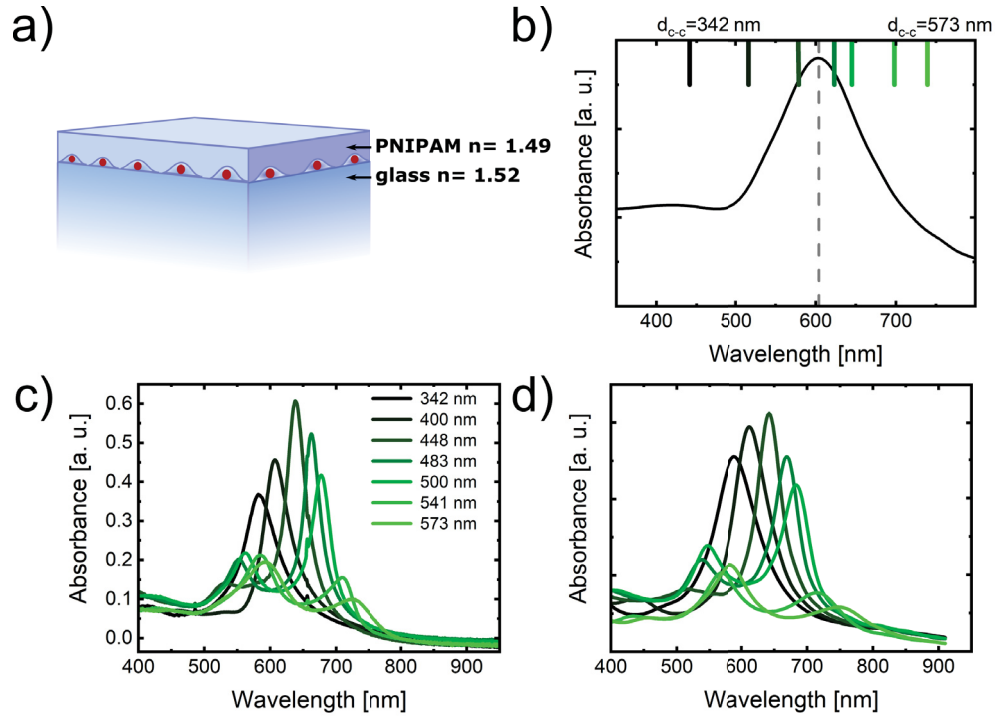


Figure 5: Optical properties of particle arrays in symmetric RI environments. (a) Schematic figure of a PNIPAM coated gold particle monolayer on the glass substrate. (b) Calculated LSPR of a single gold particle on the glass substrate coated with a 300 nm PNIPAM film with a theoretical Bragg position for each interparticle distance. (c) Absorbance with varying interparticle distance. (d) FDTD simulated absorbance spectra of particle lattices (domain size four) with varying spacing in the homogeneous RI environment. The color code in (b-d) refers to the same d_{c-c} . All spectra were normalized to account for the same number of particles per area (10 particles per μm^2).

Table 2: Calculated Wavelength of the $\{1,0\}$ Diffraction Peak, λ_{Bragg} , Resonance Positions, λ_{max} , and FWHM Values for Lattices with Various d_{c-c} for Both Asymmetric and Symmetric RI Environments. Values in brackets correspond to the results from FDTD simulations.

| d_{c-c} [nm] | λ_{Bragg} [nm] | λ_{max} [nm] | | FWHM [nm] | |
|----------------|------------------------|----------------------|-----------|------------|-----------|
| | | asymmetric | symmetric | asymmetric | symmetric |
| 342 ± 44 | 441 | 561 (572) | 583 (588) | 78 (90) | 75 (84) |
| 400 ± 52 | 516 | 569 (578) | 607 (612) | 71 (77) | 52 (65) |
| 448 ± 60 | 578 | 585 (590) | 638 (642) | 69 (79) | 40 (47) |
| 483 ± 46 | 623 | 592 (596) | 662 (670) | 106 (103) | 33 (50) |
| 500 ± 51 | 645 | 593 (596) | 678 (684) | 127 (111) | 42 (61) |
| 541 ± 30 | 698 | 595 (596) | 710 (718) | 136 (121) | 67 (107) |
| 573 ± 42 | 739 | 595 (596) | 726 (750) | 145 (127) | 124 (132) |

used (symmetric environment), which match closely the expected RIs from the experiment. With increasing period, the resonance maximum continuously redshifts, while the linewidths become smaller. For large periods the resonance positions asymptotically approach the $(0, \pm 1)$ RA (solid line), implying that the resonance character becomes more and more photonic and less plasmonic. Figure 6 b compares the electromagnetic near-field intensities calculated at the respective resonance wavelength (λ_{max}) for the asymmetric (top row) and symmetric (bottom row) RI cases for three selected lattice periods. All maps reveal the excitation of dipolar resonances with stronger field strengths for the symmetric RI case caused by the higher effective average RI. In addition to the dipole excitation, the symmetric RI cases with periods of 388 nm ($d_{c-c} = 448$ nm) and 418 nm ($d_{c-c} = 483$ nm) that are labeled with α and β show the typical in-plane diffractive band structure. The diffractive-plasmonic coupling in these two samples results in the formation of SLRs. In all cases the SLRs exhibit the highest field intensities. In experiment, we observe very similar results. Figure 6 c shows the resonance wavelength (λ_{max}) determined for monolayer samples with different lattice periods in symmetric and asymmetric RI environments. For the symmetric case, λ_{max} increases continuously with increasing period and asymptotically approaches the $(0, \pm 1)$ RA (red solid line) for the higher periods. These resonances correspond to SLRs for periods of 388 nm and larger (full circles). For smaller periods, the values of λ_{max} are close to the uncoupled LSPR (red horizontal bar) while showing a weak blueshift for decreasing periods. This blueshift is also observed in the asymmetric RI samples for periods in a very similar range (below approximately 400 nm).

For larger periods, λ_{max} approaches the uncoupled LSPR (gray horizontal bar) indicating that diffractive coupling is not supported due to the strong RI mismatch between the substrate and superstrate in the asymmetric samples. The blueshift observed for decreasing periods is attributed to long-range dipolar interactions. We now want to focus on the SLRs observed in the symmetric RI samples and use the Q-factor to discuss the coupling strength in our self-assembled monolayers. Figure 6 d compares

the resonance position and Q-factor for the symmetric RI samples as a function of the spectral difference between the diffractive mode and the single particle LSPR ($\Delta\lambda = \lambda_{RA} - \lambda_{LSPR}$). Both λ_{max} and the Q-factor decrease in a nearly linear manner for decreasing $\Delta\lambda$ below -50 nm. In this region, diffractive-plasmonic coupling is inhibited and only long-range dipolar interactions become relevant. For positive values of $\Delta\lambda$ or negative values approaching 0 where SLRs appear, the resonance shift becomes steeper and the Q-factor increases significantly, reaching a maximum for $\Delta\lambda \approx 20$ nm corresponding to a period of 418 nm. Here, the Q-factor reaches a value of approximately 20.

For further increases in $\Delta\lambda$, the Q-factor decreases significantly, indicating increasing losses. This decrease is contrary to the observation from simulation in Figure 6 a and studies reported in literature where an increase in Q-factor is observed due to the increasing photonic character and reducing plasmonic losses for larger periods. We attribute our findings to the finite domain size in our lattices and scattering losses from domain boundaries and lattice defects. To support this, we compare the resonance FWHM for various domain sizes as a function of lattice period from FDTD simulation in Figure 6 e. For domain sizes of two to five, we observe an increase in FWHM with increasing period, while for each period, the larger the FWHM, the smaller the period. In other words, the resonance linewidth increases and thus the Q-factor decreases with decreasing domain size and increasing period. The respective representation of the Q-factor can be found in the Supporting Information (Figure S9). In contrast, the simulation using periodic boundary conditions (and thus resembling an infinite lattice) reveals a decrease in FWHM with increasing period and an increase in Q-factor. Similar effects of the array size on the Q-factor of the SLR were found by Rodriguez *et al.*¹⁵⁴

To summarize, there are pronounced differences in the behavior of SLRs in asymmetric and symmetric RI samples. We find the following: (1) A close match between the RI of the substrate and superstrate is required to enable plasmonic coupling to in-plane modes of diffraction. (2) SLRs are only supported for diffraction wavelengths close to, or larger than, the single particle LSPR wavelength. (3) For diffraction wavelengths significantly smaller than the LSPR wavelength, long-range dipolar interactions are observed, leading to a blueshift with decreasing lattice period. (4) High Q-factor SLRs are observed for slightly longer wavelengths of diffraction compared to the LSPR, whereas a reduction in Q-factor is observed for larger offsets of diffraction and LSPR wavelengths. The latter reduction in Q-factor is caused by finite domain size effects and scattering losses.

Despite the obvious influence of lattice imperfections in our self-assembled lattices, the maximum Q-factor of $Q \approx 20$ for a period of 418 nm is more than half of the value obtained from FDTD simulation for an infinite lattice using periodic boundary conditions ($Q \approx 37$, see Figure S10 in the Supporting Information). Similar calculated results were obtained by Rodriguez *et al.*¹⁵⁴ for square arrays of gold disks with 120 nm diameter and 50 nm height. For an infinite array they calculated $Q \approx 30$ and for finite arrays with a few hundred particles Q already closely approached this limit.

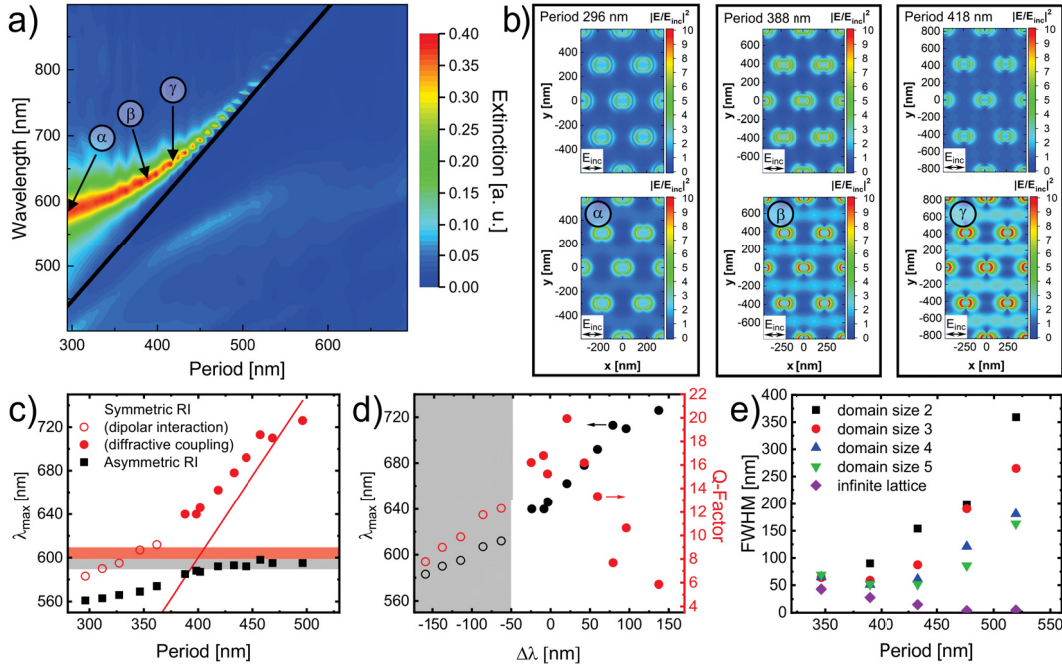


Figure 6: Comparison of different electromagnetic coupling regimes. (a) Calculated extinction cross-sections for hexagonal arrays of gold spheres (100 nm diameter) for lattice periods in 10 nm steps and a symmetric environment with RI = 1.49 for the PNIPAM topcoating and RI = 1.52 for the glass substrate. The solid line corresponds to the (0, ±1) Rayleigh anomaly (RA). (b) Near-field electromagnetic intensity maps ($|E/E_{inc}^2|$) from FDTD simulations for a hexagonal monolayer with asymmetric RI (top row) and symmetric RI environments (bottom row). Calculations were performed at the respective λ_{max} of the samples. Corresponding spectral positions for the symmetric case labeled with α , β , and γ are also indicated by arrows in (a). (c) Peak wavelength (λ_{max}) as a function of lattice period from experiments. Black squares: asymmetric RI. Red circles: symmetric RI. Filled red circles correspond to samples where diffractive-plasmonic coupling (SLRs) were observed. The red line corresponds to the (0, ±1) RA. The light red and gray bars mark the LSPR position (no coupling) in symmetric and asymmetric RI, respectively. (d) Experimental peak wavelength (λ_{max}) and Q-factor as a function of wavelength difference between LSPR and RA ($\Delta\lambda = \lambda_{RA} - \lambda_{LSPR}$). (e) FWHM of resonance peaks from FDTD simulations of hexagonal lattices in symmetric environment (RI = 1.49 for the PNIPAM topcoating, RI = 1.52 for the glass substrate) for different domain sizes. (The associated absorbance spectra from (c) and (d) are shown in Supporting Information S5)

5.5 Conclusions

We have experimentally and theoretically studied the optical properties of periodic gold nanoparticle arrays prepared via interface-mediated self-assembly. While weak electromagnetic coupling related to long-range radiative coupling of the dipoles was observed in strongly asymmetric refractive index environments, homogenization of the refractive index resulted in pronounced surface lattice resonances. In both cases, the coupling strength strongly depends on the interparticle distance. Radiative dipolar interactions increase with decreasing interparticle distance, resulting in a blueshift of the plasmon resonance. In contrast, diffractive-plasmonic coupling becomes pronounced for larger distances where the in-plane modes of diffraction are spectrally close to, or redshifted from, the single particle localized surface plasmon resonance. The spectral overlap between both modes weakens at large enough distances, and then the surface lattice resonances also become weaker in intensity and significantly broaden as a result of the finite size of the crystalline domains in the sample. As a consequence of the decreasing coupling efficiency at increasing lattice constants, the purely plasmonic contribution at lower wavelengths reappears due to energy conservation. Although our experimental samples feature lattice defects and limited single crystalline domain sizes, the deviation of the experimentally observed surface lattice resonance width and intensity from simulations of infinite size lattices is small. This implies that colloidal self-assembly is competitive compared to lithographic approaches commonly applied to the preparation of near-perfect periodic plasmonic lattices. We believe that particle arrays supporting much higher quality factor resonances are readily achievable by self-assembly because the individual plasmonic particle sizes, shapes and interparticle spacing can all be adjusted.

Our work significantly contributes to a deeper understanding of electromagnetic coupling phenomena in periodic plasmonic arrays. Furthermore, we demonstrate the enormous potential of colloidal self-assembly for the fabrication of cm^2 -scale samples with tailored plasmonic properties based on relatively simple colloidal building blocks. We believe that our findings can be transferred to other grating-like plasmonic nanostructures such as periodic lines of nanoparticles or ordered supercrystal structures, which might even support collective resonances of higher quality as long as the degree of disorder is low and domain sizes are large. In future work we will address the possibility for further improvement of the quality factor of surface lattice resonances by optimization of the plasmonic colloidal building blocks and the lattice geometry.

Associated Content

Detailed synthesis information of the Au-PNIPAM particles; representative TEM images and UV-Vis spectra of every synthesis step; microstructure analysis of particle monolayers by DFM and AFM; experimental UV-Vis spectra of all particle monolayers and an unordered particle monolayer; local transmission spectra of particle monolayers recorded with an optical light microscope; schematic FDTD simulation layout; calculated

Q-factor for various domain sizes; and extinction spectrum from FDTD simulation for the strongest coupling regime (PDF)

Self-assembly process (MP4)

Notes

The authors declare no competing financial interest.

Acknowledgements

The authors acknowledge financial support by the German Academic Exchange service (DAAD) through its Thematic Network Melbourne-Bayreuth Polymer/Colloid Network sponsored from funds of the Federal Ministry of Education and Research (BMBF). P.M. thanks the ARC for support through Grant CE170100026. M.K. acknowledges the German Research Foundation (DFG) for funding under grant KA3880/6-1. The authors thank Heyou Zhang from the University of Melbourne for his assistance with the DFM measurements and Sophia Köhler from the Heinrich-Heine-University Düsseldorf for her assistance with the TEM measurements.

5.6 Supporting Information

Synthesis of Gold Nanoparticle Cores

Spherical gold nanoparticles were synthesized according to the protocol of Turkevich *et al.*⁴⁶. In brief, 200 mL aqueous gold(III)-chloride trihydrate solution (5×10^{-4} M) were brought to boil while stirring. Then 10 mL of an aqueous sodium citrate dihydrate solution (1.0 wt%, hot) were added as reducing agent. The dark red nanoparticle dispersion was allowed to boil for another 20 minutes under continuous stirring. After that, the dispersion was allowed to cool down to room temperature under slow stirring. 1.2 mL of an aqueous SDS solution (1 mM) were added to increase the stability of the gold nanoparticles during the purification steps later on. After another 20 minutes, the surface of the particles was functionalized by adding 0.652 mL of an aqueous butenylamine hydrochloride (BA) solution (1.4 M)⁸. The dispersion was left to equilibrate for another 20 minutes. Afterwards the nanoparticles were purified and concentrated via centrifugation for 14 hours at 1400 rcf.

Synthesis of Au-PNIPAM Core-Shell Particles

The encapsulations of the gold cores were achieved by seeded precipitation polymerizations according to the protocol by Rauh *et al.*¹². The polymerizations were carried out in 100 mL of Milli-Q water in three-neck round-bottom flasks (250 mL) equipped with a reflux condenser. For each synthesis NIPAM and BIS were dissolved in water while stirring at room temperature. The respective amounts of NIPAM and BIS are listed in Table 1 in the main manuscript. The solutions were heated to 70 °C and degassed with nitrogen. After an equilibration time of 20 minutes, 7.37 mL of the functionalized gold nanoparticles in water ($c(\text{Au}^0) = 3.137$ mM) were added dropwise. Following another equilibration time of 15 minutes, 2 mg PPS dissolved in 1 mL of water were added quickly to the mixtures. The polymerization reactions were allowed to proceed for two hours and then cooled down to room temperature. The Au-PNIPAM particles were purified by centrifugation for 90 minutes at 8400 rcf and redispersion of the residues in water. The purification was repeated three times. After the last centrifugation step, the core-shell particles were redispersed in 5 mL of Milli-Q water.

Overgrowth of Plasmonic Cores

The overgrowth protocol used to increase the gold core size was adapted from Honold *et al.*²¹ Ascorbic acid and HAuCl₄ were used in a molar ratio of 1.3. First 8 mL of an aqueous CTAC solution (2.4 mM) were filled in an Erlenmeyer flask. 93 μ L of an aqueous solution of the respective Au-PNIPAM particles (5.04 wt%) were mixed in a 1:1 ratio with 10 mM CTAC solution and added to the flask under continuous stirring. Then 156 μ L of an aqueous ascorbic acid solution (49 mM) were added quickly. Next 12 mL of an aqueous solution containing CTAC (6.2 mM) and HAuCl₄ (0.5 mM) were added dropwise under strong stirring. The reactions were allowed to proceed for 30 minutes. The overgrowth steps were repeated four times while the particle size was controlled via extinction spectroscopy aiming at $\lambda_{LSPR} = 580$ nm, which corresponds to a gold core diameter of approximately 100 nm. The reaction solutions were allowed to rest overnight without stirring. Afterwards the dispersions were purified by three iterations of centrifugation at 5200 rcf for 30 minutes and redispersion of the respective residues in Milli-Q water.

Characterization of the Au-PNIPAM Core-Shell Particles

Figures S1 (a)-(c) show representative TEM images of the initial gold cores from the Turkevich synthesis (a), the Au-PNIPAM particles after seeded precipitation polymerization (b) and the final core-shell particles Au-PNIPAM₃₆₇ after overgrowth of the cores (c). Before overgrowth, the cores have an average diameter of $d_{core} = 15.3 \pm 1.3$ nm. After the overgrowth, the average core diameter is $d_{core} = 96 \pm 9$ nm. The core-shell structure in (b) and (c) is clearly visible due to the good electron contrast between core and shell. **Figure S1** (d) shows absorbance spectra for each type of particle. The gold cores prior to encapsulation into PNIPAM feature a single LSPR at $\lambda_{LSPR} = 517$ nm (black spectrum). After encapsulation, the spectrum is dominated by scattering from the PNIPAM shell and the LSPR of the gold cores is barely visible (red spectrum). The final core-shell particles with overgrown cores show a strong LSPR at $\lambda_{LSPR} = 583$ nm dominating the optical response (blue spectrum).

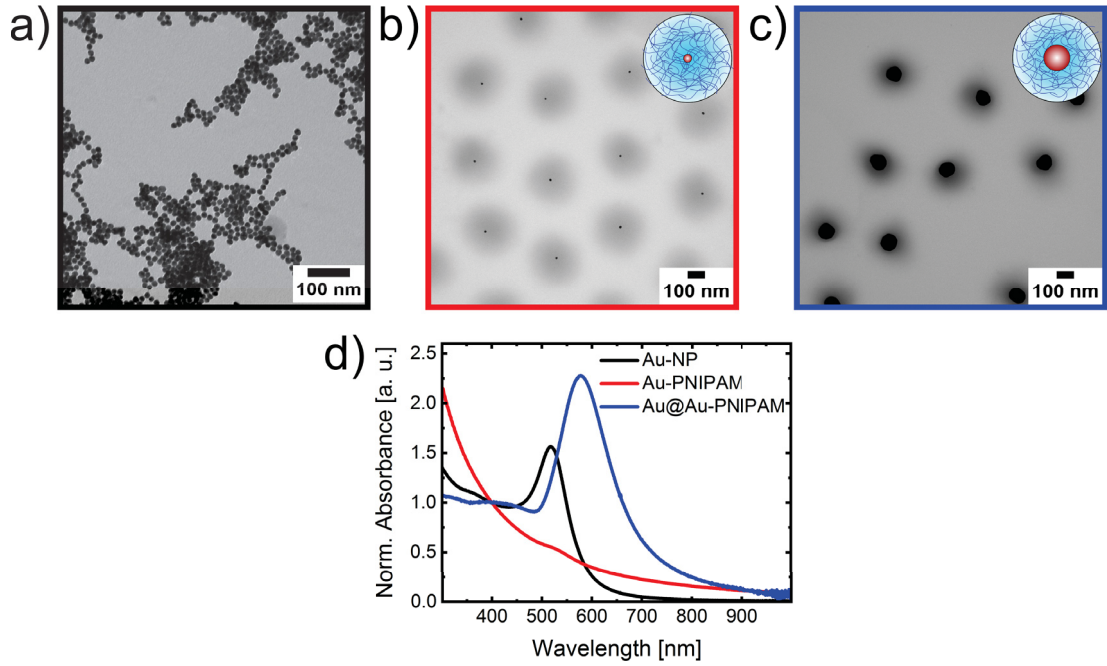


Figure S1: TEM images and UV-Vis spectra of the particles after different steps of preparation. TEM images of the gold cores (a), the core-shell particles after seeded precipitation polymerization (b) and the final core-shell particles after overgrowth of the cores (c). The particles shown in (c) correspond to the particles Au-PNIPAM₃₆₇ in the main manuscript. (d) UV-Vis absorbance spectra of the gold cores (black), the Au-PNIPAM particles before (red) and after core growth (blue). All spectra are normalized to the absorbance at 400 nm.

Microstructure Analysis of Particle Monolayers

Figure S2 shows images of particle monolayers with $d_{c-c} = 458$ nm and $d_{c-c} = 567$ nm recorded with a dark-field microscope (DFM) at 100 \times magnification. The images proof the homogeneity of the samples and the hexagonal order. For both samples the resolution is high enough to resolve single particles in the lattices.

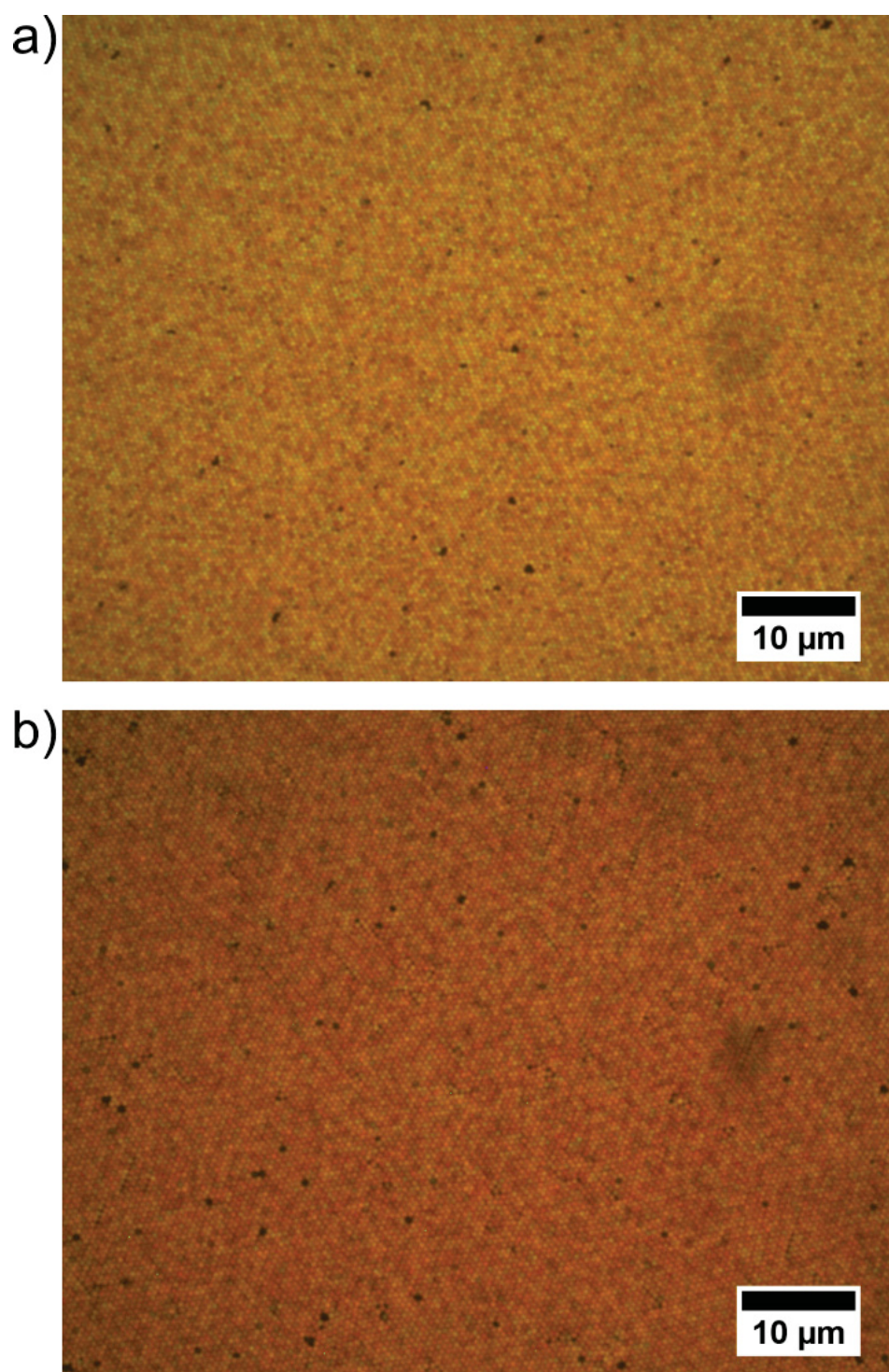


Figure S2: Microstructure analysis by DFM. DFM images recorded at 100 \times magnification for a monolayer sample with $d_{c-c} = 458$ nm (a) and $d_{c-c} = 567$ nm (b).

Figure S3 (a) shows AFM height profiles of particle monolayers with interparticle distances of $d_{c-c} = 378$ nm, $d_{c-c} = 448$ nm and $d_{c-c} = 573$ nm. The insets show fast fourier transformations (FFTs) computed from the AFM images. The FFTs support the hexagonal order of the monolayers through the six-fold symmetry of the arrangement of the Bragg peaks. Several orders of Bragg peaks are visible indicating high local order. **Figure S3** (c) shows pair correlation functions $g(r)$ calculated from the position maps in (b). The red ticks above each $g(r)$ correspond to the theoretical peak positions for a perfectly ordered hexagonal array with the same interparticle distances as in the experimental monolayers.

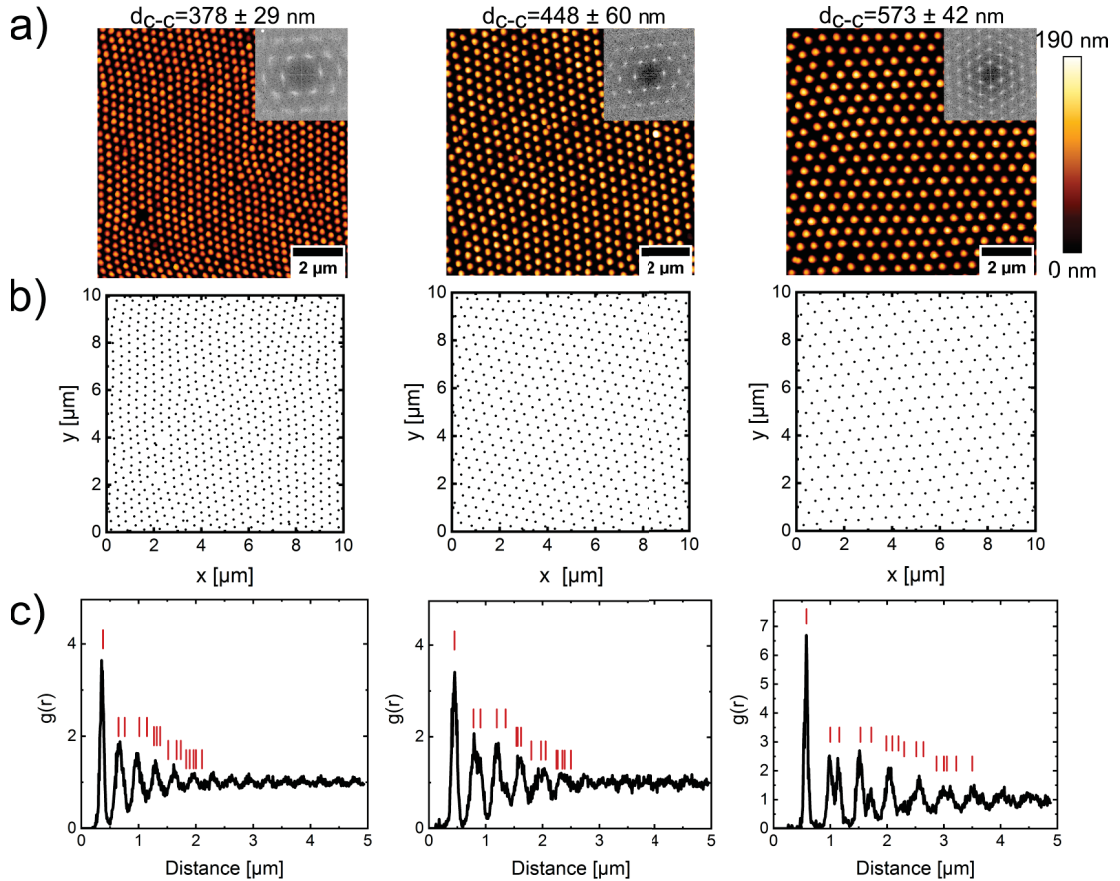


Figure S3: Microstructure analysis by AFM. $10 \times 10 \mu\text{m}^2$ height profile images measured in tapping mode against air (a). The insets show the calculated FFTs. (b) shows the computed position maps of the particle centers in the respective monolayers from (a). (c) pair correlation functions $g(r)$ of the monolayers. Red ticks indicate the theoretical peak positions for perfectly ordered reference lattices.

Figure S4 (a) shows AFM height profiles of monolayers with interparticle distances of $d_{c-c} = 375$ nm, $d_{c-c} = 458$ nm and $d_{c-c} = 567$ nm recorded with a scan size of $40 \times 40 \mu\text{m}^2$.

The size of the single crystalline, hexagonally ordered domains was analyzed adopting the algorithm reported by Hillebrand *et al.*¹⁷⁷. **Figure S4** (b) shows the AFM images superimposed with the detected domains in different colors. Each color corresponds to a different domain. Particles marked in white are not associated to any domain. All samples show large crystalline domains. With increasing interparticle distance the monolayers show fewer defects and the domain size increases. **Figure S4** (c) shows magnified parts of the monolayer images ($10 \times 10 \mu\text{m}^2$) with colored triangles connecting three neighboring particles that belong to crystalline domains resulting from our domain analysis. The selected image regions are highlighted by the red squares in (b).

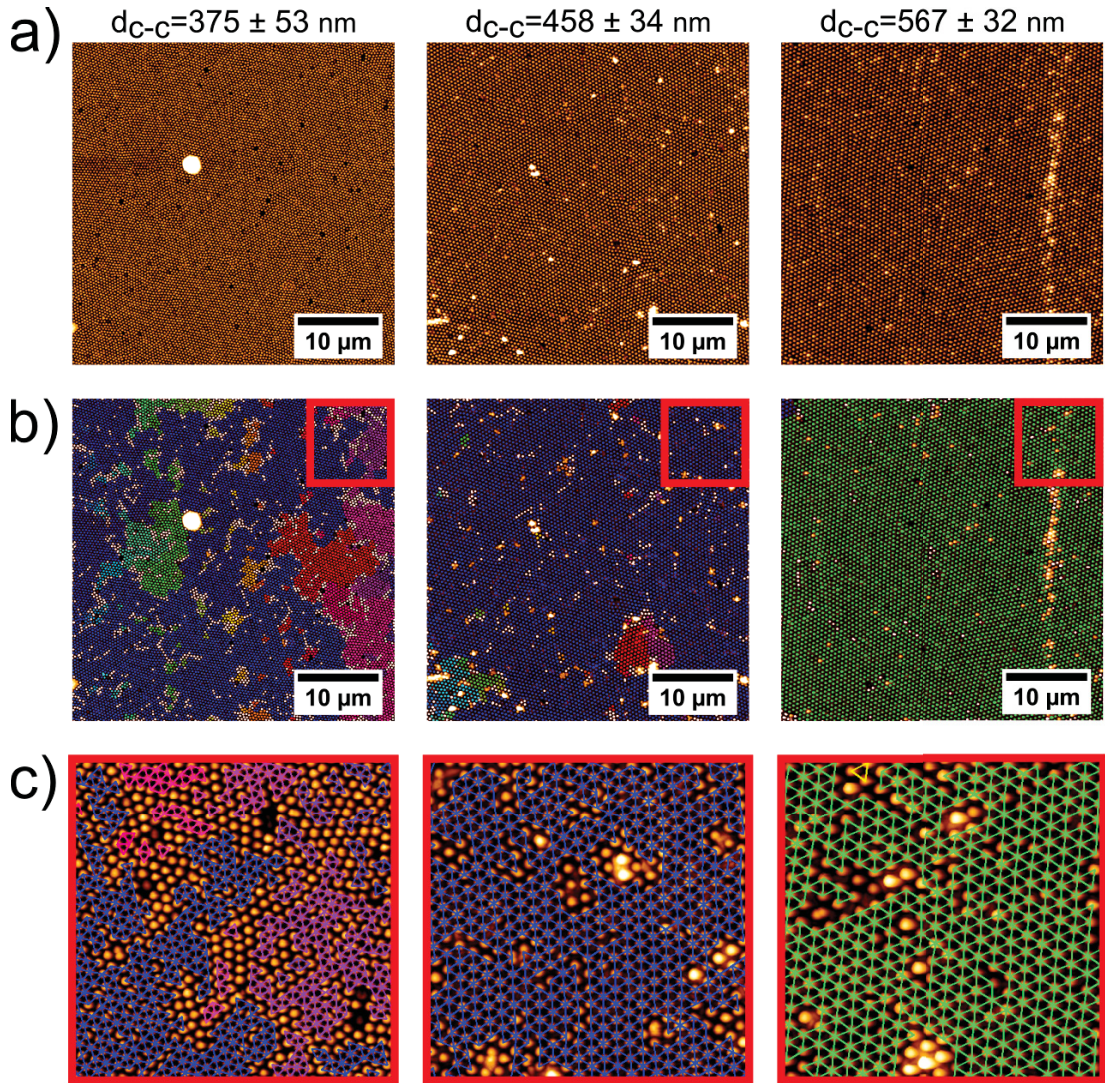


Figure S4: Analysis of domain sizes. $40 \times 40 \mu\text{m}^2$ AFM height profile images measured in tapping mode against air for monolayers with $d_{c-c} = 375 \text{ nm}$, $d_{c-c} = 458 \text{ nm}$ and $d_{c-c} = 567 \text{ nm}$ (a). (b) shows the result of the domain analysis where particles belonging to individual crystalline domains are marked by different colors. Particles marked in white are not associated to any domain. (c) triangulation resulting from domain size analysis. The shown magnified image regions ($10 \times 10 \mu\text{m}^2$) are highlighted in the corresponding images in (b).

Experimental Spectra of all Particle Monolayers

Figure S5 summarizes the absorbance spectra of all particle monolayers for asymmetric (a) and symmetric RI environment (b). The monolayers have values of d_{c-c} in the range of 342 nm to 573 nm. For the asymmetric RI case all samples show single resonance peaks only. In contrast for the symmetric RI case single resonance peaks are observed for the smaller d_{c-c} while at larger d_{c-c} two resonances appear.

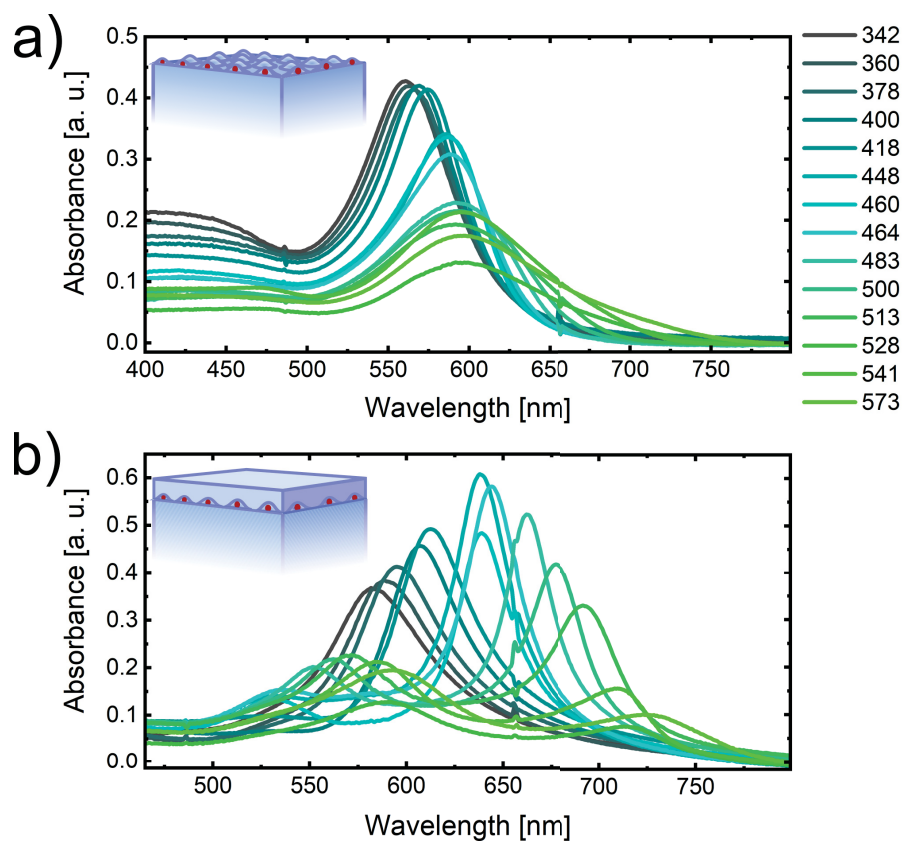


Figure S5: Experimental absorbance spectra for all particle monolayers with different d_{c-c} . (a) asymmetric RI environment; (b) symmetric RI environment. The color-coding of the individual spectra is the same in (a) and (b). The insets show schematic depictions of the respective sample geometries with glass as substrate and air as superstrate in (a) and a film of PNIPAM with 300 nm thickness as superstrate in b).

Optical Response of an Unordered Particle Monolayer

Figure S6 (a) shows an absorbance spectrum of an unordered Au-PNIPAM₃₃₆ particle monolayer on glass as substrate and air as superstrate. The sample was prepared by spin-coating using a highly dilute particle dispersion on a clean glass substrate. The AFM image in (b) shows the respective monolayer with large interparticle distances approximately in the range of 850 to 4000 nm. Due to the large distances and the absence of order, the optical response is comparable to the one of a single particle on glass. The spectrum reveals a single resonance peak at $\lambda_{LSPR} = 595$ nm.

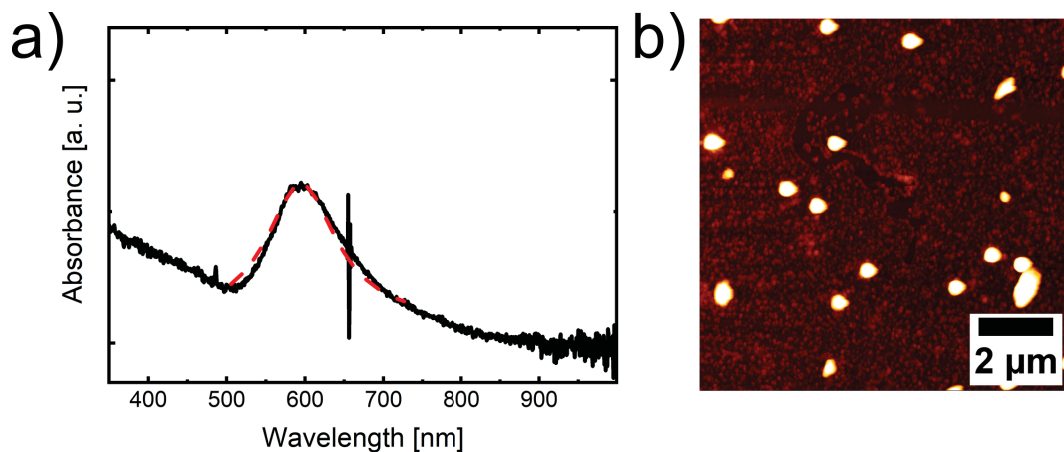


Figure S6: Optical response of an unordered, dilute particle monolayer. (a) Absorbance spectrum of the monolayer. The dashed red line is a Lorentz fit to the LSPR. (b) Corresponding AFM height profile image of the sample ($10 \times 10 \mu\text{m}^2$).

Local Transmission Spectra of Particle Monolayers

Figures S7 (a) and (b) show local absorbance spectra of monolayer samples with $d_{c-c} = 449$ nm and $d_{c-c} = 573$ nm. The spectra were recorded in transmission geometry with an optical light microscope using a $50\times$ magnification lens and transmissions were converted to absorbances. For the asymmetric RI case we measure single resonance peaks for both monolayers with resonance positions of $\lambda_{LSPR} = 582$ nm ($d_{c-c} = 449$ nm) and $\lambda_{LSPR} = 601$ nm ($d_{c-c} = 573$ nm). In contrast, for symmetric RI both samples feature two resonance peaks where the higher wavelength peaks are assigned to SLRs. The monolayer with $d_{c-c} = 449$ nm shows a narrow linewidth SLR at $\lambda_{SLR} = 631$ nm and a weak plasmonic contribution at lower wavelengths. The monolayer with $d_{c-c} = 573$ nm features a relatively weak SLR at approximately 721 nm and a significantly more pronounced plasmonic peak at lower wavelength. The plasmonic contribution almost resembles the optical response measured for the asymmetric RI case. Overall the spectra are in good agreement to the ones recorded using standard far-field extinction spectroscopy as shown in the main manuscript and in figure S5.

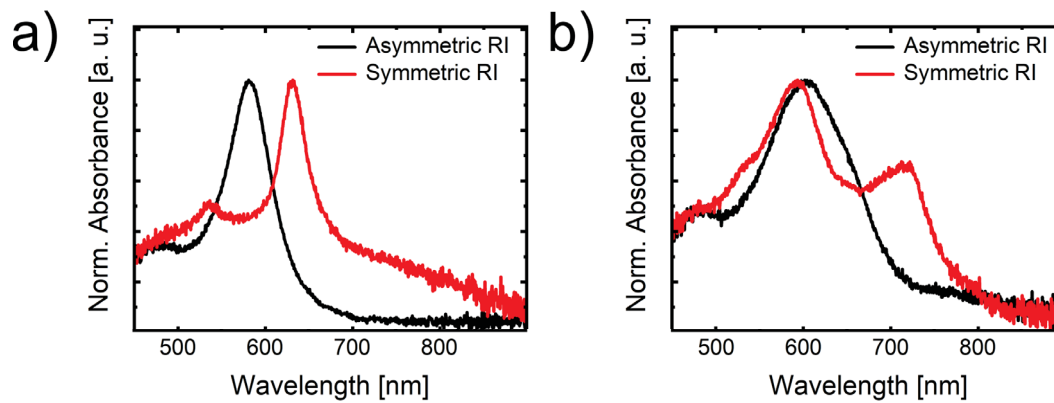


Figure S7: Local optical response. Absorbance spectra of monolayer samples with $d_{c-c} = 449$ nm (a) and $d_{c-c} = 573$ nm (b) in asymmetric RI (black lines) and symmetric RI environments (red lines) obtained from transmission measurements with an optical light microscope at $50\times$ magnification. All spectra were normalized to the maximum peak intensities.

Simulation Layout for FDTD

Figure S8 shows schematically the measurement geometry from experiment and the simulation layout (FDTD) in the XZ view (infinite lattice). All simulations were performed to match the experimental conditions. Particle sizes as well as distances were used as obtained from the experiments.

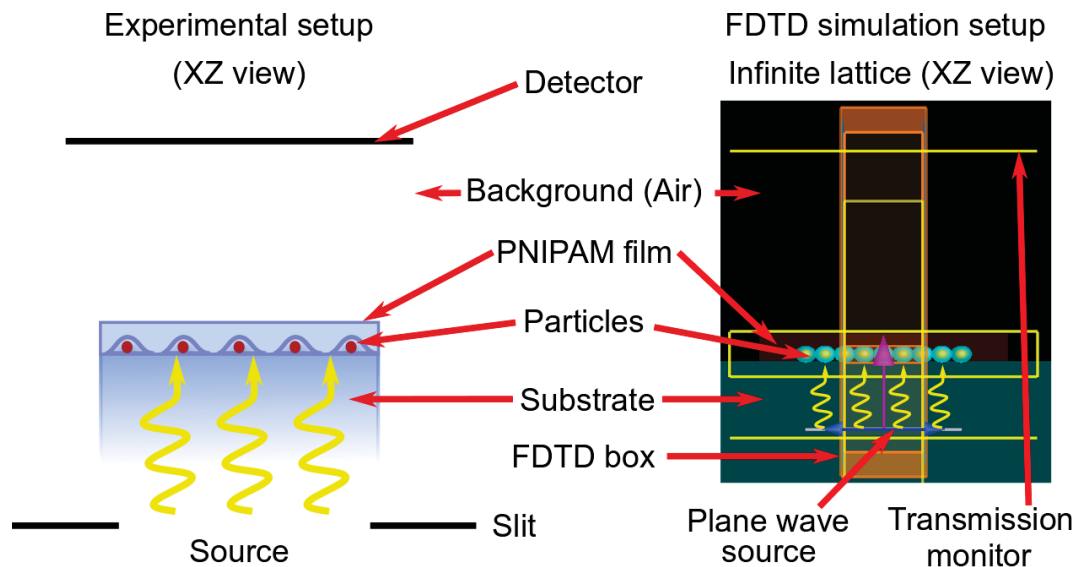


Figure S8: Schematic representation of the experimental transmission measurements and the FDTD simulation conditions for the infinite lattice.

Theoretical Q-Factor for Various Domain Sizes

Figure S9 shows the theoretical Q-factors of the highest intensity resonances obtained from FDTD simulations of particle arrays with different interparticle distances in dependence of the domain size. Compared are results for domain sizes of 2 (19 particles), 3 (37 particles), 4 (61 particles) and 5 (91 particles) as well as for the respective infinite lattices (periodic boundary conditions, PBC). The lattices with $d_{c-c} = 400$ nm feature nearly the same Q-factor independent on the domain size. At this interparticle distance diffractive-plasmonic coupling is not supported and thus the resonances are nearly independent on the lattice size. At larger values of d_{c-c} where diffractive-plasmonic coupling results in SLRs, the infinite lattice features significantly higher Q-factors that generally increase with increasing d_{c-c} . In contrast the Q-factor of all finite lattices decrease significantly for the largest d_{c-c} .

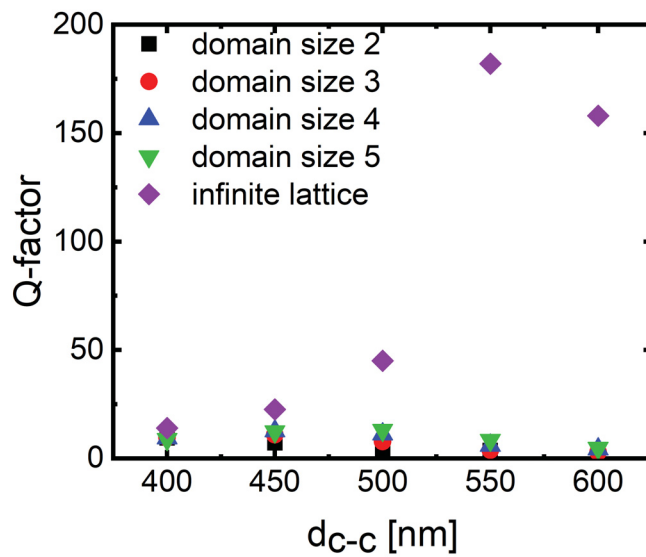


Figure S9: Comparison of Q-factors obtained from FDTD simulations. Compared are the Q-factors of Au nanoparticle arrays with different domain sizes for various d_{c-c} in symmetric RI environments. The domain size was varied in the range of 2 to 5. Data are compared to an effectively infinite lattice (PBC).

Theoretical Optical Response in the Strongest Coupling Regime

Figure S10 shows a calculated extinction spectrum from FDTD simulations of a gold particle lattice with $d_{c-c} = 483$ nm in a symmetric RI environment. The simulation was performed with PBC in x- and y-direction. The Q-factor of the SLR is 36.9.

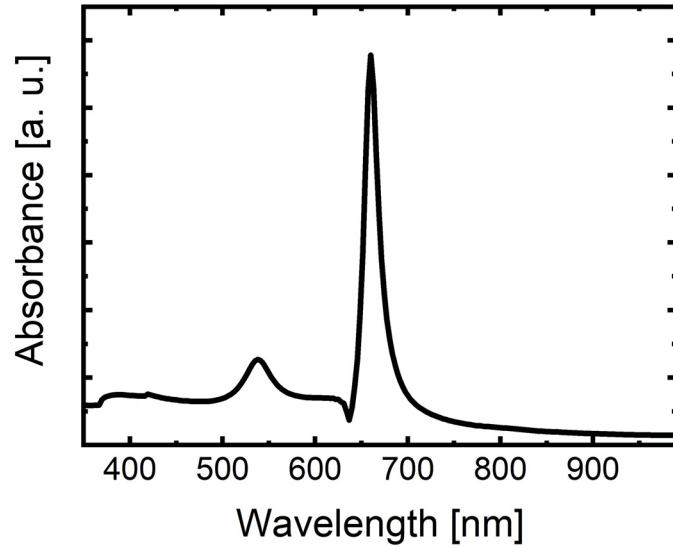


Figure S10: Optical response in the strong coupling regime. Extinction spectrum from FDTD simulation using a gold nanoparticle lattice with $d_{c-c} = 483$ nm in a symmetric RI environment and PBC yielding an infinite size lattice.

Self-Assembly Process

The full movie is available free of charge at <http://pubs.acs.org/doi/10.1021/acs.langmuir.0c02430>

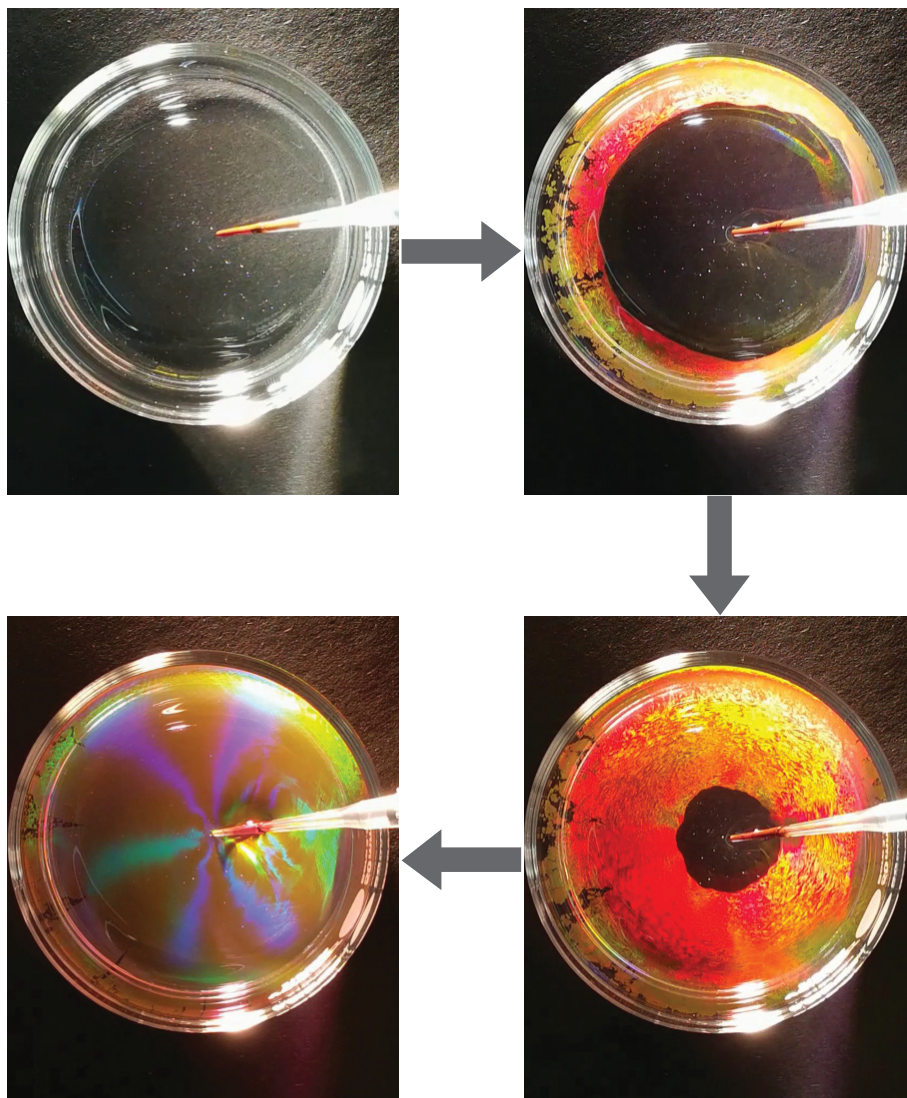


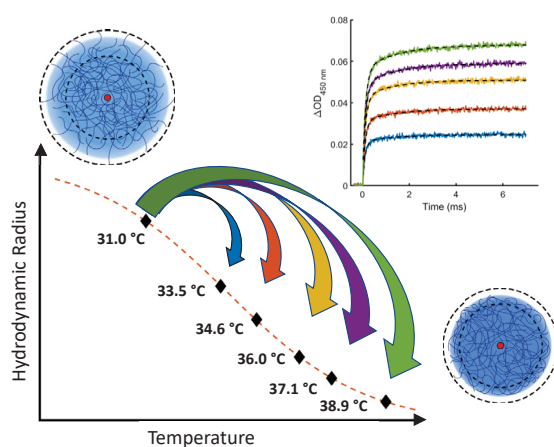
Figure S11: Self-assembly process.

6 Temperature-Jump Spectroscopy of Gold-Poly(N-isopropylacrylamide) Core-Shell Microgels

Ben Tadgell¹, Ekaterina Ponomareva², Matthias Karg², and Paul Mulvaney^{1*}

¹ARC Centre of Excellence in Exciton Science, School of Chemistry, The University of Melbourne, Parkville, VIC 3010, Australia

²Institut für Physikalische Chemie I: Kolloide und Nanooptik, Heinrich-Heine-Universität Düsseldorf, Universitätsstraße 1, D-40225 Düsseldorf, Germany



Reprinted with permission from *The Journal of Physical Chemistry C*, **2022**, *126*, (8), 4118-4131

Copyright 2022 American Chemical Society

6.1 Abstract

The collapse dynamics of gold-poly-(*N*-isopropylacrylamide) core-shell microgels were measured by capacitor-discharge temperature-jump spectroscopy. Using a series of temperature jumps from 31 °C up to 38.9 °C, we could monitor a characteristic two-component volume phase transition by changes in optical density that occurred on a time scale of milliseconds. Kinetic data were compared for microgels over a range of polymer shell thicknesses and cross-linker densities. We show that the fast component of the two-component collapse is consistent with the rapid contraction of the loosely cross-linked outer corona of the polymeric microgel, where the polymer density is lowest. The slow component corresponds to subsequent rearrangement of the polymer chains. The lifetime of the fast component scales linearly with the overall change in microgel radius and the dynamics are consistent with the collapse of long polymer chains in the outer corona. The lifetime of the slow polymer rearrangement is almost constant over all the tested parameters. The relative contribution of the slow component to the overall change in optical density is largest when the initial and final states of the transition are closer to the fully collapsed state of the microgels. The relative contribution of the fast component is largest when the microgel is initially more swollen.

6.2 Introduction

Poly-(*N*-isopropylacrylamide) (PNIPAM) is a well-known thermoresponsive polymer that undergoes a coil-to-globule transition in water due to its lower critical solution temperature (LCST).^{254,255,256} Below the LCST (~ 32 °C in water), polymer-solvent interactions are favored, while chain collapse above the LCST is observed where polymer-polymer interactions dominate. When physically and/or chemically cross-linked, for example by using a bifunctional comonomer, three-dimensional PNIPAM networks, *i.e.*, gel-like systems, can be prepared. In aqueous environment, the resulting hydrogels exhibit a volume phase transition (VPT) due to the LCST behavior of PNIPAM. These hydrogel networks can have macroscopic or microscopic dimensions. Macro gels show a significant reduction in volume at temperatures above the volume phase transition temperature (VPTT) enabling them to convert a change in temperature into mechanical work, and making them interesting for actuators and sensors.^{257,258,259} Microgels are hydrogel networks possessing dimensions in the colloidal regime and an internal gel-like structure that undergoes much more rapid switching in response to stimuli. This opens up further applications in drug-delivery,^{260,261} catalysis,^{262,263} and directed nanoparticle assembly.^{264,265}

The VPT of a microgel is typically followed by measuring the hydrodynamic diameter with dynamic light scattering (DLS) as a function of temperature.²⁶⁶ The overall volume change, VPTT, and the sharpness of the transition can be easily tuned by the choice of monomers and comonomers and their concentrations.² For example, increasing the molar ratio of cross-linking agent (typically *N,N'*-methylenebis(acrylamide), BIS) to NIPAM monomer decreases the mesh size of the microgel network, limiting the maximum

available uptake of solvent. This results in a smaller overall change in volume and a less sharp transition when heated or cooled over the VPTT. The VPTT can also be tuned by the introduction of ionizable⁵⁹ or hydrophobic²⁶⁷ comonomers. An important characteristic of PNIPAM microgels cross-linked with BIS is that they possess a gradient-like network structure with a homogeneous, more highly cross-linked core and an outer shell where cross-linker density decreases as a function of distance from the center.^{40,268} In the swollen state, the outer corona is at its largest - as the microgel collapses the thickness of the shell decreases and the polymer density approaches that of the inner region. Finally, in the fully collapsed state the polymer density is almost homogeneous over the whole gel. The fuzzy-sphere form factor is an excellent model to describe the decay in polymer density as a function of distance from the microgel center.²⁶⁹ Several recent studies have also proposed other form factors that further refine the fuzzy-sphere model and more precisely model the polymer-density variation.^{189,215} It has also been proposed that discrete microglobules form in these gel networks, increasing in density as the network collapses.²⁷⁰

While the equilibrium states of PNIPAM microgels have been well characterized, the dynamics of the volume phase transition are only beginning to be understood. In macrogels, an equation to describe the deswelling or swelling transition has been determined from a simple diffusion model.^{4,69} Here, the radius of a spherical gel that is out of equilibrium approaches its final state with a single-exponential lifetime, $\tau = R_{\text{final}}^2/D$, where R_{final} is the radius at equilibrium and D represents the diffusion coefficient of the gel network. In microgels the kinetics are further influenced by structural inhomogeneities in the gel and they also take place on much faster time scales. Several studies have characterized the collapse transition of microgels in response to fast co-nonsolvent addition,^{84,85} pressure-jumps,⁸³ and laser-induced temperature-jumps.^{80,81} Others have characterized the collapse of functionalized gels by pH-induced jumps.^{71,271} Across many of these studies, collapse of the microgels with respect to radius could be fitted to double-exponential functions with both a fast and a slow characteristic lifetime. However, the structures of the microgels varied considerably over these studies, and as a result the transition components were assigned to different physical processes. For example, in the case of a very loosely cross-linked gel collapsing following a solvent-jump (0.25% molar cross-linker density), Keidel *et al.* determined by molecular dynamics simulation that the fast component corresponded to the collapse of polymer chains into clusters around the cross-linking regions, with the slow component corresponding to the relaxation of chains to the final globule state.⁸⁵ Nothdurft *et al.* also characterized the collapse of a more tightly cross-linked PNIPAM microgel by solvent-jump (5% molar cross-linker density) and found that the fast and slow components corresponded to distinct collapsing regimes limited by solvent expulsion and polymer rearrangement respectively.⁸⁴ In the pressure-jump study undertaken by Wrede *et al.*, the fast component was attributed to the formation of a semi-impermeable skin layer due to inhomogeneous collapse at the surface the lifetime of the slow component, corresponding to polymer rearrangement in the collapsed region, was then limited by the impeded flow of solvent through this layer.⁸³ In laser-induced temperature-jump studies, the collapse of the gel was found to be extremely fast and could be modeled by a single-exponential fitting function. However,

it is likely that the kinetics in these cases were nonlinear due to extremely high, local temperatures.^{80,81}

In this work, we have systematically altered the cross-linker density and microgel size to improve our understanding of their contributions to the fast and slow processes that occur during the collapsing volume phase transition of BIS cross-linked PNIPAM microgels. Further to this, we have examined transitions to a variety of final states over the volume phase transition for the first time, and we included microgels that had large molar cross-linker densities (up to 25%, nominal value). We find that an excellent technique for this is capacitor-induced temperature-jump spectroscopy.^{86,272,273} The technique is rarely employed in colloid chemistry, although it is frequently used in biochemistry to measure dynamics in large biomolecular systems such as protein folding.^{274,275,276,277} The technique employs a microsecond electrical discharge to heat a solvent, with the addition of around 0.1 M electrolyte ensuring that heating is rapid and homogeneous. Time-resolved changes in optical density can then be used to monitor the change in composition as the system relaxes to the new equilibrium state. The technique is attractive for this study because one can easily modulate the magnitude of the temperature jump to look at varying final states, the time resolution is well-defined, and the heating mechanism creates a homogeneous temperature change.

We use core-shell microgels that consist of small gold nanocrystal cores and much larger, chemically cross-linked PNIPAM shells. These microgels are prepared by seeded precipitation polymerization where the cores (seeds) allow for the precise control of the thickness of the PNIPAM shell without the need to employ surfactants or comonomers.⁵⁰ The gold cores can also act as a plasmonic marker^{264,265} and can induce photothermal heating to initiate shell collapse in certain applications.^{80,278} Herein, we show that the fast and slow components of the collapsing volume phase transition follow well-defined trends over three principal parameters: microgel hydrodynamic radius, cross-linker density, and temperature-jump magnitude. Systematic variation of the latter parameter allows us to understand how the two components contribute to transitions to various final states. We monitor the transition by visible light scattering and carefully characterize the relationship between optical density and the microgel radius at equilibrium. As we monitor jumps between equilibrium states, the fast and slow lifetimes as well as the relative contributions of the fast and slow components to the overall change in optical density were measured. Overall, the trends in our data are consistent with the fast component corresponding to the collapse of high molecular weight, dangling chains in the outer fuzzy shell of the microgels, and the slow component corresponding to any remaining polymer rearrangement to assume the equilibrium state. As an aside, we are also able to distinguish optical density changes due to microgel deswelling and microgel aggregation that occurs in some instances. Finally, the work shows that capacitor-discharge temperature-jump spectroscopy is an excellent technique to monitor kinetics in such colloidal systems.

6.3 Experimental Methods

Chemicals

Gold (III) chloride trihydrate (HAuCl_4 ; Sigma-Aldrich, $\geq 99.999\%$), sodium citrate dihydrate (Sigma-Aldrich, $\geq 99\%$), sodium dodecyl sulfate (SDS; Sigma-Aldrich, p.a.), butenylamine hydrochloride (BA; Sigma-Aldrich, 97%), *N*-isopropylacrylamide (NIPAM; TCI, $>98.0\%$), *N,N'*-methylenebis(acrylamide) (BIS; Sigma-Aldrich, $\geq 99\%$), and potassium peroxydisulfate (PPS; Sigma-Aldrich, $\geq 99\%$) were used as received. Milli-Q water was used to make up all solutions ($R > 18\text{ M}\Omega\text{cm}$).

Gold Nanoparticle Cores

The spherical gold nanoparticles were synthesized according to the well-known protocol of Turkevich *et al.*⁴⁶ Briefly, 10 mL of a hot, aqueous sodium citrate solution (1 wt %) was added to 200 mL of an aqueous gold(III) chloride trihydrate ($5 \times 10^{-4}\text{ M}$) solution under continuous stirring and boiling. The dark red nanoparticle dispersion was then allowed to boil for another 20 min. After cooling to room temperature, 1.2 mL of SDS solution (1 mM, aqueous) was added to the dispersion, which was then stirred for 20 min. Afterward, the gold particles were functionalized by adding 0.652 mL of butenylamine hydrochloride solution (1.4 M).⁸ The functionalized particles were purified and concentrated by centrifugation for 14 h at 1400g rcf and removal of the clear and colorless supernatant.

Au-PNIPAM Core-Shell Microgels

The functionalized gold nanoparticles were encapsulated by cross-linked PNIPAM shells using seeded precipitation polymerization as described by Rauh *et al.*¹² Polymerizations were performed in 100 mL of *Milli-Q* water in three-neck round-bottom flasks. First, NIPAM and BIS were dissolved under continuous stirring. Then, the solution was heated to $70\text{ }^\circ\text{C}$ while degassing with nitrogen. 3.72 mL of the functionalized gold nanoparticles with an elemental gold concentration (Au^0) of 0.00622 mol/L was then added dropwise to the colorless solution. After an equilibration time of 15 min, 2 mg of PPS dissolved in 1 mL water was added to the mixture to initiate the polymerization. The polymerization was allowed to proceed for two hours. After cooling to room temperature, the Au-PNIPAM microgels were purified by centrifugation (90 min at 8400g rcf) and redispersion in water. The purification was repeated three times. In total we synthesized five core-shell systems (CS1 - CS5) that differed in shell thickness or cross-linker content. For the samples CS1-CS3 different amounts of NIPAM were used while the nominal BIS mole fraction was fixed at $\sim 15\text{ mol}\%$ with respect to NIPAM. For samples CS2, CS4, and CS5 a fixed amount of NIPAM was used while the amount of BIS was varied to create shells with different swelling capacities. The absolute quantities of monomer and cross-linker used in synthesis and calculations of the VPTT are outlined in the Supplementary Information (**Table S1**). Key properties of the five different core-shell microgels are summarized in **Table 1**.

Table 1: Key Properties of Core-Shell Microgels CS1 - CS5: Nominal Molar Ratio of Cross-Linker (BIS) Used in the Synthesis, Swelling Ratio at 50 °C, and Hydrodynamic Radius, R_h , at 31 °C in the Presence and Absence of KCl and Volume Phase Transition Temperatures (VPTT)

| sample | nominal cross-linker content ^a (%) | $\frac{(R_h \text{ at } 50 \text{ }^\circ\text{C})}{(R_h \text{ at } 25 \text{ }^\circ\text{C})}$ | R_h at 31 °C (nm) | R_h at 31 °C (nm) [KCl] = 0.10 M | VPTT (°C) |
|--------|--|---|---------------------|---------------------------------------|-----------|
| CS1 | 15.3 | 0.70 | 104 ± 1 | 101 ± 1 | 35.1 |
| CS2 | 16.7 | 0.69 | 158 ± 2 | 151 ± 2 | 34.9 |
| CS3 | 14.8 | 0.70 | 183 ± 1 | 171 ± 2 | 33.2 |
| CS4 | 5.0 | 0.56 | 165 ± 3 | 151 ± 2 | 33.7 |
| CS5 | 24.9 | 0.77 | 151 ± 3 | 143 ± 1 | 34.4 |

a. Molar ratio of BIS cross-linker to NIPAM monomer used in the synthesis.

Temperature Jump Experiments

Temperature-jump spectra were collected on a *Hi-Tech PTJ-64* capacitor discharge apparatus (Hi-Tech, Salisbury UK). The sample sat in a $3 \times 3 \times 5 \text{ mm}^3$ cell (path length 3 mm) surrounded by an adjustable temperature water bath. The bath temperature determined the initial temperature of the sample. The cell was connected to the two electrode terminals of an adjustable voltage capacitor, which induced a fast temperature jump upon discharge. As the system shifted to its equilibrium position at the new temperature, the dynamics were monitored by changes in OD at a wavelength selected by the monochromator. Our system employed a tungsten halide monitoring lamp and a PMT for signal collection, positioned at 180° to the monitoring lamp.

The magnitude of the temperature jump was determined by the capacitor voltage; details regarding the calibration are contained in the Supplementary Information (**Figure S1**). The magnitude of the applied voltage did not affect the time taken for the solution to reach the new temperature. The heating time was calculated by using the the "RC" time constant of the circuit.²⁷⁹ The stored capacitor charge dissipated exponentially with a lifetime (time constant τ_c) that was inversely proportional to the solution conductance and could be calculated from **6.1** given the geometry of our cell: cross-sectional electrode area ($A = 0.09 \text{ cm}^2$), the distance between the electrodes ($l = 0.9 \text{ cm}$), and the capacitance ($C = 4 \times 10^{-8} \text{ F}$).

$$\tau_c = \frac{lC}{\sigma A} \quad (6.1)$$

The time constant was determined by the solution conductivity (σ) and this in turn could be controlled by adding KCl electrolyte.²⁸⁰ It was vital to consider the time constant in capacitor-discharge temperature-jump experiments, as it determined the

minimum time-resolution for an experiment. **Table 2** outlines the corresponding time-constants for our samples for different [KCl].

Table 2: Effect of [KCl] on the Capacitor Discharge Time Constant (τ_c)

| [KCl] (M) | τ_c (ms) |
|-----------|---------------|
| 0.010 | 0.28 |
| 0.050 | 0.060 |
| 0.075 | 0.041 |
| 0.100 | 0.031 |
| 0.200 | 0.016 |

The temperature-jump experiments were conducted at an initial bath temperature of 31.0 °C. This temperature was chosen because it was close to the VPTT, and a relatively small increase in temperature results in a pronounced reduction in hydrodynamic radius, *i.e.* shell thickness. Samples were loaded into the cell through reagent ports. For each sample, five experiments were conducted in which the capacitor voltage was tuned to initiate five different temperature-jump values. The capacitor voltages used were 7.0, 8.5 kV, 10.0, 11.0, and 12.5 kV. This corresponded to temperature jumps of 2.5, 3.6, 5.0, 6.1, and 7.9 °C, respectively. At each voltage, the kinetics were determined by averaging the fits to three T-jump experiments. A time of 100 s was allowed for cooling between shots. The chosen monitoring wavelength was 450 nm as it could be shown that a change in temperature induced a well-defined ΔOD at this wavelength. The experiments were conducted first with a run time of 7 ms and then with a run time of 30 s. For the 7 ms experiments, the data were fitted to double exponential curves between $t = 0.029$ ms and $t = 7$ ms.

Transmission Electron Microscopy

Electron microscopy images were collected with a Tecnai F20 (FEI) transmission electron microscope (TEM) at an acceleration voltage of 200 kV. For the TEM images, 7 μ L of the Au-PNIPAM microgel dispersion was dried on carbon-coated, 300-mesh copper grids.

UV/Vis Spectroscopy

UV/vis spectra were collected on two different instruments. Wavelength-resolved spectra were collected on an AnalytikJena Specord S 600 UV/vis spectrometer, equipped with a temperature-controlled sample holder. Measurements were performed across the wavelength range of 250 - 1019 nm in transmission geometry. Extinction spectra of the dilute microgel dispersions were measured in 1×1 cm² PMMA cuvettes.

UV/vis experiments in which one wavelength was selected and scanned over temperature were conducted by using an *Agilent Cary 3500* spectrometer. This instrument was equipped with an air-cooled Peltier system that precisely controlled the solution temperature with a digital temperature probe that sat inside a 1×1 cm² quartz cuvettes.

In our experiments the OD at 450 nm was collected at 0.2 °C intervals, while scanning the temperature from 25 to 45 °C at a rate of 1 °C per/min, with the solution stirred at 500 rpm.

Dynamic Light Scattering

Hydrodynamic radius, R_h , was measured by dynamic light scattering (*ZetaSizer Nano Series NanoS90*), with the scattering angle set to 90°. The Z-average of the diffusion coefficient was determined over a temperature range by allowing the system to equilibrate at each temperature for 10 min, and taking the average of three to five measurements. Error bars represent the standard deviation of the averages.

Zeta Potential Measurements

Zeta potential measurements were collected on a *Brookhaven ZetaPALS* instrument at 24 °C using an average of 10 runs with 30 cycles each. The measured electrophoretic mobilities were converted into zeta potentials by using the Smoluchowski method.

Sample Preparation

We prepared dilute aqueous dispersions of all five core-shell microgels at 0.050 wt% (unless otherwise stated). The concentration is sufficiently small that we can neglect particle-particle interactions but high enough to provide optimal OD for our spectroscopic investigations. Unless otherwise specified, [KCl] values of 0.100 M were used in most experiments to ensure that the capacitor time constant was sufficiently small. Unless otherwise specified, the pH of the samples was not adjusted and was constant at around pH = 7. Otherwise, the pH of samples was adjusted upon dilution from a stock as required by addition of HCl or KOH and measured by using a pH meter (*SevenCompact Duo*, *Mettler Toledo*). *Milli-Q* water was used throughout.

6.4 Results

6.4.1 Steady-State Characterization

We synthesized Au-PNIPAM core-shell (CS) microgels with spherical gold nanocrystal cores and chemically cross-linked PNIPAM shells that differed in shell thickness or cross-linker content. **Table 1** outlines the properties of the five microgels used. The cross-linker content was varied by altering the ratio of BIS cross-linker to NIPAM monomer during synthesis, and the shell thickness was altered by increasing the absolute concentrations of these reagents. Samples CS1-CS3 have a nearly constant cross-linker density (~15% nominal molar ratio) with increasing shell thicknesses. CS4 and CS5 have varying nominal cross-linker densities (5% and 25%, respectively) and were synthesized with the same initial monomer content as CS2. **Figure 1a** shows a representative TEM image of CS3. TEM images for the other particles (CS1, CS2, CS4, and CS5) are shown in **Figure S2**. A gold core surrounded by lower electron density PNIPAM shells can be

seen in all samples. The microgels virtually all contain single gold nanoparticle cores, and the difference in shell thickness in CS1 to CS3 is visible despite the low contrast of the shell. In TEM the PNIPAM shells are imaged in their dried and collapsed state, and consequently, the shell dimensions are smaller than when measured in solution.

The five CS microgels undergo a thermoreversible volume phase transition upon heating or cooling. The volume phase transition temperature (VPTT), the sharpness of the transition around the VPTT, and the relative change in volume all depend on the varying microgel characteristics. As the VPT is associated with a change in solution turbidity and microgel hydrodynamic radius, UV/vis and DLS measurements could be used to characterize the transitions for each of the CS microgels and to establish a relationship between temperature, particle radius, and optical density in solution for each microgel. A representative temperature-dependent evolution of the optical density (OD) of a dilute aqueous dispersion of CS3 is shown in **Figure 1b**. We chose a large temperature range from 10 to 60 °C to cover the full VPT. At 10 °C the shells will be fully swollen, while at 60 °C the shells will be fully collapsed. All spectra show a continuous increase in OD with decreasing wavelength that is attributed to light scattering from the PNIPAM shells. With increasing temperature the scattering cross section increases. The gold nanoparticle core contributes to the spectra at around 520 nm due to its localized surface plasmon resonance (LSPR), but it is barely visible due to the strong scattering by the polymer shell. The contribution of the LSPR is predominantly due to light absorption rather than scattering.²⁶⁹ Wavelength-resolved spectra for the other CS microgels are shown in **Figure S3**.

We determined the temperature-dependent hydrodynamic radius for each of the microgels using dynamic light scattering. As expected, the hydrodynamic radius decreases over temperature, corresponding to increasingly collapsed equilibrium states over the VPT. **Figure 1c** compares two plots: the OD at 450 nm over temperature and the corresponding hydrodynamic radius over temperature ($c = 0.050$ wt%, CS3). At low temperatures the OD is at a minimum and the hydrodynamic radius is at a maximum. As the temperature is increased, the values increase (or decrease) until they reach their maximum (or minimum) values, respectively. For a given microgel, the radius and OD data have an inflection point at the same temperature: this was taken to correspond to the microgel VPTT and could be determined to be the point at which the double derivative with respect to temperature was equal to zero.²⁸¹ The extracted VPTT values are listed in **Table 1**. The data points for OD and hydrodynamic radius could be fitted to sigmoidal functions for interpolation over a continuous temperature range. For CS1, CS2, CS3 and CS5, fitting the curves to eqs **6.2** and **6.3** gave an excellent fit.

$$\text{OD}(T) = \text{OD}_{\max} + \frac{\text{OD}_{\min} - \text{OD}_{\max}}{1 + \exp\left(\frac{T-T_0}{h}\right)} \quad (6.2)$$

$$R(T) = R_{\min} + \frac{R_{\max} - R_{\min}}{1 + \exp\left(\frac{T-T_0}{h}\right)} \quad (6.3)$$

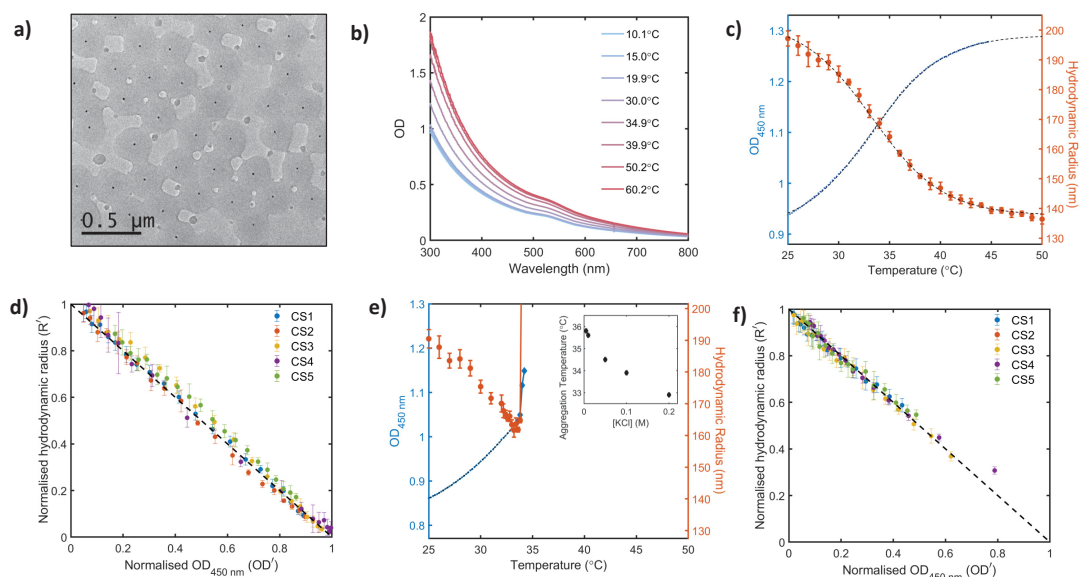


Figure 1: (a) Representative TEM image of the CS3 microgel. The PNIPAM shell is visible around the gold core. (b) UV/vis spectra recorded over different temperatures (CS3, $c = 0.017$ wt%, $[KCl] = 0$ M). (c) Equilibrium OD at 450 nm (blue) and hydrodynamic radius (orange) over temperature (CS3, $c = 0.050$ wt%, $[KCl] = 0$ M). (d) Plot of the normalized hydrodynamic radius (R' , eq 6.6) against the corresponding normalized OD at 450 nm (OD' , eq 6.5), over the set of temperatures from 25 to 50 °C. All data lie on the line $y = 1 - x$ (dashed), showing that these properties are linearly related at equilibrium for all microgel types ($c = 0.050$ wt%, $[KCl] = 0$ M, CS1: blue, CS2: orange, CS3: yellow, CS4: purple, CS5: green). (e) Equilibrium OD at 450 nm (blue) and hydrodynamic radius (orange) vs. temperature with electrolyte present (CS3, $c = 0.050$ wt%, $[KCl] = 0.100$ M). The data at $T > 35$ °C, corresponding to large aggregates, are omitted for clarity. Inset shows aggregation temperature as a function of $[KCl]$. (f) Plot of the normalized radius (R') as a function of the normalized OD at 450 nm (OD') in the presence of 0.100 M KCl.

OD(T) and R(T) correspond to the equilibrium OD at 450 nm and the hydrodynamic radius at a given temperature, T , respectively. The parameters OD_{min} and R_{max} correspond to the limiting values in the fully swollen state, where OD is at a minimum and the hydrodynamic radius is at a maximum. The parameters R_{min} and OD_{max} correspond to the limiting values in the fully collapsed state. The inflection point T_0 corresponds to the microgel VPTT, and the parameter h defines the sharpness of the transition with respect to temperature. The fitting functions (6.2) and (6.3) take the same values of T_0 and h for a given CS microgel;. For CS4, a slightly more complex fitting function is required to interpolate the curves. This is a more general model but is consistent with that used by Hellweg *et al.* to follow microgel volume phase transitions.²⁸¹ Further details are shown in the Supplementary Information. All fitting parameters and plots for the remaining CS microgels are outlined in **Table S2** and **Figure S4**.

These fits reveal that, for all of the CS microgels, including CS4, the OD is linearly related to the hydrodynamic radius at any given temperature. This establishes an important relationship between the two properties at equilibrium, defined in eq (6.4).

$$\frac{\text{OD}_T - \text{OD}_{\min}}{\text{OD}_{\max} - \text{OD}_{\min}} = 1 - \frac{R_T - R_{\min}}{R_{\max} - R_{\min}} \quad (6.4)$$

$$\text{OD}' = \frac{\text{OD}_T - \text{OD}_{\min}}{\text{OD}_{\max} - \text{OD}_{\min}} \quad (6.5)$$

$$R' = \frac{R_T - R_{\min}}{R_{\max} - R_{\min}} \quad (6.6)$$

The fraction $(\text{OD}_T - \text{OD}_{\min})/(\text{OD}_{\max} - \text{OD}_{\min})$ represents a normalized optical density value, which is equal to 0 when the microgel is completely swollen and equal to 1 when the microgel is completely collapsed. This is termed OD' , shown in equation 6.5. In the same way, the fraction $(R_T - R_{\min})/(R_{\max} - R_{\min})$ represents the normalized hydrodynamic radius: it is equal to 1 when the microgel is fully swollen and equal to 0 when the microgel is fully collapsed. This is termed R' , shown in eq 6.6. A plot of the normalized radius (R') against the normalized OD (OD'), at the corresponding temperature, confirms this relationship for all CS microgels (**Figure 1f**). This provides a convenient way to compare the dynamics of the microgels in terms of a normalized swelling ratio, with respect to both OD and microgel radius.

While these measurements reveal the VPT behavior of CS microgels in water, these dispersions are not suited for capacitor-discharge T-jump experiments due to the low ion concentration. We therefore now want to address the microgel behavior in the presence of electrolyte (KCl). The microgels are mostly stabilized by electrostatic repulsion stemming from the ionic groups incorporated by the radical, anionic initiator. Steric stabilization from dangling chains in the outer periphery of the microgels is only relevant below the VPTT. Electrolytes may induce microgel aggregation at temperatures close

to the VPTT due to charge-screening or "salting-out" effects; these have been reported by several groups.^{282,283,284}

Indeed, we found that there was a critical temperature at which the CS microgels aggregate in the presence of KCl. **Figure 1e** shows the temperature dependent hydrodynamic radius and OD_{450nm} of a solution of CS3 in the presence of 0.1 M KCl. There is a critical aggregation temperature under these conditions, which can be clearly identified in each of the traces as the point at which the curves strongly inflect upward. The increase in OD reflects the initial formation of small, well-dispersed aggregates; however, the value decreases after 1 min as aggregates become larger and start to sediment. We found that this aggregation was completely reversible. When the temperature is decreased back below the critical temperature, the aggregates redisperse with gentle shaking or stirring.

The critical temperature is not affected by whether it is determined by measurement of hydrodynamic radius or OD. When [KCl] is increased from 1 to 200 mM, the critical aggregation point is shifted from 36 to 33 °C for CS3 (**Figure 1e, inset**). The inclusion of KCl in the solution also shifts the VPTT of the CS microgels to a lower value. This is outlined in **Figure S5**, which shows that the relationship between hydrodynamic radius and temperature is shifted along the temperature axis by a constant value when the electrolyte concentration is changed from 0 to 0.1 M. This property was used to fit each of the OD_{450 nm} and hydrodynamic radius plots to the relevant sigmoidal functions, which is otherwise made difficult due to aggregation at high temperatures. The concentration of KCl has an effect on the absolute values of OD that is more difficult to characterize (**Figure S6**). This could be a result of subtle changes in microgel morphology in the presence of electrolyte.²⁶⁸ However, the relationship between OD and temperature is still a linear transformation of the relationship between radius and temperature exactly as it was in the absence of electrolyte. This means that the relationship between OD' and R' is still described by eq 6.4 at temperatures below the aggregation point. This is shown in **Figure 1f**.

When sodium dodecyl sulfate (SDS) is added to the dispersion, aggregation is prevented as long as [KCl] \lesssim 0.01 M. This is shown in **Figure S8**, where there is no large inflection corresponding to aggregation. We show using zeta potential measurements that SDS accumulates at the microgel surface, increasing the surface charge and colloid stability (**Figure S8**). This is consistent with previous studies on the interaction of SDS with PNIPAM.^{285,286}

6.4.2 Temperature-Jump Spectroscopy

Figure 2 shows typical temperature-jump traces taken for the microgels CS1 to CS5 over the course of 7 ms. In these experiments an electrolyte concentration of [KCl] = 0.100 M was used to ensure the time resolution of the experiment was well below the time scale of the experiment ($\tau_c = 0.031$ ms, **Table 2**). The initial temperature was set to 31.0 °C, which is slightly below but very close to the VPTT of the CS microgels at 0.100 M KCl, and experiments were conducted for five different temperature jumps - 2.5, 3.6, 5.0, 6.1 and 7.9 K - to measure the dynamics for temperature jumps to different equilibrium states over the Au-PNIPAM swelling curve. For CS4, two extra jumps at

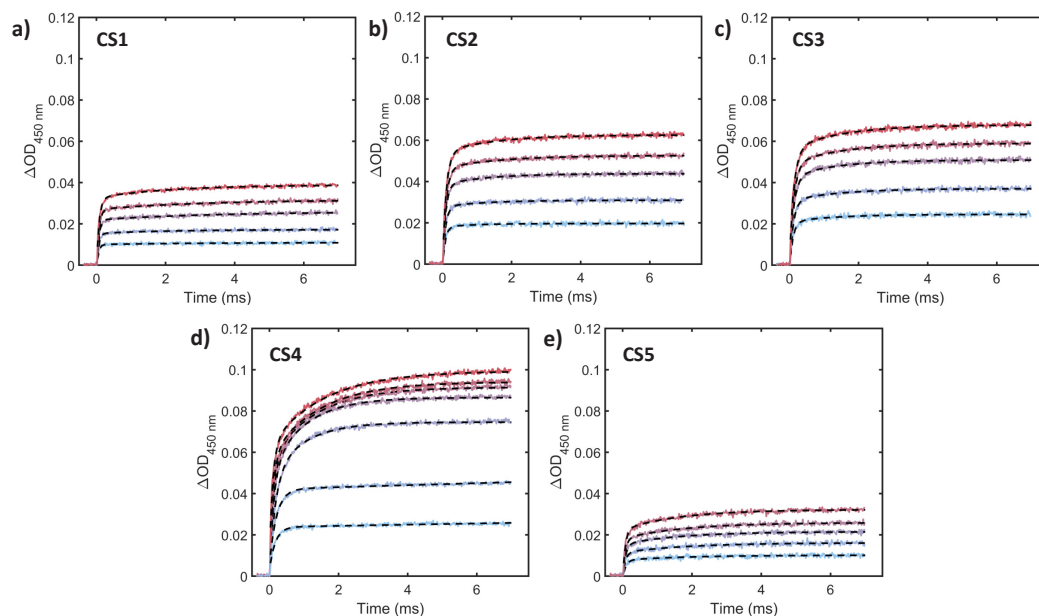


Figure 2: Temperature-jump time traces taken for CS1 to CS5 (a to e, respectively) over a 7 ms time scale ($c = 0.050$ wt%, $[KCl] = 0.100$ M). Fitted to double exponential functions of the form in eq **6.7**. ΔOD was calculated from $OD_{\text{final}} - OD_{\text{initial}}$ at 450 nm. From CS1 to CS5 the value of OD_{initial} was 0.17, 0.29, 0.36, 0.21 and 0.33, respectively. For CS1, CS2, CS3, and CS5 the initial temperature was 31 °C with final temperatures of 33.5, 34.6, 36, 37.1 and 38.9 °C (light blue to red). For CS4 two extra final temperatures were included: 32.2 °C and 32.8 °C. Fitting residuals are outlined in **Figure S12**.

lower temperatures were also included to capture a sufficient range of collapsed states. The traces were fitted to double-exponential functions with fitting parameters defined in eq 6.7. The value of ΔOD is calculated from $\text{OD}_t - \text{OD}_i$, where OD_i is the OD at 450 nm at 31 °C. For each temperature jump, the measurement was conducted in triplicate, with 100 s cooling time between jumps. The triplicate curves are virtually identical, showing that the process is highly reversible with respect to temperature and reproducible.

$$\Delta\text{OD}_{450\text{nm}} = \Delta\text{OD}_{\text{total}} - \Delta\text{OD}_{\text{fast}} \exp\left(\frac{-t}{\tau_{\text{fast}}}\right) - \Delta\text{OD}_{\text{slow}} \exp\left(\frac{-t}{\tau_{\text{slow}}}\right) \quad (6.7)$$

By fitting ΔOD over time for each of the CS microgels, over a range of temperature-jump magnitudes, we created a table for each of the fitting parameters, $\Delta\text{OD}_{\text{fast}}$, $\Delta\text{OD}_{\text{slow}}$, τ_{fast} and τ_{slow} , that shows how they are affected by microgel radius, microgel cross-linker content and temperature-jump magnitude (**Tables S4 - S11**). Experiments were also conducted focusing on one microgel type (CS3) where we investigated the effects of CS microgel concentration, KCl concentration, the inclusion of SDS at several concentrations, and pH (**Table S12 - S27**).

For completion, we note that we also observed a further transition at a much longer time-scale, up to 25 s following the temperature jumps. **Figure S9** shows the effect of KCl concentration and the presence of SDS on these slower transitions for the CS microgel CS3. For the lowest temperature-jump experiment under all three conditions, the trace increases to a maximum point within the first data point of the experiment, before reapproaching the initial OD value. At lower KCl concentrations (0.010 M), the second lowest temperature jump has the same form. Finally, with the inclusion of SDS all of the temperature-jump experiments follow this form. Otherwise the OD curves increase to a maximum value following the initial fast increase, after which it decreases and approaches the exponential component.

6.5 Discussion

6.5.1 Assigning T-Jump Spectra

We consistently observe that the polymer shell collapse occurs over two very distinct time scales. ΔOD due to the PNIPAM shell collapse is likely to correspond to the curves at the 7 ms time scale, as these fits to double-exponential functions are in agreement with PNIPAM collapse dynamics from previous studies.^{83,84,85} These traces also approach an increasingly large OD value with increasing temperature-jump magnitudes. This is what we would expect as they approach states with an increasing degree of deswelling. The ΔOD in the 25 s time regime is consistent with microgel aggregation and dissociation. A more detailed reasoning for this is outlined in the Supplementary Information.

We first focus on the shorter 7 ms time scale, and begin by addressing the general features of the kinetics apparent from adjusting several basic experimental parameters for a single microgel type (CS3). As we varied the mass concentration of the microgel, the values of τ_{fast} and τ_{slow} did not change (**Table S12 - S15**), which demonstrates that

the kinetics are not dependent on microgel collisions. Importantly this also demonstrates that ΔOD does not correspond to microgel aggregation on this time scale. The kinetics were also unchanged by the inclusion of increasing concentrations of SDS in the presence of low concentrations of KCl (**Table S20 - S23**). This further shows that ΔOD is not due to aggregation on this time scale, and more specifically that the dynamics are unaffected by whether or not the conditions are conducive to aggregation. The values of τ_{fast} and τ_{slow} were also unaffected by changing the concentration of KCl over the range 0.050 to 0.20 M. At a lower concentration than this, where $[KCl] = 0.010$ M, the calculated time constant for the capacitor discharge becomes much larger than the observed lifetimes for the fast transition (*i.e.*, $\tau_c = 0.28$ ms where the value of τ_{fast} is around 0.08 ms at higher salt concentrations). **Tables S16 - S19** show that τ_{fast} correspondingly increases under these conditions, as the kinetics become limited by the heating rate. Conversely, the fact that the lifetimes converge to a single value at salt concentrations around 0.100 M means that under these conditions the kinetics are not dependent on the rate of heating. Finally, altering the pH has no effect on kinetics (**Table S24 - S27**).

All of these properties are consistent with the interpretation that ΔOD on the 7 ms time-scale corresponds to the collapse of the PNIPAM shell. Furthermore, we are confident that the collapse transition occurs well before any subsequent microgel aggregation takes place, and that the kinetics correspond to fundamental dynamics of the system and are not limited by the rate of heating.

6.5.2 Influence of Microgel Size and Cross-Linker Density

We now investigate the trends in the PNIPAM shell collapse fitting parameters over temperature-jump magnitude, and incorporate the data over the five different microgel types to understand the effect of varying microgel radius and cross-linker density. The fast and slow exponential components are characterized by four parameters: ΔOD_{fast} , ΔOD_{slow} , τ_{fast} , and τ_{slow} . The pre-exponential factors represent the contribution to ΔOD from the fast and slow decay components. The overall change in OD over the course of the 7 ms time scale, ΔOD_{total} , is the sum of these two terms, *i.e.*, $\Delta OD_{\text{total}} = \Delta OD_{\text{fast}} + \Delta OD_{\text{slow}}$.

To compare trends in ΔOD_{total} , ΔOD_{fast} , and ΔOD_{slow} , the values were normalized by using eqs 6.5 and 6.6. **Figure 3a** outlines how $\Delta OD_{450\text{nm}}$ and $-\Delta R$ represent the difference in optical density and hydrodynamic radii between two states at equilibrium over different temperatures. **Figure 3b** shows how these quantities are transformed into normalized units, $\Delta OD'$ and $-\Delta R'$, by taking into account the limiting values at low and high temperatures. Thus, the expected $-\Delta R'$ was calculated for each of the microgels, at each of the temperature jumps, by taking into account the sigmoidal fit to the hydrodynamic radius over temperature at $[KCl] = 0.1$ M for each type of microgel. The normalized quantity $\Delta OD'_{\text{total}}$ was calculated from the fitting parameter ΔOD_{total} for each of the microgels, at each temperature jump, by incorporating the limiting values at high and low temperature (OD_{min} and OD_{max}) in the temperature-jump cell (**Figure S5**). We found that for almost all of the temperature-jump experiments the normalized fitting parameter $\Delta OD'_{\text{total}}$ was equal to the expected, normalised change in

hydrodynamic radius, $-\Delta R'$ (**Figure 3c**). The schematic in **Figure 3d** outlines that this is the expected result if we indeed monitor the entire VPT from the same initial equilibrium state at 31 °C, to the same equilibrium state at the final temperature. Our time-resolved traces therefore capture the kinetics for the entire transition for all temperature-jump experiments, with the exception of the lowest two temperature-jump magnitudes taken for CS4, for which $\Delta OD'_{\text{total}} < -\Delta R'$. This could be due to the microgel CS4 having a much sharper transition over a smaller temperature range. As the two lowest temperature jump magnitudes result in a final state close to the VPTT, we might expect deviation in $\Delta OD'_{\text{total}}$ as very small changes in temperature would result in large changes in the expected structure.

The fitting parameters $\Delta OD'_{\text{fast}}$ and $\Delta OD'_{\text{slow}}$ could also be normalized by using the same procedure. The normalized values retain the property $\Delta OD'_{\text{total}} = \Delta OD'_{\text{fast}} + \Delta OD'_{\text{slow}}$ and become values between 0 and 1, representing the changes in normalised optical density over the temperature jump due to the fast and slow processes. We found that the fitting parameters had a dependence on the initial and final hydrodynamic radii of the transition as well as the cross-linker content (**Figure 4a**). For CS1, CS2, CS3, and CS5, the value of $\Delta OD'_{\text{slow}}$ increases proportionally to the expected $-\Delta R'$ multiplied by a factor $(1 - R'_{31^\circ\text{C}}) (1 - R'_{T_{\text{final}}})$. The factor $(1 - R'_{31^\circ\text{C}}) (1 - R'_{T_{\text{final}}})$ is a product of two values between 0 and 1 that represents how collapsed both the initial and final states are. It can be thought of as a measure of how collapsed both the initial and final states are. It can be seen that the term $\Delta OD'_{\text{slow}}$ contributes to a greater fraction of $\Delta OD'_{\text{total}}$ when the microgel is either in a more collapsed initial or final state. **Figure 4b** outlines this as a schematic. Here, $\Delta OD'_{\text{total}}$ is split into the sum of the two fitting parameters $\Delta OD'_{\text{fast}}$ and $\Delta OD'_{\text{slow}}$. Given that $\Delta OD'_{\text{total}}$ is equal to $-\Delta R'$, it follows that the relative proportions of each of the slow and fast components are given by the factor $A (1 - R'_{31^\circ\text{C}}) (1 - R'_{T_{\text{final}}})$, where A is the gradient of the dashed lines in **Figure 4a**. The gradient is equal for CS1, CS2 and CS3, which have almost the same cross-linker densities and it is almost twice as large for CS5. This means that for the gel with the higher cross-linker density, the slow component contributes to the collapse transition to a greater extent. It follows that the expressions (6.8) and (6.9) can be used to estimate the values of $\Delta OD'_{\text{fast}}$ and $\Delta OD'_{\text{slow}}$ from the initial and final radii of the microgel. Once again, the trend in CS4 deviates from the other samples. As the final states become more collapsed, the contribution of $\Delta OD'_{\text{slow}}$ jumps suddenly to a larger value and remains constant for the largest jumps.

$$\Delta OD'_{\text{fast}} = -\Delta R' \times [1 - A (1 - R'_{31^\circ\text{C}}) (1 - R'_T)] \quad (6.8)$$

$$\Delta OD'_{\text{slow}} = -\Delta R' \times A (1 - R_{31^\circ\text{C}}) (1 - R_T) \quad (6.9)$$

The corresponding trends in the values of the of the lifetime components, τ_{fast} and τ_{slow} , are plotted as a function of final temperature in **Figure 5**. For all microgels except CS1, τ_{slow} is roughly constant at around 1.5 ms (**Figure 5b**). The large error bars for

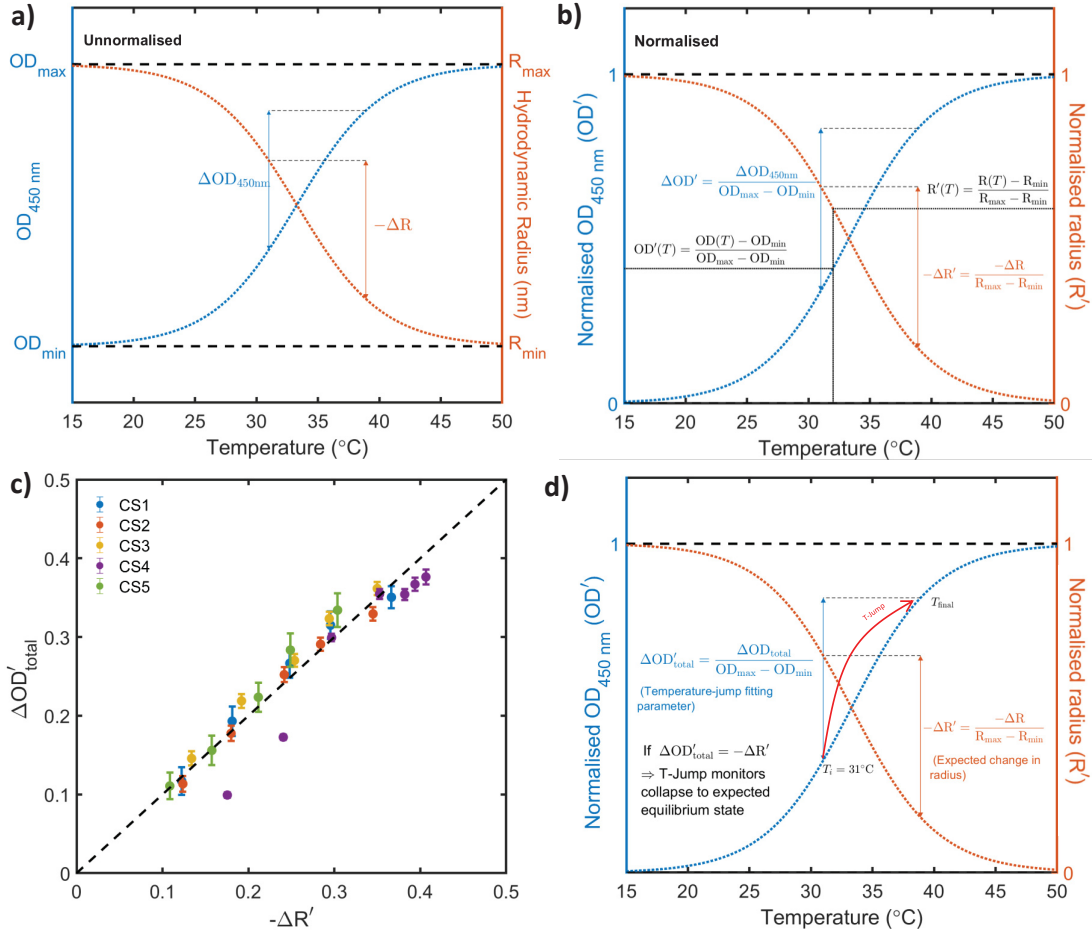


Figure 3: (a) Schematic of a typical OD_{450 nm} and hydrodynamic radius sigmoidal fit against temperature. $\Delta OD_{450\text{nm}}$ is the difference in optical density between two microgel states at equilibrium at different temperatures and $-\Delta R$ is the corresponding difference in radius. (b) Schematic of the equivalent normalized plots. $OD'(T)$ and $R'(T)$ are related to $OD_{450\text{nm}}(T)$ and $R(T)$ by the transformations (6.5) and (6.6). $\Delta OD'$ and $-\Delta R'$ are related to $\Delta OD_{450\text{nm}}$ and $-\Delta R$ by equivalent transformations. (c) Plot of $\Delta OD'_{\text{total}}$ vs $-\Delta R'$ for all of the microgels CS1 - CS5. $\Delta OD'_{\text{total}}$ was determined by the T-jump fits ($c = 0.050$ wt%, $[KCl] = 0.100$ M) and plotted against the expected $-\Delta R'$ for the collapse based on equilibrium values. The dashed line represents the line $y = x$. CS1: blue; CS2: orange; CS3: yellow; CS4: purple; CS5: green. (d) Schematic of T-jump from an initial point at equilibrium to a more collapsed state at a higher temperature. For the microgels CS1, CS2, CS3 and CS5, $\Delta OD'_{\text{total}}$ taken from the kinetic fitting data was equal to the expected $-\Delta R'$. This implies that $\Delta OD_{450\text{nm}}$ monitored over the course of the T-jump follows the entire collapse process.

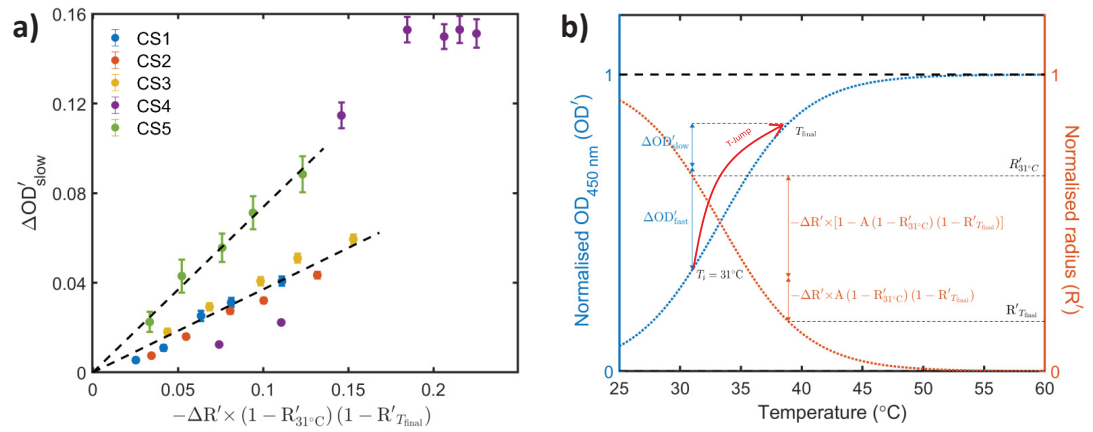


Figure 4: (a) Plot of fitting parameter $\Delta OD'_{\text{slow}}$ against $-\Delta R$ corrected by a factor corresponding to the final and initial swelling ratios, $(1 - R'_{31^\circ\text{C}}) (1 - R'_{T_{\text{final}}})$. For microgels with a nominal cross-linker density greater than 15% the relative contribution of $\Delta OD'_{\text{slow}}$ increases linearly with this parameter, which represents how collapsed both the initial and final states are. The gradient of the fit (dashed line) depends on the cross-linker density. (b) Schematic outlining this trend for CS1, CS2, CS3, and CS5. The sum of $\Delta OD'_{\text{fast}}$ and $\Delta OD'_{\text{slow}}$ is equal to $\Delta OD'_{\text{total}}$. The values of these are associated with the initial ($R'_{31^\circ\text{C}}$) and final ($R'_{T_{\text{final}}}$) normalized radii of the transition at a given cross-linker density (6.8) and (6.9).

CS1 are a result of ΔOD_{slow} being low in this system, especially for low temperature-jump magnitudes.

The values of τ_{fast} have a well-defined dependence on PNIPAM shell radius and temperature-jump magnitude for microgels with a constant cross-linker density. In the case of microgels with a 15% cross-linker density, **Figure 5a** shows that the value of τ_{fast} increases as either the temperature jump magnitude is raised or as the PNIPAM shell radius becomes larger. This reflects an apparent linear relationship between the lifetime and the final radius of the microgels (**Figure 5c**) as well as the absolute change in radius of collapse for a given temperature-jump value (**Figure 5d**). These plots represent the same data, with each lifetime value associated with the expected change in radius of collapse: the sets of data points are then grouped according to the final temperatures to compare the dynamics over shell radius at constant temperature. The reciprocal of the gradient of the fit in **Figure 5d**, $-\Delta R/\tau_{\text{fast}}$, representing the speed of collapse with respect to radius, increases with temperature (**Figure S11**). No clear relationship between τ_{fast} and cross-linker density could be determined from these data. It appears that for CS4 τ_{fast} is slowest for the two lowest temperature-jump magnitudes, becoming faster as the final temperature increases. For CS5 τ_{fast} decreases as the final temperature increases.

6.5.3 Collapse Mechanism

Several other kinetic studies have previously measured two-component collapse transitions in microgels. Keidel *et al.* undertook simulations of loosely cross-linked PNIPAM microgels ($R_{\text{collapsed}} = 331$ nm, 0.25% cross-linker density) and determined that the fast component of the collapse transition was due to the local collapse of loose polymer chains around rigid cross-linking regions ($\tau_{\text{fast}} \sim 1.3$ ms).⁸⁵ The slow component was attributed to the accumulation of these clusters by polymer chain relaxation to the globule phase ($\tau_{\text{slow}} \sim 227$ ms), and the rate of each component was dictated by the strength of monomer interactions under the new solvent conditions. The co-nonsolvency induced collapse dynamics of PNIPAM studied by Nothdurft *et al.* are largely consistent with this mechanism. However, several key differences were attributed to the variation in the microgel structure between the studies ($R_{\text{collapsed}} = 13 - 75$ μm , 5% cross-linker density).⁸⁴ The authors attributed the fast component of the deswelling ($\tau_{\text{fast}} \sim 0.1 - 1$ s) to the initial expulsion of water from the porous structure that is dominated by polymer-solvent interactions this results in a rapid collapse of the network that can be monitored by a change in radius. As the evolving structure of the microgel becomes dominated by polymer-polymer interactions, further deswelling is controlled by slower rearrangement and relaxation of polymer chains ($\tau_{\text{slow}} \sim 1 - 10$ s). The authors found, by variation of the microgel radii, that the lifetimes of the fast and slow components depend on a diffusion coefficient in a similar manner to macrogels. The lifetime of the fast component depended on $R_{\text{final}}^{1.8}$, and that of the slow component depended on R_{final}^2 (the latter in line with macrogel collapse). Microgels with lower cross-linker densities have a tendency to form bubbles at the surface upon deswelling, creating a skin layer that impedes the expulsion of water molecules. Nothdurft *et al.* found this to be the case in experiments with cross-

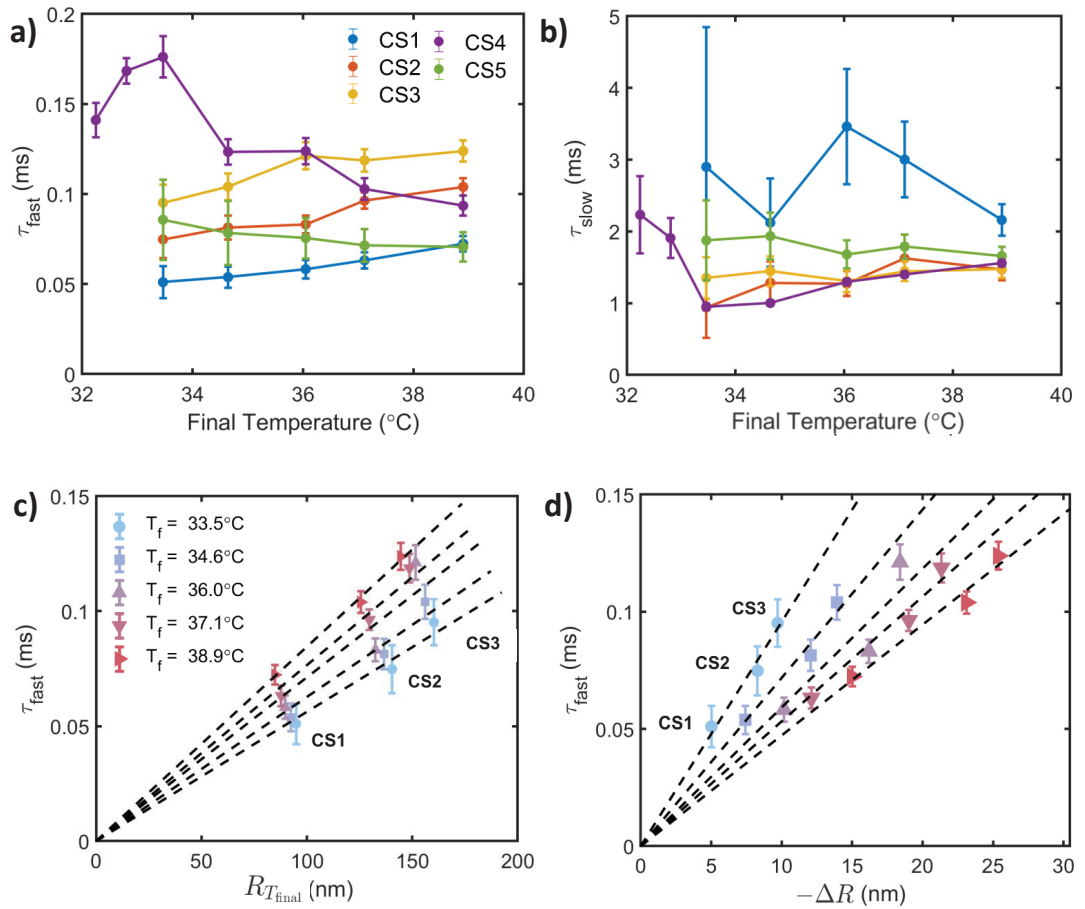


Figure 5: Fitting parameters for τ_{fast} and τ_{slow} , obtained from the T-jump experiments over microgels CS1 – CS5 ($c = 0.050$ wt% and $[\text{KCl}] = 0.100$ M). (a) The parameter τ_{fast} is plotted as a function of final temperature over all microgels (CS1: blue; CS2: orange; CS3: yellow; CS4: purple; CS5: green). (b) The parameter τ_{slow} is plotted as a function of final temperature over all microgels (CS1: blue; CS2: orange; CS3: yellow; CS4: purple; CS5: green). (c) The parameter τ_{fast} is plotted as a function of final equilibrium radius for microgels CS1, CS2, and CS3 at a given final temperature. The final temperatures are 33.5, 34.6, 36.0, 37.1 and 38.9 °C (light blue to red). (d) The parameter τ_{fast} is plotted against the expected absolute Δr for the collapse of CS1, CS2, and CS3. The final temperatures are 33.5 °C, 34.6 °C, 36.0 °C, 37.1 °C and 38.9 °C (light blue to red). The dashed lines represent linear fits.

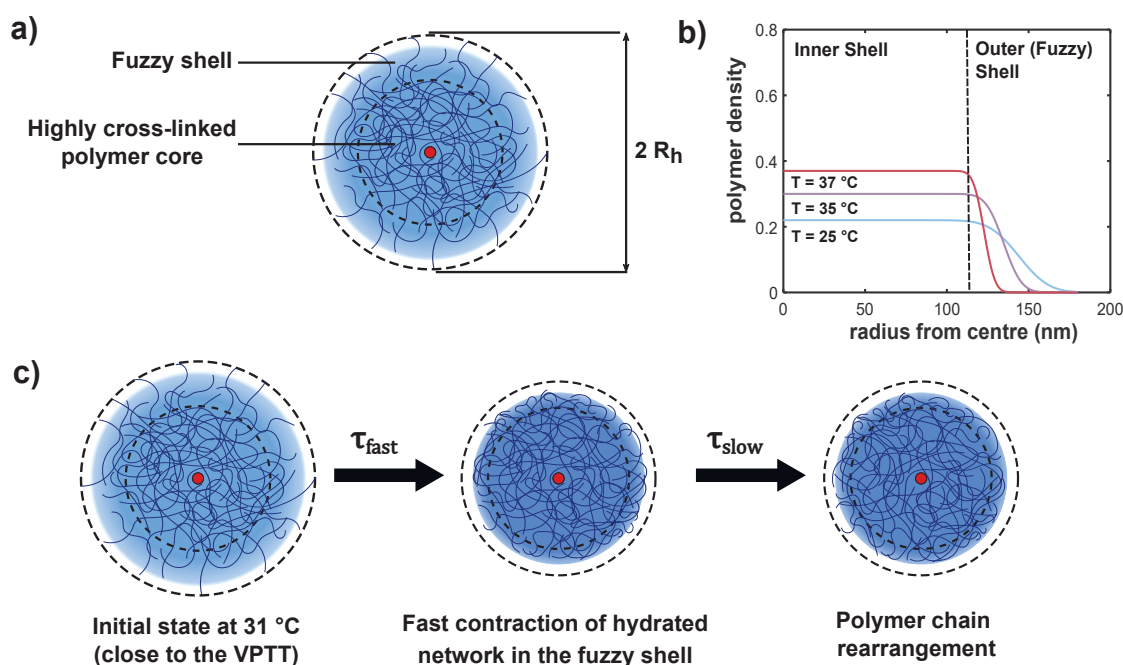


Figure 6: (a) Schematic structure of an Au-PNIPAM microgel depicted with the gold core (15.3 ± 1.5 nm diameter in all samples). R_h is the hydrodynamic radius of the CS microgel, on the scale of hundreds of nanometers. There is a distinction between the highly cross-linked inner region and the outer-shell (fuzzy) region as depicted. (b) Radial density profiles for CS3 at different temperatures around the VPTT. The fuzzy-shell form factor models the distribution, and parameters were taken from SANS measurements, described in more detail in ref²⁶⁹. (c) Proposed collapse mechanism from this work. Following a temperature jump, the longer chains in the loosely cross-linked outer corona contract first, resulting in a change in polymer density that is measured by the fast component in the temperature-jump spectra. This is followed by slower local polymer rearrangement as collapsed regions of the network relax to the new equilibrium state.

linker molar ratios of 2%, which is in agreement with studies on skin layer formation in macrogels.^{69,287,288} Wrede *et al.* concluded in their pressure-jump experiment that the fast decay component of PNNPAM microgel ($R_{\text{collapsed}} = 90$ nm, 4% cross-linker density), which has a very sharp VPT, corresponded to the formation of a skin layer, with the slow component corresponding to further polymer rearrangement limited by the impeded expulsion of water from the system.⁸³

For our samples, $\tau_{\text{fast}} \propto R_{\text{final}}$ for constant cross-linker density; *i.e.*, it deviates from the expected power dependence of 2 which represents a process limited by diffusion of the microgel network. Although exponents between 1.5 and 2 have been reported for microgels (likely as a result of inhomogeneous network structure), no other study has reported an exponent as low as 1 for such a process. However, we have also shown that $\tau_{\text{fast}} \propto -\Delta R$. This is reminiscent of the equation for the collapse of linear PNIPAM chains. Here we would expect that the lifetime (t) scales as $t^n \sim \Delta \langle R_g^2 \rangle / C$, where $\langle R_g^2 \rangle$ is the radius of gyration, C is a parameter that depends on the chain properties, and n is an exponent close to unity.²⁸⁹ This is also the equation that dictates $\Delta \langle R_g^2 \rangle$ of the loosely cross-linked PNIPAM microgel in Keidel's simulation for the fast cluster formation step.⁸⁵ In this way, the kinetics are consistent with the collapse of longer chains in the loosely cross-linked outer corona of the polymer network into clusters. The fact that the rate of collapse with respect to the equilibrium change in radius (in units of ms^{-1}) taken from the fits in **Figure 5d** increases monotonically with temperature is also consistent with this interpretation. The slow component would then correspond to further relaxation and polymer rearrangement. The lifetime for this component is not limited by the magnitude of the collapse, suggesting that local interactions control the rate. We are confident that the fast lifetime does not correspond to the formation of a skin layer, as it has a well-defined dependence on the microgel radius. This interpretation is also consistent with the microglobular structure of gels recently proposed by Yanase *et al.*²⁷⁰ In this context, the fast collapse would be the collapse of hydrated regions to form clustered microglobule regions. The slow collapse component would correspond to rearrangement of the polymer chains and microglobules within the network. We believe that collapse monitored by the fast component is confined to the fuzzy network in the outer shell, rather than being due to the accelerated collapse of chains around the rigid cross-linker regions over the whole gel network. The latter case applies to microgels with low cross-linker density, as shown in the study from Keidel *et al.*, and also generally applies to collapse transitions of star polymers.^{85,290} However, in our study the high cross-linker content used for all of the types of microgels means that the inner regions are significantly more rigid and have a smaller average chain length between linker sites. Using small-angle neutron scattering (SANS), we have also determined that the change in morphology over the deswelling transition is almost entirely due to collapse of the outer shell, which mixes into the inner shell.²⁶⁹ While polymer density in the inner region increases, its radius does not change much as would otherwise be expected if the fast collapse was universal over the entire network. This is outlined in Figure 6a,b. The polymer density profiles shown in this schematic correspond to CS3, and further details have been published elsewhere.²⁶⁹ Figure 6c gives an overview of this proposed mechanism.

We propose that differences in the properties of the fast and slow components between our study and the co-nonsolvent exchange study undertaken by Nothdurft *et al.* are the result of differing microgel initial and final states. In our study, the microgels begin in a state that is close to the VPTT, with the final states approaching but not quite being exactly the fully collapsed state. In the co-nonsolvent addition study, as well as all of the other studies mentioned, the full transition from the highly swollen to the collapsed state is monitored. This is likely to be the origin of the much faster lifetimes in our study. Furthermore, the deviation from the expected diffusion-limited kinetics could indicate that for such small changes in radius, from states that are already somewhat collapsed, the fast process is actually better described by more elementary equations for the collapse of chains. The slow polymer relaxation transition is also not dependent on the microgel radius under the conditions in this study - it is likely that this process becomes limited by local polymer and solvent rearrangement rather than network diffusion due to the much smaller changes in radius.

The use of time-resolved optical density measurements, rather than scattering techniques such as SAXS or SANS, means that we cannot directly correlate a change in signal to a change in microgel radius. Although we could determine that $OD_{450\text{ nm}}$ corresponds to the hydrodynamic radius at equilibrium, it is not the case that ΔOD directly correlates to $-\Delta R$ as the microgel collapses. Rather, using FDTD calculations and SANS analysis of these microgels, we have previously shown that changes in visible light extinction of PNIPAM microgels are directly correlated to changes in the hydrogel volume fraction in the outer fuzzy shell region as the microgel undergoes a transition.²⁶⁹ As the microgel collapses, the outer fuzzy region becomes thinner and approaches the density of the inner region until the polymer density is homogeneous over the whole gel in the most collapsed state. The trends in $\Delta OD'_{\text{fast}}$ and $\Delta OD'_{\text{slow}}$ are consistent with this interpretation. The fast and slow processes each result in an increase in polymer density in the collapsing fuzzy shell. The fast process would correspond to the density increasing via the collapse of swollen hydrated regions and the slow process via the subsequent reshuffling of the polymer network. The parameter $\Delta OD'_{\text{fast}}$ should therefore be larger when the microgel is more swollen, as the collapse of the swollen domains would result in a greater change in polymer density of the fuzzy region in these states. This is indeed what we see. Conversely, the slow polymer rearrangement should occur to a greater extent when the initial state is more collapsed. In fact, the factor $(1 - R'_{31^\circ\text{C}})(1 - R'_{T_{\text{final}}})$, which takes into account both the initial and final states, suggests that $\Delta OD'_{\text{slow}}$ contributes the most when there is a large overlap of collapsed polymer in both the initial and final states. This is the case for the microgels with at least 15% nominal cross-linker densities. For CS5, which has the largest cross-linker density, the slow contribution is larger, which would correspond to a larger extent of collapsed regions within the polymer network. The microgel with 5% cross-linker density appears to collapse via slightly different route. For the lowest temperature jumps, the relative contribution of the fast collapse and slow polymer rearrangement to the change in optical density scales in a similar way to the other microgels. However, as the final state becomes more collapsed, slow polymer rearrangement dominates and eventually approaches a constant value. This reflects that the final states for the largest temperature-jump experiments have

very similar hydrodynamic radii. The sudden jump in the slow polymer rearrangement contribution could reflect a sudden change in characteristics of the gel at temperatures above the VPTT, in contrast to the more gradual change of the other microgel types.

6.6 Conclusion

Using capacitor-discharge temperature-jump spectroscopy, we have measured the dynamics of two components of the collapse transition of Au-PNIPAM microgels, looking at the effect of temperature-jump magnitude, shell radius, and cross-linker densities. We have shown that heating is fast and homogeneous using this method, such that the collapse dynamics are not limited by the rate of solvent heating. The value of $OD_{450\text{nm}}$ was carefully related to the microgel hydrodynamic radius, in both the presence and absence of electrolyte, based on measurements conducted at steady state at temperatures near the VPTT. We found that for all microgel types ΔOD is proportional to $-\Delta r$. We measured ΔOD due to relaxation over a short (~ 7 ms) and large (~ 25 s) time scale in response to temperature jumps. ΔOD at the large time scale was assigned to thermoreversible microgel aggregation, followed by dissociation as the polymer solution cooled. ΔOD at the short time scale was assigned to the collapse of the PNIPAM shell to its equilibrium position at the new temperature. These curves were modeled by double-exponential fits, and the fitting parameters τ_{fast} , τ_{slow} , ΔOD_{fast} , and ΔOD_{slow} were determined and used to compare volume phase transition dynamics over a range of experimental parameters. We could show that normalized ΔOD_{fast} and ΔOD_{slow} have well-defined values dependent on the final and initial states of the microgels that were consistent over microgel cross-linker density. The value of τ_{fast} scales linearly with the overall change in the final radius of the transition, while τ_{slow} is almost constant over all experimental parameters. These trends are consistent with the fast component corresponding to ΔOD due to the fast collapse of the longer chains in the loosely cross-linked outer shell of the microgel. The slow component corresponds to local polymer rearrangement around these collapsed regions. These results provide brand new insights into how the microgel structure and the temperature at equilibrium, affect the deswelling dynamics. They support predictions from molecular dynamics studies, and extend upon experimental studies from the literature that have investigated microgel collapse kinetics using alternative methods. Finally, we have shown that the capacitor-induced temperature-jump technique is a useful tool to measure dynamics in nanoscale colloidal systems.

Associated Content

Extra synthesis details, temperature-resolved UV-vis spectra, DLS measurements, tables of data and residual plots (PDF)

Notes

The authors declare no competing financial interest.

Acknowledgements

This work was supported by ARC Grant CE170100026. We thank the Melbourne Advanced Microscopy Facility (Bio 21, The University of Melbourne) for access to electron microscopy. We acknowledge financial support from the German Academic Exchange Service (DAAD) through its Thematic Network Bayreuth-Melbourne Colloid/Polymer Network, sponsored by funds of the Federal Ministry of Education and Research (BMBF).

6.7 Supporting Information

Au-PNIPAM Synthesis

The relative masses of monomer (NIPAM) and cross-linking agent (BIS) used in the synthesis of the five Au-PNIPAM variants are outlined in **Table S1**

Table S1: Masses of monomer, $m(\text{NIPAM})$, and cross-linker, $m(\text{BIS})$, used in the seeded precipitation polymerizations.

| Sample | $m(\text{NIPAM})$ (g) | $m(\text{BIS})$ (g) | Cross-linker Molar Ratio |
|--------|-----------------------|---------------------|--------------------------|
| CS1 | 0.228 | 0.048 | 15.3% |
| CS2 | 0.587 | 0.134 | 16.7% |
| CS3 | 0.946 | 0.194 | 14.8% |
| CS4 | 0.587 | 0.040 | 5% |
| CS5 | 0.587 | 0.200 | 24.9% |

Calibration of Temperature-Jump Instrument

The voltage to temperature-jump calibration was determined by monitoring ΔOD of a solution of bromothymol blue (BTB) at jumps initiated by different voltage discharges.²⁹¹ The OD of BTB at 610 nm is dependent on the pH of the system as its conjugate base absorbs strongly in this region. BTB has a pK_a of 7.2 and the deprotonation equilibrium is overall exothermic: hence, a solution held at a pH around 7.2 will shift to the base upon temperature jump and the extent of reaction can be monitored by ΔOD at 610 nm.

BTB (0.00500 M) was added to a solution of tris(hydroxymethyl)aminomethane buffer (0.01 M) and KCl (0.1 M). A wavelength-resolved spectrum was taken at four different temperatures and the OD at 610 nm was modelled as a linear function of absorbance ($R^2 = 0.9978$) **Fig. S1**

Following temperature-jump at seven different voltages, the difference in ΔOD values before and after jumps were plotted versus the square of the voltage ($R^2 = 0.9995$). We could then use this to plot temperature-jump as a function of the square of the voltage, which was used as the calibration curve in experiments.

The calibration curve is given by **(6.1)**

$$\Delta T \text{ (}^\circ\text{C)} = 0.0507 \times V^2 \text{ (kV}^2\text{)} - 0.0211 \quad (6.1)$$

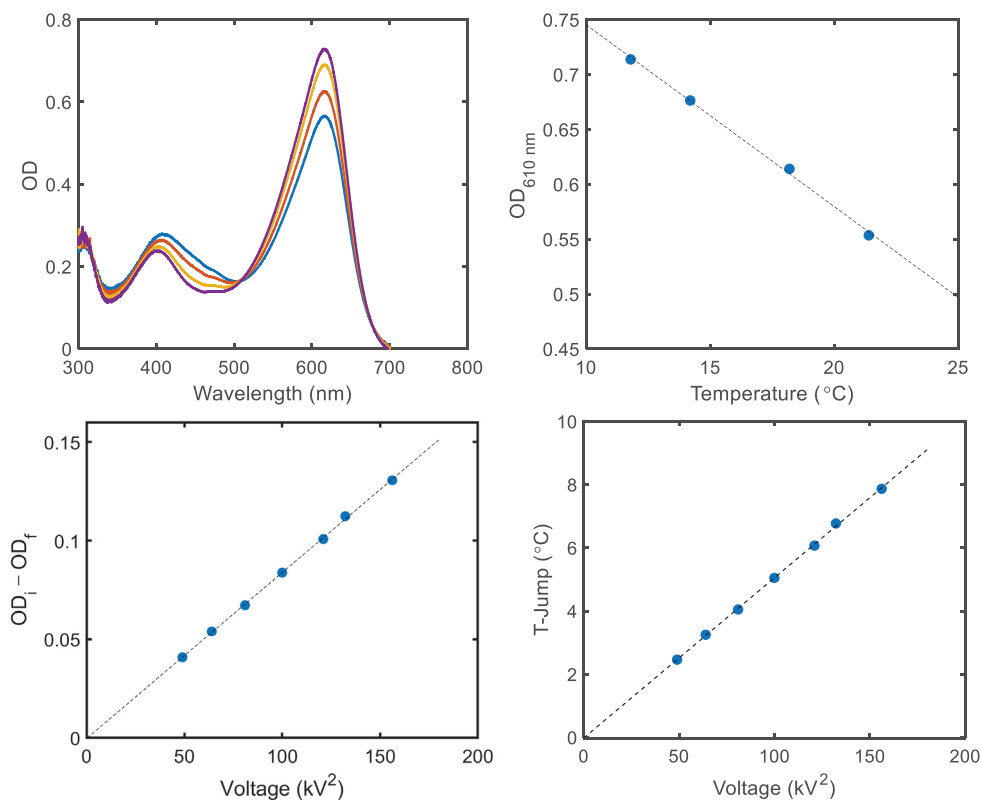


Figure S1: Top left: Wavelength-resolved UV/vis spectra for a system of BTB (0.00500 M), tris buffer (0.100 M) and KCl (0.100 M) over temperature (blue: 21.4 °C, orange: 18.2 °C, yellow: 14.2 °C, purple: 11.8 °C). Spectrum taken in sample holder ($l = 0.3$ cm) Top right: Corresponding plot of $\Delta OD_{610\text{ nm}}$ vs temperature. Bottom left: Change in optical density at 610 nm plotted as a function of capacitor voltage. Bottom Right: Temperature-Jump plotted as a function of voltage

TEM Images

TEM images for microgels CS1, CS2, CS4 and CS5 are shown in **Fig. S2**.

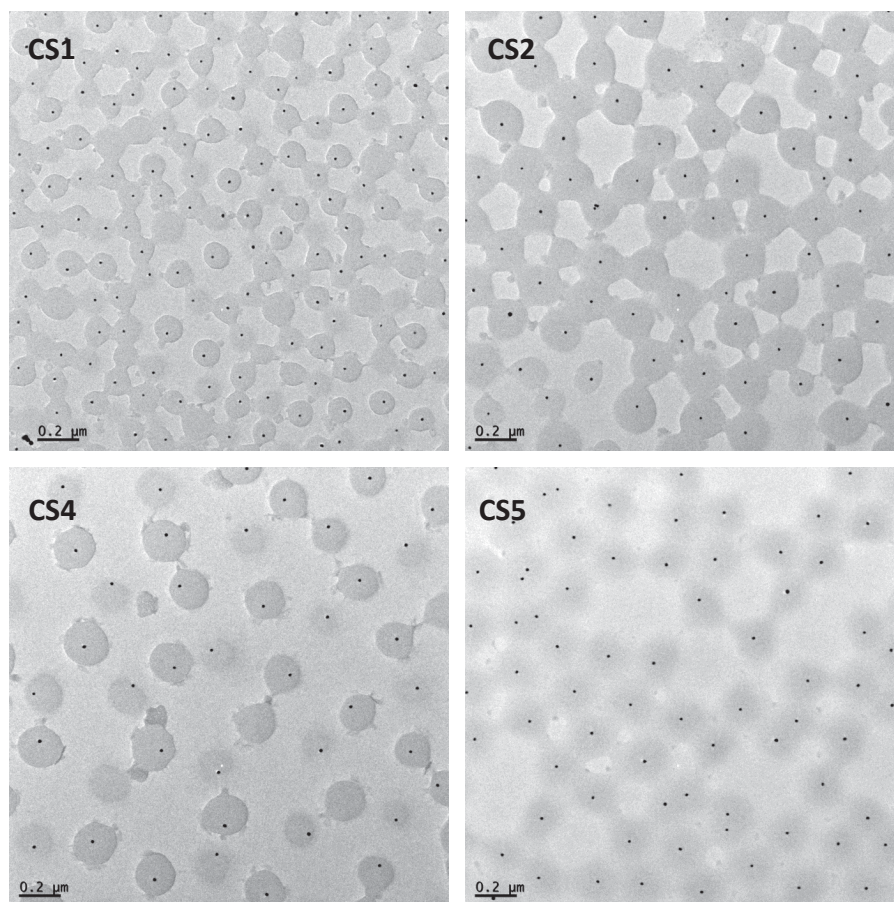


Figure S2: Representative TEM images for each of the microgel types CS1, CS2, CS4 and CS5. The variable cross-linker densities and shell thicknesses are result in varying extents of transmission. The dot in the centre of each microgel is the gold core, which is surrounded by the PNIPAM-gel.

UV/Vis Spectra

Sets of UV/vis spectra for microgels CS1, CS2, CS4 and CS5 taken over a range of temperatures, with no electrolyte, are shown in **Fig. S3**.

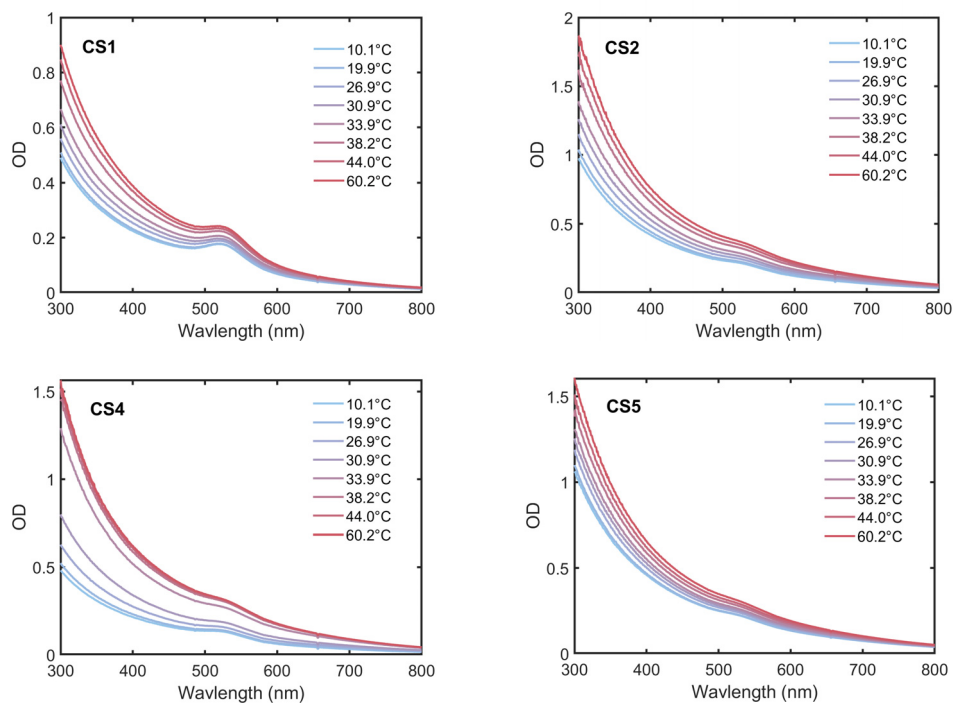


Figure S3: UV/vis spectra of core-shell microgels CS1, CS2, CS4 and CS5 taken over temperature. $c = 0.020$ wt%.

OD vs Hydrodynamic Radius for All Microgels

Comparisons of the value of OD at 450 nm against the microgel hydrodynamic radius for microgels CS1, CS2, CS4 and CS5 taken over a range of temperatures, with no electrolyte, are shown in **Fig. S4**

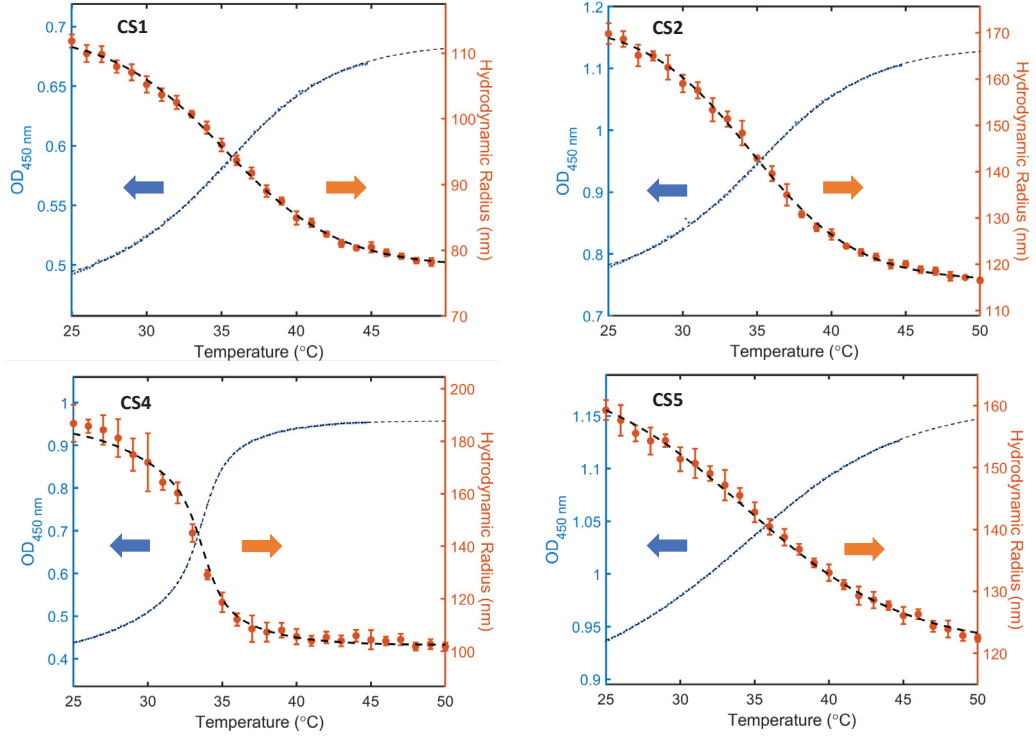


Figure S4: Comparison of OD at 450 nm against microgel hydrodynamic radius over temperature. Top Left: CS1. Top Right: CS2. Bottom Left: CS4. Bottom Right: CS5. For optical density spectra, $c = 0.050$ wt%, for hydrodynamic radius determination, $c = 0.010$ wt%

The data was interpolated by fitting each of the curves to linearly related sigmoidal functions (6.2) and (6.3) for CS1, CS2, CS3 and CS5, and the the double sigmoidal function (6.4) and (6.5) for CS4.

$$OD = OD_{\max} + \frac{OD_{\min} - OD_{\max}}{1 + \exp\left(\frac{T-T_0}{h}\right)} \quad (6.2)$$

$$R = R_{\min} + \frac{R_{\max} - R_{\min}}{1 + \exp\left(\frac{T-T_0}{h}\right)} \quad (6.3)$$

$$\text{OD} = \text{OD}_{\text{max}} + (\text{OD}_{\text{min}} - \text{OD}_{\text{max}}) \left[\frac{f}{1 + \exp\left(\frac{T-T_{01}}{h_1}\right)} + \frac{1-f}{1 + \exp\left(\frac{T-T_{02}}{h_2}\right)} \right] \quad (6.4)$$

$$\text{R} = \text{R}_{\text{min}} + (\text{R}_{\text{max}} - \text{R}_{\text{min}}) \left[\frac{f}{1 + \exp\left(\frac{T-T_{01}}{h_1}\right)} + \frac{1-f}{1 + \exp\left(\frac{T-T_{02}}{h_2}\right)} \right] \quad (6.5)$$

Fitting parameters are shown in **Table S2**

Table S2: Fitting parameters for OD_{450nm} and hydrodynamic radius against temperature (no electrolyte).

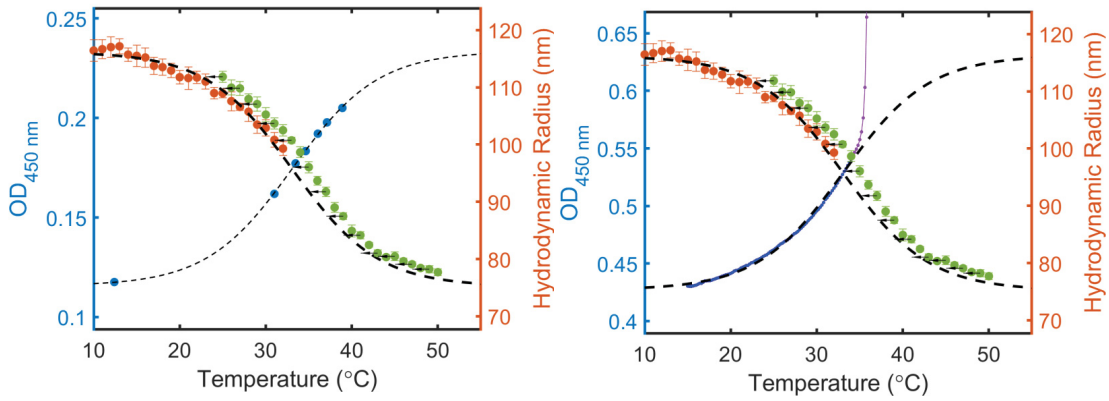
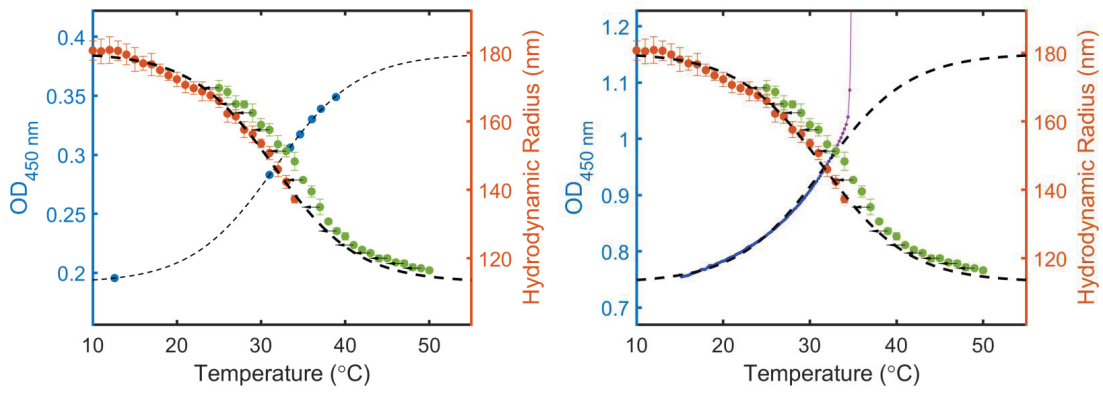
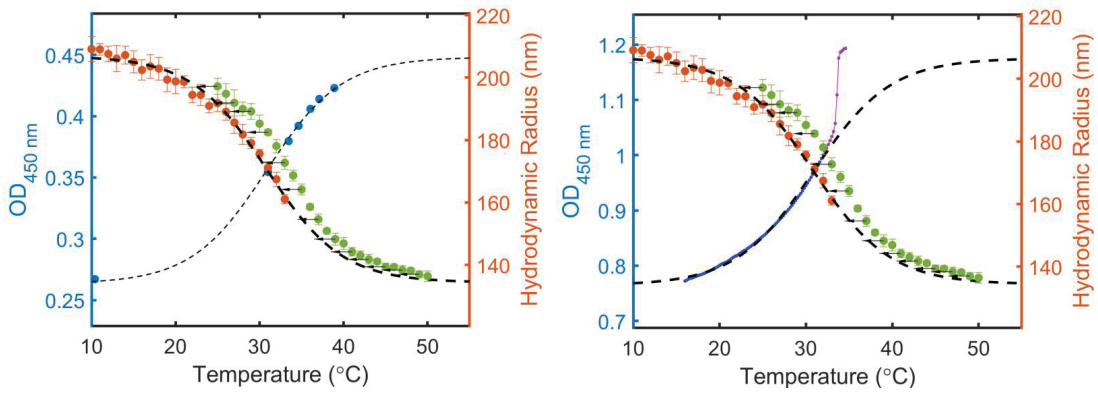
| Sample | OD _{min} | OD _{max} | R _{min} | R _{max} | T ₀ | h | | | |
|--------|-------------------|-------------------|------------------|------------------|----------------|-----------------|----------------|-----------------|----------------|
| CS1 | 0.48 | 0.69 | 77 | 113 | 35.2 | 3.8 | | | |
| CS2 | 0.76 | 1.14 | 115 | 172 | 34.9 | 3.9 | | | |
| CS3 | 0.91 | 1.29 | 139 | 199 | 33.3 | 3.5 | | | |
| CS5 | 0.89 | 1.16 | 120 | 165 | 34.4 | 5.4 | | | |
| Sample | OD _{min} | OD _{max} | R _{min} | R _{max} | f | T ₀₁ | h ₁ | T ₀₂ | h ₂ |
| CS4 | 0.41 | 0.95 | 102 | 186 | 0.46 | 33.7 | 0.68 | 32.3 | 2.85 |

A slightly different process was used to fit these curves under the conditions required for the temperature-jump experiments ([KCl] = 0.100 M), as aggregation at temperatures around the VPTT prevented the accurate fitting of the curves using the data points at low temperatures alone. This process is outlined in **Fig S5**.

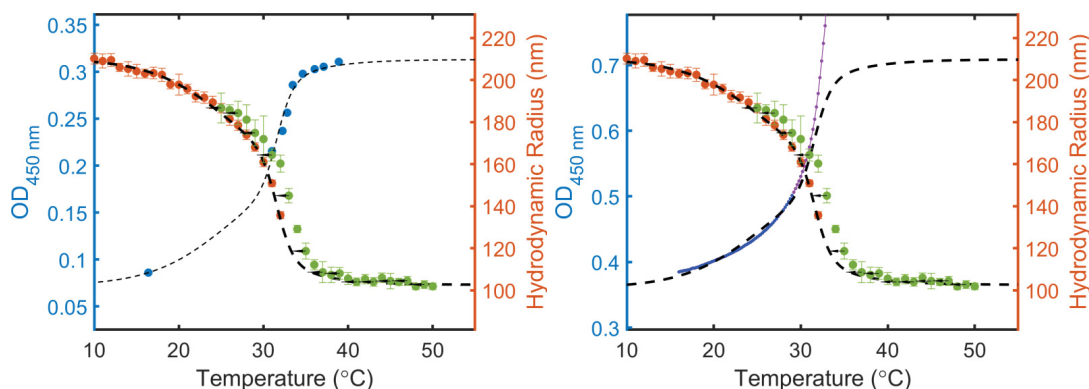
Plotting the hydrodynamic radius with and without KCl (the green and orange data points respectively) shows that the radius vs temperature curve is simply shifted to lower temperatures in the presence of salt. The fitting of this curve is supported by this observation: by translating the swelling curve in the absence of salt by the appropriate amount we are able to incorporate the data points at higher temperatures to help fit the swelling curve. **Fig S5 right** shows that we are able to fit the equilibrium OD_{450 nm} and hydrodynamic radius curves to linearly related sigmoidal functions using these extra data points to help fit at higher temperatures. We are also able to fit the swelling curve as taken in the T-Jump apparatus in order to normalise values of $\Delta\text{OD}_{450 \text{ nm}}$ over the microgel types. In **Fig S5 left** The OD vs T curve is composed of a set of T-jump data points: the data points above 31 °C correspond to the final OD values from the T-Jump fits (*i.e.* OD_{*i*} + $\Delta\text{OD}_{\text{total}}$). The data point at 31 °C corresponds to the initial OD value OD_{*i*}, and any data points at lower temperatures corresponds to equilibrium values taken at that temperature in the T-Jump apparatus. The curves fit to a scaled form of the function used to fit the temperature-scan curves plotted alongside. The fitting parameters for OD_{max} and OD_{min} were used to normalise the OD values over different microgel types. The fitting parameters are outlined in **Table S3**.

Table S3: Fitting parameters for OD_{450nm} and hydrodynamic radius against temperature ([KCl] = 0.100 M).

| Sample | OD _{min} (T-Scan) | OD _{max} (T-scan) | OD _{min} (T-jump) | OD _{max} (T-jump) | r _{min} | r _{max} | T ₀ | h | | | |
|--------|-------------------------------|-------------------------------|-------------------------------|-------------------------------|------------------|------------------|----------------|-----------------|----------------|-----------------|----------------|
| CS1 | 0.43 | 0.64 | 0.12 | 0.23 | 75 | 116 | 33.1 | 5.0 | | | |
| CS2 | 0.74 | 1.15 | 0.19 | 0.39 | 113 | 180 | 31.6 | 4.9 | | | |
| CS3 | 0.776 | 1.18 | 0.26 | 0.45 | 135 | 207 | 30.9 | 4.5 | | | |
| CS5 | 0.86 | 1.09 | 0.27 | 0.38 | 119 | 164 | 30.9 | 5.6 | | | |
| Sample | OD _{min} (T-Scan) | OD _{max} (T-scan) | OD _{min} (T-jump) | OD _{max} (T-jump) | r _{min} | r _{max} | f | T ₀₁ | h ₁ | T ₀₂ | h ₂ |
| CS4 | 0.36 | 0.71 | 0.072 | 0.31 | 103 | 211 | 0.52 | 25.6 | 4.4 | 31.6 | 0.95 |

CS1**CS2****CS3**

CS4



CS5

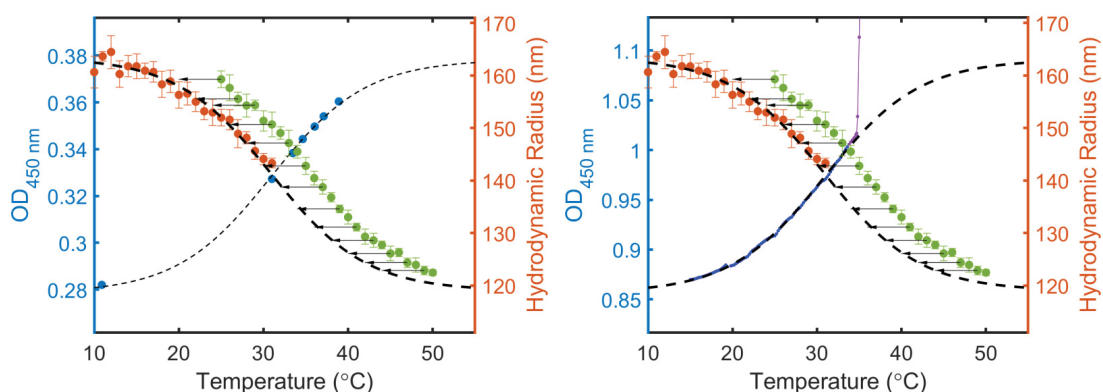


Figure S5: OD at 450 nm plotted alongside hydrodynamic radius under several conditions. Left: OD at 450 nm (blue) corresponds to the value $OD_i + \Delta OD_{total}$ ($T > 31^\circ C$) or the value of OD_i ($T = 31^\circ C$) for the double-exponential fits of the T-Jump data plotted in **Fig. 3** in the manuscript. The data point below $T < 31^\circ C$ corresponds to a measurement taken after equilibration at a cold temperature. Right: The OD at 450 nm corresponds to the temperature-scan experiments conducted using a slow temperature ramp (blue, $c = 0.050$ wt%, $[KCl] = 0.100$ M). For clarity, data points corresponding to temperatures above the critical aggregation point are not shown. The mauve curve represents the initial increase in OD arising from the beginning of aggregation. In each of the plots, the hydrodynamic radius with electrolyte present (orange, $[KCl] = 0.100$ M) and without electrolyte present (green) are shown. The arrows represent the constant value by which the green data points were transformed in each case to help fit the radius and OD curves to an appropriate sigmoidal function. The dashed curves represent fits for the function with electrolyte present to sigmoidal functions (CS1, CS2, CS3 and CS5) or a double sigmoidal function (CS4).

Effect of KCl on Microgel Radius, OD and Aggregation Temperature

The effect of [KCl] on the hydrodynamic radius, OD and critical aggregation of CS3 is outlined in **Fig. S6**.

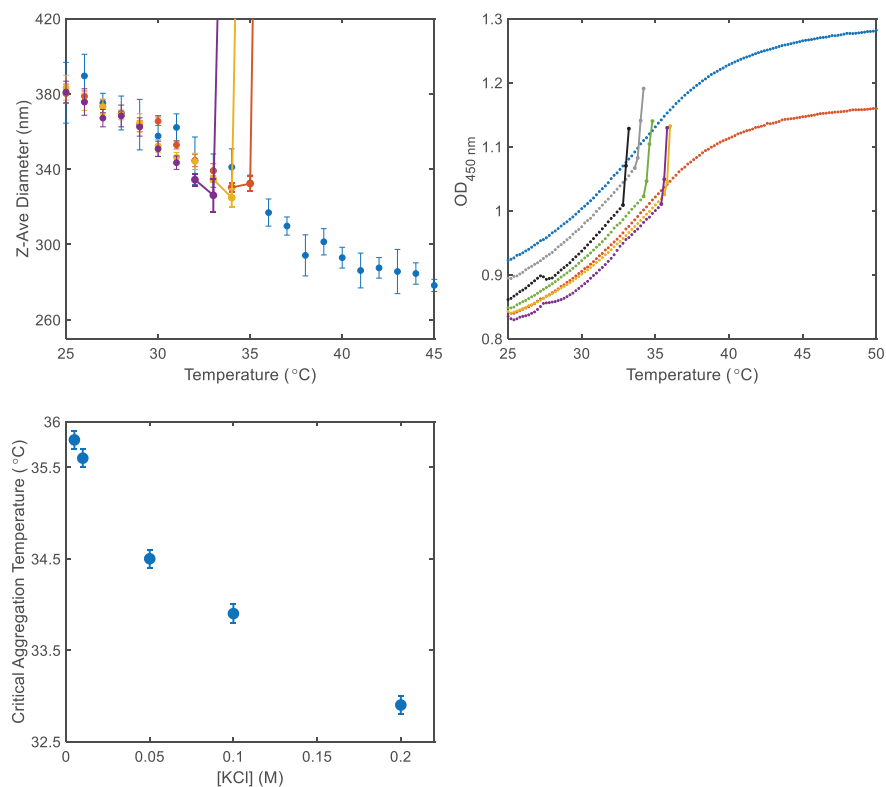


Figure S6: Top Left: The equilibrium average microgel radius plotted as a function of temperature over different values of [KCl]. Blue: [KCl] = 0 M. Orange: [KCl] = 0.0100 M. Yellow: [KCl] = 0.0500 M. Purple: [KCl] = 0.100 M. Sharp increase corresponding to microgel aggregation represented by solid line. Top Right: The equilibrium OD at 450 nm plotted as a function of temperature over different values of [KCl]. Blue: [KCl] = 0 M. Orange: [KCl] = 0.00100 M. Yellow: [KCl] = 0.00500 M. Purple: [KCl] = 0.0100 M. Green: [KCl] = 0.0500 M. Grey: [KCl] = 0.100 M. Black: [KCl] = 0.200. Bottom Left: Plot of critical aggregation temperature determined from OD as a function of [KCl] (CS3, $c = 0.050$ wt%).

Effect of Microgel Concentration on OD and Aggregation Temperature

The effect of microgel concentration on OD and the critical aggregation temperature of CS3 is outlined in **Fig. S7**

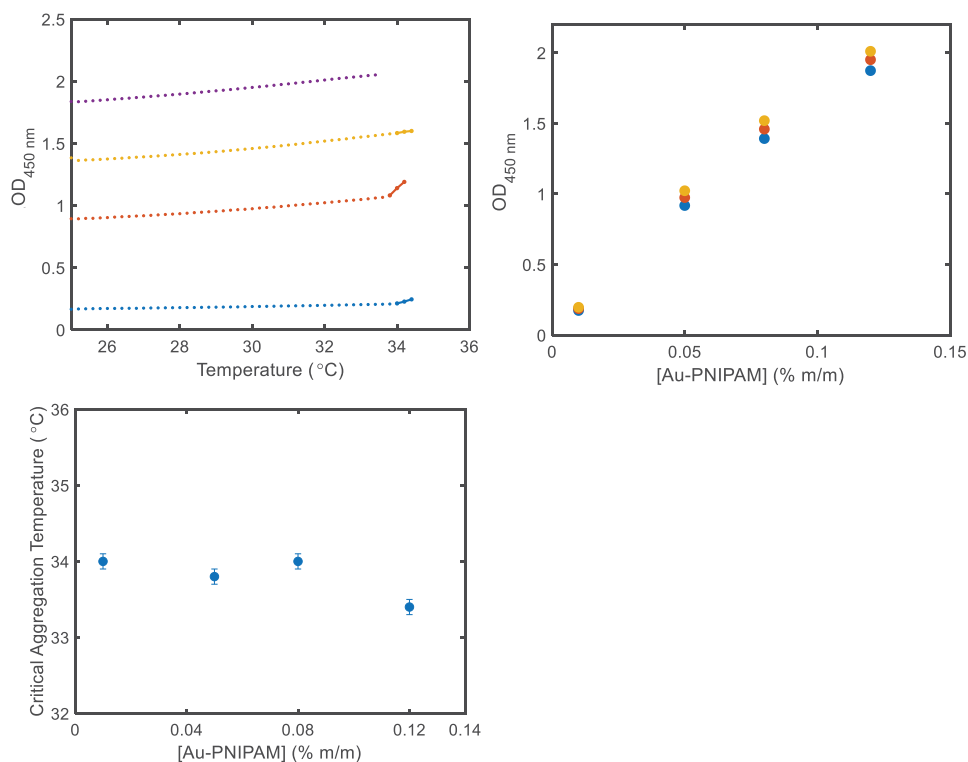


Figure S7: Top Left: The equilibrium OD at 450 nm plotted as a function of temperature over different values of [Au-PNIPAM]. Blue: [Au-PNIPAM] = 0.010 wt%. Orange: [Au-PNIPAM] = 0.050 wt%. Yellow: [Au-PNIPAM] = 0.080 wt%. Purple: [Au-PNIPAM] = 0.12 wt%. Top Right: Δ OD plotted as a function of [Au-PNIPAM] over different temperature values. Blue: T = 27 °C. Orange: T = 30 °C. Yellow: T = 32 °C. Bottom Left: Plot of critical aggregation temperature determined from Δ OD plot as a function of [Au-PNIPAM]. (CS3, [KCl] = 0.100 M)

Inclusion of SDS and Zeta Potential Measurements

When sodium dodecyl sulfate (SDS) is incorporated into solution at in the presence of KCl, aggregation is prevented so long as $[KCl] \lesssim 0.01$ M. This is demonstrated in **Fig. S8**.

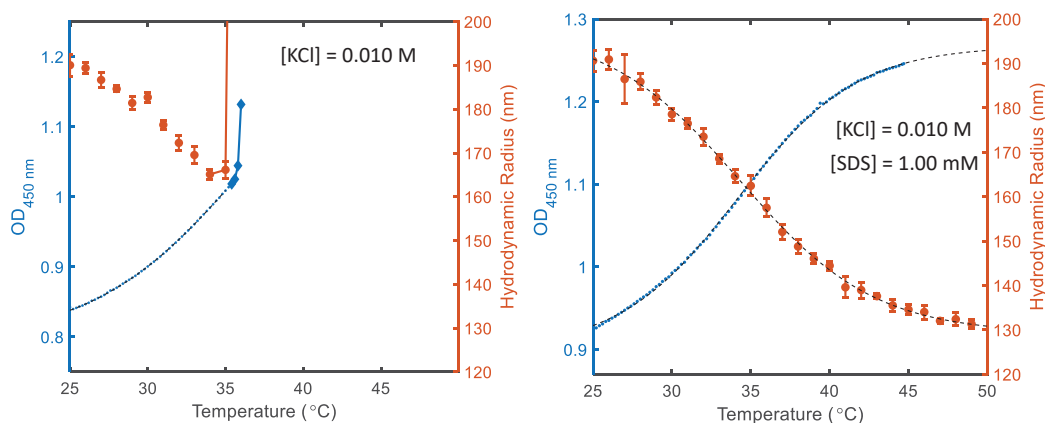


Figure S8: OD_{450 nm} (blue) and hydrodynamic radius (orange) plotted against temperature (CS3, $c = 0.050\%$) under two conditions. a) $[KCl] = 0.010$ M, b) $[KCl] = 0.010$ M, $[SDS] = 1.00$ mM

Fig. S9 demonstrates the effect that the inclusion of SDS has on the zeta potential and aggregation behaviour of the core-shell microgels. **Fig.S9 (right)** shows that the sharp critical aggregation temperature peak observed in an Au-PNIPAM sample with $[KCl] = 0.0100$ M is missing when SDS is present. Instead, the curve resembles the swelling curve for a system with no electrolyte, with a slightly shifted VPTT. The zeta potential measurements confirm that this effect is due to the influence of SDS and KCl on the microgel surface charge (**Fig. S9 (left)**). When there is little or no SDS present, the zeta potential decreases upon addition of KCl. For $[KCl] = 0.100$ M, increasing $[SDS]$ does not increase the magnitude of the zeta potential, and does not prevent aggregation. For $[KCl] = 0.0100$ M, increasing $[SDS]$ past 0.8 mM increases the zeta potential to the same value as the solution with no added electrolyte. This corresponds to the SDS concentration at which the swelling curve does not have an aggregation component, and further suggests that the surface charge is the most important factor determining resistance to aggregation.

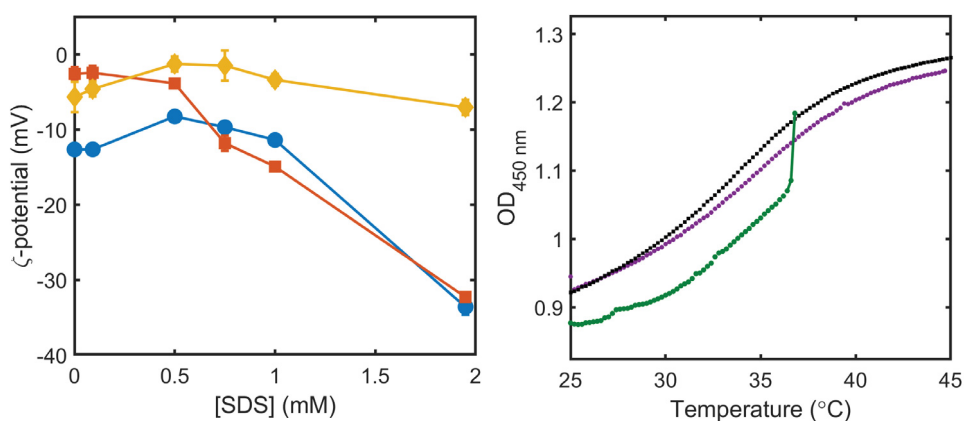


Figure S9: Left: Zeta potential values for Au-PNIPAM systems under varying [SDS] and [KCl] values. Blue: [KCl] = 0 M. Orange: [KCl] = 0.0100 M. Yellow: [KCl] = 0.100 M (CS3, [Au-PNIPAM] = 0.050 wt%), T = 24 °C. Right: OD at 450 nm vs temperature for systems under varying [KCl] and [SDS] values. Green: [KCl] = 0.0100 M. The trace is plotted up to the aggregation point. Violet: [KCl] = 0.0100 M, [SDS] = 1.00 mM. Black: [KCl] = 0 mM. (CS3, c = 0.050 wt%)

Microgel Aggregation (25 Second Timescale)

Temperature-jump data on a 25 second timescale was assigned to Au-PNIPAM microgel aggregation and dissociation as the solution cools (**Fig. S10**). While the fast deswelling occurs over a time-regime where the solution does not have time to cool (*i.e.* the temperature remains constant following the jump), over the course of 25 seconds we would expect the solution to re-equilibrate back to its original temperature. In all experiments, the fast initial increase in optical density corresponds to microgel collapse within the first data point after the jump (**S10**). Where the temperature does not jump over a critical aggregation point, the traces decrease exponentially, in line with microgel reswelling during temperature re-equilibration. Otherwise, there is a temperature-dependent curve that would track microgel aggregation and subsequent separation as the temperature cools. This is consistent with the difference in behaviour between the systems shown in **S10**. For the two systems at different electrolyte concentration, where the critical aggregation temperature of the system at $[\text{KCl}] = 0.10 \text{ M}$ is $33.9 \text{ }^\circ\text{C}$ and that of the system at $[\text{KCl}] = 0.010 \text{ M}$ is $35.6 \text{ }^\circ\text{C}$ (**Fig. 1e inset**), the fact that the $31.0 \text{ }^\circ\text{C}$ to $34.6 \text{ }^\circ\text{C}$ jump measures aggregation in one system, with reswelling in the other, is consistent with our interpretation. The system with SDS does not aggregate in the temperature range we tested, as such we only see traces corresponding reswelling for all jump magnitudes.

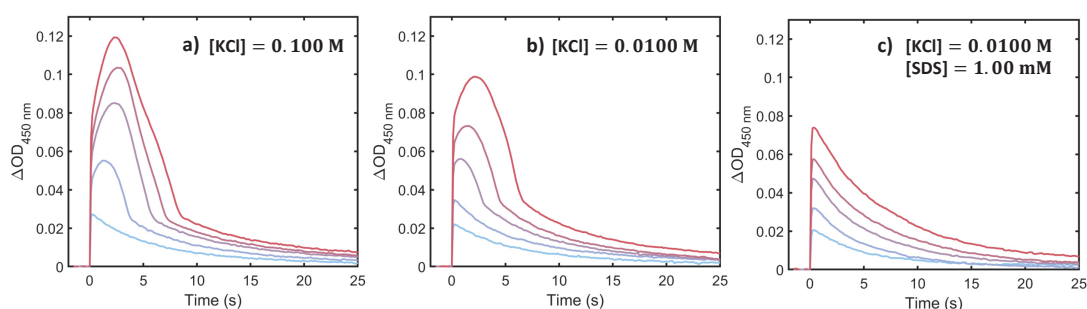


Figure S10: Temperature-jump spectra taken over 25 s timescale. (CS3, $c = 0.050 \text{ wt}\%$). Plots a – c show the presence or lack of aggregation under various KCl and SDS conditions. Initial temperature $31 \text{ }^\circ\text{C}$ with final temperatures $33.5 \text{ }^\circ\text{C}$, $34.6 \text{ }^\circ\text{C}$, $36.0 \text{ }^\circ\text{C}$, $37.1 \text{ }^\circ\text{C}$, and $38.9 \text{ }^\circ\text{C}$, (light blue to red).

Change in Hydrodynamic Radius vs Fast Lifetime over Temperature

The fitting of the data points showing τ_{fast} vs $-\Delta R$ reveal that the parameter $-\Delta R/\tau_{\text{fast}}$ increases with temperature (**Fig. S11**). This is consistent with the notion that the rate of compression, with respect to distance over time, increases with temperature exactly as we would expect.

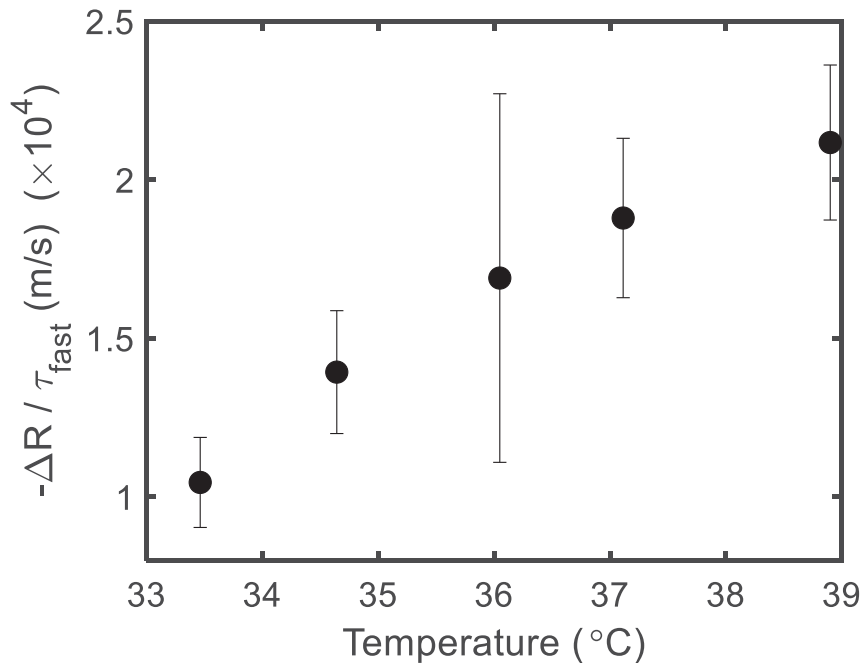


Figure S11: The parameter $-\Delta R/\tau_{\text{fast}}$, taken from the gradients of the fitting for T-Jump spectra of CS1, CS2 and CS3, and outlined in **Fig 4d**, is plotted against the final temperature of the jump. The trend shows that the rate of compression, in terms of the speed of radius change, increases with temperature.

Fitting Parameters

The following tables outline the fitting parameters for various T-Jump experiments over temperature-jump magnitude.

Table S4: Temperature-jump fitting parameters vs. microgel type ($c = 0.050$ wt% and $[KCl] = 0.100$ M): ΔOD_{fast}

| Temperature-Jump | CS1 | CS2 | CS3 | CS4 | CS5 |
|------------------|--------|--------|--------|--------|--------|
| 31 °C → 32.2 °C | | | | 0.0209 | |
| 31 °C → 32.8 °C | | | | 0.0363 | |
| 31 °C → 33.5 °C | 0.0131 | 0.0206 | 0.0233 | 0.0445 | 0.0086 |
| 31 °C → 34.6 °C | 0.0214 | 0.0314 | 0.0346 | 0.0487 | 0.0109 |
| 31 °C → 36.0 °C | 0.0284 | 0.0437 | 0.0418 | 0.0492 | 0.0162 |
| 31 °C → 37.1 °C | 0.0334 | 0.0503 | 0.0495 | 0.0516 | 0.0205 |
| 31 °C → 38.9 °C | 0.0365 | 0.0556 | 0.0549 | 0.0543 | 0.0237 |

Table S5: Temperature-jump fitting parameters vs. microgel type ($c = 0.050$ wt% and $[KCl] = 0.100$ M): ΔOD_{fast} **error**

| Temperature-Jump | CS1 | CS2 | CS3 | CS4 | CS5 |
|------------------|-------|-------|-------|-------|-------|
| 31 °C → 32.2 °C | | | | 0.001 | |
| 31 °C → 32.8 °C | | | | 0.001 | |
| 31 °C → 33.5 °C | 0.002 | 0.002 | 0.002 | 0.002 | 0.002 |
| 31 °C → 34.6 °C | 0.002 | 0.002 | 0.002 | 0.002 | 0.002 |
| 31 °C → 36.0 °C | 0.002 | 0.002 | 0.002 | 0.002 | 0.002 |
| 31 °C → 37.1 °C | 0.002 | 0.002 | 0.002 | 0.002 | 0.002 |
| 31 °C → 38.9 °C | 0.002 | 0.002 | 0.002 | 0.002 | 0.002 |

Table S6: Temperature-jump fitting parameters vs. microgel type ($c = 0.050$ wt% and $[KCl] = 0.100$ M): ΔOD_{slow}

| Temperature-Jump | CS1 | CS2 | CS3 | CS4 | CS5 |
|------------------|---------|--------|--------|--------|--------|
| 31 °C → 32.2 °C | | | | 0.0030 | |
| 31 °C → 32.8 °C | | | | 0.0054 | |
| 31 °C → 33.5 °C | 6.51E-4 | 0.0014 | 0.0036 | 0.0276 | 0.0025 |
| 31 °C → 34.6 °C | 0.0013 | 0.0031 | 0.0059 | 0.0368 | 0.0047 |
| 31 °C → 36.0 °C | 0.0030 | 0.0053 | 0.0082 | 0.0361 | 0.0061 |
| 31 °C → 37.1 °C | 0.0037 | 0.0025 | 0.0102 | 0.0369 | 0.0078 |
| 31 °C → 38.9 °C | 0.0048 | 0.0084 | 0.0119 | 0.0364 | 0.0096 |

Table S7: Temperature-jump fitting parameters vs. microgel type ($c = 0.050$ wt% and $[KCl] = 0.100$ M): ΔOD_{slow} error

| Temperature-Jump | CS1 | CS2 | CS3 | CS4 | CS5 |
|------------------|------|------|------|-------|-------|
| 31 °C → 32.2 °C | | | | 3E-4 | |
| 31 °C → 32.8 °C | | | | 5E-4 | |
| 31 °C → 33.5 °C | 3E-4 | 6E-4 | 7E-4 | 0.002 | 8E-4 |
| 31 °C → 34.6 °C | 5E-4 | 6E-4 | 7E-4 | 0.002 | 0.001 |
| 31 °C → 36.0 °C | 8E-4 | 6E-4 | 8E-4 | 0.002 | 0.001 |
| 31 °C → 37.1 °C | 5E-4 | 6E-4 | 9E-4 | 0.002 | 0.001 |
| 31 °C → 38.9 °C | 6E-4 | 7E-4 | 9E-4 | 0.002 | 0.001 |

Table S8: Temperature-jump fitting parameters vs. microgel type ($c = 0.050$ wt% and $[KCl] = 0.100$ M): τ_{fast} (ms)

| Temperature-Jump | CS1 | CS2 | CS3 | CS4 | CS5 |
|------------------|--------|--------|--------|--------|--------|
| 31 °C → 32.2 °C | | | | 0.1411 | |
| 31 °C → 32.8 °C | | | | 0.1684 | |
| 31 °C → 33.5 °C | 0.0510 | 0.0784 | 0.0951 | 0.1761 | 0.0857 |
| 31 °C → 34.6 °C | 0.0538 | 0.0814 | 0.104 | 0.1234 | 0.0783 |
| 31 °C → 36.0 °C | 0.0582 | 0.0831 | 0.1211 | 0.1238 | 0.0755 |
| 31 °C → 37.1 °C | 0.0632 | 0.0963 | 0.119 | 0.103 | 0.0714 |
| 31 °C → 38.9 °C | 0.0724 | 0.104 | 0.124 | 0.0935 | 0.0706 |

Table S9: Temperature-jump fitting parameters vs. microgel type ($c = 0.050$ wt% and $[\text{KCl}] = 0.100$ M): τ_{fast} (ms) error

| Temperature-Jump | CS1 | CS2 | CS3 | CS4 | CS5 |
|-----------------------------|-------|-------|-------|-------|-------|
| 31 °C \rightarrow 32.2 °C | | | | 0.01 | |
| 31 °C \rightarrow 32.8 °C | | | | 0.01 | |
| 31 °C \rightarrow 33.5 °C | 0.009 | 0.01 | 0.01 | 0.01 | 0.02 |
| 31 °C \rightarrow 34.6 °C | 0.006 | 0.007 | 0.007 | 0.007 | 0.02 |
| 31 °C \rightarrow 36.0 °C | 0.005 | 0.005 | 0.008 | 0.007 | 0.01 |
| 31 °C \rightarrow 37.1 °C | 0.005 | 0.005 | 0.006 | 0.006 | 0.009 |
| 31 °C \rightarrow 38.9 °C | 0.004 | 0.005 | 0.006 | 0.006 | 0.008 |

Table S10: Temperature-jump fitting parameters vs. microgel type ($c = 0.050$ wt% and $[\text{KCl}] = 0.100$ M): τ_{slow} (ms)

| Temperature-Jump | CS1 | CS2 | CS3 | CS4 | CS5 |
|-----------------------------|------|-------|------|-------|-------|
| 31 °C \rightarrow 32.2 °C | | | | 2.23 | |
| 31 °C \rightarrow 32.8 °C | | | | 1.91 | |
| 31 °C \rightarrow 33.5 °C | 2.90 | 0.941 | 1.35 | 0.951 | 1.876 |
| 31 °C \rightarrow 34.6 °C | 2.12 | 1.28 | 1.44 | 1.00 | 1.93 |
| 31 °C \rightarrow 36.0 °C | 3.46 | 1.27 | 1.31 | 1.30 | 1.68 |
| 31 °C \rightarrow 37.1 °C | 3.00 | 1.62 | 1.45 | 1.40 | 1.79 |
| 31 °C \rightarrow 38.9 °C | 2.15 | 1.47 | 1.48 | 1.56 | 1.66 |

Table S11: Temperature-jump fitting parameters vs. microgel type ($c = 0.050$ wt% and $[\text{KCl}] = 0.100$ M): τ_{slow} (ms) error

| Temperature-Jump | CS1 | CS2 | CS3 | CS4 | CS5 |
|-----------------------------|-----|-----|-----|------|-----|
| 31 °C \rightarrow 32.2 °C | | | | 0.5 | |
| 31 °C \rightarrow 32.8 °C | | | | 0.3 | |
| 31 °C \rightarrow 33.5 °C | 2 | 0.4 | 0.3 | 0.05 | 0.6 |
| 31 °C \rightarrow 34.6 °C | 0.6 | 0.3 | 0.2 | 0.03 | 0.2 |
| 31 °C \rightarrow 36.0 °C | 0.8 | 0.2 | 0.2 | 0.04 | 0.2 |
| 31 °C \rightarrow 37.1 °C | 0.5 | 0.2 | 0.1 | 0.04 | 0.2 |
| 31 °C \rightarrow 38.9 °C | 0.2 | 0.2 | 0.1 | 0.05 | 0.1 |

Table S12: Temperature-jump fitting parameters vs. microgel concentration ([CS3] and [KCl] = 0.100 M): τ_{fast} (ms)

| Temperature-Jump | 0.050 wt% | 0.080 wt% | 0.106 wt% | 0.12 wt% |
|------------------|-----------|-----------|-----------|----------|
| 31 °C → 33.5 °C | 0.095 | 0.105 | 0.0982 | 0.0886 |
| 31 °C → 34.6 °C | 0.104 | 0.109 | 0.109 | 0.107 |
| 31 °C → 36.0 °C | 0.121 | 0.109 | 0.119 | 0.116 |
| 31 °C → 37.1 °C | 0.119 | 0.124 | 0.117 | 0.111 |
| 31 °C → 38.9 °C | 0.124 | 0.123 | 0.123 | |

Table S13: Temperature-jump fitting parameters vs. microgel concentration ([CS3] and [KCl] = 0.100 M): τ_{fast} (ms) error

| Temperature-Jump | 0.050 wt% | 0.080 wt% | 0.106 wt% | 0.12 wt% |
|------------------|-----------|-----------|-----------|----------|
| 31 °C → 33.5 °C | 0.01 | 0.008 | 0.008 | 0.007 |
| 31 °C → 34.6 °C | 0.007 | 0.006 | 0.006 | 0.006 |
| 31 °C → 36.0 °C | 0.008 | 0.008 | 0.006 | 0.007 |
| 31 °C → 37.1 °C | 0.006 | 0.006 | 0.006 | 0.005 |
| 31 °C → 38.9 °C | 0.006 | 0.006 | 0.006 | |

Table S14: Temperature-jump fitting parameters vs. microgel concentration ([CS3] and [KCl] = 0.100 M): τ_{slow} (ms)

| Temperature-Jump | 0.050 wt% | 0.080 wt% | 0.106 wt% | 0.12 wt% |
|------------------|-----------|-----------|-----------|----------|
| 31 °C → 33.5 °C | 1.35 | 1.62 | 1.28 | 1.23 |
| 31 °C → 34.6 °C | 1.45 | 1.33 | 1.56 | 1.53 |
| 31 °C → 36.0 °C | 1.31 | 1.13 | 1.53 | 1.39 |
| 31 °C → 37.1 °C | 1.45 | 1.41 | 1.29 | 1.46 |
| 31 °C → 38.9 °C | 1.47 | 1.36 | 1.34 | 1.039 |

Table S15: Temperature-jump fitting parameters vs. microgel concentration ([CS3] and [KCl] = 0.100 M): τ_{slow} (ms) error

| Temperature-Jump | 0.050 wt% | 0.080 wt% | 0.106 wt% | 0.12 wt% |
|------------------|-----------|-----------|-----------|----------|
| 31 °C → 33.5 °C | 0.3 | 0.3 | 0.3 | 0.2 |
| 31 °C → 34.6 °C | 0.2 | 0.2 | 0.2 | 0.2 |
| 31 °C → 36.0 °C | 0.2 | 0.1 | 0.2 | 0.2 |
| 31 °C → 37.1 °C | 0.1 | 0.1 | 0.1 | 0.1 |
| 31 °C → 38.9 °C | 0.1 | 0.1 | 0.1 | 0.1 |

Table S16: Temperature-jump fitting parameters vs. KCl concentration (CS3, $c = 0.050$

| wt%): τ_{fast} (ms) | | | | | |
|---------------------------------|---------|---------|---------|--------|--------|
| Temperature-Jump | 0.010 M | 0.050 M | 0.075 M | 0.10 M | 0.20 M |
| 31 °C \rightarrow 33.5 °C | 0.238 | 0.106 | 0.0875 | 0.0951 | 0.120 |
| 31 °C \rightarrow 34.6 °C | 0.233 | 0.112 | 0.105 | 0.104 | 0.122 |
| 31 °C \rightarrow 36.0 °C | 0.260 | 0.126 | 0.120 | 0.121 | 0.142 |
| 31 °C \rightarrow 37.1 °C | 0.237 | 0.130 | 0.116 | 0.119 | 0.142 |
| 31 °C \rightarrow 38.9 °C | 0.233 | 0.129 | 0.111 | 0.1238 | 0.129 |

Table S17: Temperature-jump fitting parameters vs. KCl concentration (CS3, $c = 0.050$

| wt%): τ_{fast} (ms) error | | | | | |
|---------------------------------------|---------|---------|---------|--------|--------|
| Temperature-Jump | 0.010 M | 0.050 M | 0.075 M | 0.10 M | 0.20 M |
| 31 °C \rightarrow 33.5 °C | 0.02 | 0.009 | 0.01 | 0.01 | 0.01 |
| 31 °C \rightarrow 34.6 °C | 0.01 | 0.007 | 0.007 | 0.007 | 0.01 |
| 31 °C \rightarrow 36.0 °C | 0.01 | 0.006 | 0.006 | 0.008 | 0.009 |
| 31 °C \rightarrow 37.1 °C | 0.009 | 0.006 | 0.006 | 0.006 | 0.01 |
| 31 °C \rightarrow 38.9 °C | 0.008 | 0.005 | 0.006 | 0.006 | 0.009 |

Table S18: Temperature-jump fitting parameters vs. KCl concentration (CS3, $c = 0.050$

| wt%): τ_{slow} (ms) | | | | | |
|---------------------------------|---------|---------|---------|--------|--------|
| Temperature-Jump | 0.010 M | 0.050 M | 0.075 M | 0.10 M | 0.20 M |
| 31 °C \rightarrow 33.5 °C | 4.37 | 2.16 | 0.84 | 1.35 | 1.22 |
| 31 °C \rightarrow 34.6 °C | 3.31 | 1.47 | 1.32 | 1.45 | 1.26 |
| 31 °C \rightarrow 36.0 °C | 4.09 | 1.71 | 1.59 | 1.31 | 1.73 |
| 31 °C \rightarrow 37.1 °C | 2.82 | 1.59 | 1.39 | 1.45 | 1.31 |
| 31 °C \rightarrow 38.9 °C | 2.75 | 1.56 | 1.17 | 1.48 | 1.37 |

Table S19: Temperature-jump fitting parameters vs. KCl concentration (CS3, $c = 0.050$

| wt%): τ_{slow} (ms) error | | | | | |
|---------------------------------------|---------|---------|---------|--------|--------|
| Temperature-Jump | 0.010 M | 0.050 M | 0.075 M | 0.10 M | 0.20 M |
| 31 °C \rightarrow 33.5 °C | 3 | 0.7 | 0.2 | 0.3 | 0.2 |
| 31 °C \rightarrow 34.6 °C | 0.9 | 0.2 | 0.2 | 0.2 | 0.1 |
| 31 °C \rightarrow 36.0 °C | 1 | 0.2 | 0.2 | 0.2 | 0.2 |
| 31 °C \rightarrow 37.1 °C | 0.4 | 0.2 | 0.1 | 0.2 | 0.1 |
| 31 °C \rightarrow 38.9 °C | 0.2 | 0.1 | 0.1 | 0.1 | 0.1 |

Table S20: Temperature-jump fitting parameters vs. SDS concentration (CS3, $c = 0.050$ wt%, $[KCl] = 0.010$ M): τ_{fast} (ms)

| Temperature-Jump | 0 mM | 0.091 mM | 0.50 mM | 0.75 mM | 1.0 mM |
|------------------|-------|----------|---------|---------|--------|
| 31 °C → 33.5 °C | 0.212 | 0.222 | 0.203 | 0.240 | 0.217 |
| 31 °C → 34.6 °C | 0.221 | 0.225 | 0.199 | 0.232 | 0.235 |
| 31 °C → 36.0 °C | 0.228 | 0.232 | 0.207 | 0.234 | 0.247 |
| 31 °C → 37.1 °C | 0.233 | 0.225 | 0.212 | 0.240 | 0.244 |
| 31 °C → 38.9 °C | 0.233 | 0.218 | 0.207 | 0.229 | 0.226 |

Table S21: Temperature-jump fitting parameters vs. SDS concentration (CS3, $c = 0.050$ wt%, $[KCl] = 0.010$ M): τ_{fast} (ms) error

| Temperature-Jump | 0 mM | 0.091 mM | 0.50 mM | 0.75 mM | 1.0 mM |
|------------------|-------|----------|---------|---------|--------|
| 31 °C → 33.5 °C | 0.02 | 0.02 | 0.02 | 0.02 | 0.02 |
| 31 °C → 34.6 °C | 0.01 | 0.01 | 0.01 | 0.01 | 0.01 |
| 31 °C → 36.0 °C | 0.008 | 0.009 | 0.01 | 0.01 | 0.01 |
| 31 °C → 37.1 °C | 0.007 | 0.008 | 0.009 | 0.009 | 0.008 |
| 31 °C → 38.9 °C | 0.007 | 0.007 | 0.007 | 0.008 | 0.01 |

Table S22: Temperature-jump fitting parameters vs. SDS concentration (CS3, $c = 0.050$ wt%, $[KCl] = 0.010$ M): τ_{slow} (ms)

| Temperature-Jump | 0 mM | 0.091 mM | 0.50 mM | 0.75 mM | 1.0 mM |
|------------------|------|----------|---------|---------|--------|
| 31 °C → 33.5 °C | 3.41 | 3.31 | 3.33 | 3.37 | 5.11 |
| 31 °C → 34.6 °C | 3.50 | 2.56 | 2.44 | 4.09 | 3.48 |
| 31 °C → 36.0 °C | 3.24 | 2.96 | 2.34 | 2.65 | 3.78 |
| 31 °C → 37.1 °C | 3.70 | 2.63 | 2.36 | 2.86 | 4.38 |
| 31 °C → 38.9 °C | 3.70 | 2.31 | 2.50 | 2.77 | 2.69 |

Table S23: Temperature-jump fitting parameters vs. SDS concentration (CS3, $c = 0.050$ wt%, $[KCl] = 0.010$ M): τ_{slow} (ms) error

| Temperature-Jump | 0 mM | 0.091 mM | 0.50 mM | 0.75 mM | 1.0 mM |
|------------------|------|----------|---------|---------|--------|
| 31 °C → 33.5 °C | 2 | 1 | 2 | 2 | 3 |
| 31 °C → 34.6 °C | 1 | 0.7 | 0.5 | 1 | 0.8 |
| 31 °C → 36.0 °C | 0.6 | 0.6 | 0.3 | 0.5 | 0.8 |
| 31 °C → 37.1 °C | 0.6 | 0.4 | 0.3 | 0.5 | 1 |
| 31 °C → 38.9 °C | 0.6 | 0.2 | 0.3 | 0.3 | 0.6 |

Table S24: Temperature-jump fitting parameters vs. pH (CS3, $c = 0.050$ wt%, $[\text{KCl}] = 0.100$ M): τ_{fast} (ms)

| Temperature-Jump | pH = 3.3 | 5.3 | 7.1 | 9.0 |
|------------------|----------|-------|-------|-------|
| 31 °C → 33.5 °C | 0.093 | 0.109 | 0.095 | 0.082 |
| 31 °C → 34.6 °C | 0.113 | 0.111 | 0.104 | 0.097 |
| 31 °C → 36.0 °C | 0.117 | 0.117 | 0.121 | 0.111 |
| 31 °C → 37.1 °C | 0.123 | 0.124 | 0.119 | 0.129 |
| 31 °C → 38.9 °C | 0.123 | 0.124 | 0.119 | 0.129 |

Table S25: Temperature-jump fitting parameters vs. pH (CS3, $c = 0.050$ wt%, $[\text{KCl}] = 0.100$ M): τ_{fast} (ms) error

| Temperature-Jump | pH = 3.3 | 5.3 | 7.1 | 9.0 |
|------------------|----------|-------|-------|-------|
| 31 °C → 33.5 °C | 0.009 | 0.01 | 0.01 | 0.01 |
| 31 °C → 34.6 °C | 0.008 | 0.007 | 0.007 | 0.007 |
| 31 °C → 36.0 °C | 0.007 | 0.007 | 0.008 | 0.007 |
| 31 °C → 37.1 °C | 0.006 | 0.007 | 0.006 | 0.007 |
| 31 °C → 38.9 °C | 0.006 | 0.006 | 0.006 | 0.006 |

Table S26: Temperature-jump fitting parameters vs. pH (CS3, $c = 0.050$ wt%, $[\text{KCl}] = 0.100$ M): τ_{slow} (ms)

| Temperature-Jump | pH = 3.3 | 5.3 | 7.1 | 9.0 |
|------------------|----------|------|------|------|
| 31 °C → 33.5 °C | 1.18 | 1.44 | 1.35 | 0.75 |
| 31 °C → 34.6 °C | 1.52 | 1.46 | 1.45 | 1.20 |
| 31 °C → 36.0 °C | 1.49 | 1.35 | 1.31 | 1.45 |
| 31 °C → 37.1 °C | 1.72 | 1.36 | 1.45 | 1.64 |
| 31 °C → 38.9 °C | 1.77 | 1.51 | 1.48 | 1.29 |

Table S27: Temperature-jump fitting parameters vs. pH (CS3, $c = 0.050$ wt%, $[\text{KCl}] = 0.100$ M): τ_{slow} (ms) error

| Temperature-Jump | pH = 3.3 | 5.3 | 7.1 | 9.0 |
|------------------|----------|-----|-----|-----|
| 31 °C → 33.5 °C | 0.2 | 0.3 | 0.3 | 0.2 |
| 31 °C → 34.6 °C | 0.2 | 0.2 | 0.2 | 0.2 |
| 31 °C → 36.0 °C | 0.2 | 0.2 | 0.2 | 0.2 |
| 31 °C → 37.1 °C | 0.2 | 0.1 | 0.1 | 0.2 |
| 31 °C → 38.9 °C | 0.1 | 0.1 | 0.1 | 0.1 |

Residuals

The residuals for the temperature-jump time traces in **Fig 2** of the main manuscript are plotted below:

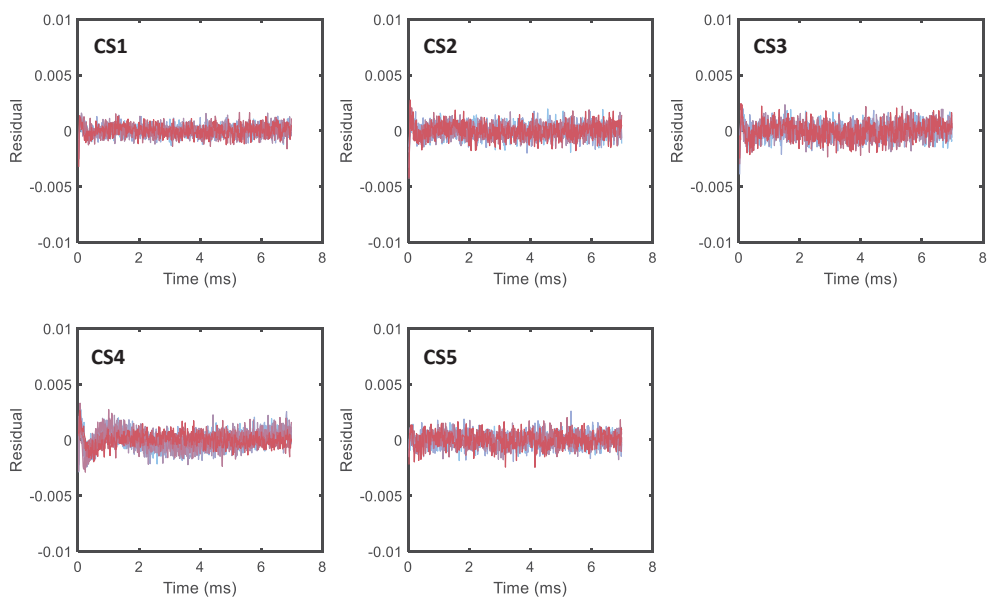


Figure S12: Residual plots for the sets of temperature-spectra in **Fig 2** ($c = 0.050$ wt%, $[KCl] = 0.100$ M). Colour scheme and conditions are outlined in the figure caption in the main manuscript

7 Conclusion and Perspectives

This work dealt with the optical properties of thermoresponsive microgels containing gold cores, either focussing on the scattering properties of dilute dispersions or on the collective absorption of periodic, self-assembled monolayers. The following key achievements were accomplished:

1. Synthesis of core-shell microgels featuring a small gold core with various polymer shell sizes and cross-linking densities, and relating changes in extinction properties to structural changes during the volume phase transition.
2. Fabrication of periodic particle arrays via colloidal self-assembly with a broad range of interparticle distances and identification of relevant criteria for radiative plasmonic coupling.
3. Determination of theoretical optical properties of individual core-shell microgels and particle arrays by using finite difference time domain simulations and supporting the experimental findings by theoretical calculations.
4. Evaluation of the collapse dynamics of microgels during the volume phase transition by capacitor-discharge temperature jump spectroscopy and determination of the impact of microgel structure on the collapse kinetics.

The first part of this work focused on the properties and characterization of core-shell microgels consisting of a small gold core and a PNIPAM shell. The polymer shell was systematically varied in size from 222 to 380 nm and the cross-linker density was also varied between 5 and 25 mol% BIS. TEM measurements were acquired to evaluate the success of the encapsulation of the gold cores into the PNIPAM shells. On average, more than 95 % of the microgels featured exactly one core. Notably, the gold cores here were too small to significantly influence the swelling behaviour of the polymer shells. However, the cores were crucial for precisely controlling the shell thickness and they acted as markers to extract polymer volume fractions of the microgels. In particular, combining the metal core with a microgel allowed for the precise determination of the number density N by using the high X-ray contrast of gold in SAXS measurements. Knowing that each microgel contains only one core, the number of cores gave direct access to the number of microgels. Commonly, the precise determination of N is challenging because the knowledge of the microgel volume fraction in the dispersion and the volume of a single microgel is required. The microgel volume is especially difficult to define due to the fuzziness of the spheres. Moreover, the microgel volume strongly depends on the radius definition (*e.g.* radius from SLS or hydrodynamic radius) used for the calculation.

Hence, the advantage of the approach used here to determine N is that the radius of a single microgel is not required. Instead, the absolute intensity of the gold cores measured by SAXS was used to calculate the number density N .

The morphology of the different microgels at different stages of swelling was obtained by analyzing scattering data from SANS measurements. At 25 °C, all microgels were in their swollen state, and the fuzzy-sphere model accurately described their form factor. Microgels with similar cross-linker densities showed similar polymer volume fractions ranging between 0.18 and 0.22 for the inner region of the microgel despite various shell thicknesses. Hence, the inner homogenous parts of microgels contained on average 80 % solvent by volume. In contrast, the cross-linking strongly affected the polymer volume fractions, resulting in approximately 90 % solvent by volume for the lowest cross-linked microgel and 76 % for the microgel with the highest cross-linker density. Higher amounts of cross-linker led to smaller polymer network meshes and, therefore, more rigid structures resulting in higher polymer densities. All microgels collapsed with increasing temperature, leading to reduced sizes and increased polymer densities and thus increased refractive indices of the polymer shells. At 50 °C, all microgels were fully collapsed, showing very similar polymer densities, and their form factor could be described by a homogeneous, polydisperse sphere model similar to simple hard spheres. The obtained polymer volume fractions ranged between 0.37 and 0.5. The collapsed state was used as a reference state to predict temperature-dependent profiles of the effective polymer volume fractions of different microgels.

Surprisingly, the spectroscopic properties of thermoresponsive microgel dispersions have not been widely reported in the literature. Thus, this study provides new physical insights into the light scattering properties of microgels and links the optical properties of the PNIPAM microgel to its structural transition during the VPT for the first time. Absorbance measurements of all microgels during the volume phase transition in the temperature range from 10 to 60 °C were performed using UV-Vis spectroscopy. The optical response comprised the LSPR contribution of the gold core and the scattering contribution of the polymer shell. However, since the PNIPAM shell was significantly larger than the gold core, scattering of the shell strongly dominated absorption of the core. For all microgels, absorbances (and therefore turbidity) increased during the VPT. Interestingly, although all microgels fulfilled the RDG criteria, the RDG calculations could not reproduce the observed increase in absorbance. The increased absorbances with increasing temperature were attributed to changes from inhomogeneous fuzzy spheres to homogeneous hard sphere-like scatterers. In the swollen state, scattering was dominated by the homogeneous polymer core. The fuzzy shell with gradually decreasing polymer density towards the shell surface did not contribute remarkably to the scattering. With increasing temperature, the fuzzy shell collapsed onto the inner homogeneous core. The collapse was accompanied by increases in the polymer density and refractive index. As a result, the scattering of the microgels increased.

Obtained radii and refractive indices for all microgels from SANS analysis were taken for theoretical calculations using FDTD simulations. This work provides the first simulation results considering the fuzzy sphere structure of microgels. For the swollen state, a simple core-shell model was used. The polymer core corresponded to the inner

homogeneous region as defined by the fuzzy sphere model, and the shell corresponded to the thickness of the fuzzy shell with half the polymer density of the inner polymer core. Collapsed microgels were simulated as homogeneous spheres. In all cases, the FDTD simulations confirmed the absorbance increase from the swollen to collapsed state and showed overall reasonable agreement with experiments. However, scattering intensity of the polymer shells was underestimated for all microgels.

This work has shown that scattering methods can be used to obtain information on microgel structures with various shell thicknesses and polymer densities. However, higher-resolution scattering measurements would allow fitting the data with more complex models. Using a more complex model would provide a more accurate microgel structure. These findings can be used to generate a more detailed simulation model for the light scattering properties to improve the agreement between the experimental absorbances and simulated spectra. Moreover, this thesis aims to stimulate further research on the optical response of thermoresponsive microgels. A theory that correctly describes the experimentally observed scattering properties of microgels has not yet been introduced. Understanding how the microgel structure affects optical properties during the volume phase transitions would allow the use of simple and quick absorbance measurements to follow the microgel transition with great time resolution and reveal structural changes.

In the second part of the work, the introduced core-shell microgels were post-modified by increasing the size of the small gold core in order to achieve a pronounced LSPR contribution despite the strong scattering contribution of the polymer shell. The modified Au-PNIPAM microgels were used as building blocks for ordered periodic arrays. The particle arrays were prepared via interface-mediated self-assembly with interparticle distances ranging between 342 and 573 nm. These distances were achieved by i) using different shell thicknesses and by ii) using a multistep transfer process from floating particle arrays at the air/water interface where particle spacing increased after each withdrawal of a monolayer sample. In this part, the focus was on investigating the optical properties of the gold particle arrays and how various parameters, such as interparticle distance, structural disorder, and refractive index affect the resonance quality. The structure of the particle arrays was analysed from images obtained via AFM and DFM. While DFM confirmed the homogeneity of the samples over large areas on the order of mm^2 , AFM measurements allowed for a closer look at the microstructures. The crystalline domains were evaluated by triangulation analysis, and the degree of lattice order was studied quantitatively using the pair correlations function. Despite lattice defects, all fabricated particle arrays revealed overall hexagonal ordering with large crystalline domains where the largest domain contained over 5000 particles. Furthermore, the domain sizes increased with increasing interparticle distances.

The observed optical coupling phenomena were strongly dependent on the interparticle distances or lattice period and the refractive index environment. In an asymmetric environment, only weak electromagnetic coupling occurred due to long-range radiative dipolar interactions. These interactions manifested in a blueshift of the plasmon resonance and were most pronounced in particle arrays with the smallest interparticle distances. Homogenization of the refractive index surrounding the gold particles resulted in pronounced SLRs. The diffractive-plasmonic coupling was most pronounced for

particle distances where the Bragg modes were spectrally close or redshifted from the single particle LSPR. The SLR modes became broader and weaker with further increases in the lattice period. Simultaneously, at large interparticle distances, the LSPR mode reappeared. Experimental observations for both symmetric and asymmetric environments were reproduced with FDTD simulations. Moreover, simulations allowed for the comparison of the resonance quality of finite with infinite lattices. Despite lattice defects and finite domain sizes in experimental self-assembled particle arrays, the deviation between experimental and theoretical SLR quality of infinite lattices was relatively small. While the self-assembled array with d_{c-c} of 483 nm showed the highest quality factor $Q \approx 20$, the simulated lattice with a similar period had a value of 37. These results demonstrate that interface-mediated self-assembly is an excellent method to fabricate ordered particle arrays supporting collective resonances with high optical quality.

The introduced Au-PNIPAM microgels are attractive as building blocks for 2D structures due to the possibility of adjusting the particles' individual properties and, therefore, fabricating particle lattices supporting different optical phenomena. Various polymer shell sizes and densities can be achieved, which strongly affects the interparticle distances and the order of the arrays. Moreover, the porous PNIPAM shell allows for numerous post-modifications of the metal core, *e.g.* tuning the size, shape, or incorporating another metal, resulting in drastically changed optical properties. This work presented only a few engineering options for core-shell microgels; however, the possibilities are far from exhausted. In order to further increase the optical quality of presented particle arrays, various strategies can be applied. On one hand, the quality of the LSPR mode can be improved by optimizing the synthesis protocol and reducing the Au-NP polydispersity. On the other hand, a highly ordered lattice is necessary to avoid optical losses that hamper strong plasmonic-photonic coupling. Therefore, the self-assembly method must be adjusted to reduce the lattice defects and increase domain sizes, especially for smaller interparticle distances. However, the rapid and low-cost colloidal self-assembly method is very promising for engineering optical miniature devices. Recently, Volk *et al.*³⁴ introduced free-standing polymer films with embedded self-assembled periodic plasmonic particles featuring SLRs. Moreover, the self-assembly method can become competitive with lithographic approaches. For example until now, lasing action was only reported for periodic particle arrays fabricated using lithography methods^{25,292}. However, the lasing action in self-assembled structures may be realized in the near future. Another potential application of particle arrays is ultrasensitive molecular sensing due to the SLR sensitivity to the RI environment²⁹³.

One way to alter the refractive index environment is to make use of the thermosensitive character of the PNIPAM shells. This was used in the third part of the work, which studied the dynamics of the collapse of the Au-PNIPAM microgels during the VPT using capacitor-discharge temperature-jump spectroscopy. Here it was investigated how the temperature-jump magnitude, the particle size and the cross-linker density affect the collapse dynamics of the microgels. A two-step collapsing process characterized by slow and fast lifetimes was identified for all microgels. The fast lifetime corresponded to the fast deswelling of the fuzzy shell, while the slow lifetime described the polymer chains slowly rearranging within the shell. It was found that the fast lifetime scales linearly

with overall radius during shrinkage. In comparison, the slow lifetime remained almost constant independent of the microgel morphology and the temperature jump.

While the first two parts addressed only the static behaviour of core-shell microgels at fixed temperatures, the last part focused on the dynamical behaviour of the PNIPAM shell. The obtained results demonstrated quantitatively how the microgel size and morphology affects its deswelling process. Moreover, the study showed how quickly the various microgels reacted to temperature changes. In the future, it will also be interesting to investigate the swelling dynamics of microgels from collapsed to swollen states and how the microgel structure might affect the swelling time. Nevertheless, the work demonstrated the potential of thermoresponsive microgels for switchable devices since many potential applications, *e.g.* drug delivery or sensors, require systems responding on-demand to external stimuli².

In summary, this thesis focused on the optical properties of core-shell Au-PNIPAM microgels and contributed to a deeper understanding of such systems. In particular, the work addressed both the temperature-dependent scattering behaviour of the polymer shell and the plasmonic properties of the gold core. Furthermore, the work demonstrated various optical responses from single particles to periodic assemblies and showed the potential of the investigated systems for various future applications.

References

- [1] Plamper, F. A.; Richtering, W. Functional Microgels and Microgel Systems. *Accounts of Chemical Research* **2017**, *50*, 131–140.
- [2] Karg, M.; Pich, A.; Hellweg, T.; Hoare, T.; Lyon, L. A.; Crassous, J. J.; Suzuki, D.; Gumerov, R. A.; Schneider, S.; Potemkin, I. I.; Richtering, W. Nanogels and Microgels: From Model Colloids to Applications, Recent Developments, and Future Trends. *Langmuir* **2019**, *35*, 6231–6255.
- [3] Rey, M.; Fernandez-Rodriguez, M. A.; Karg, M.; Isa, L.; Vogel, N. Poly-N-isopropylacrylamide Nanogels and Microgels at Fluid Interfaces. *Accounts of Chemical Research* **2020**, *53*, 414–424.
- [4] Tanaka, T.; Fillmore, D. J. Kinetics of swelling of gels. *The Journal of Chemical Physics* **1979**, *70*, 1214–1218.
- [5] Li, Y.; Tanaka, T. Kinetics of swelling and shrinking of gels. *The Journal of Chemical Physics* **1990**, *92*, 1365–1371.
- [6] Pelton, R. H.; Chibante, P. Preparation of aqueous latices with N-isopropylacrylamide. *Colloids and Surfaces* **1986**, *20*, 247–256.
- [7] Heskins, M.; Guillet, J. E. Solution Properties of Poly(N-isopropylacrylamide). *Journal of Macromolecular Science: Part A - Chemistry* **1968**, *2*, 1441–1455.
- [8] Karg, M.; Jaber, S.; Hellweg, T.; Mulvaney, P. Surface Plasmon Spectroscopy of Gold-Poly-N-isopropylacrylamide Core-Shell Particles. *Langmuir* **2011**, *27*, 820–827.
- [9] Wedel, B.; Hertle, Y.; Wrede, O.; Bookhold, J.; Hellweg, T. Smart Homopolymer Microgels: Influence of the Monomer Structure on the Particle Properties. *Polymers* **2016**, *8*, 162.
- [10] Karg, M.; Pastoriza-Santos, I.; Pérez-Juste, J.; Hellweg, T.; Liz-Marzán, L. Nanorod-Coated PNIPAM Microgels: Thermoresponsive Optical Properties. *Small* **2007**, *3*, 1222–1229.
- [11] Reufer, M.; Diaz-Leyva, P.; Lynch, I.; Scheffold, F. Temperature-sensitive poly(N-Isopropyl-Acrylamide) microgel particles: A light scattering study. *The European Physical Journal E* **2009**, *28*, 165–171.

- [12] Rauh, A.; Honold, T.; Karg, M. Seeded precipitation polymerization for the synthesis of gold-hydrogel core-shell particles: the role of surface functionalization and seed concentration. *Colloid and Polymer Science* **2016**, *294*, 37–47.
- [13] Daruich De Souza, C.; Ribeiro Nogueira, B.; Rostelato, M. E. C. M. Review of the methodologies used in the synthesis gold nanoparticles by chemical reduction. *Journal of Alloys and Compounds* **2019**, *798*, 714–740.
- [14] Freestone, I.; Meeks, N.; Sax, M.; Higgitt, C. The Lycurgus Cup — A Roman nanotechnology. *Gold Bulletin* **2007**, *40*, 270–277.
- [15] Rodríguez-Fernández, J.; Pérez-Juste, J.; de Abajo, F. J. G.; Liz-Marzán, L. M. Seeded Growth of Submicron Au Colloids with Quadrupole Plasmon Resonance Modes. *Langmuir* **2006**, *22*, 7007–7010.
- [16] Maier, S. A.; Brongersma, M. L.; Kik, P. G.; Meltzer, S.; Requicha, A. a. G.; Atwater, H. A. Plasmonics—A Route to Nanoscale Optical Devices. *Advanced Materials* **2001**, *13*, 1501–1505.
- [17] Jain, P. K.; Huang, X.; El-Sayed, I. H.; El-Sayed, M. A. Review of Some Interesting Surface Plasmon Resonance-enhanced Properties of Noble Metal Nanoparticles and Their Applications to Biosystems. *Plasmonics* **2007**, *2*, 107–118.
- [18] Willets, K. A.; Van Duyne, R. P. Localized surface plasmon resonance spectroscopy and sensing. *Annual Review of Physical Chemistry* **2007**, *58*, 267–297.
- [19] Noginov, M. A.; Zhu, G.; Belgrave, A. M.; Bakker, R.; Shalaev, V. M.; Narimanov, E. E.; Stout, S.; Herz, E.; Suteewong, T.; Wiesner, U. Demonstration of a spaser-based nanolaser. *Nature* **2009**, *460*, 1110–1112.
- [20] Ueno, K.; Misawa, H. Surface plasmon-enhanced photochemical reactions. *Journal of Photochemistry and Photobiology C: Photochemistry Reviews* **2013**, *15*, 31–52.
- [21] Honold, T.; Volk, K.; Rauh, A.; Fitzgerald, J. P. S.; Karg, M. Tunable plasmonic surfaces via colloid assembly. *Journal of Materials Chemistry C* **2015**, *3*, 11449–11457.
- [22] Sönnichsen, C.; Franzl, T.; Wilk, T.; von Plessen, G.; Feldmann, J.; Wilson, O.; Mulvaney, P. Drastic Reduction of Plasmon Damping in Gold Nanorods. *Physical Review Letters* **2002**, *88*, 077402.
- [23] Kravets, V. G.; Kabashin, A. V.; Barnes, W. L.; Grigorenko, A. N. Plasmonic Surface Lattice Resonances: A Review of Properties and Applications. *Chemical Reviews* **2018**, *118*, 5912–5951.
- [24] Utyushev, A. D.; Zakomirnyi, V. I.; Rasskazov, I. L. Collective lattice resonances: Plasmonics and beyond. *Reviews in Physics* **2021**, *6*, 100051.

-
- [25] Zhou, W.; Dridi, M.; Suh, J. Y.; Kim, C. H.; Co, D. T.; Wasielewski, M. R.; Schatz, G. C.; Odom, T. W. Lasing action in strongly coupled plasmonic nanocavity arrays. *Nature Nanotechnology; London* **2013**, *8*, 506–11.
- [26] Vecchi, G.; Giannini, V.; Rivas, J. G. Shaping the fluorescent emission by lattice resonances in plasmonic crystals of nanoantennas. *Physical Review Letters* **2009**, *102*, 146807.
- [27] Singh, C. R.; Honold, T.; Gujar, T. P.; Retsch, M.; Fery, A.; Karg, M.; Thelakkat, M. The role of colloidal plasmonic nanostructures in organic solar cells. *Physical Chemistry Chemical Physics* **2016**, *18*, 23155–23163.
- [28] Eitan, M.; Iluz, Z.; Yifat, Y.; Boag, A.; Hanein, Y.; Scheuer, J. Degeneracy Breaking of Wood's Anomaly for Enhanced Refractive Index Sensing. *ACS Photonics* **2015**, *2*, 615–621.
- [29] Wang, H.; Wang, X.; Yan, C.; Zhao, H.; Zhang, J.; Santschi, C.; Martin, O. J. F. Full Color Generation Using Silver Tandem Nanodisks. *ACS Nano* **2017**, *11*, 4419–4427.
- [30] Khlopin, D.; Laux, F.; Wardley, W. P.; Martin, J.; Wurtz, G. A.; Plain, J.; Bonod, N.; Zayats, A. V.; Dickson, W.; Gérard, D. Lattice modes and plasmonic linewidth engineering in gold and aluminum nanoparticle arrays. *Journal of the Optical Society of America B* **2017**, *34*, 691–700.
- [31] Gupta, V.; Probst, P. T.; Gößler, F. R.; Steiner, A. M.; Schubert, J.; Brasse, Y.; König, T. A. F.; Fery, A. Mechanotunable Surface Lattice Resonances in the Visible Optical Range by Soft Lithography Templates and Directed Self-Assembly. *ACS Applied Materials & Interfaces* **2019**, *11*, 28189–28196.
- [32] Wang, D.; Bourgeois, M. R.; Guan, J.; Fumani, A. K.; Schatz, G. C.; Odom, T. W. Lasing from Finite Plasmonic Nanoparticle Lattices. *ACS Photonics* **2020**, *7*, 630–636.
- [33] Scarabelli, L.; Vila-Liarte, D.; Mihi, A.; Liz-Marzán, L. M. Templated Colloidal Self-Assembly for Lattice Plasmon Engineering. *Accounts of Materials Research* **2021**, *2*, 816–827.
- [34] Volk, K.; Fitzgerald, J. P. S.; Karg, M. In-Plane Surface Lattice and Higher Order Resonances in Self-Assembled Plasmonic Monolayers: From Substrate-Supported to Free-Standing Thin Films. *ACS Applied Materials & Interfaces* **2019**, *11*, 16096–16106.
- [35] Juodėnas, M.; Peckus, D.; Tamulevičius, T.; Yamauchi, Y.; Tamulevičius, S.; Henzie, J. Effect of Ag Nanocube Optomechanical Modes on Plasmonic Surface Lattice Resonances. *ACS Photonics* **2020**, *7*, 3130–3140.

- [36] Goerlitzer, E. S. A.; Mohammadi, R.; Nechayev, S.; Banzer, P.; Vogel, N. Large-Area 3D Plasmonic Crescents with Tunable Chirality. *Advanced Optical Materials* **2019**, *7*, 1801770.
- [37] Henzie, J.; Lee, M. H.; Odom, T. W. Multiscale patterning of plasmonic metamaterials. *Nature Nanotechnology* **2007**, *2*, 549–554.
- [38] Volk, K.; Fitzgerald, J. P. S.; Retsch, M.; Karg, M. Time-Controlled Colloidal Superstructures: Long-Range Plasmon Resonance Coupling in Particle Monolayers. *Advanced Materials* **2015**, *27*, 7332–7337.
- [39] Vogel, N.; Retsch, M.; Fustin, C.-A.; del Campo, A.; Jonas, U. Advances in Colloidal Assembly: The Design of Structure and Hierarchy in Two and Three Dimensions. *Chemical Reviews* **2015**, *115*, 6265–6311.
- [40] Stieger, M.; Richtering, W.; Pedersen, J. S.; Lindner, P. Small-angle neutron scattering study of structural changes in temperature sensitive microgel colloids. *The Journal of Chemical Physics* **2004**, *120*, 6197–6206.
- [41] Flory, P. J.; Rehner, J. Statistical Mechanics of Cross-Linked Polymer Networks I. Rubberlike Elasticity. *The Journal of Chemical Physics* **1943**, *11*, 512–520.
- [42] Flory, P. J. *Principles of polymer chemistry*; Cornell University Press, 1953; OCLC: 542497.
- [43] Brust, M.; Walker, M.; Bethell, D.; Schiffrin, D. J.; Whyman, R. Synthesis of thiol-derivatised gold nanoparticles in a two-phase Liquid–Liquid system. *Journal of the Chemical Society, Chemical Communications* **1994**, 801–802.
- [44] Jana, N. R.; Gearheart, L.; Murphy, C. J. Seeding Growth for Size Control of 5-40 nm Diameter Gold Nanoparticles. *Langmuir* **2001**, *17*, 6782–6786.
- [45] Khan, Z.; Singh, T.; Hussain, J. I.; Hashmi, A. A. Au(III)-CTAB reduction by ascorbic acid: preparation and characterization of gold nanoparticles. *Colloids and Surfaces. B, Biointerfaces* **2013**, *104*, 11–17.
- [46] Turkevich, J.; Stevenson, P. C.; Hillier, J. A study of the nucleation and growth processes in the synthesis of colloidal gold. *Discussions of the Faraday Society* **1951**, *11*, 55–75.
- [47] Kimling, J.; Maier, M.; Okenve, B.; Kotaidis, V.; Ballot, H.; Plech, A. Turkevich Method for Gold Nanoparticle Synthesis Revisited. *The Journal of Physical Chemistry B* **2006**, *110*, 15700–15707.
- [48] Suzuki, D.; Horigome, K.; Kureha, T.; Matsui, S.; Watanabe, T. Polymeric hydrogel microspheres: design, synthesis, characterization, assembly and applications. *Polymer Journal* **2017**, *49*, 695–702.

- [49] Din, M. I.; Khalid, R.; Akbar, F.; Ahmad, G.; Najeeb, J.; Nisa Hussain, Z. U. Recent progress of poly (N-isopropylacrylamide) hybrid hydrogels: synthesis, fundamentals and applications – review. *Soft Materials* **2018**, *16*, 228–247.
- [50] Contreras-Cáceres, R.; Sánchez-Iglesias, A.; Karg, M.; Pastoriza-Santos, I.; Pérez-Juste, J.; Pacifico, J.; Hellweg, T.; Fernández-Barbero, A.; Liz-Marzán, L. M. Encapsulation and Growth of Gold Nanoparticles in Thermoresponsive Microgels. *Advanced Materials* **2008**, *20*, 1666–1670.
- [51] Contreras-Cáceres, R.; Pastoriza-Santos, I.; Alvarez-Puebla, R.; Pérez-Juste, J.; Fernández-Barbero, A.; Liz-Marzán, L. Growing Au/Ag Nanoparticles within Microgel Colloids for Improved Surface-Enhanced Raman Scattering Detection. *Chemistry – A European Journal* **2010**, *16*, 9462–9467.
- [52] Rodríguez-Fernández, J.; Pérez-Juste, J.; Mulvaney, P.; Liz-Marzán, L. M. Spatially-Directed Oxidation of Gold Nanoparticles by Au(III)-CTAB Complexes. *The Journal of Physical Chemistry B* **2005**, *109*, 14257–14261.
- [53] Kratz, K.; Hellweg, T.; Eimer, W. Structural changes in PNIPAM microgel particles as seen by SANS, DLS, and EM techniques. *Polymer* **2001**, *42*, 6631–6639.
- [54] Fernández-Barbero, A.; Fernández-Nieves, A.; Grillo, I.; López-Cabarcos, E. Structural modifications in the swelling of inhomogeneous microgels by light and neutron scattering. *Physical Review E* **2002**, *66*, 051803.
- [55] Wu, X.; Pelton, R. H.; Hamielec, A. E.; Woods, D. R.; McPhee, W. The kinetics of poly(N-isopropylacrylamide) microgel latex formation. *Colloid and Polymer Science* **1994**, *272*, 467–477.
- [56] Conley, G. M.; Nöjd, S.; Braibanti, M.; Schurtenberger, P.; Scheffold, F. Superresolution microscopy of the volume phase transition of pNIPAM microgels. *Colloids and Surfaces A: Physicochemical and Engineering Aspects* **2016**, *499*, 18–23.
- [57] Otto, P.; Bergmann, S.; Sandmeyer, A.; Dirksen, M.; Wrede, O.; Hellweg, T.; Huser, T. Resolving the internal morphology of core–shell microgels with super-resolution fluorescence microscopy. *Nanoscale Advances* **2020**, *2*, 323–331.
- [58] Lopez, C. G.; Richtering, W. Does Flory–Rehner theory quantitatively describe the swelling of thermoresponsive microgels? *Soft Matter* **2017**, *13*, 8271–8280.
- [59] Karg, M.; Pastoriza-Santos, I.; Rodríguez-González, B.; von Klitzing, R.; Wellert, S.; Hellweg, T. Temperature, pH, and Ionic Strength Induced Changes of the Swelling Behavior of PNIPAM-Poly(allylacetic acid) Copolymer Microgels. *Langmuir* **2008**, *24*, 6300–6306.

- [60] Pelton, R. Temperature-sensitive aqueous microgels. *Advances in Colloid and Interface Science* **2000**, *85*, 1–33.
- [61] Hertle, Y.; Zeiser, M.; Hasenöhrl, C.; Busch, P.; Hellweg, T. Responsive P(NIPAM-co-NtBAM) microgels: Flory-Rehner description of the swelling behaviour. *Colloid and Polymer Science* **2010**, *288*, 1047–1059.
- [62] Geisel, K.; Isa, L.; Richtering, W. The Compressibility of pH-Sensitive Microgels at the Oil–Water Interface: Higher Charge Leads to Less Repulsion. *Angewandte Chemie International Edition* **2014**, *53*, 4905–4909.
- [63] Harrer, J.; Rey, M.; Ciarella, S.; Löwen, H.; Janssen, L. M. C.; Vogel, N. Stimuli-Responsive Behavior of PNIPAM Microgels under Interfacial Confinement. *Langmuir* **2019**, *35*, 10512–10521.
- [64] Dusek, K., Ed. *Responsive Gels: Volume Transitions II*; Volume 110 of Advances in Polymer Science; 1 edn. Springer: Berlin Heidelberg, 1993.
- [65] Eichinger, B. E.; Flory, P. J. Thermodynamics of polymer solutions. Part 1.—Natural rubber and benzene. *Transactions of the Faraday Society* **1968**, *64*, 2035–2052.
- [66] Hirotsu, S.; Hirokawa, Y.; Tanaka, T. Volume-phase transitions of ionized N-isopropylacrylamide gels. *The Journal of Chemical Physics* **1987**, *87*, 1392–1395.
- [67] Karg, M.; Prévost, S.; Brandt, A.; Wallacher, D.; von Klitzing, R.; Hellweg, T. Poly-NIPAM Microgels with Different Cross-Linker Densities. Progress in Colloid and Polymer Science, 140. Springer International Publishing Switzerland, 2013; pp 63–76.
- [68] Varga, I.; Gilányi, T.; Mészáros, R.; Filipcsei, G.; Zrínyi, M. Effect of Cross-Link Density on the Internal Structure of Poly(N-isopropylacrylamide) Microgels. *The Journal of Physical Chemistry B* **2001**, *105*, 9071–9076.
- [69] Sato Matsuo, E.; Tanaka, T. Kinetics of discontinuous volume–phase transition of gels. *The Journal of Chemical Physics* **1988**, *89*, 1695–1703.
- [70] Peters, A.; Candau, S. J. Kinetics of swelling of polyacrylamide gels. *Macromolecules* **1986**, *19*, 1952–1955.
- [71] Yin, J.; Dupin, D.; Li, J.; Armes, S. P.; Liu, S. pH-Induced Deswelling Kinetics of Sterically Stabilized Poly(2-vinylpyridine) Microgels Probed by Stopped-Flow Light Scattering. *Langmuir* **2008**, *24*, 9334–9340.
- [72] Nikolov, S.; Fernandez-Nieves, A.; Alexeev, A. Mesoscale modeling of microgel mechanics and kinetics through the swelling transition. *Applied Mathematics and Mechanics* **2018**, *39*, 47–62.

-
- [73] Biot, M. A. General Theory of Three-Dimensional Consolidation. *Journal of Applied Physics* **1941**, *12*, 155–164.
- [74] Scherer, G. W. Measurement of permeability I. Theory. *Journal of Non-Crystalline Solids* **1989**, *113*, 107–118.
- [75] Scherer, G. W. Crack-tip stress in gels. *Journal of Non-Crystalline Solids* **1992**, *144*, 210–216.
- [76] Johnson, D. L. Elastodynamics of gels. *The Journal of Chemical Physics* **1982**, *77*, 1531–1539.
- [77] Hu, Y.; Chan, E. P.; Vlassak, J. J.; Suo, Z. Poroelastic relaxation indentation of thin layers of gels. *Journal of Applied Physics* **2011**, *110*, 086103.
- [78] Hong, W.; Zhao, X.; Zhou, J.; Suo, Z. A theory of coupled diffusion and large deformation in polymeric gels. *Journal of the Mechanics and Physics of Solids* **2008**, *56*, 1779–1793.
- [79] Bouklas, N.; Huang, R. Swelling kinetics of polymer gels: comparison of linear and nonlinear theories. *Soft Matter* **2012**, *8*, 8194–8203.
- [80] Murphy, S.; Jaber, S.; Ritchie, C.; Karg, M.; Mulvaney, P. Laser Flash Photolysis of Au-PNIPAM Core–Shell Nanoparticles: Dynamics of the Shell Response. *Langmuir* **2016**, *32*, 12497–12503.
- [81] Wang, J.; Gan, D.; Lyon, L. A.; El-Sayed, M. A. Temperature-Jump Investigations of the Kinetics of Hydrogel Nanoparticle Volume Phase Transitions. *Journal of the American Chemical Society* **2001**, *123*, 11284–11289.
- [82] Seiffert, S. Impact of Polymer Network Inhomogeneities on the Volume Phase Transition of Thermoresponsive Microgels. *Macromolecular Rapid Communications* **2012**, *33*, 1135–1142.
- [83] Wrede, O.; Reimann, Y.; Lülldorf, S.; Emmrich, D.; Schneider, K.; Schmid, A. J.; Zauser, D.; Hannappel, Y.; Beyer, A.; Schweins, R.; Gölzhäuser, A.; Hellweg, T.; Sottmann, T. Volume phase transition kinetics of smart N-n-propylacrylamide microgels studied by time-resolved pressure jump small angle neutron scattering. *Scientific Reports* **2018**, *8*, 13781.
- [84] Nothdurft, K.; Müller, D. H.; Mürtz, S. D.; Meyer, A. A.; Guerzoni, L. P. B.; Jans, A.; Kühne, A. J. C.; De Laporte, L.; Brands, T.; Bardow, A.; Richtering, W. Is the Microgel Collapse a Two-Step Process? Exploiting Cononsolvency to Probe the Collapse Dynamics of Poly-N-isopropylacrylamide (pNIPAM). *The Journal of Physical Chemistry B* **2021**, *125*, 1503–1512.
- [85] Keidel, R.; Ghavami, A.; Lugo, D. M.; Lotze, G.; Virtanen, O.; Beumers, P.; Pedersen, J. S.; Bardow, A.; Winkler, R. G.; Richtering, W. Time-resolved

- structural evolution during the collapse of responsive hydrogels: The microgel-to-particle transition. *Science Advances* **2018**, *4*, eaao7086.
- [86] Czerlinski, G.; Eigen, M. Eine Temperatursprungmethode zur Untersuchung chemischer Relaxation. *Zeitschrift für Elektrochemie, Berichte der Bunsengesellschaft für physikalische Chemie* **1959**, *63*, 652–661.
- [87] Borsali, R.; Pecora, R. *Soft-Matter Characterization*, 2008th ed.; Springer: New York, 2008.
- [88] Zemb, T.; Lindner, P. *Neutron, X-rays and Light. Scattering Methods Applied to Soft Condensed Matter*; Elsevier Science: North-Holland Delta Series, 2002.
- [89] Stetefeld, J.; McKenna, S. A.; Patel, T. R. Dynamic light scattering: a practical guide and applications in biomedical sciences. *Biophysical Reviews* **2016**, *8*, 409–427.
- [90] Siegert, A. J. F. *On the Fluctuations in Signals Returned by Many Independently Moving Scatterers*; Radiation Laboratory, Massachusetts Institute of Technology: 465. MIT, Cambridge, 1943.
- [91] Frisken, B. J. Revisiting the method of cumulants for the analysis of dynamic light-scattering data. *Applied Optics* **2001**, *40*, 4087–4091.
- [92] Provencher, S. W. A constrained regularization method for inverting data represented by linear algebraic or integral equations. *Computer Physics Communications* **1982**, *27*, 213–227.
- [93] Provencher, S. W. CONTIN: A general purpose constrained regularization program for inverting noisy linear algebraic and integral equations. *Computer Physics Communications* **1982**, *27*, 229–242.
- [94] Pedersen, J. S. In *Modern Aspects of Small-Angle Scattering*; Brumberger, H., Ed.; Springer Netherlands: Dordrecht, 1995; pp 57–91.
- [95] Schnablegger, H.; Singh, Y. *The SAXS Guide. Getting acquainted with the principles*; Anton Paar GmbH: Austria, 2017.
- [96] Instrument layout - ILL Neutrons for Society. <https://www.ill.eu/fr/users/instruments/instruments-list/d11/description/instrument-layout>, Accessed: 2021-08-12.
- [97] Pedersen, J. S. Analysis of small-angle scattering data from colloids and polymer solutions: modeling and least-squares fitting. *Advances in Colloid and Interface Science* **1997**, *70*, 171–210.
- [98] Hecht, A. M.; Duplessix, R.; Geissler, E. Structural inhomogeneities in the range 2.5-2500 .ANG. in polyacrylamide gels. *Macromolecules* **1985**, *18*, 2167–2173.

-
- [99] Shibayama, M.; Tanaka, T.; Han, C. C. Small angle neutron scattering study on poly(N-isopropyl acrylamide) gels near their volume-phase transition temperature. *The Journal of Chemical Physics* **1992**, *97*, 6829–6841.
- [100] Li, F.; Josephson, D. P.; Stein, A. Colloidal Assembly: The Road from Particles to Colloidal Molecules and Crystals. *Angewandte Chemie International Edition* **2011**, *50*, 360–388.
- [101] von Freymann, G.; Kitaev, V.; Lotsch, B. V.; Ozin, G. A. Bottom-up assembly of photonic crystals. *Chemical Society Reviews* **2013**, *42*, 2528–2554.
- [102] Derjaguin, B.; Landau, L. Theory of the stability of strongly charged lyophobic sols and of the adhesion of strongly charged particles in solutions of electrolytes. *Progress in Surface Science* **1993**, *43*, 30–59.
- [103] Verwey, E. W.; Overbeek, J. T. G.; with the collaboration of van Ness, K., *Theory of the stability of lyophobic colloids. The interaction of particles having an electric double layer.*; Elsevier: New York-Amsterdam, 1948; 216 pp.
- [104] Butt, H.-J.; Graf, K.; Kappl, M. *Physics and Chemistry of Interfaces*; Wiley-VCH Verlag GmbH & Co. KGaA: Weinheim, 2003.
- [105] Li, Q.; Jonas, U.; Zhao, X. S.; Kappl, M. The forces at work in colloidal self-assembly: a review on fundamental interactions between colloidal particles. *Asia-Pacific Journal of Chemical Engineering* **2008**, *3*, 255–268.
- [106] Vogel, N.; Weiss, C. K.; Landfester, K. From soft to hard: the generation of functional and complex colloidal monolayers for nanolithography. *Soft Matter* **2012**, *8*, 4044–4061.
- [107] Pieranski, P. Two-Dimensional Interfacial Colloidal Crystals. *Physical Review Letters* **1980**, *45*, 569–572.
- [108] Kralchevsky, P. A.; Nagayama, K. Capillary forces between colloidal particles. *Langmuir* **1994**, *10*, 23–36.
- [109] Kralchevsky, P. A.; Nagayama, K. Capillary interactions between particles bound to interfaces, liquid films and biomembranes. *Advances in Colloid and Interface Science* **2000**, *85*, 145–192.
- [110] Fulda, K.-U.; Tieke, B. Langmuir films of monodisperse 0.5 μm spherical polymer particles with a hydrophobic core and a hydrophilic shell. *Advanced Materials* **1994**, *6*, 288–290.
- [111] Park, J. Y.; Advincula, R. C. Nanostructuring polymers, colloids, and nanomaterials at the air–water interface through Langmuir and Langmuir–Blodgett techniques. *Soft Matter* **2011**, *7*, 9829–9843.

- [112] Rauh, A.; Rey, M.; Barbera, L.; Zanini, M.; Karg, M.; Isa, L. Compression of hard core–soft shell nanoparticles at liquid–liquid interfaces: influence of the shell thickness. *Soft Matter* **2016**, *13*, 158–169.
- [113] Smoluchowski, M. v. Zur kinetischen Theorie der Brownschen Molekularbewegung und der Suspensionen. *Annalen der Physik* **1906**, *326*, 756–780.
- [114] Tsuji, S.; Kawaguchi, H. Self-Assembly of Poly(N-isopropylacrylamide)-Carrying Microspheres into Two-Dimensional Colloidal Arrays. *Langmuir* **2005**, *21*, 2434–2437.
- [115] Denkov, N.; Velev, O.; Kralchevski, P.; Ivanov, I.; Yoshimura, H.; Nagayama, K. Mechanism of formation of two-dimensional crystals from latex particles on substrates. *Langmuir* **1992**, *8*, 3183–3190.
- [116] Dimitrov, A. S.; Nagayama, K. Continuous Convective Assembling of Fine Particles into Two-Dimensional Arrays on Solid Surfaces. *Langmuir* **1996**, *12*, 1303–1311.
- [117] Malaquin, L.; Kraus, T.; Schmid, H.; Delamarche, E.; Wolf, H. Controlled Particle Placement through Convective and Capillary Assembly. *Langmuir* **2007**, *23*, 11513–11521.
- [118] Toolan, D. T. W.; Fujii, S.; Ebbens, S. J.; Nakamura, Y.; Howse, J. R. On the mechanisms of colloidal self-assembly during spin-coating. *Soft Matter* **2014**, *10*, 8804–8812.
- [119] Zhang, X.; Zhang, J.; Zhu, D.; Li, X.; Zhang, X.; Wang, T.; Yang, B. A Universal Approach To Fabricate Ordered Colloidal Crystals Arrays Based on Electrostatic Self-Assembly. *Langmuir* **2010**, *26*, 17936–17942.
- [120] Kallepalli, L. N. D.; Constantinescu, C.; Delaporte, P.; Utéza, O.; Grojo, D. Ultra-high ordered, centimeter scale preparation of microsphere Langmuir films. *Journal of Colloid and Interface Science* **2015**, *446*, 237–243.
- [121] Vogel, N.; Fernández-López, C.; Pérez-Juste, J.; Liz-Marzán, L. M.; Landfester, K.; Weiss, C. K. Ordered Arrays of Gold Nanostructures from Interfacially Assembled Au@PNIPAM Hybrid Nanoparticles. *Langmuir* **2012**, *28*, 8985–8993.
- [122] Lenzmann, F.; Li, K.; Kitai, A. H.; Stover, H. D. H. Thin-film micropatterning using polymer microspheres. *Chemistry of Materials* **1994**, *6*, 156–159.
- [123] Weekes, S. M.; Ogrin, F. Y.; Murray, W. A.; Keatley, P. S. Macroscopic Arrays of Magnetic Nanostructures from Self-Assembled Nanosphere Templates. *Langmuir* **2007**, *23*, 1057–1060.
- [124] Petty, M. C. *Langmuir-Blodgett Films: An Introduction*; Cambridge University Press: Cambridge, 1996.

-
- [125] Bardosova, M.; Pemble, M. E.; Povey, I. M.; Tredgold, R. H. The Langmuir-Blodgett Approach to Making Colloidal Photonic Crystals from Silica Spheres. *Advanced Materials* **2010**, *22*, 3104–3124.
- [126] Bertonecello, P.; Notargiacomo, A.; Nicolini, C. Langmuir-Schaefer Films of Nafion with Incorporated TiO₂ Nanoparticles. *Langmuir* **2005**, *21*, 172–177.
- [127] Facci, P.; Erokhin, V.; Nicolini, C. Nanogravimetric gauge for surface density measurements and deposition analysis of langmuir-blodgett films. *Thin Solid Films* **1993**, *230*, 86–89.
- [128] Retsch, M.; Zhou, Z.; Rivera, S.; Kappl, M.; Zhao, X. S.; Jonas, U.; Li, Q. Fabrication of Large-Area, Transferable Colloidal Monolayers Utilizing Self-Assembly at the Air/Water Interface. *Macromolecular Chemistry and Physics* **2009**, *210*, 230–241.
- [129] Vogel, N.; Goerres, S.; Landfester, K.; Weiss, C. K. A Convenient Method to Produce Close- and Non-close-Packed Monolayers using Direct Assembly at the Air–Water Interface and Subsequent Plasma-Induced Size Reduction. *Macromolecular Chemistry and Physics* **2011**, *212*, 1719–1734.
- [130] Zhang, J.-T.; Wang, L.; Lamont, D. N.; Velankar, S. S.; Asher, S. A. Fabrication of Large-Area Two-Dimensional Colloidal Crystals. *Angewandte Chemie International Edition* **2012**, *51*, 6117–6120.
- [131] Volk, K.; Fitzgerald, J. P. S.; Ruckdeschel, P.; Retsch, M.; König, T. A. F.; Karg, M. Reversible Tuning of Visible Wavelength Surface Lattice Resonances in Self-Assembled Hybrid Monolayers. *Advanced Optical Materials* **2017**, *5*, 1600971.
- [132] Maier, S. A. *Plasmonics: Fundamentals and Applications*; Springer US, 2007.
- [133] Drude, P. Zur Elektronentheorie der Metalle. *Annalen der Physik* **1900**, *306*, 566–613.
- [134] Johnson, P. B.; Christy, R. W. Optical Constants of the Noble Metals. *Physical Review B* **1972**, *6*, 4370–4379.
- [135] Ph. D. Haynes, W. M.; Ph. D. Lide, D. R.; Ph. D. Bruno, T. J. *CRC Handbook of Chemistry and Physics*, 95th ed.; CRC Press Taylor & Francis Group: Boca Raton, 2014.
- [136] Rodríguez-González, B.; Burrows, A.; Watanabe, M.; Kiely, C. J.; Marzán, L. M. L. Multishell bimetallic AuAg nanoparticles: synthesis, structure and optical properties. *Journal of Materials Chemistry* **2005**, *15*, 1755.
- [137] Kelly, K. L.; Coronado, E.; Zhao, L. L.; Schatz, G. C. The Optical Properties of Metal Nanoparticles: The Influence of Size, Shape and Dielectric Environment. *The Journal of Physical Chemistry B* **2003**, *107*, 668–677.

- [138] Mock, J. J.; Barbic, M.; Smith, D. R.; Schultz, D. A.; Schultz, S. Shape effects in plasmon resonance of individual colloidal silver nanoparticles. *The Journal of Chemical Physics* **2002**, *116*, 6755–6759.
- [139] Nehl, C. L.; Hafner, J. H. Shape-dependent plasmon resonances of gold nanoparticles. *Journal of Materials Chemistry* **2008**, *18*, 2415.
- [140] Mulvaney, P. Surface Plasmon Spectroscopy of Nanosized Metal Particles. *Langmuir* **1996**, *12*, 788–800.
- [141] Bohren, C. F.; Huffman, D. R. *Absorption and Scattering of Light by Small Particles*; John Wiley & Sons: New York, NY, 1983.
- [142] Mie, G. Beiträge zur Optik trüber Medien, speziell kolloidaler Metallösungen. *Annalen der Physik* **1908**, *330*, 377–445.
- [143] Nordlander, P.; Oubre, C.; Prodan, E.; Li, K.; Stockman, M. I. Plasmon Hybridization in Nanoparticle Dimers. *Nano Letters* **2004**, *4*, 899–903.
- [144] Prodan, E.; Radloff, C.; Halas, N. J.; Nordlander, P. A Hybridization Model for the Plasmon Response of Complex Nanostructures. *Science* **2003**, *302*, 419–422.
- [145] Pinchuk, A. O.; Schatz, G. C. Nanoparticle optical properties: Far- and near-field electrodynamic coupling in a chain of silver spherical nanoparticles. *Materials Science and Engineering: B* **2008**, *149*, 251–258.
- [146] Jain, P. K.; Huang, W.; El-Sayed, M. A. On the Universal Scaling Behavior of the Distance Decay of Plasmon Coupling in Metal Nanoparticle Pairs: A Plasmon Ruler Equation. *Nano Letters* **2007**, *7*, 2080–2088.
- [147] Jain, P. K.; El-Sayed, M. A. Plasmonic coupling in noble metal nanostructures. *Chemical Physics Letters* **2010**, *487*, 153–164.
- [148] Ghosh, S. K.; Pal, T. Interparticle Coupling Effect on the Surface Plasmon Resonance of Gold Nanoparticles: From Theory to Applications. *Chemical Reviews* **2007**, *107*, 4797–4862.
- [149] Ruda, H. E.; Matsuura, N. In *Springer Handbook of Electronic and Photonic Materials*; Kasap, S., Capper, P., Eds.; Springer Handbooks; Springer International Publishing: Cham, 2017; pp 1–1.
- [150] Rodriguez, S. R. K.; Abass, A.; Maes, B.; Janssen, O. T. A.; Vecchi, G.; Rivas, J. G. Coupling Bright and Dark Plasmonic Lattice Resonances. *Physical Review X* **2011**, *1*, 021019.
- [151] Auguie, B.; Barnes, W. L. Collective Resonances in Gold Nanoparticle Arrays. *Physical Review Letters* **2008**, *101*, 143902.

-
- [152] Wang, W.; Watkins, N.; Yang, A.; Schaller, R. D.; Schatz, G. C.; Odom, T. W. Ultrafast Dynamics of Lattice Plasmon Lasers. *The Journal of Physical Chemistry Letters* **2019**, *10*, 3301–3306.
- [153] West, P. R.; Ishii, S.; Naik, G. V.; Emani, N. K.; Shalaev, V. M.; Boltasseva, A. Searching for better plasmonic materials. *Laser & Photonics Reviews* **2010**, *4*, 795–808.
- [154] Rodriguez, S. R. K.; Schaafsma, M. C.; Berrier, A.; Gómez Rivas, J. Collective resonances in plasmonic crystals: Size matters. *Physica B: Condensed Matter* **2012**, *407*, 4081–4085.
- [155] Zou, S.; Janel, N.; Schatz, G. C. Silver nanoparticle array structures that produce remarkably narrow plasmon lineshapes. *The Journal of Chemical Physics* **2004**, *120*, 10871–10875.
- [156] Grepstad, J. O.; Greve, M. M.; Holst, B.; Johansen, I.-R.; Solgaard, O.; Sudbø, A. Finite-size limitations on Quality Factor of guided resonance modes in 2D Photonic Crystals. *Optics Express* **2013**, *21*, 23640–23654.
- [157] Auguié, B.; Barnes, W. L. Diffractive coupling in gold nanoparticle arrays and the effect of disorder. *Optics Letters* **2009**, *34*, 401–403.
- [158] Humphrey, A. D.; Barnes, W. L. Plasmonic surface lattice resonances on arrays of different lattice symmetry. *Physical Review B* **2014**, *90*, 075404.
- [159] Taflove, A.; Hagness, S. C. *Computational Electrodynamics: The Finite-Difference Time-Domain Method*, 3rd ed.; ARTECH HOUSE INC: Boston, 2005.
- [160] DeVoe, H. Optical Properties of Molecular Aggregates. I. Classical Model of Electronic Absorption and Refraction. *The Journal of Chemical Physics* **1964**, *41*, 393–400.
- [161] DeVoe, H. Optical Properties of Molecular Aggregates. II. Classical Theory of the Refraction, Absorption, and Optical Activity of Solutions and Crystals. *The Journal of Chemical Physics* **1965**, *43*, 3199–3208.
- [162] Purcell, E. M.; Pennypacker, C. R. Scattering and Absorption of Light by Nonspherical Dielectric Grains. *The Astrophysical Journal* **1973**, *186*, 705–714.
- [163] Laor, U.; Schatz, G. C. The role of surface roughness in surface enhanced raman spectroscopy (SERS): the importance of multiple plasmon resonances. *Chemical Physics Letters* **1981**, *82*, 566–570.
- [164] Yang, W.; Schatz, G. C.; Van Duyne, R. P. Discrete dipole approximation for calculating extinction and Raman intensities for small particles with arbitrary shapes. *The Journal of Chemical Physics* **1995**, *103*, 869–875.

- [165] Hafner, C. *The Generalized Multipole Technique for Computational Electromagnetics*, illustrated edition ed.; ARTECH HOUSE INC: Boston, 1990.
- [166] Moreno, E.; Erni, D.; Hafner, C.; Vahldieck, R. Multiple multipole method with automatic multipole setting applied to the simulation of surface plasmons in metallic nanostructures. *Journal of the Optical Society of America A* **2002**, *19*, 101–111.
- [167] Yee, K. Numerical solution of initial boundary value problems involving maxwell's equations in isotropic media. *IEEE Transactions on Antennas and Propagation* **1966**, *14*, 302–307.
- [168] Berenger, J.-P. *Perfectly Matched Layer (PML) for Computational Electromagnetics*; Morgan & Claypool, 2007.
- [169] Nanophotonic FDTD Simulation Software - Lumerical FDTD. <https://www-origin.lumerical.com>, Accessed: 2021-06-02.
- [170] Kashiwa, T.; Fukai, I. A treatment by the FD-TD method of the dispersive characteristics associated with electronic polarization. *Microwave and Optical Technology Letters* **1990**, *3*, 203–205.
- [171] Schneider, C. A.; Rasband, W. S.; Eliceiri, K. W. NIH Image to ImageJ: 25 years of image analysis. *Nature Methods* **2012**, *9*, 671–675.
- [172] Zhu, J.; Balieu, R.; Lu, X.; Kringos, N. Microstructure evaluation of polymer-modified bitumen by image analysis using two-dimensional fast Fourier transform. *Materials & Design* **2018**, *137*, 164–175.
- [173] Ziman, J. M.; Ziman, P. J. M.; Ziman, *Models of Disorder: The Theoretical Physics of Homogeneously Disordered Systems*; Cambridge University Press, Cambridge, 1979.
- [174] Leach, A. R.; AR, L. *Molecular Modelling: Principles and Applications*; Pearson Education, 2001.
- [175] Scheeler, S. P.; Mühlig, S.; Rockstuhl, C.; Hasan, S. B.; Ullrich, S.; Neubrech, F.; Kudera, S.; Pacholski, C. Plasmon Coupling in Self-Assembled Gold Nanoparticle-Based Honeycomb Islands. *The Journal of Physical Chemistry C* **2013**, *117*, 18634–18641.
- [176] Liao, Y. Practical Electron Microscopy and Database - An Online Book. <https://www.globalsino.com/EM/page3097.html>, 2006; Accessed: 2021-04-02.
- [177] Hillebrand, R.; Müller, F.; Schwirn, K.; Lee, W.; Steinhart, M. Quantitative Analysis of the Grain Morphology in Self-Assembled Hexagonal Lattices. *ACS Nano* **2008**, *2*, 913–920.

-
- [178] Mátéfi-Tempfli, S.; Mátéfi-Tempfli, M.; Piraux, L. Characterization of nanopores ordering in anodic alumina. *Thin Solid Films* **2008**, *516*, 3735–3740.
- [179] Plamper, F. A.; Richtering, W. Functional Microgels and Microgel Systems. *Accounts of Chemical Research* **2017**, *50*, 131–140.
- [180] Senff, H.; Richtering, W. Temperature sensitive microgel suspensions: Colloidal phase behavior and rheology of soft spheres. *The Journal of Chemical Physics* **1999**, *111*, 1705–1711.
- [181] Bachman, H.; Brown, A. C.; Clarke, K. C.; Dhada, K. S.; Douglas, A.; Hansen, C. E.; Herman, E.; Hyatt, J. S.; Kodlekere, P.; Meng, Z.; Saxena, S.; Jr, M. W. S.; Welsch, N.; Lyon, L. A. Ultrasoft, highly deformable microgels. *Soft Matter* **2015**, *11*, 2018–2028.
- [182] Bergman, M. J.; Gnan, N.; Obiols-Rabasa, M.; Meijer, J.-M.; Rovigatti, L.; Zaccarelli, E.; Schurtenberger, P. A new look at effective interactions between microgel particles. *Nature Communications* **2018**, *9*, 5039.
- [183] Kureha, T.; Minato, H.; Suzuki, D.; Urayama, K.; Shibayama, M. Concentration dependence of the dynamics of microgel suspensions investigated by dynamic light scattering. *Soft Matter* **2019**, *15*, 5390–5399.
- [184] Bochenek, S.; Scotti, A.; Richtering, W. Temperature-sensitive soft microgels at interfaces: air–water versus oil–water. *Soft Matter* **2021**, *17*, 976–988.
- [185] Scotti, A. Characterization of the volume fraction of soft deformable microgels by means of small-angle neutron scattering with contrast variation. *Soft Matter* **2021**, *17*, 5548–5559.
- [186] Gelissen, A. P. H.; Oppermann, A.; Caumanns, T.; Hebbeker, P.; Turnhoff, S. K.; Tiwari, R.; Eisold, S.; Simon, U.; Lu, Y.; Mayer, J.; Richtering, W.; Walther, A.; Wöll, D. 3D Structures of Responsive Nanocompartmentalized Microgels. *Nano Letters* **2016**, *16*, 7295–7301.
- [187] Otto, P.; Bergmann, S.; Sandmeyer, A.; Dirksen, M.; Wrede, O.; Hellweg, T.; Huser, T. Resolving the internal morphology of core–shell microgels with super-resolution fluorescence microscopy. *Nanoscale Advances* **2020**, *2*, 323–331.
- [188] Rovigatti, L.; Gnan, N.; Tavagnacco, L.; Moreno, A. J.; Zaccarelli, E. Numerical modelling of non-ionic microgels: an overview. *Soft Matter* **2019**, *15*, 1108–1119.
- [189] Ninarello, A.; Crassous, J. J.; Paloli, D.; Camerin, F.; Gnan, N.; Rovigatti, L.; Schurtenberger, P.; Zaccarelli, E. Modeling Microgels with a Controlled Structure across the Volume Phase Transition. *Macromolecules* **2019**, *52*, 7584–7592.
- [190] Quesada-Pérez, M.; Maroto-Centeno, J. A.; Forcada, J.; Hidalgo-Alvarez, R. Gel swelling theories: the classical formalism and recent approaches. *Soft Matter* **2011**, *7*, 10536–10547.

- [191] Crassous, J. J.; Wittemann, A.; Siebenbürger, M.; Schrunner, M.; Drechsler, M.; Ballauff, M. Direct imaging of temperature-sensitive core-shell latexes by cryogenic transmission electron microscopy. *Colloid and Polymer Science* **2008**, *286*, 805–812.
- [192] Sbeih, S.; Mohanty, P. S.; Morrow, M. R.; Yethiraj, A. Structural parameters of soft PNIPAM microgel particles as a function of crosslink density. *Journal of Colloid and Interface Science* **2019**, *552*, 781–793.
- [193] Arleth, L.; Xia, X.; Hjelm, R. P.; Wu, J.; Hu, Z. Volume transition and internal structures of small poly(N-isopropylacrylamide) microgels. *Journal of Polymer Science Part B: Polymer Physics* **2005**, *43*, 849–860.
- [194] Saunders, B. R. On the Structure of Poly(N-isopropylacrylamide) Microgel Particles. *Langmuir* **2004**, *20*, 3925–3932.
- [195] Schmidt, S.; Motschmann, H.; Hellweg, T.; von Klitzing, R. Thermoresponsive surfaces by spin-coating of PNIPAM-co-PAA microgels: A combined AFM and ellipsometry study. *Polymer* **2008**, *49*, 749–756.
- [196] Gawlitza, K.; Turner, S. T.; Polzer, F.; Wellert, S.; Karg, M.; Mulvaney, P.; von Klitzing, R. Interaction of gold nanoparticles with thermoresponsive microgels: influence of the cross-linker density on optical properties. *Physical Chemistry Chemical Physics* **2013**, *15*, 15623.
- [197] Wedel, B.; Hertle, Y.; Wrede, O.; Bookhold, J.; Hellweg, T. Smart Homopolymer Microgels: Influence of the Monomer Structure on the Particle Properties. *Polymers* **2016**, *8*, 162.
- [198] Tagliacruzchi, M.; Blaber, M. G.; Schatz, G. C.; Weiss, E. A.; Szleifer, I. Optical Properties of Responsive Hybrid Au@Polymer Nanoparticles. *ACS Nano* **2012**, *6*, 8397–8406.
- [199] Contreras-Cáceres, R.; Pacifico, J.; Pastoriza-Santos, I.; Pérez-Juste, J.; Fernández-Barbero, A.; Liz-Marzán, L. M. Au@pNIPAM Thermosensitive Nanostructures: Control over Shell Cross-linking, Overall Dimensions, and Core Growth. *Advanced Functional Materials* **2009**, *19*, 3070–3076.
- [200] Rodríguez-Fernández, J.; Fedoruk, M.; Hrelescu, C.; Lutich, A. A.; Feldmann, J. Triggering the volume phase transition of core-shell Au nanorod-microgel nanocomposites with light. *Nanotechnology* **2011**, *22*, 245708.
- [201] Guarrotxena, N.; Quijada-Garrido, I. Optical and Swelling Stimuli-Response of Functional Hybrid Nanogels: Feasible Route to Achieve Tunable Smart Core@Shell Plasmonic@Polymer Nanomaterials. *Chemistry of Materials* **2016**, *28*, 1402–1412.
- [202] Rauh, A.; Carl, N.; Schweins, R.; Karg, M. Role of Absorbing Nanocrystal Cores in Soft Photonic Crystals: A Spectroscopy and SANS Study. *Langmuir* **2018**, *34*, 854–867.

-
- [203] Kohlbrecher, J. *SASfit: A Program for Fitting Simple Structural Models to Small Angle Scattering Data*; Paul Scherrer Institut, Laboratory for Neutron Scattering, Villigen, Switzerland, 2008.
- [204] Zhang, Q.; Weber, C.; Schubert, U. S.; Hoogenboom, R. Thermoresponsive polymers with lower critical solution temperature: from fundamental aspects and measuring techniques to recommended turbidimetry conditions. *Materials Horizons* **2017**, *4*, 109–116.
- [205] Halperin, A.; Kröger, M.; Winnik, F. M. Poly(N-isopropylacrylamide) Phase Diagrams: Fifty Years of Research. *Angewandte Chemie International Edition* **2015**, *54*, 15342–15367.
- [206] Månsson, L. K.; Peng, F.; Crassous, J. J.; Schurtenberger, P. A microgel-Pickering emulsion route to colloidal molecules with temperature-tunable interaction sites. *Soft Matter* **2020**, *16*, 1908–1921.
- [207] van der Hulst, H. *Light Scattering by Small Particles*; Dover Publications, Inc., 1981.
- [208] Kerker, M. *The Scattering of Light and Other Electromagnetic Radiation*; Academic Press: New York, 1969.
- [209] Eitel, K.; Bryant, G.; Schöpe, H. J. A Hitchhiker’s Guide to Particle Sizing Techniques. *Langmuir* **2020**, *36*, 10307–10320.
- [210] Rauh, A.; Rey, M.; Barbera, L.; Zanini, M.; Karg, M.; Isa, L. Compression of hard core–soft shell nanoparticles at liquid–liquid interfaces: influence of the shell thickness. *Soft Matter* **2017**, *13*, 158–169.
- [211] Jain, P. K.; Lee, K. S.; El-Sayed, I. H.; El-Sayed, M. A. Calculated Absorption and Scattering Properties of Gold Nanoparticles of Different Size, Shape, and Composition: Applications in Biological Imaging and Biomedicine. *The Journal of Physical Chemistry B* **2006**, *110*, 7238–7248.
- [212] Stieger, M.; Pedersen, J. S.; Lindner, P.; Richtering, W. Are Thermoresponsive Microgels Model Systems for Concentrated Colloidal Suspensions? A Rheology and Small-Angle Neutron Scattering Study. *Langmuir* **2004**, *20*, 7283–7292.
- [213] Garnett, J. C. M.; Larmor, J. XII. Colours in metal glasses and in metallic films. *Philosophical Transactions of the Royal Society of London. Series A, Containing Papers of a Mathematical or Physical Character* **1904**, *203*, 385–420.
- [214] Born, M.; Wolf, E. *Principles of Optics: Electromagnetic Theory of Propagation, Interference and Diffraction of Light*; Elsevier, 2013.
- [215] Bergmann, S.; Wrede, O.; Huser, T.; Hellweg, T. Super-resolution optical microscopy resolves network morphology of smart colloidal microgels. *Physical Chemistry Chemical Physics* **2018**, *20*, 5074–5083.

- [216] Wrede, O.; Reimann, Y.; Lülldorf, S.; Emmrich, D.; Schneider, K.; Schmid, A. J.; Zauser, D.; Hannappel, Y.; Beyer, A.; Schweins, R.; Gölzhäuser, A.; Hellweg, T.; Sottmann, T. Volume phase transition kinetics of smart N-n-propylacrylamide microgels studied by time-resolved pressure jump small angle neutron scattering. *Scientific Reports* **2018**, *8*, 13781.
- [217] Rudyak, V. Y.; Kozhunova, E. Y.; Chertovich, A. V. Towards the realistic computer model of precipitation polymerization microgels. *Scientific Reports* **2019**, *9*, 13052.
- [218] Scotti, A.; Bochenek, S.; Brugnoli, M.; Fernandez-Rodriguez, M. A.; Schulte, M. F.; Houston, J. E.; Gelissen, A. P. H.; Potemkin, I. I.; Isa, L.; Richtering, W. Exploring the colloid-to-polymer transition for ultra-low crosslinked microgels from three to two dimensions. *Nature Communications* **2019**, *10*, 1418.
- [219] Dulle, M.; Jaber, S.; Rosenfeldt, S.; Radulescu, A.; Förster, S.; Mulvaney, P.; Karg, M. Plasmonic gold–poly(N-isopropylacrylamide) core–shell colloids with homogeneous density profiles: a small angle scattering study. *Physical Chemistry Chemical Physics* **2014**, *17*, 1354–1367.
- [220] Hale, G. M.; Querry, M. R. Optical Constants of Water in the 200-nm to 200- μ m Wavelength Region. *Applied Optics* **1973**, *12*, 555.
- [221] Small, A.; Hong, S.; Pine, D. Scattering properties of core–shell particles in plastic matrices. *Journal of Polymer Science Part B: Polymer Physics* **2005**, *43*, 3534–3548.
- [222] Heller, W.; Bhatnagar, H. L.; Nakagaki, M. Theoretical Investigations on the Light Scattering of Spheres. XIII. The "Wavelength Exponent" of Differential Turbidity Spectra. *The Journal of Chemical Physics* **1962**, *36*, 1163–1170.
- [223] Heller, W. Theoretical Investigations on the Light Scattering of Spheres. XV. The Wavelength Exponents at Small α Values. *The Journal of Chemical Physics* **1964**, *40*, 2700–2705.
- [224] NCNR. <https://www.ncnr.nist.gov/resources/activation/>, Accessed: 2021-02-10.
- [225] Dingenouts, N.; Seelenmeyer, S.; Deike, I.; Rosenfeldt, S.; Ballauff, M.; Lindner, P.; Narayanan, T. Analysis of thermosensitive core–shell colloids by small-angle neutron scattering including contrast variation. *Physical Chemistry Chemical Physics* **2001**, *3*, 1169–1174.
- [226] Ebeling, B.; Vana, P. RAFT-Polymers with Single and Multiple Trithiocarbonate Groups as Uniform Gold-Nanoparticle Coatings. *Macromolecules* **2013**, *46*, 4862–4871.
- [227] Daoud, M.; Cotton, J. P.; Farnoux, B.; Jannink, G.; Sarma, G.; Benoit, H.; Duplessix, C.; Picot, C.; de Gennes, P. G. Solutions of Flexible Polymers. Neutron Experiments and Interpretation. *Macromolecules* **1975**, *8*, 804–818.

- [228] Peña-Rodríguez, O.; González Pérez, P. P.; Pal, U. MieLab: A Software Tool to Perform Calculations on the Scattering of Electromagnetic Waves by Multilayered Spheres. *International Journal of Spectroscopy* **2011**, *2011*, 583743.
- [229] Kasani, S.; Curtin, K.; Wu, N. A review of 2D and 3D plasmonic nanostructure array patterns: fabrication, light management and sensing applications. *Nanophotonics* **2019**, *8*, 2065–2089.
- [230] Wang, W.; Ramezani, M.; Väkeväinen, A. I.; Törmä, P.; Rivas, J. G.; Odom, T. W. The rich photonic world of plasmonic nanoparticle arrays. *Materials Today* **2018**, *21*, 303–314.
- [231] Fitzgerald, J. P. S.; Karg, M. Plasmon resonance coupling phenomena in self-assembled colloidal monolayers. *Physica Status Solidi A* **2017**, *214*, 1600947.
- [232] Funston, A. M.; Gómez, D. E.; Karg, M.; Vernon, K. C.; Davis, T. J.; Mulvaney, P. Aligned Linear Arrays of Crystalline Nanoparticles. *The Journal of Physical Chemistry Letters* **2013**, *4*, 1994–2001.
- [233] Mayer, M.; Potapov, P. L.; Pohl, D.; Steiner, A. M.; Schultz, J.; Rellinghaus, B.; Lubk, A.; König, T. A. F.; Fery, A. Direct Observation of Plasmon Band Formation and Delocalization in Quasi-Infinite Nanoparticle Chains. *Nano Letters* **2019**, *19*, 3854–3862.
- [234] Maier, S. A.; Kik, P. G.; Atwater, H. A.; Meltzer, S.; Harel, E.; Koel, B. E.; Requicha, A. A. Local detection of electromagnetic energy transport below the diffraction limit in metal nanoparticle plasmon waveguides. *Nature Materials* **2003**, *2*, 229–232.
- [235] Bastús, N. G.; Merkoçi, F.; Piella, J.; Puentes, V. Synthesis of Highly Monodisperse Citrate-Stabilized Silver Nanoparticles of up to 200 nm: Kinetic Control and Catalytic Properties. *Chemistry of Materials* **2014**, *26*, 2836–2846.
- [236] Giannini, V.; Fernández-Domínguez, A. I.; Heck, S. C.; Maier, S. A. Plasmonic Nanoantennas: Fundamentals and Their Use in Controlling the Radiative Properties of Nanoemitters. *Chemical Reviews* **2011**, *111*, 3888–3912.
- [237] Atwater, H. A.; Polman, A. Erratum: Plasmonics for improved photovoltaic devices. *Nature Materials* **2010**, *9*, 865–865.
- [238] Bastús, N. G.; Comenge, J.; Puentes, V. Kinetically Controlled Seeded Growth Synthesis of Citrate-Stabilized Gold Nanoparticles of up to 200 nm: Size Focusing versus Ostwald Ripening. *Langmuir* **2011**, *27*, 11098–11105.
- [239] Ross, M. B.; Mirkin, C. A.; Schatz, G. C. Optical Properties of One-, Two-, and Three-Dimensional Arrays of Plasmonic Nanostructures. *The Journal of Physical Chemistry C* **2016**, *120*, 816–830.

- [240] Auguie, B.; Bendaña, X. M.; Barnes, W. L.; García de Abajo, F. J. Diffractive arrays of gold nanoparticles near an interface: Critical role of the substrate. *Physical Review B* **2010**, *82*, 155447.
- [241] Kravets, V. G.; Schedin, F.; Grigorenko, A. N. Extremely Narrow Plasmon Resonances Based on Diffraction Coupling of Localized Plasmons in Arrays of Metallic Nanoparticles. *Physical Review Letters* **2008**, *101*, 087403.
- [242] Cherqui, C.; Bourgeois, M. R.; Wang, D.; Schatz, G. C. Plasmonic Surface Lattice Resonances: Theory and Computation. *Accounts of Chemical Research* **2019**, *52*, 2548–2558.
- [243] Humphrey, A. D.; Meinzer, N.; Starkey, T. A.; Barnes, W. L. Surface Lattice Resonances in Plasmonic Arrays of Asymmetric Disc Dimers. *ACS Photonics* **2016**, *3*, 634–639.
- [244] Henzie, J.; Lee, M. H.; Odom, T. W. Multiscale patterning of plasmonic metamaterials. *Nature Nanotechnology* **2007**, *2*, 549–554.
- [245] Honold, T.; Volk, K.; Retsch, M.; Karg, M. Binary plasmonic honeycomb structures: High-resolution EDX mapping and optical properties. *Colloids and Surfaces A: Physicochemical and Engineering Aspects* **2016**, *510*, 198–204.
- [246] Chu, Y.; Schonbrun, E.; Yang, T.; Crozier, K. B. Experimental observation of narrow surface plasmon resonances in gold nanoparticle arrays. *Applied Physics Letters* **2008**, *93*, 181108.
- [247] Müller, M. B.; Kuttner, C.; König, T. A. F.; Tsukruk, V. V.; Förster, S.; Karg, M.; Fery, A. Plasmonic Library Based on Substrate-Supported Gradienital Plasmonic Arrays. *ACS Nano* **2014**, *8*, 9410–9421.
- [248] Brasse, Y.; Müller, M. B.; Karg, M.; Kuttner, C.; König, T. A. F.; Fery, A. Magnetic and Electric Resonances in Particle-to-Film-Coupled Functional Nanostructures. *ACS Applied Materials & Interfaces* **2018**, *10*, 3133–3141.
- [249] Haynes, C. L.; McFarland, A. D.; Zhao, L.; Van Duyne, R. P.; Schatz, G. C.; Gunnarsson, L.; Prikulis, J.; Kasemo, B.; Käll, M. Nanoparticle Optics: The Importance of Radiative Dipole Coupling in Two-Dimensional Nanoparticle Arrays. *The Journal of Physical Chemistry B* **2003**, *107*, 7337–7342.
- [250] Jenkins, J. A.; Zhou, Y.; Thota, S.; Tian, X.; Zhao, X.; Zou, S.; Zhao, J. Blue-Shifted Narrow Localized Surface Plasmon Resonance from Dipole Coupling in Gold Nanoparticle Random Arrays. *The Journal of Physical Chemistry C* **2014**, *118*, 26276–26283.
- [251] Mueller, M.; Tebbe, M.; Andreeva, D. V.; Karg, M.; Puebla, R. A. A.; Perez, N. P.; Fery, A. Large-Area Organization of pNIPAM-Coated Nanostars as SERS Platforms for Polycyclic Aromatic Hydrocarbons Sensing in Gas Phase. *Langmuir* **2012**, *28*, 9168–9173.

-
- [252] Yang, A.; Li, Z.; Knudson, M. P.; Hryn, A. J.; Wang, W.; Aydin, K.; Odom, T. W. Unidirectional Lasing from Template-Stripped Two-Dimensional Plasmonic Crystals. *ACS Nano* **2015**, *9*, 11582–11588.
- [253] Wang, D.; Yang, A.; Hryn, A. J.; Schatz, G. C.; Odom, T. W. Superlattice Plasmons in Hierarchical Au Nanoparticle Arrays. *ACS Photonics* **2015**, *2*, 1789–1794.
- [254] Maeda, Y.; Higuchi, T.; Ikeda, I. Change in Hydration State during the Coil-Globule Transition of Aqueous Solutions of Poly(N-isopropylacrylamide) as Evidenced by FTIR Spectroscopy. *Langmuir* **2000**, *16*, 7503–7509.
- [255] Wang, X.; Qiu, X.; Wu, C. Comparison of the Coil-to-Globule and the Globule-to-Coil Transitions of a Single Poly(N-isopropylacrylamide) Homopolymer Chain in Water. *Macromolecules* **1998**, *31*, 2972–2976.
- [256] Schild, H. G. Poly(N-isopropylacrylamide): experiment, theory and application. *Progress in polymer science* **1992**, *17*, 163–249.
- [257] Kim, J.; Kim, B.; Ryu, J.; Jeong, Y.; Park, J.; Kim, H.; Chun, K. Potential of Thermo-Sensitive Hydrogel as an Actuator. *Japanese Journal of Applied Physics* **2005**, *44*, 5764–5768.
- [258] Gerlach, G.; Guenther, M.; Sorber, J.; Suchanek, G.; Arndt, K.-F.; Richter, A. Chemical and pH sensors based on the swelling behavior of hydrogels. *Sens. Actuators, B* **2005**, *111-112*, 555–561.
- [259] Li, X.; Gao, Y.; Serpe, M. J. Responsive Polymer-Based Assemblies for Sensing Applications. *Macromol. Rapid Commun.* **2015**, *36*, 1382–1392.
- [260] Guerzoni, L. P. B.; Bohl, J.; Jans, A.; Rose, J. C.; Koehler, J.; Kuehne, A. J. C.; De Laporte, L. Microfluidic fabrication of polyethylene glycol microgel capsules with tailored properties for the delivery of biomolecules. *Biomaterials Science* **2017**, *5*, 1549–1557.
- [261] Mura, S.; Nicolas, J.; Couvreur, P. Stimuli-responsive nanocarriers for drug delivery. *Nature Materials* **2013**, *12*, 991–1003.
- [262] Yan, N.; Zhang, J.; Yuan, Y.; Chen, G.-T.; Dyson, P. J.; Li, Z.-C.; Kou, Y. Thermoresponsive polymers based on polyvinylpyrrolidone: applications in nanoparticle catalysis. *Chemical Communications* **2010**, *46*, 1631–1633.
- [263] Wu, S.; Dzubiella, J.; Kaiser, J.; Drechsler, M.; Guo, X.; Ballauff, M.; Lu, Y. Thermosensitive Au-PNIPAM Yolk-Shell Nanoparticles with Tunable Selectivity for Catalysis. *Angewandte Chemie International Edition* **2012**, *51*, 2229–2233.
- [264] Jaber, S.; Karg, M.; Morfa, A.; Mulvaney, P. 2D assembly of gold-PNIPAM core-shell nanocrystals. *Physical Chemistry Chemical Physics* **2011**, *13*, 5576–5578.

- [265] Karg, M.; Hellweg, T.; Mulvaney, P. Self-Assembly of Tunable Nanocrystal Superlattices Using Poly-(NIPAM) Spacers. *Advanced Functional Materials* **2011**, *21*, 4668–4676.
- [266] Wu, C.; Zhou, S.; Au-Yeung, S. C. F.; Jiang, S. Volume phase transition of spherical microgel particles. *Die Angewandte Makromolekulare Chemie* **1996**, *240*, 123–136.
- [267] Gan, D.; Lyon, L. A. Tunable Swelling Kinetics in Core-Shell Hydrogel Nanoparticles. *Journal of American Chemical Society* **2001**, *123*, 7511–7517.
- [268] Bergman, M. J.; Pedersen, J. S.; Schurtenberger, P.; Boon, N. Controlling the morphology of microgels by ionic stimuli. *Soft Matter* **2020**, *16*, 2786–2794.
- [269] Ponomareva, E.; Tadgell, B.; Hildebrandt, M.; Krüsmann, M.; Prevost, S.; Mulvaney, P.; Karg, M. The fuzzy sphere morphology is responsible for the increase in light scattering during the shrinkage of thermoresponsive microgels. *Soft Matter* **2022**, *18*, 807–825.
- [270] Yanase, K.; Buchner, R.; Sato, T. Microglobule formation and a microscopic order parameter monitoring the phase transition of aqueous poly (N-isopropylacrylamide) solution. *Physical Review Materials* **2018**, *2*, 085601.
- [271] Dupin, D.; Rosselgong, J.; Armes, S. P.; Routh, A. F. Swelling Kinetics for a pH-Induced Latex-to-Microgel Transition. *Langmuir* **2007**, *23*, 4035–4041.
- [272] Gianni, S.; Morrone, A.; Giri, R.; Brunori, M. A folding-after-binding mechanism describes the recognition between the transactivation domain of c-Myb and the KIX domain of the CREB-binding protein. *Biochemical and Biophysical Research Communications* **2012**, *428*, 205–9.
- [273] Bernasconi, C. *Relaxation Kinetics*; Academic Press Inc, 1976.
- [274] Ferguson, N.; Berriman, J.; Petrovich, M.; Sharpe, T. D.; Finch, J. T.; Fersht, A. R. Rapid amyloid fiber formation from the fast-folding WW domain FBP28. *Proceedings of the National Academy of Sciences* **2003**, *100*, 9814–9819.
- [275] Bonetti, D.; Camilloni, C.; Visconti, L.; Longhi, S.; Brunori, M.; Vendruscolo, M.; Gianni, S. Identification and structural characterization of an intermediate in the folding of the measles virus X domain. *Journal of Biological Chemistry* **2016**, *291*, 10886–10892.
- [276] Bonetti, D.; Toto, A.; Giri, R.; Morrone, A.; Sanfelice, D.; Pastore, A.; Temussi, P.; Gianni, S.; Brunori, M. The kinetics of folding of frataxin. *Physical Chemistry Chemical Physics* **2014**, *16*, 6391–6397.
- [277] Bonetti, D.; Troilo, F.; Toto, A.; Brunori, M.; Longhi, S.; Gianni, S. Analyzing the folding and binding steps of an intrinsically disordered protein by protein engineering. *Biochemistry* **2017**, *56*, 3780–3786.

- [278] Carl, N.; Sindram, J.; Gallei, M.; Egelhaaf, S. U.; Karg, M. From normal diffusion to superdiffusion: Photothermal heating of plasmonic core-shell microgels. *Physical Review E* **2019**, *100*, 052605.
- [279] Hayt Jr. William, H.; Kemmerly. Jack, E.; Durbin. Steven, M. *Engineering Circuit Analysis*, 9th ed.; McGraw-Hill Education: USA, 2018.
- [280] McKee, C. B. An Accurate Equation for the Electrolytic Conductivity of Potassium Chloride Solutions. *Journal of Solution Chemistry* **2009**, *38*, 1155–1172.
- [281] Cors, M.; Wiehemeier, L.; Oberdisse, J.; Hellweg, T. Deuteration-induced volume phase transition temperature shift of PNIPMAM microgels. *Polymers* **2019**, *11*, 620.
- [282] Gibson, M. I.; O'Reilly, R. K. To aggregate, or not to aggregate? considerations in the design and application of polymeric thermally-responsive nanoparticles. *Chemical Society Reviews* **2013**, *42*, 7204–7213.
- [283] Turek, V. A.; Cormier, S.; Sierra-Martin, B.; Keyser, U. F.; Ding, T.; Baumberg, J. J. The Crucial Role of Charge in Thermoresponsive-Polymer-Assisted Reversible Dis/Assembly of Gold Nanoparticles. *Advanced Optical Materials* **2018**, *6*.
- [284] Zhang, Z.; Maji, S.; Antunes, A. B. d. F.; De Rycke, R.; Zhang, Q.; Hoogenboom, R.; De Geest, B. G. Salt Plays a Pivotal Role in the Temperature-Responsive Aggregation and Layer-by-Layer Assembly of Polymer-Decorated Gold Nanoparticles. *Chemistry of Materials* **2013**, *25*, 4297–4303.
- [285] Gilányi, T.; Varga, I.; Mészáros, R.; Filipcsei, G.; Zrínyi, M. Interaction of Monodisperse Poly(N-isopropylacrylamide) Microgel Particles with Sodium Dodecyl Sulfate in Aqueous Solution. *Langmuir* **2001**, *17*, 4764–4769.
- [286] Wang, G.; Pelton, R.; Zhang, J. Sodium dodecyl sulfate binding to poly(N-isopropylacrylamide) microgel latex studied by isothermal titration calorimetry. *Colloids and Surfaces A: Physicochemical and Engineering Aspects* **1999**, *153*, 335–340.
- [287] Shibayama, M.; Nagai, K. Shrinking Kinetics of Poly(N-isopropylacrylamide) Gels T-Jumped across Their Volume Phase Transition Temperatures. *Macromolecules* **1999**, *32*, 7461–7468.
- [288] Okajima, T.; Harada, I.; Nishio, K.; Hirotsu, S. Kinetics of volume phase transition in poly(N-isopropylacrylamide) gels. *The Journal of Chemical Physics* **2002**, *116*, 9068–9077.
- [289] Pham, T. T.; Bajaj, M.; Prakash, J. R. Brownian dynamics simulation of polymer collapse in a poor solvent: influence of implicit hydrodynamic interactions. *Soft Matter* **2008**, *4*, 1196–1207.

- [290] Timoshenko, E. G.; Kuznetsov, Y. A. Equilibrium and kinetics at the coil-to-globule transition of star and comb heteropolymers in infinitely dilute solutions. *Colloids and Surfaces A: Physicochemical and Engineering Aspects* **2001**, *190*, 135–144.
- [291] *AN.019.T64: Temperature Calibration of T-Jump Instrument TJ-64 using Tris / Phenol Red*; Hi Tech Scientific.
- [292] Hakala, T. K.; Rekola, H. T.; Väkeväinen, A. I.; Martikainen, J.-P.; Nečada, M.; Moilanen, A. J.; Törmä, P. Lasing in dark and bright modes of a finite-sized plasmonic lattice. *Nature Communications* **2017**, *8*, 13687.
- [293] Minopoli, A.; Acunzo, A.; Della Ventura, B.; Velotta, R. Nanostructured Surfaces as Plasmonic Biosensors: A Review. *Advanced Materials Interfaces* **2021**, 2101133.